UCLA
UCLA Electronic Theses and Dissertations

Title
Effects of Plasma Etching on GeSbTe Compositional Control

Permalink
https://escholarship.org/uc/item/99v6p6sx

Author
Chen, Ernest Lloyd

Publication Date
2020

Peer reviewed|Thesis/dissertation

UNIVERSITY OF CALIFORNIA

Los Angeles

Effects of Plasma Etching on GeSbTe Compositional Control

A dissertation submitted in partial satisfaction of the

requirements of the degree, Doctor of Philosophy in

Chemical Engineering

by

Ernest Lloyd Chen

2020

ABSTRACT OF THE DISSERTATION

Effects of Plasma Etching on GeSbTe Compositional Control

by

Ernest Lloyd Chen

Doctor of Philosophy in Chemical Engineering

University of California, Los Angeles, 2020

Professor Jane Pei-Chen Chang, Chair

This work addressed the processing challenges associated with the phase-change material GeSbTe (GST) for use in phase-change memory (PCM) devices. As the GST composition dictates its crystallization temperature, a careful control of the composition is essential to ensure the targeted phase-change characteristics. This work focused on studying the effect of surface states and plasma chemistries on the compositional control of GST.

The study of surface states focused on the effect of ambient exposure on changing the GST composition and reactivity. Ambient oxidation of GST was shown to be most strongly influenced by water vapor in the atmosphere, which resulted in a greater extent of oxidation than those exposed to N_2 or O_2. To restore the GST composition by wet chemical processing, the effectiveness depends significantly on whether the native oxides were removed, as the difference in polarity between metallic Ge, Sb, Te bonds and Ge-O, Sb-O, Te-O bonds made the oxides more susceptible to removal by polar chemistries. For example, citric acid resulted in significantly greater change in composition on the oxidized GST than on sputter-cleaned GST.

For plasma etching of GST, thermochemical analysis was used to assess the viability of etch chemistries by quantifying the volatility of the potential etch products, followed by plasma etching experiments. First, halogen chemistries including Cl_2 and SF_6/Ar were evaluated based on

thermochemical analysis, predicting that GST could be etched by both chemistries, with Ge being preferentially removed, followed by Sb then Te. Plasma etch experiments demonstrated an etch rate of GST by Cl_2/Ar was 13.1 nm/min and that by SF_6/Ar was negligible. The extent of halogen incorporation on the etched films followed the increasing bond energies between individual GST elements with the halogen species. SF_6/Ar resulted in the smaller composition change and less crystallization temperature change, but the significant halogenation was problematic.

For H_2 plasma, thermochemical analysis predicted that atomic hydrogen could etch all elements, but molecular hydrogen could not. The effect of H_2 plasma was examined first by etching each GST element separately. It was found that hydrogen plasmas etched Sb the fastest (with SbH_x as dominant etch products) and Ge the slowest (with no observed gas phase products). The etch rate of GST in a H_2 plasma was 32.7 nm/min when etched directly but was reduced to zero in a downstream configuration. Sb and Te were preferentially removed by H_2 plasma. This observed preferential removal of Sb and Te over Ge followed the order of the measured etch rates of Ge, Sb, and Te, suggesting that the preferential removal was due to the reaction kinetics rather than the desorption of the etch products from the surface. H_2 plasma resulted in greater composition change than SF_6/Ar plasma, less composition change than Cl_2/Ar plasma, and greater crystallization temperature change than either halogen plasma.

For the CH_4 plasmas, only thermodynamic data for Ge was available, and it suggested that CH_3 could etch Ge while CH_4 could not. CH_4 plasmas were found to etch Ge the fastest, Te moderately, but deposited on Sb (no etch). Consistent with these observations, in etching GST, preferential removal of Ge and Te was observed, leaving the surface enriched with Sb, with an etch rate of 16.8 nm/min. The addition of N_2 to CH_4 plasma led to the formation of HCN and NH_x, which reduced the etch rate to 8.4 nm/min., likely due to the dilution of CH_4 and scavenging of

atomic H. Among the CH$_4$-containing plasmas, CH$_4$/N$_2$ plasma resulted in the smallest composition and crystallization temperature changes in GST.

In summary, considering the effects of surface states and plasma chemistries on GST composition and crystallization temperature, the removal of the surface oxides followed by CH$_4$/N$_2$ or H$_2$ plasma processing was suggested to be most suitable for etching GST while maintaining the target composition and crystallization temperature.

The dissertation of Ernest Lloyd Chen is approved.

Dante Simonetti

Vasilios Manousiouthakis

Richard Wirz

Jane Pei-Chen Chang, Committee Chair

University of California, Los Angeles

2020

Dedicated to the memory of my aunt

Beatrice Hsu

Table of Contents

List of Figures

ACKNOWLEDGEMENTS

I'd like to begin this section by thanking Prof. Jane Chang for serving as my research advisor for the past five years. Your expertise and attention to detail and the high standards you set for research in your lab have forever influenced how I approach and carry out my research. I also greatly admire how you strive for excellence in all your duties as a professor, from teaching to research to leadership.

Next, I want to thank Prof. Dante Simonetti, Prof. Vasilios Manousiouthakis, and Prof. Richard Wirz for serving on my committee. I have had the chance to take courses taught by each of you and thoroughly enjoyed all of them. I also want to acknowledge the generous funding support I have received throughout my PhD, including from C-DEN and SRC. I especially want to thank Meihua Shen, Thorsten Lill, and John Hoang at Lam Research for their funding support and technical advising and their colleagues Nerissa Draeger and Lubab Sheet for the opportunities to visit Lam Research campuses to present the work supported by them. I look forward to seeing you all again in my professional career. I would also like to thank Changju Choi and Tristan Tronic at Intel and Nathan Marchack at IBM for funding support for other projects I worked on during my PhD. Lastly, I would like to thank Scott Fong, Chris Neumann, and Prof. Philip Wong at Stanford University, as well as Lei Pan and Prof. Kang Wang at UCLA for providing the samples used throughout this thesis.

I must thank Nick Altieri, my lab mentor, for his patience in teaching me to be a functioning member of the Chang Lab, Hamid Razavi, for his expertise in plasma physics and electronics that made some of the work in this thesis possible, Gary Sang, for his diligence and his shared love of Nintendo products, and Jae Hwang, for his efforts in helping me with my thesis revisions. I would also like to thank other past and present members of the Chang Lab, including Wilson Lin, Jack

Chen, Diana Chien, Colin Rementer, Cyrus Cheung, Jeffrey Chang, Kevin Fitzell, Adrian Acosta, and Taylor Smith. Finally, I want to thank Ryan Sheil, who joined the lab with me five years ago. I don't think I would have made it through this process without you. Here's to late nights in the lab and Sundays spent watching football (and losing in fantasy every weekend)!

I would never have made it to graduate school in the first place without mentors and guidance along the way. I want to thank Prof. Marty Grove for giving me the chance to spend my high school summers in a basement taking blurry grayscale pictures of tiny crystals on a scanning electron microscope and for teaching me how to put together a poster in PowerPoint. Fast-forward almost ten years later, and I am still frequently in a basement taking blurry grayscale pictures on a scanning electron microscope and putting together posters in PowerPoint. I also want to thank Prof. Roya Maboudian and Anna Harley-Trochimczyk. In working with you, I learned to apply chemical engineering principles to surface science and electronic devices and gained an appreciation for simple solutions to the problems we faced in lab. I also want to acknowledge Prof. David Graves, whose course on microelectronic fabrication (that I admittedly did pretty poorly in) convinced me to pursue a career in the field. I'd also like to thank Aniruddha Joi, Zhongwei Zhu, Katie Nardi, Yezdi Dordi, and YS Kim at Lam Research for having been such great mentors and managers to me at my internships. I look forward to seeing you all again in my professional career.

I couldn't have come this far without the support of friends outside the lab to keep me sane. To the UCLA Archery club, thank you for giving me a space at UCLA that didn't revolve around graduate school, especially Daniel Kho, Kimberly Wang, Kaley Kubokawa, Peter Ferguson and coaches Stanley Cheng, Mikkiel Cheng, and Alan Chan. To my fellow Golden Bears-who-went-to-grad-school, including Kevin Hou, Michael Tsang, Gary Li, Ryan Sawadichai, Chris Choi, and Alisha Chou. To Ryan Sawadichai, who went from sitting next to me in multivariable calculus to

following me around at AVS conferences (and taking pictures of me practicing my talk with Prof. Chang -- no wonder I'm always looking over my shoulder)? To Gary Li, I'm not sure how we both went from UC Berkeley to UCLA to work on plasma-related fields, but it happened. Thank you for always fielding my questions on plasmas, even after you were done being TA for Prof. Wirz's class.

Finally, I want to acknowledge my family members who have been with me along the way, especially Roger Tsai and Hantine Hsu. Last but perhaps most important of all, I want to thank my mother and father for their unconditional love and support throughout my life and especially these last five years. I could not have become who I am today without all of your hard work and sacrifice, and this dissertation could not have been done without you.

2011-2015	B. S., Chemical Engineering Minor in Electrical Engineering/Computer Sciences University of California, Berkeley Berkeley, CA
2014, 2015	Process Engineer Intern Lam Research Corporation Fremont, CA
2015-2020	Graduate Student Researcher Department of Chemical and Biomolecular Engineering University of California, Los Angeles Los Angeles, CA
2018, 2019, 2020	Teaching Assistant Department of Chemical and Biomolecular Engineering University of California, Los Angeles Los Angeles, CA

AWARDS

2014	Lam Research Core Values Scholarship
2019	UCLA Chemical and Biomolecular Engineering 4th Year Department Symposium Best Talk Award

PUBLICATIONS

J. K. Chen, N. D. Altieri, T. Kim, **E. Chen**, T. Lill, M. Shen, and J. P. Chang, "Directional etch of magnetic and noble metals. II. Organic chemical vapor etch," *J. Vac. Sci. Technol. A,* 35 (5) (2017) 05C305

J. K. Chen, T. Kim, N. D. Altieri, **E. Chen**, and J. P. Chang, "Ion beam assisted organic chemical vapor etch of magnetic thin films," *J. Vac. Sci. Technol. A,* 35 (3) (2017) 031304

X. Sang, **E. Chen**, and J.P. Chang, "Patterning nickel for extreme ultraviolet lithography mask application I. Atomic layer etch processing," *J. Vac. Sci. Technol. A,* 38 (4) (2020) 042603

M. Shen, T. Lill, N. D. Altieri, J. Hoang, S. Chiou, J. Sims, A. McKerrow, R. Dylewicz, **E. Chen**, H. Razavi, and J.P. Chang, "A Review on the Recent Progress in Patterning Phase Change Materials," *J. Vac. Sci. Technol. A* 38 (6) (2020) 060802

PRESENTATIONS

E. Chen, N.D. Altieri, C. Neumann, S. Fong, H.S.P. Wong, M. Shen, T. Lill, and J.P. Chang, "Plasma Processing of Phase Change Materials for PCRAM," AVS 66th International Symposium & Exhibition, Columbus, OH, Oct. 22, (2019).

E. Chen, J.P. Chang, N.D. Altieri, M. Shen, and T. Lill, "Plasma Processing of Phase Change Materials," Lam Research University Collaboration Showcase, Fremont, CA, Aug. 9, (2019).

E. Chen, N.D. Altieri, and J.P. Chang, "Surface Chemistry Controlled Patterning of Cobalt & Palladium," C-DEN Workshop, San Diego, CA, Nov. 16, (2018).

N.D. Altieri, **E. Chen**, S. Fong, C. Neumann, H.S.P. Wong, M. Shen, T. Lill, and J.P. Chang, "Plasma Processing of Phase Change Materials for PCRAM," AVS 65th International Symposium & Exhibition, Long Beach, CA, Oct. 24, (2018).

E. Chen, J.P. Chang, N.D. Altieri, M. Shen, and T. Lill, "Plasma Processing of Phase Change Materials," Lam Research University Collaboration Showcase, Tualatin, OR, Aug. 9, (2018).

N.D. Altieri, **E. Chen**, M. Shen, T. Lill, and J.P. Chang, "Pursuing Vapor Phase Cleaning of Metals," Lam Research University Collaboration Showcase, Tualatin, OR, Aug. 9, (2018).

E. Chen, N.D. Altieri, and J.P. Chang, "Surface Chemistry Controlled Patterning of EUV Masks," C-DEN Workshop, San Jose, CA, May 18, (2018).

Chapter 1 Background and Motivation

This section introduces the materials and nanoscale structures that were the focus of this work, with an emphasis on the current state-of-the-art in techniques used for patterning these materials and structures and the shortcomings of these techniques in light of the manufacturing challenges faced by the semiconductor industry for the enablement of phase change memory

1.1 Memory Technology Overview

Since it was first coined by Gordon Moore in a magazine article in 1965, Moore's Law, the observation that the number of transistors in an integrated circuit doubles roughly every two years, has been used as a guide by the semiconductor industry for long-term planning and setting milestones for research and development, and as the semiconductor industry has continued to scale down feature sizes in order to meet these goals, the challenge of keeping Moore's Law alive has gotten exponentially more difficult (Moore 2006). Figure 1-1 shows how transistor scaling has progressed through three distinct eras of scaling: geometric scaling, equivalent scaling, and hyper-scaling.
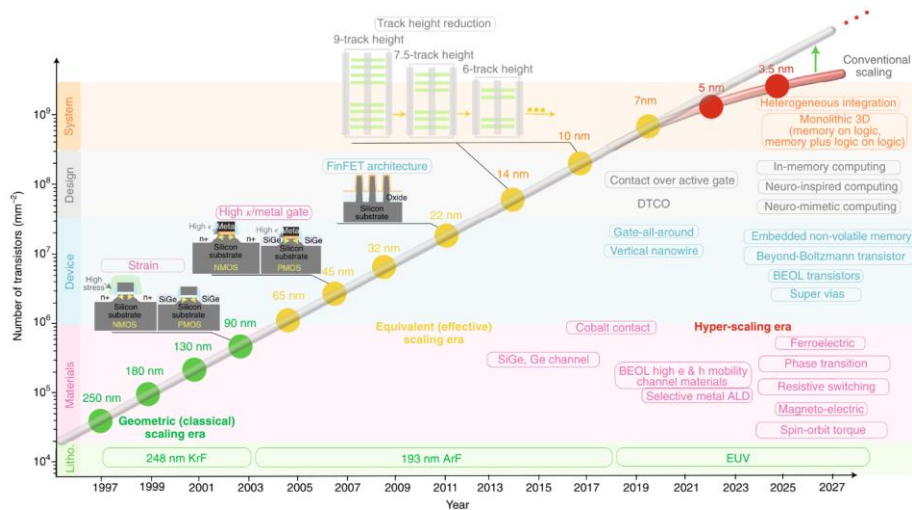
Figure 1-1. Transistor density scaling over the years through distinct eras of scaling and projected through 2027. Phase transition materials, embedded non-volatile memory, and neuro-mimetic computing are all relevant to the material system studied in this dissertation. (Salahuddin 2018)

The majority of semiconductor production is either for logic or memory (Badaroglu 2017). In the logic segment, which includes products such as the processors that power modern computers and phones, transistor dimensions continue to be shrunk, but the device architecture known as FinFET is expected to continue to be the state-of-the-art through the early 2020's, with further advancements after that relying on continued refinements to the transistor, such as gate-all-around (GAA) transistors (Hisamoto 2000, 2017). Meanwhile, in memory, flash memory continues to displace older hard disk drives (HDD) media and static random-access memory (SRAM) and dynamic random-access memory (DRAM) continue to scale using 3D stacking of cells. However, charge-based storage such as flash has gone from storing single bits per cell to stacking three (triple-level cell flash) and is facing challenges in continued scaling due to both quantum effects and the complexity of engineering such structures (Badaroglu 2017). These improvements in logic and memory technologies have led to ever-increasing processor speed and memory capacity in logic and memory, respectively. This lead to a gap in the performance of processors and memory, which is depicted in Figure 1-2. At its worst from 1980 to the mid 2000's, when both processor speed and memory latency plateaued, and this processor-memory performance gap still exists today.
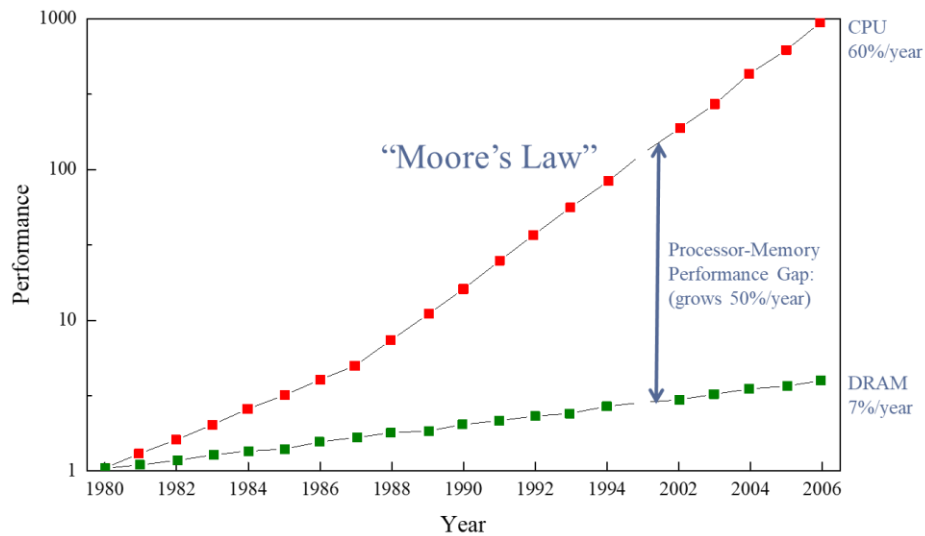
Figure 1-2. Illustration of the memory-wall problem, where processor and memory performance rapidly diverged from one another between 1980 and the mid-2000's before both began to plateau. The disparity continues to exist today. Adapted from (Clauset 2015)

One of four technology innovations needed to usher in the era of hyper-scaling, the scaling of a technology from a few billion to a few trillion transistors, is the embedded high performance memory beyond Static Random Access Memory (SRAM) and Dynamic Random Access Memory (DRAM), which allows the semiconductor industry to close the processor-memory gap (Salahuddin 2018). The pursuit of these embedded high-performance memories has required the development of new memory structures and technologies that do not rely on the same materials and storage mechanisms as the current state-of-the-art. Some of these memory structures, summarized in Figure 1-1 and Table 1-1 include phase-change memory and ferroelectric RAM, which rely on magnetic or structural changes in a material and are often read as a change in electrical resistance. The simultaneous development of so many memory devices has accordingly required the development of the many material systems needed to make these next-generation memory devices, and with these new material systems comes a host of processing challenges that need to be overcome, which forms the motivation for this work.

3

Table 1-1. Table of relevant operating characteristics of different memory types, including PCRAM and STT-MRAM (Kent 2015).

	SRAM	DRAM	HDD	NAND Flash	FeRAM	RRAM	PC-RAM	STT-MRAM
Speed	1 ns	30 ns	9 ms	10^3-10^4 ns	30 ns	1-100 ns	50 ns	1-10 ns
Endurance	High	High	High	Low	High	Low	Low	Very High
Density (F^2)	100	6-8	(2/3)	4-8	6-10	6-10	6-10	8-20
Write Energy	1 pJ	2 pJ	100 mJ	10 nJ	1 pJ	1 pJ	100 pJ	100 fJ
Non-volatile	No	No	Yes	Yes	Yes	Yes	Yes	Yes
Maturity	Prod.	Prod.	Prod.	Prod.	Prod.	Dev.	Prod.	Prod.

Prod. = in production; Dev. = in development

While PCRAM does not conclusively have an advantage any of the other nonvolatile memories in performance, its advantages (multibit operation, lower resistance variability), as qualitatively represented in Table 1-2, warrants further consideration of its practical implementation.

Table 1-2. Comparison of different nonvolatile memory properties. ✓✓ - Excellent; ✓ - Good; ✗ - Poor. (Gupta 2019)

Property	FeRAM	PCM	MRAM	RRAM
Scalability	✗	✓✓	✓	✓✓
Multibit Programming	✗	✓✓	✗	✓
Data Retention	✓	✓	✓	✓✓
Endurance	✓✓	✓	✓✓	✓
Power	✓✓	✗	✓	✓
CMOS/3D Integration	✓✓	✓✓	✓	✓✓
Speed/Latency	✓✓	✓	✓✓	✓
Variability/Mismatch	✓✓	✓	✗	✗

One important property of different memory devices is volatility, which describes whether a memory device is capable of retaining information when no power is supplied to it. Nonvolatile memory can still hold information when turned off, while volatile memory does not hold information when turned off and is frequently much faster than nonvolatile memory. Most RAM used today is volatile and holds information currently being used by a computer. SRAM and

DRAM are two examples of volatile RAM, and both rely on powered circuit elements to store information. On the other hand, mass storage memory such as HDD and NAND flash needs to be nonvolatile. An HDD stores data based on the patterns of magnetized domains in a layer of magnetized materials, while flash memory stores data by trapping electrons within an array of floating gate transistors. A typical computer that one might purchase today uses a combination of volatile and nonvolatile memory to handle the needs of the computer.

More recently, memory devices that combine the aspects of RAM and mass storage have been developed. Memory such as ferroelectric RAM (FeRAM), phase-change RAM (PCRAM), resistive RAM (RRAM), and spin-torque transfer magnetoresistive RAM (STT-MRAM) are all nonvolatile random-access memories capable of speeds approaching those of SRAM and DRAM while still being nonvolatile. FeRAM is similar to DRAM, which stores data by charging and discharging an array of capacitors but differs in that FeRAM uses a ferroelectric layer such lead zirconium titanate (PZT) rather than a dielectric layer. RRAM and PCRAM are similar in that they both rely on the change of resistance in a material. In PCRAM, the resistance in a phase-change material such as $Ge_2Sb_2Te_5$ (GST) changes with the phase transition between amorphous and crystalline states. In the case of RRAM, the resistance across a dielectric layer such as HfO_2 changes due to the formation of a conductive filament through the layer. In STT-MRAM, the tunneling magnetoresistance in a magnetic tunnel junction consisting of layer of ferromagnetic materials such as CoFe changed based upon the ordering of the magnetic layers.

As shown in Table 1-1, PCM has comparable density to other nonvolatile memories but is not quite as fast, requires more energy for operation, and has worse endurance than the other nonvolatile memories. However, it does have other advantages, which are described in Table 1-2. PCM is expected to have better scalability than other nonvolatile memories, as well as the best

potential for multibit operation. It also integrates well with CMOS (complementary metal-oxide-semiconductor) technology and 3D integration schemes (i.e. stacking of multiple layers of PCM cells) and exhibits less variability between on-off states between cells (Badaroglu 2017). Due to the nature of its memory storage mechanism (changing crystal structure), PCM is also radiation-hard, which makes it an attractive candidate for aerospace applications where radiation may be a concern (Raoux 2009).

1.2 Phase-Change Memory

Phase-change random access memory (PCRAM) is a memory structure that takes advantage of the difference in electrical resistivity between two crystalline phases of a material, known as a phase-change material (PCM) (Wong 2010). Generally, these phases are crystalline (low resistance) and amorphous (high resistance) and switching between the crystalline and the amorphous state allows a PCRAM cell to flip between the off and on states (i.e., 0 and 1). It is also possible for a PCM to exhibit multiple crystal structures with distinct electrical resistivities, potentially allowing for multi-bit operation (i.e., 0, 1, 2, and so on). The crystalline-amorphous transition is accomplished by heating one side of the PCM layer, usually by applying a voltage to the adjacent electrode. By heating the PCM layer, a mushroom-shaped switching region forms, and only the material in this region undergoes the phase-transition (Wong 2015). Figure 1-3(a) illustrates this switching region (Wong 2015). To set the PCM layer (amorphous to crystalline), the temperature of the PCM layer is held above the crystallization temperature (T_c) until the crystalline region has formed. To reset the PCM layer (crystalline to amorphous), the temperature of the PCM layer is quickly ramped above the melting temperature (T_{melt}) and allowed to cool down to room temperature. Reading the PCRAM cell does not push the temperature past T_c or T_{melt} (Wong 2010). The temperature v. time curves for each of these actions is illustrated in Figure

6

1-3(b) (Wong 2010), and the length of these steps determines the read and write speeds of a

PCRAM device. Figure 1-3 (c) shows an SEM of a PCRAM cell showing each of the major

components (Kau 2009). The width of the PCRAM cell is on the order of 40 to 230 nm (Kau 2009).
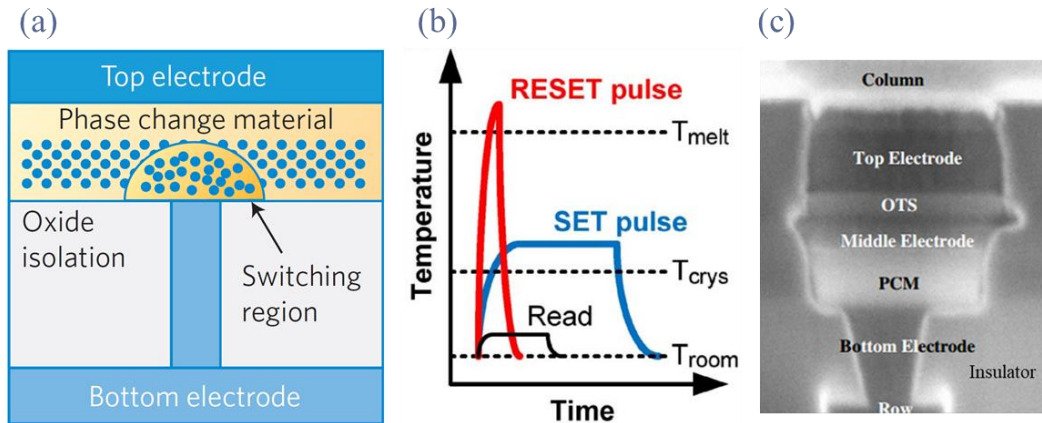
Figure 1-3. (a) Illustration of a mushroom-shaped switching region in a PCM, which is the only portion of the PCM that undergoes the phase transition (Wong 2015). (b) Temperature v. time curve showing the pulses used to set, reset, and read a PCM cell. T_{melt}, T_c, and T_{room} are the melting, crystallization and room temperatures, respectively (Wong 2010). (c) Close-up of a phase-change memory cell illustrating its main components, with width scale on the order of 40-230 nm (Kau 2009).

A PCRAM cell consists of different electrodes surrounded by an insulator, with the PCM

layer sandwiched between the bottom and middle electrode and the selector device (such as an

Ovonic threshold switch (OTS) or a diode) sandwiched between the middle and top electrodes. A

table of typical materials used for each layer is shown in Table 1-3.

Table 1-3. Typical materials used in each layer of the device shown in Figure 1-3(c). (Kau 2009).

Layer	Materials			
Electrode	TiN	TaN	W	
OTS	PolySi	CuO	NiO	TiO_2
Phase Change	$Ge_xSb_yTe_z$			
Column/Row	TiN	W		
Insulator	SiO_2	Si_3N_4		

To serve as a PCM, a material needs to have a high-speed phase transition (on the order of 100's of ns or less), long-term thermal stability of its amorphous state (on the order of 10 years or greater), and a large resistance change between its amorphous and crystalline states (at least 2 orders of magnitude) (Wong 2010). Table 1-4 shows a selection of PCM's and their relevant characteristics, including crystallization temperature and the activation energy for the process, which partly dictate the speed of the phase transition, as well as the data lifetime, which is reported as the temperature at which the PCM can retain data for 10 years, and the ratio of the electrical resistance between the reset and set states. $Al_{50}Sb_{50}$ is notable due to having a two-step resistance change between its on and off states, and their ratios are reported in the table.

Of the different phase-change materials, the family of chalcogenide glasses composed of Ge, Sb, and Te has been the most commonly used. As seen in Table 1-4, $Ge_2Sb_2Te_5$ has the lowest activation energy and crystallization temperature of the materials listed, which should translate to faster switching and lower power consumption in a memory device, while still maintaining acceptable data lifetime. $Ge_2Sb_2Te_5$ has been previously used in Blu-Ray technology, where the changes in optical reflectivity associated with the phase transitions were stimulated and detected using a laser. The most commonly used PCM's belong to the family of materials along the GeTe-Sb_2Te_3 tie line, which is shown in Figure 1-4. $Ge_1Sb_4Te_7$, $Ge_1Sb_2Te_4$, and $Ge_2Sb_2Te_5$ are the eutectic compositions of GeTe-Sb_2Te_3, and $Ge_2Sb_2Te_5$ (GST) is the most commonly used PCM for PCRAM applications (Wong 2010, Wong 2015).

Table 1-4. Table of different PCM's and their relevant characteristics. AlSb has two reset/set resistance ratios due to the presence of multiple crystalline phases.

Material	E_a (eV)	T_c (ºC)	Ratio of Reset/Set Resistance	Thickness (nm)	Data Lifetime	Reference
$Ge_2Sb_2Te_5$	2.23	142	100	-	10 yrs @ 110ºC	(Lacaita 2006)
$Ge_{14.5}Sb_{85.5}$	-	240	100	50-100	-	(Raoux 2009)
$Sn_{12}Sb_{88}$	3.18	252	100	180	10 yrs @ 143ºC	(Rao 2009)
$Al_{50}Sb_{50}$	2.52	209	10; 10	200	10 yrs @ 90ºC	(Zhou 2013)
$Mg_{56.6}$-$Sb_{41.3}$	3.01	204	1000	100	10 yrs @ 128ºC	(Chang 2010)
Ga_{14}-Sb_{86}	4.68	220	100	200	10 yrs @ 162ºC	(Lu 2011)

The phase-change that makes GST viable for use in memory is a change between an amorphous phase and a rock-salt crystalline phase (Yamada 1996). In this rock-salt structure, Te forms one sub-lattice, while Ge, Sb, and vacancies form the other sub-lattice. Due to these vacancies, Te has a lower coordination number than Ge or Sb. Furthermore, first-principles studies, summarized in Table 1-5, have demonstrated that the lower coordination number of Te should still be observed in amorphous GST as well.

Table 1-5. Reported GST cohesive energies and coordination numbers of Ge, Sb, and Te in different GST crystal structures from first-principles studies

| Material | Crystallinity | Coordination # | | | Cohesive Energy | Reference |
		Ge	Sb	Te		
$Ge_2Sb_2Te_5$	Amorphous	3.96	4.15	2.97		(Caravati 2009)
$Ge_2Sb_{1.8}Te_5$	Amorphous	3.91	4.17	2.99		(Caravati 2009)
$Ge_{2.2}Sb_{1.8}Te_5$	Amorphous	4.16	4.31	3.12		(Caravati 2009)
GST-225	Amorphous (low density)	5.25	5.67	3.98		(Sun 2009)
GST-225	Amorphous (high density)	5.72	6.25	4.46		(Sun 2009)
GST-225	Crystalline (rock salt)	6	6	4.8	0.10 eV/atom at 0K	(Sun 2009)
$Ge_1Sb_2Te_4$	Crystalline (rock salt)				-3.5887 to -3.7568 eV/atom	(Sun 2007)
$Ge_3Sb_2Te_6$	Crystalline (rock salt)				-3.8021 to -3.8200 eV/atom	(Sun 2007)
$Ge_1Sb_4Te_7$	Crystalline (rock salt)				-3.5855 to -3.7260 eV/atom	(Sun 2007)
GeTe	Crystalline				-3.898 eV/atom	(Miao 2010)
$Ge_4Sb_1Te_5$	Crystalline				-3.814 eV/atom	(Miao 2010)
$Ge_4Sb_1Te_5$	Crystalline				-3.813 eV/atom	(Miao 2010)
$Ge_3Sb_2Te_5$	Crystalline				-3.746 eV/atom	(Miao 2010)
GST-225	Crystalline				-3.78 to -3.60 eV/atom	(Sa 2011)
GST-225	Crystalline				-3.76 to -3.58 eV/atom	(Sa 2011)
GST-225	Amorphous	3.9	3.5	2.7	2.62 eV	(Akola 2009)
GST-225	Crystalline				2.6258 eV	(Akola 2009)
GST-225	Amorphous	3.9	2.8	2.4		(Akola 2007)
GST-225	Amorphous	4.2	3.7	2.9		(Akola 2007)
GST-225	Crystalline	6	6	4.8		(Akola 2007)

	Ge	Sb	Te	T_c
$Ge_1Sb_2Te_4$	14.3	28.6	57.1	133
$Ge_2Sb_2Te_5$	22.2	22.2	55.6	145
$Ge_1Sb_2Te_7$	8.3	16.7	58.3	110
GeTe	50	50	0	129
Sb_2Te_3	0	40	60	94
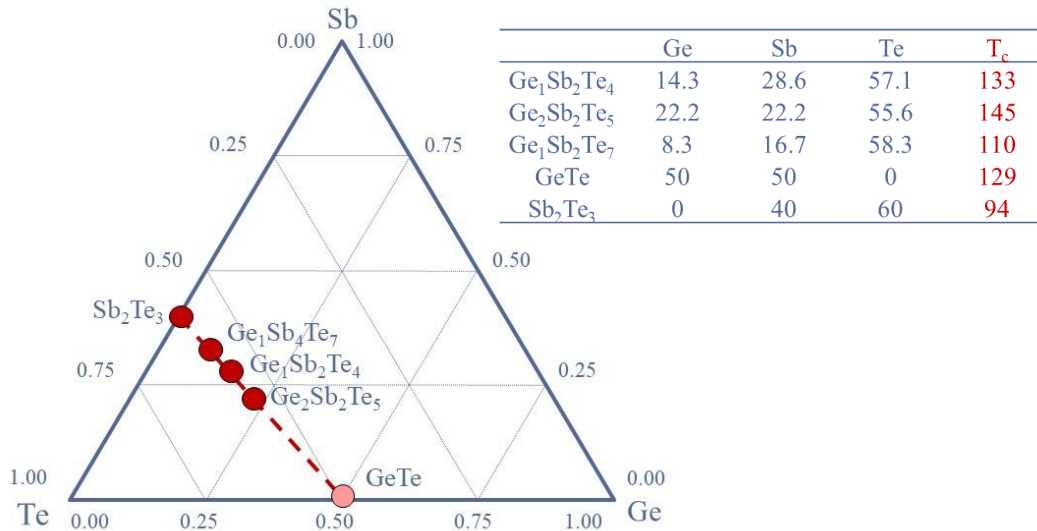
Figure 1-4. Ternary phase diagram of Ge-Sb-Te system with GeTe-Sb_2Te_3 tie line and eutectic compositions plotted. The table shows the percent composition and crystallization temperature (T_c) of the eutectic compositions and Sb_2Te_3 (Kolobov 2003, Arciniega 2012).

As illustrated in Figure 1-5, the relationship between crystallization temperature and GST composition is quite complex. The compositions of GST with the lowest crystallization temperatures (~120ºC) fall on the Ge_2Te_3-Sb_2Te_3 tie line rather than the better-studied GeTe-Sb_2Te_3 tie line, and even minor deviations in composition can cause the crystallization temperature to rise. For example, a 10% increase in Te content in the Ge_2Te_3-Sb_2Te_3 tie line region could result in a ~70ºC increase in crystallization temperature. The eutectic compositions, which fall on the GeTe-Sb_2Te_3 tie line, are partially in the region with the lowest crystallization temperatures as well, but the target $Ge_2Sb_2Te_5$ composition is positioned at the edge of this region. From the crystallization temperature map, it can be concluded that the Te composition can vary within 20% from the target composition while still maintaining the crystallization temperature, but Ge enrichment and Sb depletion should be avoided to keep the crystallization temperature within the minimum region. In order to understand the effects of semiconductor fabrication processes, specifically etching and wet cleaning, on crystallization temperature, their effects on GST

composition need to be determined. The remaining sections detail the current literature on the wet cleaning and plasma etching of GST, as well as the effects of damage to GST phase-change properties.
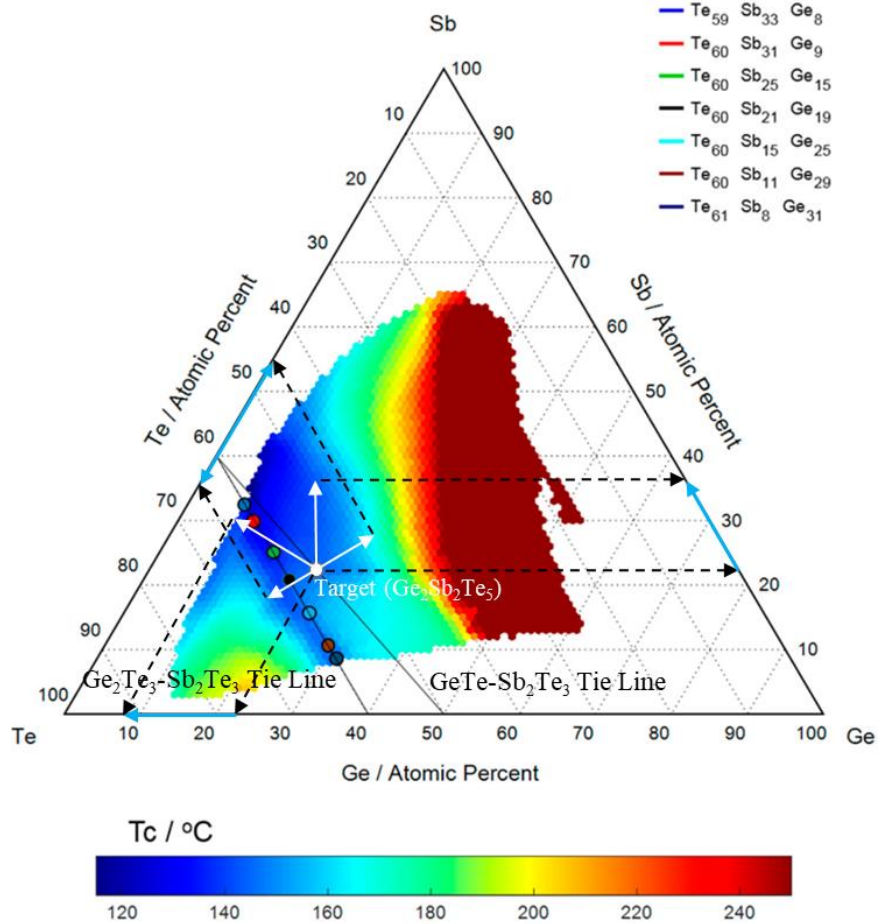
Figure 1-5. Crystallization temperature map of the Ge-Sb-Te system (Guerin 2017). GeTe-Sb$_2$Te$_3$ and Ge$_2$Te$_3$-Sb$_2$Te$_3$ tie lines, the target Ge$_2$Sb$_2$Te$_5$ composition (○), and changes from the target composition that maintain the crystallization temperature are also shown. The white solid arrows represent the acceptable changes to Ge, Sb, and Te that remain within the minimum crystallization temperature region. These are projected on the Ge, Sb, and Te axes by the black dashed arrow lines to determine the composition.

The crystallization temperature map reproduced in Figure 1-5 is not a typical phase diagram. A typical ternary phase diagram shows the different phases of three component system at equilibrium conditions, i.e., for a given temperature and pressure. This figure plots the

crystallization temperature for different compositions of GST, i.e., temperature is not constant. As such, this figure is referred to as a crystallization temperature (T_c) map in this work. Furthermore, it should also be noted that the crystallization temperature shown in this map is for the amorphous to cubic phase change. This phase change occurs at a lower crystallization temperature than other phase changes for GST (amorphous to hexagonal, cubic to hexagonal) (Guerin 2017).

Part of the process flow for producing a phase-change memory device is shown in Figure 1-6. In this process flow, the device stack has been patterned down to the word-line, leaving the GST layer exposed on the sidewall, and a complex scheme was designed to protect the sidewalls from the etching and deposition cycles needed to pattern the word-lines. Without this protection, the GST could be damaged during the processing of other layers of the device, potentially rendering the device inoperable. In addition, each of the arrows in Figure 1-6 represented a transfer of the wafer the device was fabricated on between different processing chambers. If the transfer was done with a vacuum break, or in vacuum but without sufficient purging, the exposed GST sidewall could be subject to oxidation, which could also degrade the performance of the final device (Shen 2020).
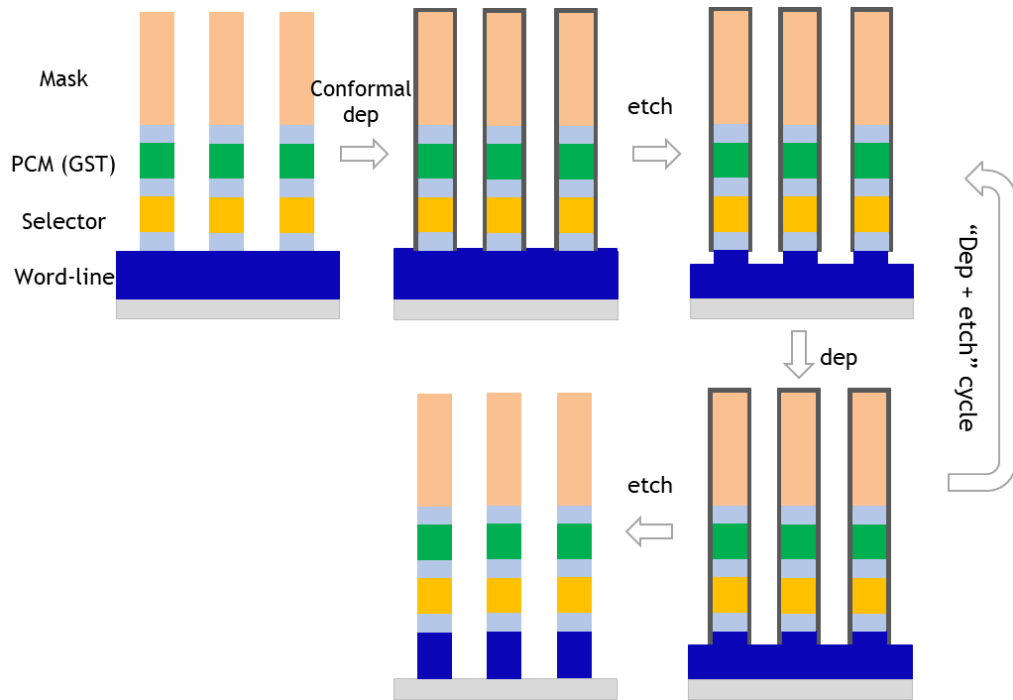
Figure 1-6. Cross-sections illustrating partial process flow and protection scheme for preventing damage to phase-change memory stacks consisting of Mask, GST, selector device, and word line during the processing of other layers. (Shen 2020)

1.3 Wet Cleaning of Ge, Sb, Te, and GST

During the course of fabricating a phase-change memory device, the phase-change material needs to be patterned, which has been accomplished by halogen-containing plasmas, and these etch processes can damage GST. However, there are other processes needed to fabricate the final device that can also damage the GST layer. For example, ashing of photoresists by oxygen plasma has been shown to affect the performance of GST devices by introducing an oxide at TiN/GST interfaces (Dan 2015). Wet cleaning of phase change materials is a crucial step in PCRAM device fabrication and serves to remove damaged layers induced by plasma etching or dry stripping processes which would otherwise negatively affect device performance.

There are numerous studies on the wet cleaning of Ge, but there are very few studies on the wet cleaning of Sb and Te or GST as a ternary compound. For example, the complexation of

14

Si and Ge with organic species such as citric acid and tartaric acid has been demonstrated (Pokrovski 1998). It was shown that Ge was most soluble in citric acid and tartaric acid (0.18 and 0.13 mol_{Ge}/kg_{H2O}, respectively), with NaOH added to alter the pH of the solution. However, the tartaric acid was quite acidic (pH = 3.04) compared to the citric acid solutions (pH = 7.05). The formation of Ge-citrate complexes in a system of H^+-Ge(OH)$_4$-citric acid was also studied, and Ge-citrate complexes were found to be the dominant species over a range of pH 2-7, with Ge(OH)$_4$ being the dominant species at extremely acidic (pH <2) and at basic conditions (pH >7) (Figure 1-7(a)) (Pokrovski 1998).
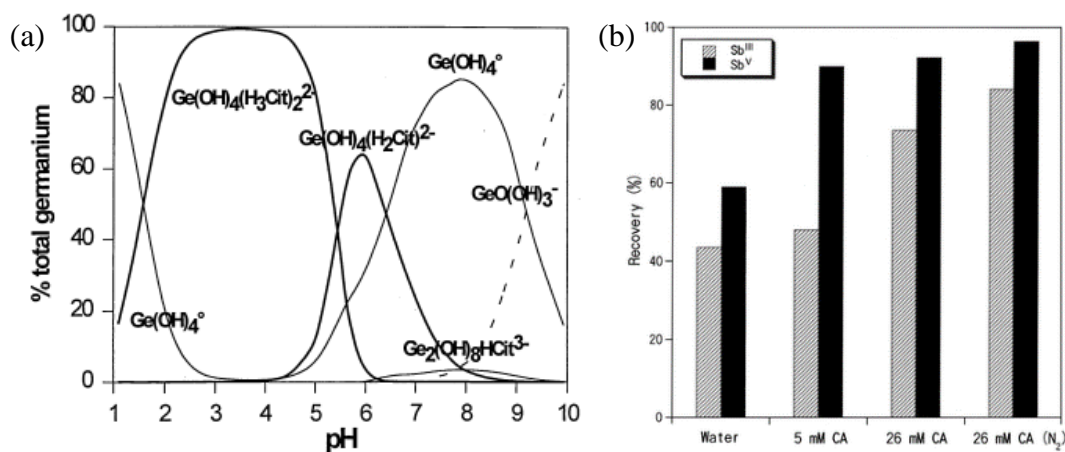
Figure 1-7. (a) Distribution of Ge aqueous species at 25°C in the H^+-Ge(OH)$_4$-citric acid system (Pokrovski 1998). (b) Recovery percentage of Sb(III) and Sb(V) as a function of citric acid concentration (Zheng 2001).

Similarly, Sb complexation by citric acid has also been studied, using citric acid to extract Sb from airborne particulate matter and water samples, and the Sb-citrate complexes were found to be stable in an aqueous environment. Sb-citrate complexes were found to have Sb in both the Sb^{3+} and the Sb^{5+} oxidation states, and these could be separated by a high-performance liquid chromatography-inductively-coupled mass spectrometry (HPLC-ICP-MS) technique (Figure 1-7(b)) (Zheng 2001). While not directly comparable to wet cleaning, citric acid has been used in

slurries for the chemical mechanical planarization of GST (Wang 2009). Another study of the wet cleaning of GST used carboxylic, oxalic and hydrofluoric acids and examined the extent of oxidation of Ge, Sb, and Te after each treatment. It was determined that oxalic acid with and without added hydrofluoric acid resulted in reduced oxidation of the GST (Votta 2012).

The use of hydrofluoric acid to clean Ge-rich GST that had been etched by HBr plasma then stripped of photoresist by an oxygen plasma has also been reported. The GST surface was found to be quite oxidized (57% O) following the stripping process, but this was almost entirely removed after the hydrofluoric acid clean (2% O). However, the ratio of Ge:Sb:Te, which was still close to the desired Ge-rich ratio being studied after the use of the oxygen stripping plasma, was significantly altered and became depleted in Ge (79% of desired) and Sb (68% of desired) and enriched in Te (186% of desired) (Canvel 2020).
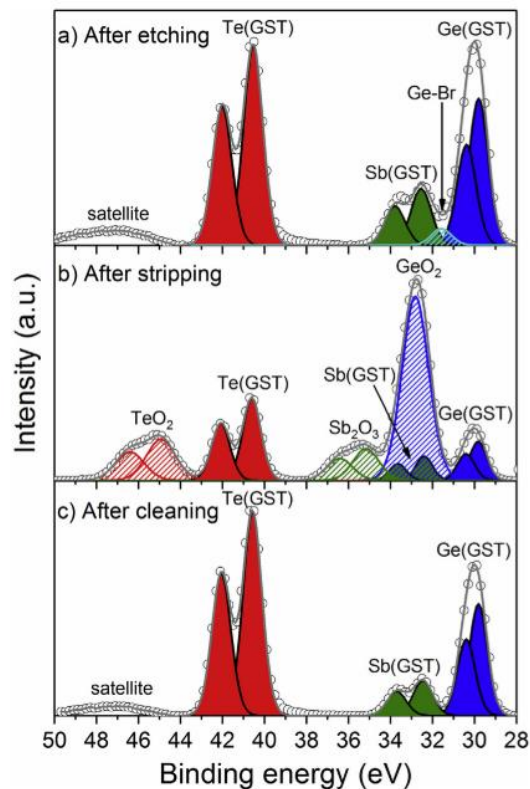
Figure 1-8. XPS Spectra of GST after etching in HBr plasma, photoresist stripping by O_2 plasma, and wet cleaning by HF (Canvel 2020).

16

In summary, the wet cleaning of GST has been largely reported for its ability to remove oxides from GST. These reported wet cleans were summarized in Table 1-6.

Table 1-6. Summary of reported wet cleans of GST and their effects.

Material	Wet Clean	Etch Rate (nm/min)	Other Effects	Reference
GST	Oxalic Acid	n/a	Removes GST oxides	(Votta 2012)
GST	Monocarboxylic acid	n/a	Does not remove GST oxides	(Votta 2012)
GST*	HF	n/a	Ge and Sb preferentially removed, resulting in Te enriched surface	(Canvel 2020)

*after etching and stripping, Ge-rich

1.4 Plasma Etching of GST

Phase-change memory performance relies on the phase-change layer maintaining the as-deposited stoichiometry. not only during the deposition of the phase-change material but also throughout all the processing steps that the phase-change memory stacks go through. The most common phase-change material, and the one being studied in this work, is the chalcogenide glass $Ge_2Sb_2Te_5$, which is a ternary compound that lies on the $GeTe$-Sb_2Te_3 tie line. One of the challenges involved in processing multi-element thin films is that each element is expected to react differently to any etch technique. Fundamentally, the elements differ by such parameters as mass and bonding energy, which results in complications for physical etching techniques such as sputtering. The sputtering yields for Ge, Sb, and Te at 0° and 45° angles of incidence are shown in Table 1-7, and it is important to note that the sputtering yield of Ge can be as little as one seventh of that of Te in a 100 eV Ar^+ beam. As the film is sputtered, it can be expected that the film become a richer in Ge as Sb and Te are preferentially sputtered away.

Table 1-7. Table of sputtering yields of Ge, Sb, and Te at 0º and 45º angle of incidence for an Ar^+ ion beam with energy 100, 200, 500, or 1000 eV (Seah 2005, Seah 2005).

Element	Sputtering Yield (M/Ar^+)			
(θ)	100 eV	200 eV	500 eV	1000 eV
Ge (0°)	0.2	0.5	1.0	1.5
Ge (45°)	0.4	0.8	1.6	2.3
Sb (0°)	0.7	1.5	2.8	4.1
Sb (45°)	1.3	2.3	4.2	6.1
Te (0°)	1.5	2.5	4.7	6.7
Te (45°)	2.1	3.8	6.9	9.9

A number of chemistries have been studied for etching GST, and most of them rely on halogens or halogen-containing compounds. Halogen-containing etch chemistries produce etch rates on the order of 100's of nm/min, but they also damage the GST layer and change its stoichiometry. For instance, the CF_4 etch was noted to deplete Te and observed to form a Teflon-like C-F polymer layer on sidewalls (Kang 2011). The use of a CF_4 plasma to etch $Ge_2Sb_2Te_5$ was expected to result in the fluorides of the constituent elements (Li 2016). It can be seen in Table 1-8 that the enthalpy of formation changes quite drastically between TeF_4 and GeF_4 or SbF_5, and the vapor pressure is also quite different between the different fluorine compounds.

Table 1-8. Table of potential etch products of $Ge_2Sb_2Te_5$ in fluorine-containing chemistry.

Compound	ΔH_f (kJ/mol)	P_{vap} (Torr)
GeF_4	-1190	3030
TeF_4	27	2
SbF_5	-1324	10

Another issue with the use of halogen-based etch chemistries is that the etched film can be quite halogenated, which can result in degraded device performance. CF_4 has been noted to result in the greatest halogenation (35% F in the etched surface), while HBr resulted in the least halogenation (5% Br in the etched surface) (Canvel 2019). However, while HBr resulted in the

least halogenation of the surface, another study on HBr shows that it still degraded device performance, as characterized by the resistance ratio of the GST after cycling between crystal phases, and the same study showed that NH_3 could be used to etch GST without degrading the device performance (Park 2016). While the H content, as determined by time-of-flight secondary ion mass spectrometry (TOF-SIMS), was not reported, it was noted to be significantly less than the Br content (Park 2016). A selection of etch chemistries for GST is presented in Table 1-9. All the reported etch chemistries, with the exception of NH_3, contain halogens.

Table 1-9. Table of etch chemistries reported for $Ge_xSb_yTe_z$ compounds. For entries where post-etch compositions were reported, ΔT_c has been determined using the crystallization temperature map from (Guerin 2017), rounded to the nearest 5℃.

Etchant	Comp.	Power (W)	Bias	Pressure (mTorr)	Etch Rate (nm/min)	PCM	ΔT_c (℃)	Ref.
Cl_2/Ar	10:90	600	150 W	5	480	GST-225	-5 ℃	(Yoon 2005)
CHF_3/Ar	20:80	600	150 W	5	410	GST-225	-5 ℃	(Yoon 2005)
CHF_3/O_2	50:2	200	-	30	40	GST-225	N/A	(Feng 2007)
Cl_2	-	500	-100 V	3	432	GST-225	-20 ℃	(Kang 2011)
CF_4	-	500	-100 V	3	366	GST-225	25 ℃	(Kang 2011)
HBr	-	500	-100 V	3	252	GST-225	-5 ℃	(Kang 2011)
CF_4	-	500	-150 V	7	320	GST-225	N/A	(Kang 2008)
CF_4:C_4F_8	50:50	500	-150 V	7	172	GST-225	N/A	(Kang 2008)
C_4F_8	-	500	-150 V	7	88	GST-225	N/A	(Kang 2008)
CF_4/Ar	3:1	550	200 W	8	236	GST-225	N/A	(Li 2016)
Cl_2/Ar	3:1	550	85 W	8	158	GST-225	N/A	(Li 2016)
HBr/Ar	3:1	550	200 W	8	150	GST-225	N/A	(Li 2016)
Cl_2	-	770	205 V	3	714	Ge-rich GST	N/A	(Canvel 2019)
CF_4	-	770	205 V	3	163	Ge-rich GST	N/A	(Canvel 2019)
HBr	-	770	205 V	3	192	Ge-rich GST	N/A	(Canvel 2019)
Cl_2	-	770	-	3	627	Ge-rich GST	N/A	(Canvel 2019)
CF_4	-	770	-	3	~98	Ge-rich GST	N/A	(Canvel 2019)
HBr	-	770	-	3	~60	Ge-rich GST	N/A	(Canvel 2019)
NH_3/Ar	50:50	n/a				GST-20:35:45 + C doping	N/A	(Park 2016)

In summary, the etching of GST has been studied in literature, but nearly all the reported etch chemistries relied on halogen-containing chemistries, which have been noted to result in halogenation of the GST films as well as preferential removal of certain elements from the GST, such as Te in the case of CF_4 (Kang 2011). The preferential removal of Ge during these halogen-based etches were reported to be due to the volatility of the GST-halogen etch products (Kang 2011, Li 2016, Canvel 2019). The use of hydrogen and hydrogen-containing plasmas to etch GST has not been studied as extensively, but the use of NH_3 was reported to result in no degradation of device performance (Park 2016). As such, it was proposed that both halogen and hydrogen plasma etching of GST should be studied in this work in order to compare their effects. Methane plasma etching of GST could also be studied as another hydrogen-containing plasma.

1.5 Effect of GST Stoichiometry on PCM Functionality

Etching GST can induce physical damage, such as roughening of the sidewall by halogen-based chemistries, particularly by Cl_2. This could occur on the exposed GST sidewalls shown in Figure 1-6 if there was no protective layer deposited. In addition, the thermal stress on the GST due to repeated etch processes can result in enrichment of Sb or depletion of Ge in the film (Anam 2019). A recent computational study showed the effect of etching on GST roughening and composition change (Anam 2019). The composition change was approximated by altering the thermal conductivity of a pseudo-GST (p-GST) domain that represented the damaged portion of GST at the sidewall of a PCM device (Figure 1-9(a)). It was found that, while the change in maximum temperature (ΔT_{max}) for a given range of reset current did not change significantly with wider GST features (>200 nm), it increased significantly as the GST width was reduced below 130 nm, which can have a negative effect as PCRAM devices continue to shrink in dimension (Figure 1-9 (b)).

W$_{PCM}$ (nm)	ΔT_{max} (K)
143	75.5
133	101.8
123	143.1
113	216.4
103	387.3
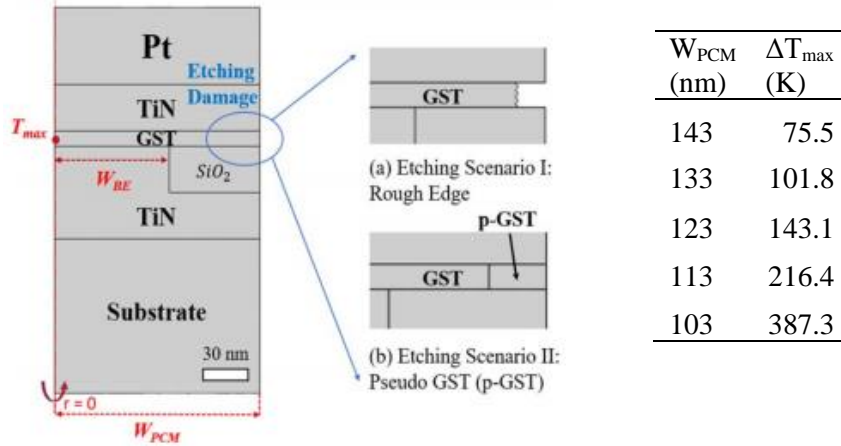
Figure 1-9. (Left) Schematic of a simulated GST device with the damage to the GST sidewall due to edge roughening or the formation of an etched pseudo-GST region. The effect of the damage was approximated by changing the thermal conductivity of the GST sidewall region. (Right) Changes in maximum temperature of the simulated GST device as the device dimensions were shrunk, showing that the effect of damaged GST was more pronounced as GST devices were scaled down (Anam 2019).

As shown in Figure 1-6, there can be many points in the manufacturing of a GST device where the GST can suffer from inadvertent damage to unprotected GST surfaces, such as oxidation due to air exposure between processing steps (Canvel 2020). In addition, as covered previously in Section 0, the etching of GST itself can result in changes to the GST composition. Literature reports on the effects of damage to GST phase-change properties and device performance are discussed in this section. Damage can be in the form of changes to the stoichiometry of the GST film or the bonding of other elements to the GST, such as oxygen or fluorine.

Figure 1-6 depicted a process requiring multiple transfers between processing chambers in order to pattern part of a phase-change memory device, which can open up the exposed GST to damage from ambient oxidation (Canvel 2020). An example of the effects of this can be seen in Figure 1-10 for $Ge_2Sb_2Te_5$ and GeTe, which is one of the binary compounds that can be said to make up $Ge_2Sb_2Te_5$ along with Sb_2Te_3. It was determined that the ambient oxidation of GeTe and GeSbTe caused a "drift" in the activation energy of the crystallization process and the

crystallization temperature. This drift was referred to a change in the switching speed and energy of the phase-change memory device, which affects the performance of the device. The change in the activation energy was determined by measuring the change in optical reflectivity with changing temperature for the different samples, and the activation energies were calculated from these results. The increase in activation energy due to oxidation of the GeTe and GST films likely results in greater power consumption if a device is made using the aged films as opposed to the fresh films.
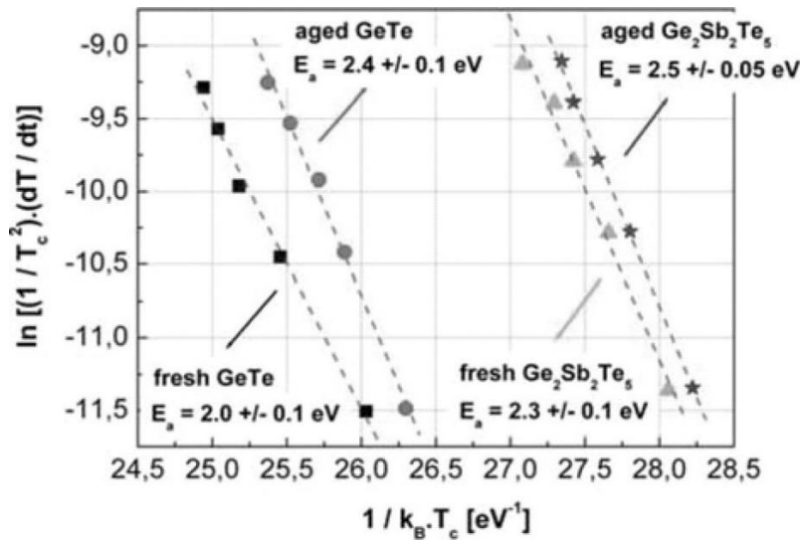
Figure 1-10. Extraction of the $Ge_2Sb_2Te_5$ and GeTe activation energies from optical measurements with Kissinger's method (Gourvest 2012). GeTe and $Ge_2Sb_2Te_5$ samples were subjected to ambient oxidation.

Chemical and physical damage can affect many of the phase-change properties of GST. It has been shown that the use of NH_3 instead of HBr plasma to etch GST resulted better cycling performance (Park 2016). Figure 1-11 shows the set cycles of a phase-change memory device, with TEM images of the device after set failure (Park 2016). The HBr-etched device had appreciable amounts of Br incorporated after etch, and voids formed in the device that were also attributed to the HBr etch. H was detected in the NH_3 etched device, and while the amount was

22

not reported, it was noted to be significantly less than the amount of Br in the HBr-etched device. The changes in crystallization temperature due to etching-induced composition change for reported etches in Table 1-9 where GST composition was reported are shown on the GST crystallization temperature map in Figure 1-12.
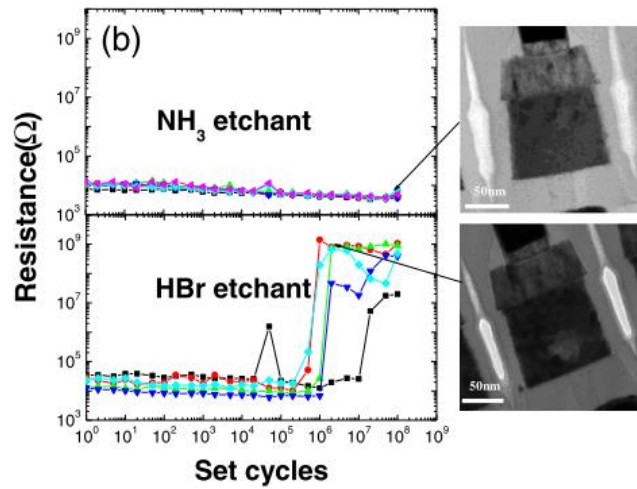
Figure 1-11. Set cycles of phase-change memory devices etched with either NH_3 or HBr, with TEM images of the device after set failure (Park 2016).
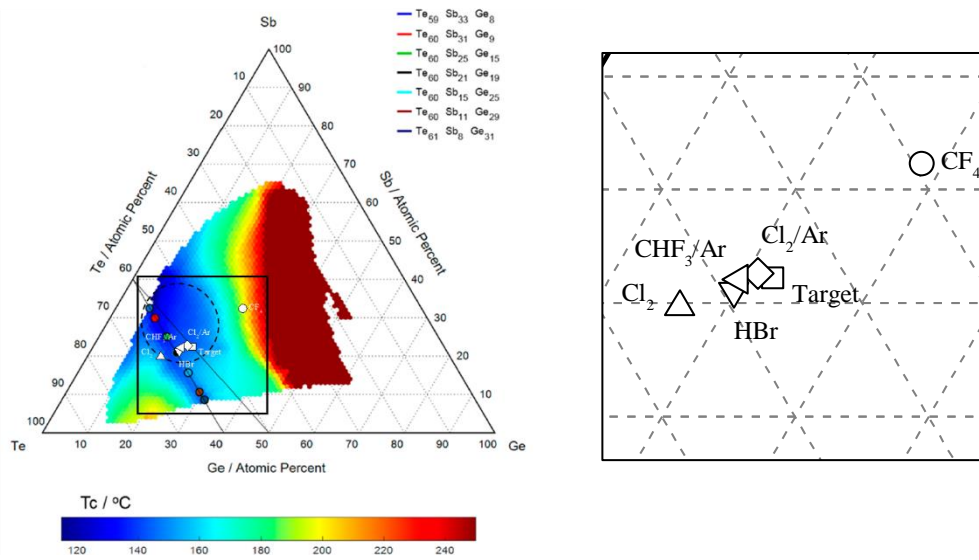
Figure 1-12. Crystallization temperature map of Ge-Sb-Te system (Guerin 2017). The target $Ge_2Sb_2Te_5$ composition (□) as well as the reported compositions of GST etched by Cl_2 (△), CF_4 (○), HBr (▽), Cl_2/Ar (◇)and CHF_3/Ar (◁)plasmas are also shown (Yoon 2005). The distribution of these composition is expanded and shown on the right.
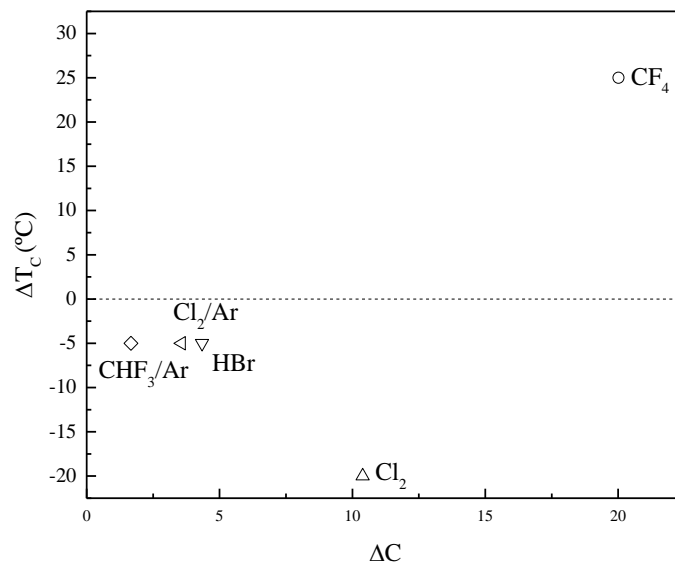
Figure 1-13. The change in crystallization temperature (ΔT_c) versus the composition change (ΔC) for the etch processes shown in Figure 1-12.

24

In summary, GST phase change properties are sensitive to changes in composition during the manufacture of the phase-change memory device. This can come from many sources, and two were presented in this section: the ambient oxidation of GST and the etching of GST. Other processing steps, such as wet cleaning (presented in Section 1.3) and the ashing and stripping of photoresists from GST (Canvel 2020), can also cause damage to the GST film that would be expected to result in changes in the GST phase-change properties.

1.6 Motivation and Scope

The phase-change properties of the GST are dependent on the stoichiometry of the film. The GST itself is susceptible to oxidation, and oxidation alone can significantly alter the phase-change properties of the material. The etching of the GST can induce physical damage (in the form of roughening of the GST), chemical damage (in the form of incorporation of etchants such as halogens into the GST), or stoichiometry change (due to preferential removal of one or more elements from the film). All these effects alter the phase-change properties of the GST and the performance of the final device.

The goal of this research is to achieve a better understanding of how the processing of GST affects the composition of the film. The entirety of a process flow to produce a phase-change memory device requires many steps, and this research limited itself to studying the effects of wet cleaning and etching of the GST film and understanding how these processes affect GST, especially with respect to changes in composition. First, the ambient oxidation of GST was studied to determine which components of the atmosphere had the greatest effect on the oxidation of GST. Then, the wet cleaning of as-received GST was studied. Methods of cleaning as-received GST to remove oxides were then evaluated, and the wet cleans were studied again on the cleaned GST. The effects of wet cleaning on as-received and cleaned GST were compared to reveal how Ge, Sb,

and Te oxides were affected by the wet cleans. Surface oxides would be removed prior to all plasma etching studies on GST in order to simplify the analysis. Halogen plasma etching of GST was studied using Cl_2/Ar and SF_6/Ar plasma, and these results were compared against the available literature. Then, hydrogen and methane plasma etching of GST were studied. In order to help determine the mechanism for the preferential removal of Ge, Sb, and Te from GST during plasma etching, Ge, Sb, and Te films were also etched. Finally, the effects of these plasma etches and wet cleans were compared to determine how each process affected composition and which ones best maintained crystallization temperature.

Chapter 2 Experimental Setup

This chapter describes the thermochemical analyses of the etch chemistries as well as experimental setups used to carry out the studies for the wet cleaning and plasma etching of GST thin films. The systems for handling and processing samples and analysis and characterization of the samples are also described. The chemistry and characterization of the plasmas used in this work are also summarized. Finally, the process for evaluating treatment effects is discussed.

2.1 Thermodynamic Analysis

When evaluating an etch chemistry and material system, it can be helpful to examine the potential etch reactions and products using physical properties and thermodynamics to assess the viability of the etch chemistry. Proposed etch reactions should have a negative change in Gibbs energy indicating that they are spontaneous, i.e., the reaction is thermodynamically favorable. A more negative change in Gibbs free energy does not indicate that a reaction occurs more quickly than a reaction, it simply suggests that the reaction is feasible (i.e., thermodynamics does not predict reaction kinetics). The standard Gibbs energies of formation of the GST oxides was considered (Table 2-1). From these values, it could be predicted that at thermodynamic equilibrium Sb should be the most oxidized, followed by Ge, then Te. This would prove to be the case for ambient oxidized GST.

Table 2-1. Table of the standard Gibbs energy of formation for Ge, Sb, and Te oxides. (Haynes 2011)

Component	ΔG_f^0 (@ 25°C) (kJ/mol)
GeO_2	-520.9
Sb_2O_3	-623.9
Sb_2O_5	-828.3
TeO_2	-342.1

For the calculation of ΔG_{rxn} for proposed reactions, all reactions were assumed to occur at 25ºC. All GST and GST oxides were considered as their single element constituents, such as Ge or GeO_2 due to the availability of thermodynamic data for the constituents as opposed the relative lack of data for the ternary compound. In all reactions, the material being etched (Ge, Sb, Te, or their oxides) was considered to be in the solid phase, while all etchants and products were considered to be in the gas phase. Only ground state species were considered, thermodynamic data for charged species and non-ground state species was not available.

2.1.1 Analysis of Reactions of Ge, Sb, and Te with Fluorine and Chlorine

To assess the reactions of Ge, Sb, Te and their oxides with Cl_2 and SF_6 plasmas, the ΔG_{rxn} for reactions of Ge, Sb, and Te and their oxides with both atomic and molecular halogen species were determined using HSC Chemistry at various temperatures and summarized in Table 2-2, Table 2-3, and Table 2-5 for Cl and F. The ΔG_{rxn} values summarized in Table 2-2 and Table 2-3 suggested that Ge, Sb, and Te would be reactive with atomic and molecular chlorine and with atomic and molecular fluorine. Potential reactions of Ge, Sb, and Te with SF_x were not considered, as there was no data available for such reactions or potential Ge, Sb, Te-SF_x compounds. Although data for GeSbTe was not available, thermodynamic data was available for the binary compounds GeTe and Sb_2Te_3, shown in Table 2-4, and the reaction data suggested that compounds of Ge, Sb, and Te would also react with atomic and molecular Cl and F.

Table 2-2. Summary of predicted etch reactions of Ge, Sb, and Te with atomic and molecular chlorine, calculated using HSC Chemistry for various temperatures (Roine 2018). All reactions were determined to be thermodynamically favorable.

Reaction	ΔG_{rxn} (kJ/mol)			
	0ºC	25ºC	50ºC	100ºC
$Ge + 2Cl \rightarrow GeCl_2$	-396.66	-394.03	-392.38	-388.99
$Ge + 4Cl \rightarrow GeCl_4$	-887.18	-878.61	-870.01	-852.72
$Ge + Cl_2 \rightarrow GeCl_2$	-182.38	-183.42	-184.46	-186.51
$Ge + 2Cl_2 \rightarrow GeCl_4$	-460.61	-457.38	-454.17	-447.76
$Sb + 3Cl \rightarrow SbCl_3$	-620.54	-615.49	-610.41	-600.19
$Sb + 5Cl \rightarrow SbCl_5$	-877.59	-865.87	-854.11	-830.47
$Sb + 1.5Cl_2 \rightarrow SbCl_3$	-300.61	-299.57	-298.53	-296.47
$Sb + 2.5Cl_2 \rightarrow SbCl_5$	-344.38	-339.34	-334.31	-324.26
$Te + 2Cl \rightarrow TeCl_2$	-334.04	-332.20	-330.34	-326.51
$Te + 4Cl \rightarrow TeCl_4$	-599.94	-591.63	-583.27	-566.42
$Te + Cl_2 \rightarrow TeCl_2$	-120.76	-121.59	-122.41	-124.03
$Te + 2Cl_2 \rightarrow TeCl_4$	-173.37	-170.40	-167.43	-161.46

Table 2-3. Summary of predicted etch reactions of Ge, Sb, and Te with atomic and molecular fluorine, calculated using HSC Chemistry for various temperatures (Roine 2018). All reactions were determined to be thermodynamically favorable.

Reaction	ΔG_{rxn} (kJ/mol)			
	0ºC	25ºC	50ºC	100ºC
$Ge + 2F \rightarrow GeF_2$	-711.48	-709.56	-707.60	-703.55
$Ge + 4F \rightarrow GeF_4$	-1408.16	-1399.10	-1389.96	-1371.52
$Ge + F_2 \rightarrow GeF_2$	-584.07	-585.00	-585.92	-587.71
$Ge + 2F_2 \rightarrow GeF_4$	-1153.34	-1149.98	-1146.60	-1139.84
$Sb + 3F \rightarrow SbF_3$	-1009.05	-1003.58	-998.05	-986.87
$Sb + 5F \rightarrow SbF_5$	-1529.31	-1517.95	-1504.50	-1479.44
$Sb + 1.5F_2 \rightarrow SbF_3$	-817.93	-816.74	-815.54	-813.12
$Sb + 2.5F_2 \rightarrow SbF_5$	-1210.78	-1205.55	-1200.31	-1189.85
$Te + 4F \rightarrow TeF_4$	-1167.19	-1158.22	-1149.18	-1130.95
$Te + 6F \rightarrow TeF_6$	-1663.34	-1646.74	-1630.05	-1596.45
$Te + 2F_2 \rightarrow TeF_4$	-912.37	-909.10	-905.83	-899.28
$Te + 3F_2 \rightarrow TeF_6$	-1281.11	-1273.07	-1265.02	-1248.94

Table 2-4. Summary of predicted etch reactions of GeTe and Sb_2Te_3 with atomic and molecular chlorine and fluorine, calculated using HSC Chemistry for various temperatures (Roine 2018). All reactions were determined to be thermodynamically favorable.

Reaction	ΔG_{rxn} (kJ/mol)			
	0ºC	25ºC	50ºC	100ºC
$GeTe + 8Cl \rightarrow GeCl_4 + TeCl_4$	-1468.63	-1451.51	-1434.31	-1399.69
$GeTe + 4Cl_2 \rightarrow GeCl_4 + TeCl_4$	-615.49	-609.07	-602.63	-589.77
$GeTe + 8F \rightarrow GeF_4 + TeF_4$	-2556.86	-2538.59	-2520.18	-2483.02
$GeTe + 4F_2 \rightarrow GeF_4 + TeF_4$	-2047.22	-2040.36	-2033.47	-2019.67
$Sb_2Te_3 + 18Cl \rightarrow 2SbCl_3 + 3TeCl_4$	-2982.88	-2947.65	-2912.22	-2840.81
$Sb_2Te_3 + 9Cl_2 \rightarrow 2SbCl_3 + 3TeCl_4$	-1063.32	-1052.13	-1040.94	-1018.49
$Sb_2Te_3 + 18F \rightarrow 2SbF_3 + 3TeF_4$	-5461.63	-5423.59	-5385.24	-5307.79
$Sb_2Te_3 + 9F_2 \rightarrow 2SbF_3 + 3TeF_4$	-4314.93	-4302.55	-4290.14	-4265.25

The ΔG_{rxn} values summarized in Table 2-5 suggested that Ge, Sb, and Te oxides would be reactive only to atomic Cl and that the formation of $GeCl_2$ was not thermodynamically favorable, suggesting that these oxides could be more resistant to etching by Cl_2 plasma than metallic Ge, Sb, and Te. It was also predicted that Ge, Sb, and Te oxides would be susceptible to etching by both atomic and molecular fluorine. As with metallic GST, reactions with SF_6 were not considered, as thermodynamic data for SF_x species or potential GST-SF_x compounds was not available.

Table 2-5. Summary of predicted etch reactions of GST oxides with atomic and molecular chlorine and fluorine, calculated using HSC Chemistry at 25ºC (Roine 2018). All reactions except those forming $GeCl_2$ and the reactions of molecular Cl_2 and GST-oxides were determined to be thermodynamically favorable.

Reaction	ΔG_{rxn} (kJ/mol)
$GeO_2 + 2Cl \rightarrow GeCl_2 + O_2$	127
$GeO_2 + 4Cl \rightarrow GeCl_4 + O_2$	-357
$GeO_2 + Cl_2 \rightarrow GeCl_2 + O_2$	338
$GeO_2 + 2Cl_2 \rightarrow GeCl_4 + O_2$	64
$GeO_2 + 2F \rightarrow GeF_2 + O_2$	-188
$GeO_2 + 4F \rightarrow GeF_4 + O_2$	-878
$GeO_2 + F_2 \rightarrow GeF_2 + O_2$	-64
$GeO_2 + 2F_2 \rightarrow GeF_4 + O_2$	-629
$Sb_2O_3 + 6Cl \rightarrow 2SbCl_3 + 1.5O_2$	-603
$Sb_2O_5 + 10Cl \rightarrow 2SbCl_5 + 2.5O_2$	-903
$Sb_2O_3 + 3Cl_2 \rightarrow 2SbCl_3 + 1.5O_2$	29
$Sb_2O_5 + 5Cl_2 \rightarrow 2SbCl_5 + 2.5O_2$	151
$Sb_2O_3 + 6F \rightarrow 2SbF_3 + 1.5O_2$	-1379
$Sb_2O_5 + 10F \rightarrow 2SbF_5 + 2.5O_2$	-2406
$Sb_2O_3 + 3F_2 \rightarrow 2SbF_3 + 1.5O_2$	-1005
$Sb_2O_5 + 5F_2 \rightarrow 2SbF_5 + 2.5O_2$	-1582
$TeO_2 + 2Cl \rightarrow TeCl_2 + O_2$	-66
$TeO_2 + 4Cl \rightarrow TeCl_4 + O_2$	-326
$TeO_2 + Cl_2 \rightarrow TeCl_2 + O_2$	145
$TeO_2 + 2Cl_2 \rightarrow TeCl_4 + O_2$	96
$TeO_2 + 4F \rightarrow TeF_4 + O_2$	-892
$TeO_2 + 6F \rightarrow TeF_6 + O_2$	-1381
$TeO_2 + 2F_2 \rightarrow TeF_4 + O_2$	-643
$TeO_2 + 6F_2 \rightarrow TeF_6 + O_2$	-1007

Proposed Ge-F, Sb-F, and Te-F and Ge-Cl, Sb-Cl, Te-Cl etch products and their boiling points were summarized in Table 2-6. The boiling points of the etch products were used to assess the volatility of each etch product, although it should be noted that the conditions that boiling points are measured at (atmospheric pressure, pure substance) are quite different from the conditions of an etch product that needs to be desorbed (in vacuum, on a surface). Data from thermally programmed desorption (TPD) would be more suitable, as it better replicates the conditions of the plasma etch experiments in this work, but this data is not available for many of the etch products studied in this work. It has been reported in literature that stoichiometry change

31

due to the etching of GST by Cl- and F-containing plasmas followed the trend set by the boiling

points of the etch products (Kang 2011, Li 2016, Canvel 2019). The order of the boiling points

suggested that Ge might be most susceptible to etch, since its etch products have the lowest boiling

points (i.e., they are the easiest to volatilize), followed by Sb and then Te for Cl or by Te then Sb

for F.

Table 2-6. Table of Ge, Sb, Te-F and Ge, Sb, Te-Cl etch products and the boiling
point for each proposed etch product. Etch product boiling points are evaluated to
determine the volatility of each etch product. Based on these values, Ge should be
the most easily removed, followed by Sb then Te in the case of Cl and by Te then
Sb in the case of F. (Haynes 2011, Roine 2018).

Etchant	Ge		Sb		Te	
	Product	B.P. (°C)	Product	B.P. (°C)	Product	B.P. (°C)
F	GeF_4	-37	SbF_5	141	TeF_4	196
	GeF_2	130	SbF_3	345	TeF_6	-39
Cl	$GeCl_4$	87	$SbCl_3$	220	$TeCl_2$	328
	$GeCl_2$	n/a	$SbCl_5$	140	$[TeCl_4]_4$	387

It was also reported in literature that the extent of halogenation on GST films etched by

Cl-, F-, and Br-containing plasmas followed the trend set by the bond energies of Ge, Sb, and Te

with halogens (Kang 2011, Li 2016, Canvel 2019). Known bond energies were summarized in

Table 2-7, and from these bond energies, it could be predicted that a F-containing plasma would

result in greater halogenation of the GST than a Cl-containing plasma since the bond energies of

Ge-F and Sb-F are greater than that of Ge-Cl and Sb-Cl. Te-halogen bond energy data was not

available. This was reported that GST etched with CF_4 was 35% F post-etch, while GST etched

with Cl_2 was 11% Cl post-etch (Canvel 2019).

Table 2-7. Table of Ge, Sb, and Te bonds with Cl and F. Based on these values, greater halogenation of the GST film is expected with F and lesser halogenation of the GST is expected with Cl. (Lide 2004)

Bond	Bond Energy (kJ/mol)
Ge-F	485±21
Ge-Cl	431
Sb-F	439±96
Sb-Cl	360±50
Te-F	n/a
Te-Cl	n/a

In summary, analysis of reaction thermodynamics suggested that the etching of GST with fluorine and chlorine in both atomic and molecular forms would be thermodynamically favorable and that the etching of GST oxides with atomic and molecular fluorine and atomic Cl would also be thermodynamically favorable. On the other hand, the etching of GST oxides with molecular Cl_2 was not predicted to be thermodynamically favorable. Analysis of the etch product boiling points determined that Ge should be preferentially removed by both fluorine- and chlorine-containing plasmas, followed by Sb then Te in the case of chlorine and by Te then Sb in the case of fluorine, which was reported to be the case in literature. The etch product bond energies suggested that greater halogenation of the GST would occur in a F-containing plasma as opposed to a Cl-containing plasma, which was also reported to be the case in literature and suggested that the Cl-containing plasma would be preferred for avoiding halogenation.

2.1.2 Analysis of Reactions of Ge, Sb, and Te with Hydrogen

Table 2-8 summarizes the reactions of each element in GST with atomic and molecular hydrogen. The reactions of GST with atomic hydrogen were calculated to be thermodynamically favorable, while the reactions of GST with molecular hydrogen were calculated to be thermodynamically unfavorable. This was consistent with the limited TPD literature on the interactions of Sb and Te with hydrogen, which suggested that Sb and Te were inert to molecular hydrogen and suggested that a hydrogen plasma used to etch GST should consist primarily of

atomic hydrogen (Outka 1990, Kraus 2016). The thermodynamic analysis suggested that a similar

effect would occur with Ge, Sb and Te oxides, as shown in Table 2-9, where reactions with atomic

hydrogen were expected to occur but reactions with molecular hydrogen were not. A similar effect

was also observed with GeTe and Sb_2Te_3, as shown in Table 2-10.

Table 2-8. Summary of predicted etch reactions of GST and GST-oxides with atomic and molecular hydrogen, calculated using HSC Chemistry at 25ºC (Roine 2018). Reactions of GST and GST oxides with atomic hydrogen were determined to be thermodynamically favorable, while reactions with molecular hydrogen were not.

Reaction	ΔG_{rxn} (kJ/mol)			
	0ºC	25ºC	50ºC	100ºC
$Ge + 4H \rightarrow GeH_4$	-706.65	-699.89	-693.02	-678.94
$Sb + 3H \rightarrow SbH_3$	-466.34	-462.47	-458.51	-450.33
$Te + 2H \rightarrow TeH_2$	-322.60	-321.37	-320.08	-317.32
$Ge + 2H_2 \rightarrow GeH_4$	111.37	113.21	115.13	119.13
$Sb + 1.5H_2 \rightarrow SbH_3$	147.17	147.36	147.60	148.23
$Te + H_2 \rightarrow TeH_2$	86.45	85.18	83.99	81.71

Table 2-9. Summary of predicted etch reactions of GST-oxides with atomic and molecular hydrogen, calculated using HSC Chemistry at 25ºC (Roine 2018). Reactions of GST and GST oxides with atomic hydrogen were determined to be thermodynamically favorable, while reactions with molecular hydrogen were not.

Reaction	ΔG_{rxn} (kJ/mol)
$GeO_2 + 4H \rightarrow GeH_4 + O_2$	-179
$Sb_2O_3 + 6H \rightarrow 2SbH_3 + 1.5O_2$	-297
$Sb_2O_5 + 6H \rightarrow 2SbH_3 + O_2$	-96
$TeO_2 + 2H \rightarrow TeH_2 + O_2$	-55
$GeO_2 + 2H_2 \rightarrow GeH_4 + O_2$	635
$Sb_2O_3 + 3H_2 \rightarrow 2SbH_3 + 1.5O_2$	923
$Sb_2O_5 + 3H_2 \rightarrow 2SbH_3 + 2O_2$	1091
$TeO_2 + H_2 \rightarrow TeH_2 + O_2$	351

Table 2-10. Summary of predicted etch reactions of GeTe and Sb_2Te_3 with atomic and molecular hydrogen, calculated using HSC Chemistry for various temperatures (Roine 2018). Reactions with atomic hydrogen were determined to be thermodynamically favorable, while reactions with molecular hydrogen were not.

Reaction	ΔG_{rxn} (kJ/mol)			
	0ºC	25ºC	50ºC	100ºC
$GeTe + 6H \rightarrow GeH_4 + TeH_2$	-1010.76	-1002.55	-994.14	-976.81
$GeTe + 3H_2 \rightarrow GeH_4 + TeH_2$	216.27	217.11	218.07	220.30
$Sb_2Te_3 + 10H \rightarrow 2SbH_3 + 3TeH_2$	-1842.46	-1830.85	-1818.85	-1793.80
$Sb_2Te_3 + 5H_2 \rightarrow 2SbH_3 + 3TeH_2$	611.60	608.48	605.59	600.42

The etch products of these proposed reactions were also assessed. The reported boiling points, summarized in Table 2-11, for the proposed etch products indicated that all the etch products should be quite volatile since all boiling points were below 0ºC. The trend for hydrogen etch product volatility had GeH_4 as the most volatile, followed by SbH_3, then TeH_2, so it could be predicted that Ge would be preferentially removed, followed by Sb, then Te. The metal-hydrogen bond energies suggested that Ge might undergo greater hydrogenation than Sb or Te, although the incorporation of H into the GST film could not be confirmed in this work due to the limitations of XPS.

Table 2-11. Summary of the etch products for Ge, Sb, and Te etched by hydrogen, the reported boiling points of each etch product (Lide 2004, Air Liquide 2010), and the bond energy of each element with hydrogen (Luo 2007).

	GeH_4	SbH_3	TeH_2
B.P. (ºC)	-88	-18	-1
P_{vap} (Vapor Pressure)	>1atm	>1atm	n/a
Bond Energy (kJ/mol)	348.9±8.4	288.3±2.1	272.0±2.4

In summary, Ge, Sb, Te and their oxides were predicted to be readily etched by atomic H but not molecular H_2, which indicated that hydrogen dissociation is essential to facilitate etching of Ge, Sb, and Te. Analysis of the metal hydride etch products predicted that Ge would be preferentially removed, followed by Sb then Te based on etch product boiling points, and that hydrogenation of Ge would be favorable over Sb and Te based on bond energies.

2.1.3 Analysis of Reactions of Ge, Sb, and Te with Methane

Table 2-12 summarized the reactions of Ge, Sb, Te and their oxides with methane. This analysis was limited by the availability of thermodynamic data for the reactions of Sb and Te with CH_3 species (i.e., $Sb(CH_3)_4$ and $Te(CH_3)_4$ thermodynamic data was unavailable), and neither Ge nor GeO_2 were predicted to react with methane.

Table 2-12. Summary of predicted etch reactions of Ge, Sb, and Te with CH_4 and CH_3, calculated using HSC Chemistry at 25ºC (Roine 2018). For the reactions with available data, Ge was expected to react with CH_3 but not CH_4.

Reaction	ΔG_{rxn} (kJ/mol)			
	0ºC	25ºC	50ºC	100ºC
$Ge + 4CH_4 \rightarrow Ge(CH_3)_4 + 2H_2$	230.97	234.25	237.48	243.76
$Sb + 3CH_4 \rightarrow Sb(CH_3)_3 + 1.5H_2$	n/a	n/a	n/a	n/a
$Te + 2CH_4 \rightarrow Te(CH_3)_2 + H_2$	n/a	n/a	n/a	n/a
$Ge + 4CH_3 \rightarrow Ge(CH_3)_4$	-572.88	-562.38	-551.78	-530.40
$Sb + 3CH_3 \rightarrow Sb(CH_3)_3$	n/a	n/a	n/a	n/a
$Te + 2CH_3 \rightarrow Te(CH_3)_2$	n/a	n/a	n/a	n/a

Table 2-13 summarized the reactions of Ge, Sb, Te and their oxides with methyl radicals (CH_3), which could be generated in a plasma by the removal of a hydrogen from CH_4. As with methane, this analysis was limited by the availability of thermodynamic data for the reactions of Sb and Te with CH_3 species. Both Ge and GeO_2 would be expected to react with CH_3 but not with CH_4. Data for CH and CH_2 species was not available.

Table 2-13. Summary of predicted etch reactions of GST-oxides with CH_4 and CH_3, calculated using HSC Chemistry at 25ºC (Roine 2018). For the reactions with available data, GeO_2 was expected to react with CH_3 but not CH_4.

Reaction	ΔG_{rxn} (kJ/mol)
$GeO_2 + 4CH_4 \rightarrow Ge(CH_3)_4 + 2H_2O$	298
$Sb_2O_3 + 6CH_4 \rightarrow 2Sb(CH_3)_3 + 3H_2O$	n/a
$Sb_2O_5 + 3CH_4 + 2H_2 \rightarrow Sb(CH_3)_3 + 5H_2O$	n/a
$TeO_2 + 2CH_4 + H_2 \rightarrow Te(CH_3)_2 + 2H_2O$	n/a
$GeO_2 + 4CH_3 \rightarrow Ge(CH_3)_4 + O_2$	-41
$Sb_2O_3 + 6CH_3 \rightarrow 2Sb(CH_3)_3 + 1.5O_2$	n/a
$Sb_2O_5 + 6CH_3 \rightarrow 2Sb(CH_3)_3 + 2.5O_2$	n/a
$TeO_2 + 2CH_3 \rightarrow Te(CH_3)_2 + O_2$	n/a

Table 2-14 lists the boiling points of the proposed etch products of Ge, Sb, and Te reacting with CH_3 groups. The boiling points of these compounds were higher than those of the hydrogen etch products (-1°C or lower) but fell in a smaller range (87°C v. 39°C, for hydrogen and methane etch products, respectively). If the volatility of the etch products was the property that determined preferential removal during the etch process, as reported in literature for GST-halogen etching, then it could be predicted that Ge would be preferentially removed, followed by Sb then Te. The effects of adding Ar or N_2 to CH_4 were also examined in this work, but reaction data for potential etch products, such as those with CN, was not available.

Table 2-14. Summary of proposed etch products for GST + CH_4 plasma and their boiling points (EpiChem Inc. 2005, American Elements 2015, Roine 2018, Sigma-Aldrich Corp. 2020).

	$Ge(CH_3)_4$	$Sb(CH_3)_3$	$Te(CH_3)_2$
B.P. (°C)	43	81	82
P_{vap} (mmHg at 25°C)	348 (20°C)	104	51

Overall, thermodynamic data for the reactions of Ge, Sb, and Te with methane was limited, but the available data indicated that Ge would react with methyl radicals but not methane. As such, a methane plasma would be required to etch Ge. Thermochemical analysis of the etch product boiling points and vapor pressures suggested that Ge would be preferentially removed since $Ge(CH_3)_4$ had the lowest boiling point, followed by Sb and Te. The boiling points of the Ge, Sb, and Te-methyl radical etch products fell within a smaller range than the Ge, Sb, Te-hydrogen etch products, which could result in less compositional change due to etching with methane plasma.

In summary, it was predicted that F, Cl, H, and CH_3 could all be used as etchants for GST. For Cl_2 and SF_6 species, this distinction was less critical, as GST was expected to react with both atomic and molecular fluorine and chlorine species. However, it was also observed that the Ge, Sb, and Te oxides could be inert to Cl_2 but reactive to Cl, which could result in etch resistance. This

was not observed for oxides etched with fluorine, as they were predicted to react with both atomic and molecular fluorine. For H_2 plasma, a plasma with majority atomic H species would be preferred since the GST would be expected to be inert to molecular H_2 species, and for CH_4 plasma, a plasma with CH_3 species would be preferred based on the limited thermodynamic data available. Analysis of the boiling points of the etch products for all chemistries considered this section concluded that Ge should be preferentially removed, followed by Sb, then Te every chemistry except fluorine, where Ge would still be preferentially removed, followed by Te then Sb.

2.2 Sample Preparation and Characterization

2.2.1 Samples of Ge, Sb, Te, and GST

The conditions used to deposit the samples used in this work are listed in Table 2-15. Sb and Te thin films were grown using molecular beam epitaxy. The Ge and GST thin films were sputtered from targets (Ge elemental target for Ge and $Ge_2Sb_2Te_5$ target for GST), while Sb and Te thin films were grown by molecular beam epitaxy (MBE).

Table 2-15. Summary of samples used and their preparation.

Sample	Method	Power	Pressure	Cell Type	Temperature	Thickness (nm)
Ge	Sputtered	100W	$2 \cdot 10^{-6}$ Torr	n/a	Not heated	100
Sb	MBE	n/a	n/a	Thermal cracker	200ºC	20
Te	MBE	n/a	n/a	Thermal cracker	200ºC	20
GeSbTe	Sputtered	150W	4 mTorr	n/a	Not heater	100

Due to the time that elapsed between the deposition of the GST and the XPS analysis of said samples, ambient oxidation occurred and resulted in changes to the GST composition on the as-received surface, which meant that the as-received GST surfaces had different starting compositions. The compositions of these samples and the experiments that they were used in are summarized in Table 2-16. For ease of comparison in this work, the GST composition is given as a ratio normalized to Ge. For example, the ratio of Ge:Sb:Te for the as-received composition before

38

ambient exposure was 8:15:23. After normalizing by the Ge composition, this ratio became

1:1.8:3.0. The Ge portion of the ratio is always given as 1 due to the normalization.

Table 2-16. Summary of as-received GST compositions prior to experiments.

Experiment(s)	Composition (At. %)					Ratio (norm. to Ge)		
	Ge	Sb	Te	O	C	Ge	Sb	Te
Ambient Exposure	8	15	23	54	n/a	1	1.8	3.0
Wet Cleaning	7	10	14	53	17	1	1.3	1.9
HF Cleaning	4	9	11	50	26	1	2.4	2.8
Ion Beam Sputtering	4	12	16	57	13	1	3.0	4.0
Halogen and H_2 Plasma Etching	8	12	18	43	19	1	1.5	2.3
CH_4 Plasma Etching	7	10	9	47	27	1	1.4	1.3
CH_4 Passivation	5	7	12	31	44	1	1.4	2.4

While GST is useful for phase-change memory due to its ability to change between

different crystal phases and the different electrical and optical properties of each crystal phase, the

effect of each chemistry on each crystal phase is not considered in this work. All samples were

amorphous as-deposited, as confirmed by XRD. The interior of the ICP chamber can reach

approximately 60ºC when the plasma is ignited, which is approximately 50% of the lowest known

crystallization temperature for GST and also the highest temperature any of the GST samples in

this work would have been exposed to. As such, all samples in this work were considered to be

amorphous.

2.2.2 Scanning Electron Microscopy

In order to observe the etched blanket thin film samples studied in this work, scanning

electron microscopy (SEM) was needed, as optical microscopy could not achieve the resolution

needed at these length scales. SEM relies on the acceleration electrons, which are accelerated

towards an anode with energies ranging from 200 V to 30 kV and then pass through magnetic

lenses which focus the electron beam as it impinges on the sample surface. The secondary electrons

generated by the interaction between the electron beam and the surface are collected to construct

an image of the sample. Other electrons, such as Auger electrons and backscattered electrons, can

also be collected and used for other analyses of the surface. Figure 2-1 illustrates the set-up of an electron beam and shows sample SEM cross-sections for GST before and after etching in a 200 eV Ar$^+$ beam for 10 min. By measuring the thickness of the sample using SEM before and after processing, etch rates and the thickness of material removed can be determined using SEM.
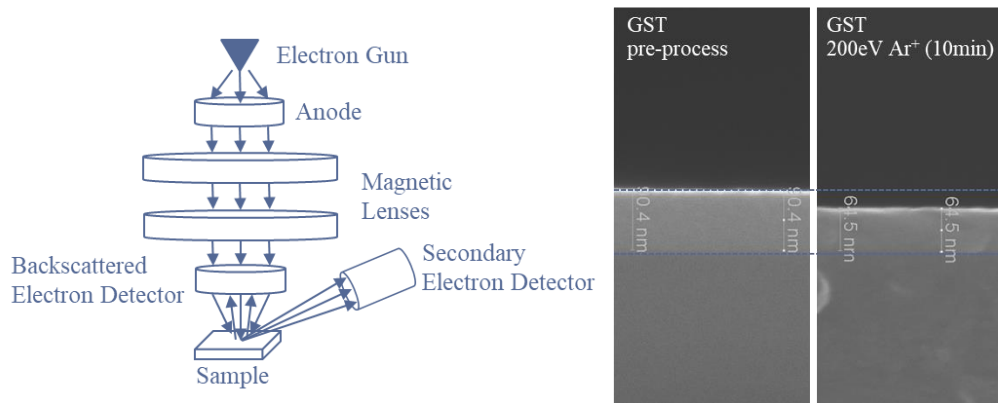
Figure 2-1. Diagram of the scanning electron microscopy set-up and typical cross-section SEM images, taken for GST before and after sputtering by an Ar$^+$ ion beam. Dashed lines are added to highlight the removal of the GST layer post-process.

The measurement of the thickness of the film was limited by how well resolved the features were and the actual placement of the measurement by the operator. For this work, an FEI Nova 600 was used, with all images taken using 10kV and 0.54 nA. The SEM images presented in this research were taken at a magnification of 100,000x, with slight variation ($\pm$100) to account for the distance the sample was moved in order to focus the image. All images were saved as TIF files measuring 1024 by 884 pixels without scale bar (1024x943 pixels including scale bar). At this magnification, each pixel of the image corresponded to approximately 1.4 nm, so the error of the thickness measurement could be considered to be 1.4 nm, corresponding to $\pm$1 pixel. A larger source of error was the resolution of the SEM itself, which was specified to be approximately 5 nm by the manufacturer. For the propagation of this error when applied to the calculation of an etch rate, the 5 nm resolution was simply divided the appropriate time step, as the time step was assumed to be a constant with no error associated with it. As such, the two sets of SEM shown in

Figure 2-2 could be calculated to have etch rates of 0.6 nm/min. and 2.2 nm/min. for Ge and Sb, respectively, with an associated error of ±1 nm/min. since they were measured over 5 min. As such, the Ge could be concluded to not have etched, and the Sb could be concluded to have etched.
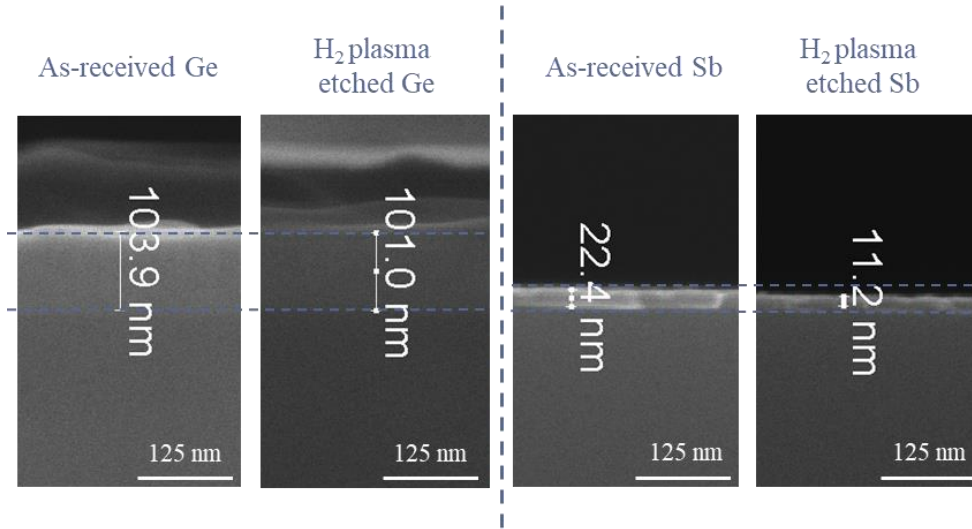
Figure 2-2. Cross-section SEM of a Ge thin film and an Sb thin film as-received and after downstream H_2 at baseline conditions for 5 min. The Ge thin film is an example of an etch measurement where the thickness change falls within the uncertainty of the thickness measurement, while the Sb thin film is an example of an etch measurement where the thickness change is greater than the associated uncertainty.

2.2.3 X-Ray Photoelectron Spectroscopy

This section needs some re-ordering. You can discuss the technique in general, then your specific system. Show table 2.25 first, then the first sample data

X-ray photoelectron spectroscopy (XPS) is a technique for surface analysis that takes advantage of the photoelectric effect to analyze chemical bonding states and composition in a surface. The emission of core-shell electrons by x-ray bombardment is illustrated in Figure 2-3. The binding energy of the emitted photoelectrons can be determined by the following equation:

$$E_k = h\nu - E_b - \Phi \qquad (2.1)$$

where E_k is the kinetic energy of the electron, $h\nu$ is the energy of the incident x-ray, E_b is the binding energy of the emitted photoelectron, and Φ is the work function of the spectrometer. The chemical environment around any particular atom, including such factors as its charge, oxidation state, and local bonding structure, impacts the binding energies of its electrons, resulting in shifts in binding energy that can be observed in XPS spectra. The photoelectron energy analyzer counts all the incoming electrons within a range of binding energies to construct an XPS spectra. These spectra can be collected over a very wide range of binding energies (1200 eV to 0 eV) to construct survey spectra, or they can be over a very narrow window of binding energies (~40-50 eV range) to construct detailed spectra such as the ones shown for Ge, Sb, and Te, in Figure 2-4. Due to the scattering of electrons escaping from a sample, XPS is a surface-sensitive technique that samples from the first 7-10 nm of a surface. Using a Gaussian-Lorentzian fit, the contribution of each peak to the overall collected spectra shape can be determined, and the results can be used to determine the chemical composition of the sample.

Figure 2-3. Diagram of the x-ray photoemission process.

The XPS data in this work was performed using a PSP Vacuum CTX 400 X-ray source and a VG Scientific VG100AX hemispheric energy analyzer. The x-ray source was equipped with both Al and Mg filaments, but only Al k-alpha x-rays (1486 eV) were used in this work. The X-

ray source was not monochromated, and some ghost peaks associated with the Cu housing of the source were observed (Moulder 1995). The scans were controlled using SPECTRA v8 software and an SPCI721F interface card (both available from PSP Vacuum) and operated in Constant Analyzer Energy (CAE) mode, which held the pass energy constant at 50 eV for detailed scans and 100 eV for survey scans. The XPS data was fit using CASA XPS.

Table 2-17. Binding energies and associated spin orbit splitting of Ge, Sb, Te and their oxides (Wagner 1979).

Region	Peak	Binding Energy (eV)	Spin Orbit Splitting (eV)
Ge 3d	Ge	29.4	0.58
Ge 3d	GeO_2	32.7	
Te 3d	Te	572.8	10.4
Te 3d	TeO_2	576.2	
Sb 3d	Sb	528.3	
Sb 3d	Sb_2O_3	530.5	9.34
Sb 3d	Sb_2O_5	531.6	

The XPS analysis of GST was complicated by overlapping in two sets of spectra. Sb 3d and O 1s overlapped one another, and this was accounted for by first fitting the Sb $3d_{3/2}$ peaks, which did not overlap O 1s, and using the ratio of the Sb to Sb^{x+} components determined from the Sb $3d_{3/2}$ peaks to constrain the ratio of Sb to Sb^{x+} components in the Sb $3d_{5/2}$ peaks, with areas multiplied by a known factor for the change in intensity between the Sb $3d_{5/2}$ and Sb $3d_{3/2}$. With all of the Sb accounted for, the remainder of the area under the curves was fit using two peaks for O 1s.

The other set of overlapping spectra was that of Ge 3d and Sb 4d. One alternative would have been to use the Ge 2p region, which did not overlap with other regions of interest in the GST samples. However, due to the age of the XPS detector and the low kinetic energy (i.e., high binding energy) of the Ge 2p electrons, Ge 2p data could not be reliably collected *in-situ*, so Ge 3d was used instead. With Ge 3d and Sb 4d, Sb 4d peaks corresponding to the 0+ oxidation state of Sb

(i.e., metallic Sb) overlapped the Ge 3d peaks corresponding to the 4+ oxidation state of Ge (i.e., Ge oxide). This overlap was mitigated by the Ar cleaning of the GST film, which removed the GST-oxides and thus the overlap between the Ge 3d and Sb 4d spectra. If higher oxidation states of Ge were expected to be present, perhaps due to chlorination or fluorination of the film, the ratio of Sb^{0+} to Sb^{x+} could be fixed based on the known ratio from the Sb 3d spectra. The splitting in the Ge 3d spectra was noted to be quite small (0.58 eV), compared to splitting in Sb 3d and Te 3d (9.34 and 10.4 eV, respectively). The splitting of Ge 3d was not fit in the pure Ge thin film, but for fitting of GST, a second Ge peak, reported in literature to be due to Ge-Te and separated from metallic Ge by 0.6 eV, was used to improve fitting of the Ge 3d spectra.

Te proved to be relatively easy to fit compared to the other elements. The Te 3d region did not overlap any other regions of interest in the GST films, so Te 3d was fit with two sets of peaks, one for the 0+ oxidation state and one for the 4+ oxidation state. The XPS spectra were aligned to the Te $3d_{5/2}$ 0+ since the more suitable peaks for alignment (C 1s and O 1s) were not available as they were either not present due to Ar ion beam cleaning (in the case of C 1s and O 1s) or overlapped with another regions (in the case of O 1s and Sb 3d).
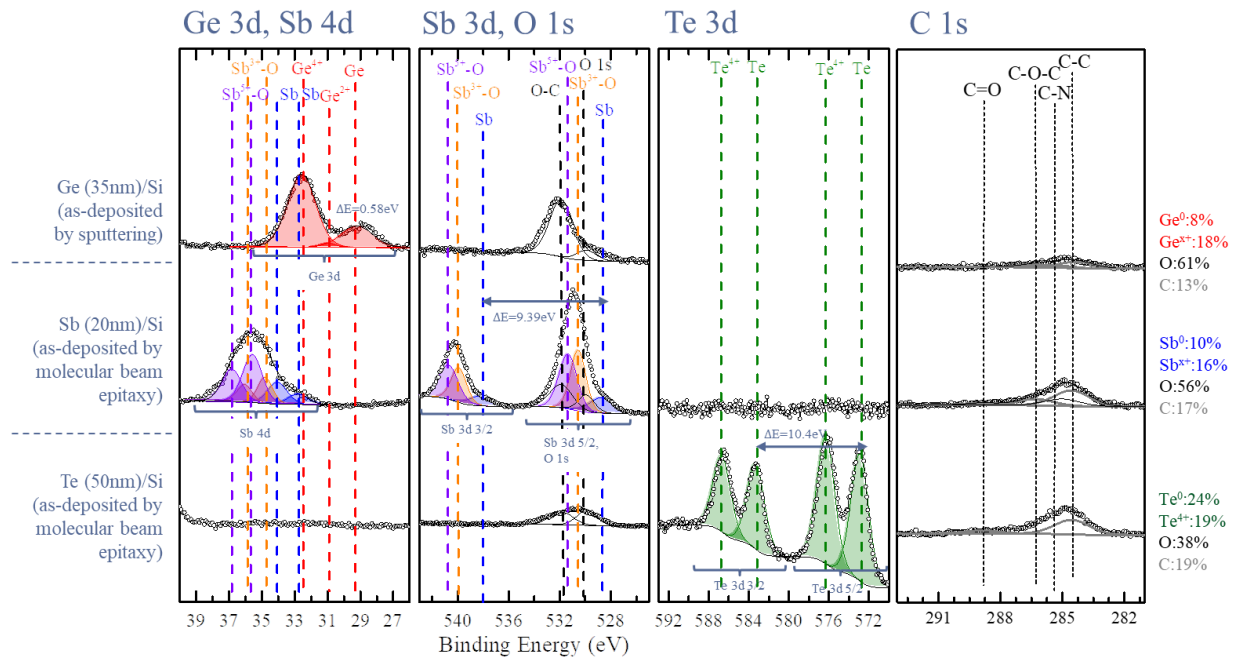
Figure 2-4. Representative XPS spectra of Ge, Sb, and Te thin films.

Table 2-18. XPS model used to fit GST spectra, including peaks, atomic sensitivity factor (ASF), binding energy (BE) (or position), full-width half maximum (FWHM), and any constraints used. The number after the underscore denotes the peak being used to constrain.

	Ge 3d, Sb 4d				
#	Peak	ASF	BE (eV)	FWHM	Constraint(s)
1	Ge 3d 0+ (Ge)	0.536	29.4	1.71	
2	Ge 3d 0+ (GeTe)	0.536	30.0	1.71	FWHM_2=FWHM_1
3	Ge 3d 4+	0.536	32.7	1.71	FWHM_3=FWHM_1
4	Sb 4d 5/2 0+	1.199	32.8	1.62	
5	Sb 4d 5/2 3+	1.199	34.6	1.62	FWHM_5=FWHM_4
6	Sb 4d 5/2 5+	1.199	35.4	1.62	FWHM_6=FWHM_4
7	Sb 4d 3/2 0+	1.199	34.0	1.62	BE_4+1.25; FWHM_7=FWHM_4
8	Sb 4d 3/2 3+	1.199	35.8	1.62	BE_5+1.25; FWHM_8=FWHM_4
9	Sb 4d 3/2 5+	1.199	36.6	1.62	BE_6+1.25; FWHM_9=FWHM_4
10	Te 4d 5/2 0+	1.392	40.5	1.60	
11	Te 4d 5/2 4+	1.392	42.0	1.60	FWHM_11=FWHM_10
12	Te 4d 3/2 0+	1.392	44.0	1.60	BE_10+3.5; FWHM_12=FWHM_10
13	Te 4d 3/2 4+	1.392	45.5	1.60	BE_11+3.5; FWHM_13=FWHM_10
	Sb 3d, O 1s				
#	Peak	ASF	BE (eV)	FWHM	Constraint(s)
14	Sb 3d 5/2 0+	8.627	528.4	1.9	BE_15-9.34
15	Sb 3d 3/2 0+	8.627	537.8	1.9	FWHM_15=FWHM_14
16	Sb 3d 5/2 3+	8.627	530.5	1.9	BE_17-9.34; FWHM_16=FWHM_14
17	Sb 3d 3/2 3+	8.627	539.9	1.9	FWHM_17=FWHM_14
18	Sb 3d 5/2 5+	8.627	531.36	1.9	BE_19-9.34; FWHM_18=FWHM_14
19	Sb 3d 3/2 5+	8.627	540.72	1.9	FWHM_19=FWHM_14
20	O 1s (metallic)	0.78	529.9	2.0	
21	O 1s (carbon)	0.78	531.7	2.0	
	Te 3d				
#	Peak	ASF	BE (eV)	FWHM	Constraint(s)
22	Te 3d 5/2 0+	9.508	572.8	2.0	
23	Te 3d 3/2 0+	9.508	583.2	2.0	BE_22 + 10.4; FWHM_23=FWHM_22
24	Te 3d 5/2 4+	9.508	576.2	2.0	FWHM_24=FWHM_22
25	Te 3d 3/2 4+	9.508	586.6	2.0	BE_24 + 10.4; FWHM_25=FWHM_22

When applicable (i.e., when exposed to a halogen-containing plasma), the presence of Ge, Sb, and Te halides was also considered. These could have been very difficult to distinguish from Ge, Sb, and Te oxides in the spectra, but the use of Ar cleaning removed the oxides prior to exposure to halogen-containing plasma and simplified this XPS analysis.

Quantification of the GST films was accomplished using the Ge 3d, Sb 3d, and Te 3d regions, as well as the C 1s and O 1s spectra and, when applicable, other spectra such as Si 2p, Cl 2p and F 2p. Since the quantified percentages could be changed significantly by the presence of non-Ge, Sb, and Te elements and since the ratio of Ge:Sb:Te was considered to be the factor that determined the GST phase-change properties, the ratios of Ge:Sb:Te from quantified XPS were normalized by the Ge content to ease comparison between different GST samples, as described in Section 2.1.1. Changes in the stoichiometry could be calculated for Sb and Te using this normalization. The ratio of Ge:Sb:Te, normalized to Ge, follows the $1:x_1:x_2$ format described in this chapter. The percent composition change between two compositions $1:x_1:x_2$ and $1:y_1:y_2$ can be calculated as follows:

$$\% \text{ Change in Sb } = \frac{y_1 - x_1}{x_1}; \; \% \text{ Change in Te } = \frac{y_2 - x_2}{x_2} \qquad (2.2)$$

For instance, the change in Ge:Sb:Te ratio from 1:1.0:2.5 (target stoichiometry) to 1:0.8:1.25 (Sb-and Te-depleted) would be calculated to be a (0.8-1.0)/1.0=-20% change in Sb content and a (1.25-2.5)/2.5=-50% change in Te content. Changes in the Sb and Te stoichiometry calculated this way were referred to as % Change Sb (norm. to Ge) or % Change Te (norm. to Ge).

When viewing the raw and fitted XPS data, the intensity of the spectra across different regions on the same sample were adjusted to keep the spectra at roughly the same size for the reader. However, it should be kept in mind that the intensity of the XPS data was in arbitrary units, and that the different elemental peaks needed to be scaled by their atomic sensitivity factors (ASF), which was a factor specific to each detector that the raw area of that particular peak was scaled by to correct for the sensitivity to the detector. These factors are specific to different models of XPS detectors. The ASF for the GST peaks, along with the other factors needed to reproduce the XPS

47

model for fitting the GST spectra in CASA XPS such as binding energy (BE), full width half maximum (FWHM), and constraints on position and area are shown in Table 2-18. Binding energy was allowed to vary within ±0.2 eV. FWHM values were averages of the XPS shown in this work, but they can be expected to vary within ±0.3, except for O 1s, where FWHM could vary over a greater range. Gaussian-Lorentzian line shapes (30% Gaussian) were used for all peaks. Shirley backgrounds were used for all XPS fitting.

Figure 2-5 is an example of the XPS data used in this work. In the top spectra, oxidized Ge, Sb, and Te can be observed, but these are removed by the downstream Ar clean in the bottom spectra. In particular, the removal of Ge 4+ states by Ar cleaning makes the fitting in the Ge 3d, Sb 4d region simpler. The atomic percentages are calculated based on the elements shown for each spectra (Ge, Sb, Te, O, and C in this case). For these samples, the downstream Ar cleaning resulted in (1.0-1.5)/1.0 = -50% change in Sb and (2.4-2.3)/2.3 = +4% change in Te.
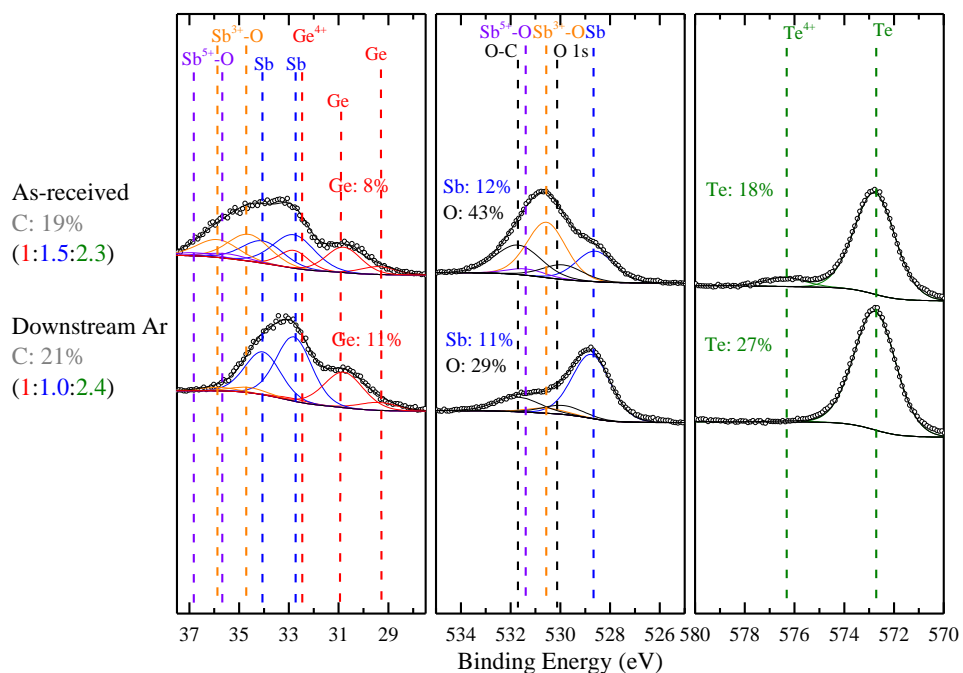
Figure 2-5. Example spectra of GST as-received and after downstream Ar clean at baseline conditions for 5 min.

2.3 Wet Chemical Processing

The wet clean chemistries used in this work are summarized in Table 2-19. DI water was chosen since it is a common cleaning agent and makes up the bulk of other wet clean solutions. Isopropyl alcohol was chosen for being a common cleaning chemistry in semiconductor processing to remove organic species from surfaces. As discussed previously, citric acid has been demonstrated to form stable complexes with Ge and Sb. Citric acid is a weak acid, so a weak base, ammonium hydroxide, was also chosen for study. For wet cleaning, all processes were carried out at room temperature in a 50 mL beaker in a fume hood, then dried using N_2 before being loaded into vacuum systems for XPS analysis.

Table 2-19. Summary of wet etchants and cleans used.

	Boiling Point (ºC)	P_{vap} (Torr, 25ºC)	Conc. Used (%)	Vendor
Isopropyl Alcohol	82.6	40	99.5 (stock)	Fisher Scientific
Citric Acid	Decomposes	1.70E-08	0.08	Sigma Aldrich
Ammonium Hydroxide	38	2160	1.00	Sigma Aldrich
Hydrofluoric Acid	105	n/a	0.3	Sigma Aldrich

The effects of water vapor on the oxidation of GST was also studied in this work, and for these experiments the humidity level was controlled by evaporating DI water in a Pyrex dish on a hot plate in a glove box equipped with a hygrometer to determine the humidity in the glove box, which was considered to be the humidity that the GST sample was exposed to. GST samples were loaded into the humid glove box, and humidity levels of 30%, 70%, and 90% were tested using this setup. No inert gas was used in the glove box during these experiments, so the humidity experiments is of ambient conditions at varying humidity levels.

2.4 Integrated Gas-Phase Chemical Processing

In order to prevent atmospheric exposure, a system consisting of a transfer tube held at ultra-high vacuum (10^{-8}-10^{-9} Torr) and connected processing and analysis chambers is used. A

portion of the system is illustrated in Figure 2-6, showing the inductively-coupled plasma (ICP) chamber and the x-ray photoelectron spectroscopy (XPS) chamber attached to the transfer tube. Several magnetic transfer arms are attached to the system and are used to move samples in and out of chambers and on to and off of a cart located on tracks inside the transfer tube. Samples are mounted to Cab-Fast® platen sample holders and transferred using Cab-Fast® platen forks attached to the ends of the magnetic transfer arms, allowing samples to be transferred between the different chambers while staying in an ultra-high vacuum environment. Three pumps are used to maintain ultra-high vacuum in the transfer tube. A rotary vane pump was used as the roughing pump and was capable of reaching pressures of $\sim 10^{-2}$-10^{-3} Torr on its own. The roughing pump backed a turbomolecular pump, which can achieve a pressure of $\sim 10^{-6}$ in the transfer tube. Lastly, a CTI CryoTorr 8 cryogenic pump was used to reach pressures of $\sim 10^{-8}$-10^{-9} Torr. Pressure was monitored using a cold cathode gauge. A load lock was used to transfer samples into the system and was kept under vacuum by another mechanical pump and turbomolecular pump. Samples could also be transferred in from the ICP chamber.
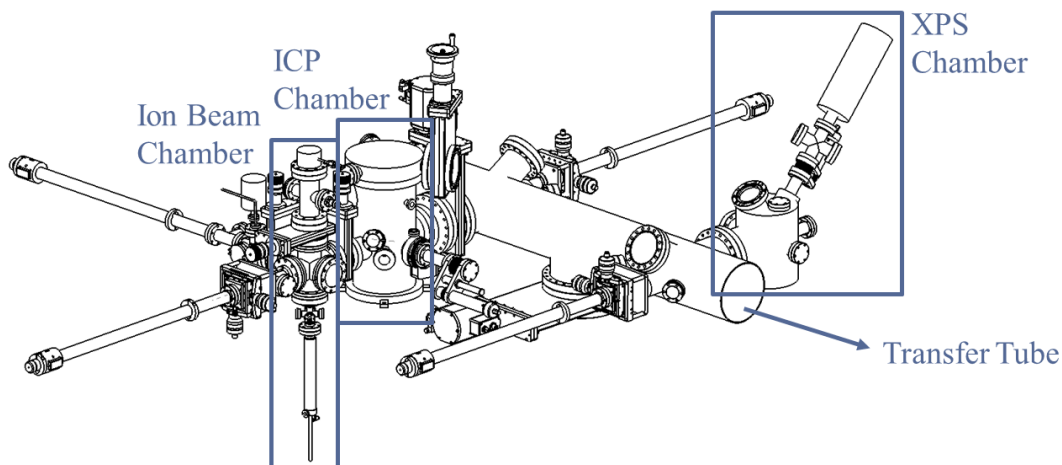
Figure 2-6. Schematic of inductively-coupled plasma (ICP) chamber, ion beam chamber, transfer tube, and x-ray photoelectron spectroscopy (XPS) chamber.

2.4.1 Inductively-Coupled Plasma System

The custom-built ICP chamber was integrated onto the transfer tube and was the primary system in which the plasma processes described in this work were conducted. A cross-sectional view of this chamber is given in Figure 2-7. The chamber was made of stainless steel and consisted of an upper and lower chamber separated by an orifice plate with a circular mesh grid 0.7" in diameter. The upper chamber was lined with a quartz piece shaped like an inverted bell jar to isolate the plasma from the chamber wall. A quartz window separated the chamber and the RF coil. The RF coil was a planar three-turn copper coil seated within a grounded cage and was used to generate and sustain the plasma by inducing a time-varying magnetic field, which ionized gas molecules by stripping them of electrons. The magnetic field was initially symmetric about the plane of the coil, but once the plasma was struck, a plasma current was induced with the opposite direction to the current in the coil, and the corresponding magnetic field had the opposite orientation to the field from the coil and suppressed the penetration of the magnetic field from the coil into the plasma. This depth of penetration, known as the skin depth, and depended on the electron density and collision frequency, and power absorption from the coil was limited to the skin depth. Planar coils are frequently used in semiconductor processing applications due to their generation of a uniform cylindrical plasma. For operation, the RF coil was connected to an automatic matching network and a Seren RF power source capable of supplying 200-1100 W at a frequency of 13.56 MHz. The plasma was struck in the upper chamber and could be extracted through the orifice plate to the lower chamber using a bias wire ring connected to a Kepco DC power supply capable of supplying +500 to -500 V, although in practice voltage has to be limited to prevent sparking in the top chamber. Samples processed in the upper chamber could also be electrically connected to the voltage source to bias the samples.

51
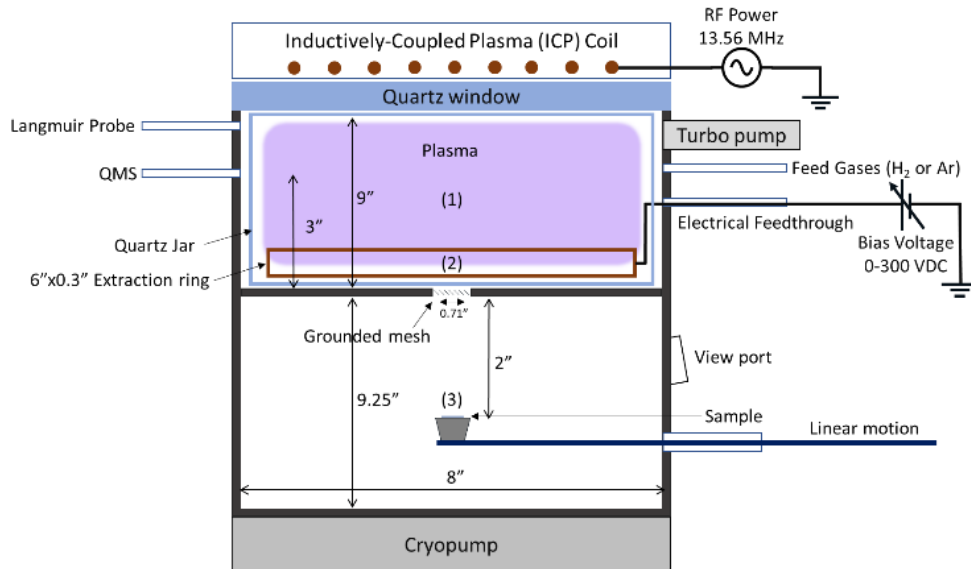
Figure 2-7. Cross-section schematic of the ICP system, including division of the top and bottom chambers, and the three mounting positions for samples studied in this work.

The samples processed in the ICP system in this work were placed in one of three positions. Position (1) was in line-of-sight of the QMS and used to help identify etch products. The wafer or target was mounted to a steel plate, to which a substrate bias of -500V was applied. A high bias was used in hopes of increasing the energy of species to the sample to generate as much etch product as possible. The sample was held at this position by a quartz pedestal. Due to toxicity concerns of Sb, Te, and their reaction products, only a few experiments of limited duration were performed in this configuration.

Position (2) was directly above the circular opening between the two chamber compartments. The sample was mounted on a steel plate to which a substrate bias of -100V was applied. In this position, the sample was directly exposed to the plasma, and thus these experiments were referred to as direct exposure experiments.

Position (3) was 2 inches below the extraction grid in the bottom chamber (a "downstream" configuration). The sample was mounted on a stainless holder and no bias was applied to the

sample. The ion energy was controlled through the potential applied to the extraction ring (100V). When extracting the plasma from the top chamber to the bottom chamber, the extraction bias has to be limited to prevent sparking in the chamber. This process was referred to as a downstream process in this work. Since the gridded mesh has only 25% transmission, it was expected that the etch rate in bottom chamber would be lower than that in the upper chamber, due to reduced number of reactive species reaching the surface. From this position, the etched sample could be transferred into an XPS system without a vacuum break (base pressure of the transfer system at 10^{-8} Torr), thereby allowing for more accurate measurement of the surface composition after etching. The XPS analysis was thus considered to be *in-situ*. The extraction grid could also be removed, allowing for the plasma to emanate from the top chamber to the bottom chamber. While the transmission would be higher in this case due to the removal of the grid, the flux of plasma species to the sample surface would still be lower than in the case of direct exposure to the plasma.

The upper chamber also contained the gas inlets and plasma diagnostics. The gases available on the ICP system were N_2, O_2, Ar, H_2, CH_4, SF_6, Cl_2, and BCl_3 and are summarized below in Table 2-20, and the flow rates of these gases were controlled using MKS and Laminar Technologies mass flow controllers (MFC's). A UTI 100C quadrupole mass spectrometer was attached to the upper chamber for the identification of gas phase species. An Ocean Optics optical emission spectrometer or a Lam Research OES2 optical emission spectrometer could be attached to the quartz window to study optical emissions from the plasma. A Hiden Espion Langmuir probe was available to take I-V curves of the plasma to determine plasma parameters such as plasma potential and electron temperature. The upper and lower chamber were pumped using the same mechanical roughing pump, which also backs the two turbomolecular pumps on the upper chamber. Another turbomolecular pump was attached to the QMS and helped improve the transport of

species to the QMS for detection. The other turbomolecular pump was used to pump the upper

chamber to a pressure of ~10^{-5}-10^{-6} Torr. A cryopump was used to provide pumping for the lower

chamber since conductance through the separating orifice plate is quite low, achieving base

pressures of ~10^{-8} Torr.

Table 2-20. Summary of process gases for use in ICP reactor with corresponding purity and maximum flow rate.

Gas	Ar	N_2	O_2	Cl_2	BCl_3	SF_6	H_2	CH_4
Purity (%)	99.999	99.999	99.993	99.999	99.996	99.996	99.999	99.97
Max. flow rate (sccm)	50	100	50	50	50	50	20	36

The baseline condition for all plasma processes in the ICP chamber was an RF power of

500W applied via the three-turn copper coil and a pressure of approx. 15 mTorr. For downstream

processes, an extraction bias voltage of 100V was applied, and for top chamber processes, a bias

voltage of -100V was applied. These conditions are summarized in Table 2-21.

Table 2-21. Baseline conditions for plasma processes

	Position	RF Power (W)	Pressure (mTorr)	Bias (V)	Time
Direct Exposure	Top Chamber (1), (2)	500	~15	-100	Varies
Downstream	Bottom Chamber (3)	500	~15	100	Varies
Downstream, No Grid	Bottom Chamber (3)	500	~15	n/a	Varies

2.4.2 Optical Emission Spectroscopy

Plasmas consist of many energetic species such as electrons, ions, and neutrals, and the

interactions between these species, such as collisions and charge exchange, result in the generation

of species with excited electronic states. These excited electronic states have a finite lifetime, and

upon relaxation to the ground state, a photon is emitted with energy equal to the change in energy

between the excited and ground states. This optical emission process is illustrated in Figure 2-8.

Excited states can also relax to intermediate energy states, emitting multiple photons, in a process

called cascading. The measured energy of the emitted photons corresponds to a wavelength of

light, which can be used to determine the identity of species in the plasma. More careful analysis of OES using specific compositions of trace rare gases, called actinometry, can be used to determine plasma parameters such as Debye length and electron temperature (Malyshev, MV 1997).
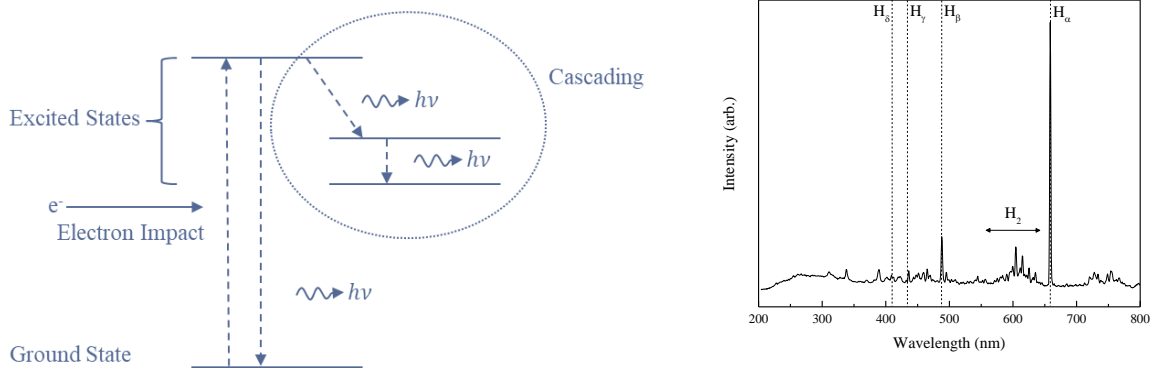
Figure 2-8. Diagram of the optical emission process and OES data taken in ICP chamber for H_2 discharge at baseline conditions.

Figure 2-8 shows the collected OES spectra for an H_2 discharge produced in the ICP chamber at baseline conditions and can be used to illustrate the analysis of OES data. Some features observed in the OES data include the first few lines of the Balmer series: H_α (656 nm), H_β (486 nm), H_γ (434 nm), and H_δ (410 nm), and the Fulcher band for molecular hydrogen (H_2). The intensity ratio of the most intense peak within the Fulcher band (602 nm) divided by the most intense line of the Balmer series (656 nm) was 0.211, which suggested that the H_2 plasmas produced in the ICP chamber were mainly atomic hydrogen. A more quantitative analysis of the species in the plasma can be accomplished through the use of trace rare gas actinometry, but these measurements were not pursued in this work.

2.4.3 Quadrupole Mass Spectrometry

Quadrupole mass spectrometry (QMS) can be used to determine a more detailed compositional analysis of species in a plasma and study these larger and more complex species. Mass spectrometry relies on the filtering charged species using a variable magnetic field, allowing species of a particular mass-to-charge ratio (m/z) to be collected and producing a spectrum. In a quadrupole mass spectrometer, a square array of four parallel metal rods is used to maintain an RF/DC field that serves as a mass filter and increases collector sensitivity and analysis speed. QMS systems are sensitive to the occurrence of natural isotopes and can also detect residual left over in vacuum chambers from exposure to atmosphere. The ionizer filament is set to a voltage of 50V and the QMS is capable of measuring m/z of 1-300, although scans approximately 50-80 m/z wide were used. Figure 2-9 shows QMS for a Cl_2 plasma with Si sample at a baseline condition. Here the data shows the presence of several Cl_2 peaks, which could correspond to different isotopes of Cl. However, these are not as intense as the peaks around 35 m/z, which correspond to atomic Cl and its isotopes, as well as contributions from HCl, which could form due to available H from water vapor adsorbed to the walls of the chamber. Another peak around 17 m/z was identified as the presence of OH groups, although the peak is wide enough to have contributions from water (H_2O, 18 m/z). Given the need to vent the chamber to mount samples for etch product measurement, all etch product measurements in this work should expect to have water vapor contamination. In this case, a Si wafer was mounted at position (2), and a Si peak is readily observed. An expected etch product, $SiCl_4$ would have a m/z of 168, which is well beyond what was included in this scan. The peaks at small m/z are convoluted with the RF envelope of the QMS, as such, they are not used in detecting the presence of atomic H.

Figure 2-9. QMS of Cl_2 plasma in ICP system with Si sample (500W/12mTorr, ionizer: 1mA).

2.4.4 Plasma Chemistry

2.4.4.1 H_2 Plasma

While Langmuir probe measurements were not available, literature on inductively-coupled H_2 plasmas suggests that the electron temperature (T_e) at the baseline conditions was approximately 4 eV (Gao 2018). Although the pressure, RF frequency, and gas composition were similar to that used in this work, this T_e is expected to be an overestimate due to the higher RF power used. QMS measurements of the H_2 plasma were not available, as the QMS did not have the necessary resolution at such small m/z (1 to 2 for H and H_2, respectively). Table 2-22 presents a list of major reactions in a hydrogen plasma by the rate constants in descending order. The most dominant reactions in the plasma are electron-impact excitation and ionization. Ions are produced via H_2 ionization in H_2 plasma resulting in H_2^+. Electron impact can also dissociate molecular H_2 and H_2^+ ions, generating atomic H and H^+ species. Charge transfer between H_2^+ and H or H_2 and

H^+, although the charge transfer from atomic ionic hydrogen to molecular hydrogen (reaction 6) is quite slow. Reactions between H_2 and H_2^+ species can generate H_3^+ ions, which can dissociate completely into three atomic H or to H_2 and H.

Table 2-22. Hydrogen plasma reaction set, adapted mainly from (Mendez 2006)

No.	Reaction	Rate Constant k (cm^3s^{-1})	Ref.
1	$e + H \rightarrow H^+ + 2e$	$6.5\times10^{-9}T_e^{0.5}\times e^{-12.9/Te}$	(Mendez 2006),(Jiménez-Redondo 2014)
2	$e + H_2 \rightarrow H^+ + H + 2e$	$3\times10^{-8}T_e^{0.4}\times e^{-37.7/Te}$	(Mendez 2006)
3	$e + H_2^+ \rightarrow H^+ + H + e$	$1.1\times10^{-7}T_e^{0.05}\times e^{-9.7/Te}$	(Mendez 2006)
4	$e + H_2^+ \rightarrow H^+ + H^+ + 2e$	$2.1\times10^{-9}T_e^{0.3}\times e^{-23.3/Te}$	(Mendez 2006)
5	$H_2^+ + H \rightarrow H_2 + H^+$	9.0×10^{-10}	(Mendez 2006)
6	$H_2 + H^+ \rightarrow H_2^+ + H$	1.2×10^{-22}	(Mendez 2006)
7	$e + H_2 \rightarrow H_2^+ + 2e$	$3.1\times10^{-8}T_e^{0.2}\times e^{-20/Te}$	(Mendez 2006)
8	$e + H_3^+ \rightarrow H_2^+ + H + e$	$4.8\times10^{-7}T_e^{-0.05}\times e^{-19.1/Te}$	(Mendez 2006)
9	$e + H_2^+ \rightarrow H + H$	$7.5\times10^{-9}-1.1\times10^{-9}T_e+1.0\times10^{-10}T_e^2-4.1\times10^{-12}T_e^3+5.9\times10^{-14}T_e^4$	(Mendez 2006)
10	$H_2^+ + H_2 \rightarrow H_3^+ + H$	2.6×10^{-9}	(Mendez 2006)
11	$e + H_3^+ \rightarrow 3H$	$0.5\times8.4\times10^{-9}+3.0\times10^{-9}T_e-3.8\times10^{-10}T_e^2+1.3\times10^{-11}T_e^3+2.4\times10^{-13}T_e^4-2.3\times10^{-14}T_e^5+3.5\times10^{-16}T_e^6$	(Mendez 2006)
12	$e + H_3^+ \rightarrow H_2 + H$	$0.5\times8.4\times10^{-9}+3.0\times10^{-9}T_e-3.8\times10^{-10}T_e^2+1.3\times10^{-11}T_e^3+2.4\times10^{-13}T_e^4-2.3\times10^{-14}T_e^5+3.5\times10^{-16}T_e^6$	(Mendez 2006)
13	$e + H_2 \rightarrow 2H + e$	$1.8\times10^{-7}T_e^{-1.2}\times e^{-12.6/Te}$	(Mendez 2006)
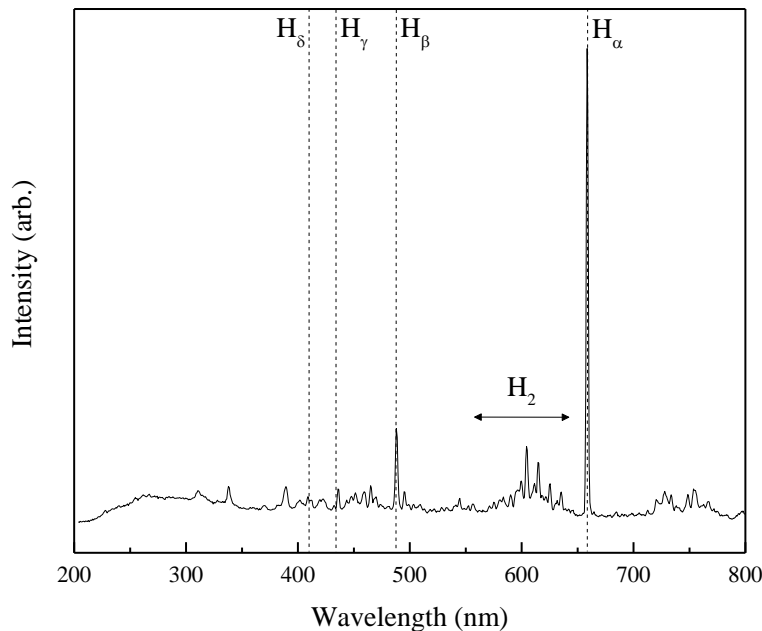
Figure 2-10. OES data taken in ICP chamber for H_2 discharge at baseline conditions. The first 4 lines of the Balmer series can be observed, as can the Fulcher band. The relative intensities of the Balmer series and the Fulcher band suggested that the plasma was majority atomic hydrogen.

Figure 2-10 shows the collected OES spectra for an H_2 discharge produced in the ICP chamber at baseline conditions and can be used to illustrate the analysis of OES data. Features observed in the OES data include the first few lines of the Balmer series: H_α (656 nm), H_β (486 nm), H_γ (434 nm), and H_δ (410 nm), and the Fulcher band for molecular hydrogen (H_2). The intensity ratio of the most intense peak within the Fulcher band (602 nm) divided by the most intense line of the Balmer series (656 nm) was 0.211, which suggested that the H_2 plasmas produced atomic hydrogen, which should be suitable for the etching of GST with atomic hydrogen, as predicted by thermodynamics in Section 2.1.

2.4.4.2 Cl_2 Plasma

While Langmuir probe measurements were not available, literature on inductively-coupled Cl_2 plasmas suggests that the electron temperature at the baseline conditions was around 3 eV

(Malyshev, M. V. 1998). Although the pressure, RF frequency, and gas composition were similar to that used in this work, this T_e is expected to be an overestimate due to the higher RF power used. Reactions in a Cl_2 plasma are summarized in Table 2-23. Dissociative ionization of the molecule was not included, as the authors concluded that the probability of the reaction was low. Metastable chlorine states were not included in this table due to the high threshold energy required for their generation, and dissociative ionization of the Cl_2 was also not included due to high threshold energy and the density of the molecular species being low. The formation of Cl_2^+ by electron impact (reaction 1) is the fastest among the electron impact reactions, but there should still be little Cl_2^+ in the plasma since reaction 7 consumes Cl_2^+ and has a larger rate coefficient. As such it would be expected that the Cl_2 plasma is mostly dissociated Cl, Cl^+, and Cl^-.

Table 2-23. Chlorine plasma reaction set, reproduced from (Lee, C. 1995)

No.	Reaction	Rate Coefficients	Reference
1	$e + Cl_2 \rightarrow Cl_2^+ + 2e$	$k_1 = 9.21*10^{-8} \exp(-12.9/T_e)$ cm^3 s^{-1}	(Kurepa 1978)
2	$e + Cl_2 \rightarrow Cl^+ + Cl + 2e$	$k_1 = 3.88*10^{-9} \exp(-15.5/T_e)$ cm^3 s^{-1}	(Kurepa 1978)
3	$e + Cl_2 \rightarrow Cl^+ + Cl^- + e$	$k_1 = 8.55*10^{-10} \exp(-12.65/T_e)$ cm^3 s^{-1}	(Kurepa 1978)
4	$e + Cl_2 \rightarrow 2Cl(^2P) + e$	$k_2 = 3.80*10^{-8} \exp(-3.824/T_e)$ cm^3 s^{-1}	(Cosby 1992)
5	$e + Cl_2 \rightarrow Cl(^2P) + Cl^-$	$k_3 = 3.69*10^{-10} \exp(-1.68/T_e + 1.457/T_e^2 - 0.44/T_e^3 + 0.0572/T_e^4 - 0.0026/T_e^5)$ cm^3 s^{-1}	(Kurepa 1978)
6	$e + Cl(^2P) \rightarrow Cl^+ + 2e$	$k_4 = (T_e/12.96)^{0.5} \exp(12.96/T_e)(1.419*10^{-7} - 1.864*10^{-8}\log(T_e/12.96) - 5.439*10^{-8}\log(T_e/12.96)^2 + 3.306*10^{-8} \log(T_e/12.96)^3 - 3.54*10^{-9}\log(T_e/12.96)^4 - 2.915*10^{-8} \log(T_e/12.96)^5$ cm^3 s^{-1}	(Lennon 1988)
7	$Cl^- + Cl_2^+ \rightarrow Cl(^2P) + Cl_2$	$k_5 = 5.8*10^{-8}$ cm^3 s^{-1}	(Rogoff 1986)
8	$Cl^- + Cl^+ \rightarrow Cl(^2P) + Cl(^2P_u)$	$k_6 = 5.0*10^{-8}$ cm^3 s^{-1}	(Rogoff 1986)
9	$e + Cl^- \rightarrow Cl(^2P) + 2e$	$k_7 = 2.63*10^{-8} \exp(-5.37/T_e)$ cm^3 s^{-1}	(Lee, C. 1995)
10	$Cl(^2P) \rightarrow \frac{1}{2} Cl_2$	$k_{12} = \gamma_{rec}D_{eff}/\Lambda^2$ s^{-1}	(Lee, C 1994)
11	$Cl^+ \rightarrow Cl(^2P)$	$k_{14} = 2u_{B,Cl^+}(R^2h_L + RLh_R)/R^2L$ s^{-1}	(Lee, C. 1995)
12	$Cl_2^+ \rightarrow Cl_2(g)$	$k_{15} = 2u_{B,Cl_2^+}(R^2h_L + RLh_R)/R^2L$ s^{-1}	(Lee, C. 1995)

For Table 2-23, reaction 10, γ_{rec} is the surface recombination coefficient, D_{eff} is the effective diffusion constant for the neutral species, and Λ is the effective diffusion length. For reactions 11 and 12, R and L are the radius and length of the plasma reactor, respectively, h_R and

h_L are the ratios of ion sheath edge density to bulk average ion density at the radial and axial sheath edges, respectively, and u_B is the Bohm velocity.

Figure 2-11 shows QMS for a Cl_2 discharge at baseline conditions with a Si wafer sample. Here the data shows the presence of several Cl_2 peaks, which could correspond to different isotopes of Cl. However, these are not as intense as the peaks around 35 m/z, which correspond to atomic Cl and its isotopes, as well as contributions from HCl, which could form due to available H from water vapor adsorbed to the walls of the chamber. Another peak around 17 m/z was identified as the presence of OH groups, although the peak is wide enough to have contributions from water (H_2O, 18 m/z). Given the need to vent the chamber to mount samples for etch product measurement, all etch product measurements in this work should expect to have water vapor contamination. In this case, a Si wafer was mounted at position (2), and a Si peak is readily observed. An expected etch product, $SiCl_4$, would have a m/z of 168, which is well beyond what was included in this scan. The peaks at small m/z are convoluted with the RF envelope of the QMS, as such, they are not used in detecting the presence of atomic H.

Figure 2-11. QMS of Cl$_2$ plasma in ICP system with Si sample (500W/12mTorr, ionizer: 1mA). Both atomic and molecular chlorine species can be observed. HCl species are also observed, which is likely due to the presence of water vapor in the chamber. Si can also be observed, although the SiCl$_4$ etch product is outside the m/z range of this scan. The relative intensities of atomic v. molecular chlorine species suggested that the plasma is majority atomic chlorine species.
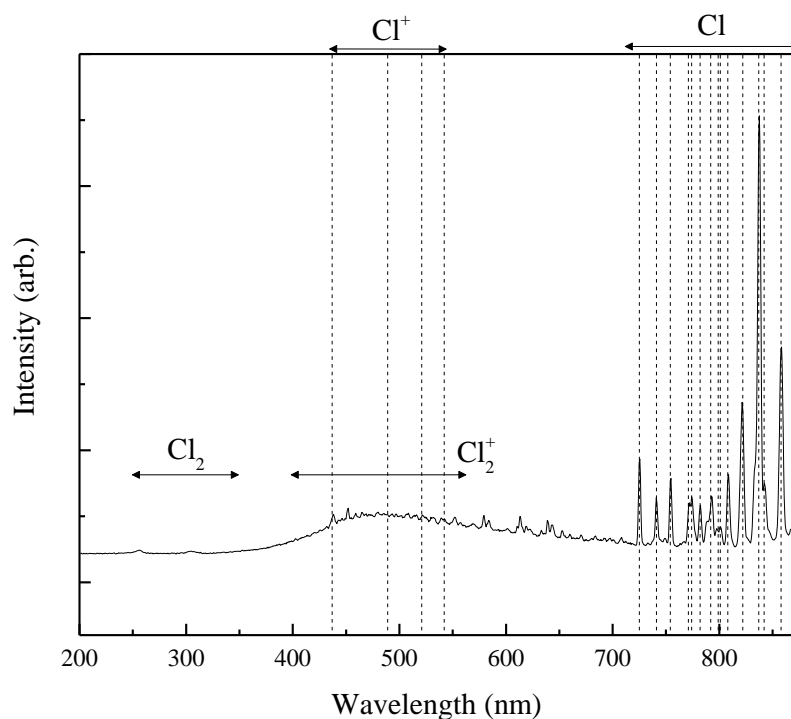
Figure 2-12. OES of Cl_2 plasma in ICP system at baseline conditions. Atomic Cl lines and the band for Cl_2^+ can be observed. Only one line for Cl^+ can be distinguished against the band for Cl_2^+, and the band for Cl_2 cannot be distinguished. The spectrum suggests that the Cl_2 plasma is majority atomic Cl.

In the OES of the Cl_2 plasma, shown in Figure 2-12, the presence of strong Cl lines between 720 and 860 nm was observed, while the Cl_2 band at 305 nm, Cl_2^+ bands between 400 and 550 nm, and Cl^+ lines in the 370-550 nm region were all weak in intensity by comparison (Malyshev, M. V. 1998). The relative intensities of these features of the Cl_2 spectrum indicated that the plasma was well-dissociated and majority atomic Cl.

2.4.4.3 SF$_6$ Plasma

While Langmuir probe measurements were not available, literature on inductively-coupled SF$_6$/Ar plasmas suggests that the electron temperature at the baseline conditions was around 2.8 eV (Lallement 2009). Although the pressure, RF frequency, and gas composition were similar to that used in this work, this T_e is expected to different due to the higher RF power used. Reactions

in an SF_6 plasma are summarized in Table 2-24, Table 2-25 and Table 2-26, where the rate coefficient has the form:

$$k_G = \exp\left(A + B\ln(T_e) + \frac{C}{T_e} + \frac{D}{T_e^2} + \frac{E}{T_e^3}\right) \tag{2.3}$$

A survey of the rate coefficients reported suggested that reactions 22-27 (momentum transfer) and 42-49 (ion recombination) are the fastest occurring reactions. Of the neutral dissociations, reaction 1, 4, and 5 are occur more quickly than reactions 2 or 3, which reflects the likelihood of a single electron causing more than one F atom to dissociate, which is also apparent by the higher threshold energy required. Most F was assumed to be from dissociation. Reactions 6 and 7 had a slower reaction rate than other neutral dissociations, but it was noted that the only reaction that appears to produce F_2 was ion-molecule recombination (reaction 50), which was a relatively slow reaction and would likely limit formation of F_2. Ionization was the next fastest class of reactions, with reactions 8, 11, and 15 occurring the most rapidly among them. Reactions 20-21 (detachment) and 35-41 (neutral recombination were the slowest to occur). From this set of reaction data, it was suggested that an SF_6 plasma would be composed mostly of atomic F and SF_x species from which the F had been dissociated by electron impact. These impacts occur through a multistep process, where SF_6 dissociates to F and SF_5, which dissociates to F and SF_4, which dissociates to F and SF_3. The multiple-fluorine dissociations are not as likely to occur. The formation of larger dimers such as S_2F_{10} was not included in the reaction set.

Table 2-24. SF_6 reaction sets of neutral dissociations and ionizations, reproduced from (Kokkoris 2009), using a Maxwellian electron energy distribution function to integrate cross-section data to determine rate coefficient parameters.

No.	Reaction	E_{th} (eV)	A	B	C	D	E	Ref.
				Parameters for Rate Coefficients				
Neutral Dissociations								
1	$SF_6 + e \rightarrow SF_5 + F + e$	9.6	-29.57	-0.2859	-13.80	1.148	-0.0781	(1)
2	$SF_6 + e \rightarrow SF_4 + 2F + e$	12.1	-31.37	-0.3721	-14.42	0.5679	-0.0375	(1)
3	$SF_6 + e \rightarrow SF_3 + 3F + e$	16.0	-33.91	1.237	-15.06	-0.0081	-0.0042	(1)
4	$SF_5 + e \rightarrow SF_4 + F + e$	9.6	-29.57	-0.2859	-13.80	1.148	-0.0781	(1)
5	$SF_4 + e \rightarrow SF_3 + F + e$	9.6	-29.57	-0.2859	-13.80	1.148	-0.0781	(1)
6	$F_2 + e \rightarrow 2F + e$	3.16	-31.89	-0.5549	-5.238	0.4288	-0.0266	(2)
7	$F_2 + e \rightarrow 2F + e$	4.34	-33.36	-0.2982	-5.312	0.1970	-0.0124	(2)
Ionizations								
8	$SF_6 + e \rightarrow SF_5^+ + 2e + F$	15.5	-31.46	0.5827	-15.62	0.0392	-0.0028	(3)
9	$SF_6 + e \rightarrow SF_4^+ + 2e + 2F$	18.5	-34.41	0.7534	-18.39	0.0054	-0.0010	(3)
10	$SF_6 + e \rightarrow SF_3^+ + 2e + 3F$	20	-33.01	0.6900	-19.32	-0.1185	0.0065	(3)
11	$SF_5 + e \rightarrow SF_5^+ + 2e$	11.2	-32.78	0.8601	-10.76	0.0558	0.0025	(4)
12	$SF_5 + e \rightarrow SF_4^+ + F + 2e$	14.5	-33.20	1.0177	-13.76	-0.1309	0.0075	(4)
13	$SF_4 + e \rightarrow SF_4^+ + 2e$	13	-32.01	0.5939	-14.83	2.220	-0.9045	(4)
14	$SF_4 + e \rightarrow SF_3^+ + F + 2e$	14.5	-31.78	0.5357	-16.26	1.974	-0.7729	(4)
15	$SF_3 + e \rightarrow SF_3^+ + 2e$	11	-33.23	1.073	-10.36	-0.1016	0.0055	(4)
16	$F_2 + e \rightarrow F_2^+ + 2e$	15.69	-33.38	0.8249	-15.96	0.0655	-0.0041	(4)

(1) Iio 1995, Christophorou 2000; (2) (Morgan 1992); (3) (Stanski 1983, Iio 1995, Christophorou 2000); (4) (Tarnovsky 1998)

Table 2-25. SF_6 reaction sets of attachments, detachments, momentum transfer, excitations, and neutral recombination, reproduced from (Kokkoris 2009), using a Maxwellian electron energy distribution function to integrate cross-section data to determine rate coefficient parameters.

No.	Reaction	E_{th} (eV)	A	B	C	D	E	Ref.
			Parameters for Rate Coefficients					
Attachments								
17	$SF_6 + e \rightarrow SF_5 + F^-$	0.1	-33.40	-1.061	-0.1017	-0.0161	0.0006	(1)
18	$SF_6 + e \rightarrow SF_5^-$		-32.77	-1.500	-0.0788	0.0013	0	(1)
19	$F_2 + e \rightarrow F + F^-$		-32.81	-1.440	-0.5283	0.0558	-0.0028	(2)
Detachment								
20	$F^- + N \rightarrow F + N + e$, $N = SF_6$, SF_5, SF_4, SF_3, F, F_2		-44.39	0	0	0	0	(1)
21	$SF_6^- + N \rightarrow SF_6 + N + e$, $N = SF_6$, SF_5, SF_4, SF_3, F, F_2		-44.98	0	0	0	0	(1)
Momentum Transfer								
22	$SF_6 + e \rightarrow SF_6 + e$		-29.23	0.2158	-1.400	0.2460	-0.0145	(1)
23-25	$SF_x + e \rightarrow SF_x + e$, x = 3,4,5		-29.23	0.2158	-1.400	0.2460	-0.0145	(1)
26	$F_2 + e \rightarrow F_2 + e$		-29.01	-0.1088	-0.6889	0.0533	-0.0011	(2)
27	$F + e \rightarrow F + e$		-29.01	-0.1088	-0.6889	0.0533	-0.0011	(2)
Excitations								
28	Total vibrational excitation of SF_6	0.09	-26.84	-1.461	-8.346	7.867	-2.913	(1)
29	Vibrational excitation of F_2	0.1108	-33.47	-1.460	-0.9889	0.1224	-0.0070	(2)
30	Vibrational excitation of F_2	0.2188	-33.19	-1.460	-1.061	0.1228	-0.0071	(2)
31	Vibrational excitation of F_2	0.3237	-33.53	-1.460	-1.1440	0.1037	-0.0060	(2)
32	Vibrational excitation of F_2	0.4205	-34.62	-1.460	-1.1440	0.1037	-0.0060	(2)
33	Excitation of F_2	11.57	-32.57	0.3734	-12.69	0.3318	0.0227	(2)
34	Excitation of F_2	13.08	-36.25	0.9008	-13.30	0.1361	-0.0107	(2)
Neutral Recombination								
35	$F + SF_5 \rightarrow SF_6$		-42.83	0	0	0	0	(3)
36	$F + SF_4 \rightarrow SF_5$		-42.83	0	0	0	0	(3)
37	$F + SF_3 \rightarrow SF_4$		-42.83	0	0	0	0	(3)
38	$F_2 + SF_5 \rightarrow SF_6 + F$		-46.41	0	0	0	0	(4)
39	$F_2 + SF_4 \rightarrow SF_5 + F$		-46.41	0	0	0	0	(4)
40	$F_2 + SF_3 \rightarrow SF_4 + F$		-46.41	0	0	0	0	(4)
41	$SF_5 + SF_5 \rightarrow SF_6 + SF_4$		-41.50	0	0	0	0	(3)

(1) (Christophorou 2000), (2) (Morgan 1992), (3) (Ryan 1990), (4) (Anderson 1986)

Table 2-26. SF_6 reaction sets of ion recombination and ion-molecule reactions, reproduced from (Kokkoris 2009), using a Maxwellian electron energy distribution function to integrate cross-section data to determine rate coefficient parameters.

No.	Reaction	E_{th} (eV)	A	B	C	D	E	Ref.
				Parameters for Rate Coefficients				
Ion Recombination								
42-49	$I^+ + J^- \rightarrow I + J$ $I = SF_5,\ SF_4,\ SF_3,$ $F_2,\ J = SF_6,\ F$		-29.93	0	0	0	0	(1)
Ion-Molecule Reactions								
50	$SF_6 + SF_5^+ \rightarrow SF_6$ $+ SF_3^+ + F_2$		-39.65	0	0	0	0	(2)

(1) (Anderson 1986, Rauf 2002), (2) (Talib 1992)

QMS of the SF_6/Ar plasma was not available due to instrument failure. OES of the SF_6/Ar plasma, shown in Figure 2-13 showed that Ar and F lines were present, although the intensity of the F lines was low compared to Ar. Only one line for S was observed at 675 nm, but this line overlapped an Ar line. Other S lines at 792 and 469 nm were not observed, so it was concluded that the line at 675 nm was from Ar and that no atomic S could be detected by OES. SF_x signals were reported to be between 250-350 nm, but these could not be detected by OES (Shim 2012).
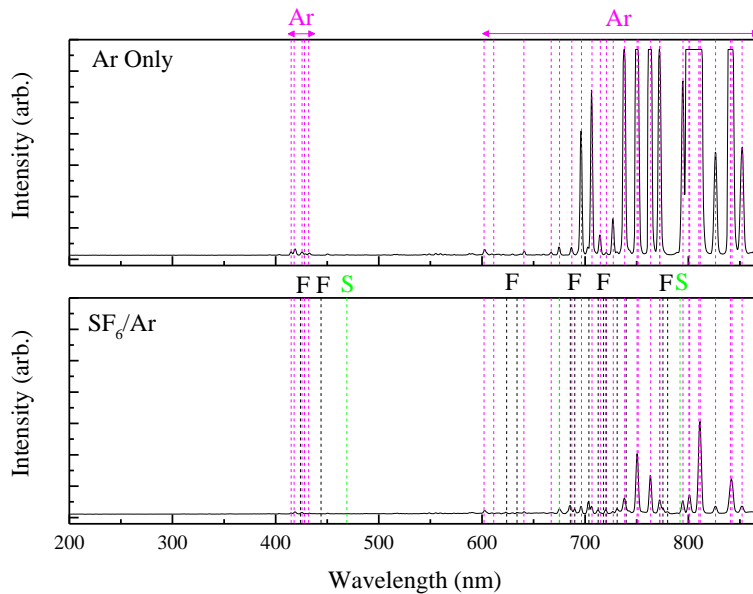
Figure 2-13. OES of Ar and SF$_6$/Ar plasmas at baseline conditions. Some atomic F lines can be distinguished, but no molecular fluorine, sulfur, or SF$_x$ signals can be distinguished. Both spectra are scaled to the OES detector maximum.

2.4.4.4 CH$_4$ Based Plasmas

Table 2-27 presents a list of major reactions in Ar and CH$_4$ plasmas by their rate constants in descending order. In an Ar plasma, Ar* and Ar$^+$ are the dominant species. In a pure CH$_4$ plasma, the electron-impact ionization and dissociation of CH$_4$ results in the production of H and other hydrocarbons and an increase in electron number density in the plasma. Additionally, ion-neutral reactions 15-24 mostly generate ionized methyl groups and H atoms. C$_2$H$_6$, C$_2$H$_4$, and C$_2$H$_5$ molecules are other major molecules in CH$_4$ plasma that are produced by reactions 14-23 and 20-27, and 29.

In mixtures such as CH$_4$/Ar, more complex gas-phase reaction pathways need to be considered. For CH$_4$/Ar plasma, the contribution of Ar-ion assisted etching and the reactive gas composition in the etch process needs to be considered. It has been reported that the degree of dissociation of methane in CH$_4$/Ar plasma is about 50% higher than that in a pure CH$_4$ plasma.

68

The methyl radical concentration in CH_4/Ar plasma has been reported in order of 10^{12} cm^{-3} and slightly lower concentrations of other radicals and stable molecules such as CH_2, C_2H_2, CH, C_2H_4, and C_2H_6, respectively.(Schulz-von Der Gathen 2001) The concentration of stable volatile molecules such as C_2H_2 and C_2H_6 was shown to depend inversely on the removal concentration of CH_4 (Schulz-von Der Gathen 2001).

Table 2-27. List of electron-impact ionization and dissociation reactions in Ar/CH_4 plasmas.

No.	Reaction	Rate Constant k (cm^{3}s^{-1})	Ref.
	Electron-impact ionization and dissociation		
1	$e^- + CH_4 \rightarrow CH_4^+ + 2e^-$	3.0×10^{-7}	(1,2,3)
2	$e^- + C_2H_4 \rightarrow C_2H_4^+ + 2e^-$	3.0×10^{-7}	(3,4,5)
3	$e^- + CH_4 \rightarrow CH_3 + H + e^-$	4.5×10^{-8}	(2,6)
4	$e^- + CH_3 \rightarrow CH_2 + H + e^-$	-	(5)
5	$e^- + CH_3 \rightarrow CH + 2H + e^-$	-	(5)
6	$e^- + CH_4 \rightarrow CH_3^+ + H + 2e^-$	3.2×10^{-8}	(1,2)
7	$e^- + H_2 \rightarrow 2H + e^-$	2.0×10^{-8}	(1,7)
8	$e^- + H_2^+ \rightarrow H^+ + H + e^-$	$1.1\times10^{-7}T_e^{0.05}\times e^{-9.7/Te}$	(8,9)
9	$e^- + CH_4 \rightarrow CH_2 + H_2 + e^-$	7.3×10^{-9}	(2)
10	$H_2^+ + H_2 \rightarrow H + H_3^+$	2.5×10^{-9}	(2)
11	$e^- + Ar \rightarrow Ar^+ + 2e^-$	$2.5\times10^{-8}T_e^{0.5}\times e^{-16.3/Te}$	(8,9)
12	$Ar^+ + H_2 \rightarrow Ar + H_2^+$	2.1×10^{-9}	(10,11)
13	$e^- + H \rightarrow H^+ + 2e^-$	$6.5\times10^{-9}T_e^{0.5}\times e^{-12.9/Te}$	(8,9)
14	$e^- + H_2 \rightarrow H_2^+ + 2e^-$	$3.1\times10^{-8}T_e^{0.2}\times e^{-20/Te}$	(8,9)

(1) (Davies 1989), (2) (Kline 1989), (3) (Denysenko 2004), (4) (Hayashi 1990), (5) (Alman 2000), (6) (Nakano 1991), (7) (Engelhardt 1963), (8) (Jiménez-Redondo 2014), (9) (Mendez 2006), (10) (Bedford 1990), (11) (Ellis 2016)

Table 2-28. List ion-neutral dissociation and neutral-neutral reactions in Ar/CH$_4$ plasmas.

No.	*Reaction*	Rate Constant k (cm3s-1)	Ref.
	Ion-neutral dissociation		
15	$CH_4 + C_2H_2^+ \rightarrow C_2H_3^+ + CH_3$	4.1×10^{-9}	(1)
16	$C_2H_6 + H_3^+ \rightarrow C_2H_5^+ + 2H_2$	2.0×10^{-9}	(2)
17	$CH_4 + H_3^+ \rightarrow CH_5^+ + H_2$	1.6×10^{-9}	(1)
18	$CH_4 + CH_4^+ \rightarrow CH_5^+ + CH_3$	1.5×10^{-9}	(1,3)
19	$CH_4 + C_2H_2^+ \rightarrow C_2H_5^+ + H$	1.4×10^{-9}	(1)
20	$CH_4 + CH_3^+ \rightarrow C_2H_5^+ + H_2$	1.2×10^{-9}	(1,3)
21	$C_2H_4 + H_3^+ \rightarrow C_2H_5^+ + H_2$	1.9×10^{-9}	(1)
22	$C_2H_2 + H_3^+ \rightarrow C_2H_3^+ + H_2$	1.9×10^{-9}	(1)
23	$CH_4 + Ar^+ \rightarrow CH_3^+ + H + Ar$	1.0×10^{-9}	(4)
24	$C_2H_4 + C_2H_4^+ \rightarrow C_3H_5^+ + CH_3$	3.9×10^{-10}	(1)
	Neutral-neutral reactions		
25	$CH_4 + CH \rightarrow C_2H_x + H_y$	3.6×10^{-10}	(5)
26	$CH_3 + CH_x \rightarrow C_2H_x$	1.8×10^{-10}	(5)
27	$CH_3 + CH_3 \rightarrow C_2H_6$	6.0×10^{-11}	(6)
28	$H + C_2H_5 \rightarrow 2CH_3$	6.0×10^{-11}	(1,5)
29	$H + C_2H_5 \rightarrow C_2H_4 + H_2$	5.0×10^{-11}	(5)

(1) (Tachibana 1984), (2) (Herrebout 2001), (3) (Kline 1989), (4) (Chatham 1983), (5) (Heintze 2002), (6) (Denysenko 2004)

QMS studies of Ar, CH$_4$ and CH$_4$/Ar plasmas are shown in Figure 2-14. The mixture of Ar with CH$_4$ was expected to lower the electron temperature (Gordillo-Vázquez 2005). The QMS of the Ar plasma showed the presence of both Ar and Ar$^+$ as well as residual moisture. The QMS of CH$_4$ plasma showed the dissociation of CH$_4$ into CH$_x$ species. The majority of the plasma was CH$_4$ and CH$_3$, with significantly less CH$_2$ and CH and little to no C. Although it was not as well-resolved as the CH$_4$ plasma, the QMS of the mixed CH$_4$/Ar plasma showed a CH$_3$ peak that was relatively smaller compared to CH$_4$, suggesting that the addition of Ar resulted in more cracking of CH$_4$, which could be expected to increase the atomic H available for reaction. CH$_2$ appeared to be relatively larger as well. The peaks at 26 and 27 m/z were considered to be C$_2$H$_x$ species such as C$_2$H$_2$, which could result in greater C deposition on a GST surface from a CH$_4$/Ar plasma.
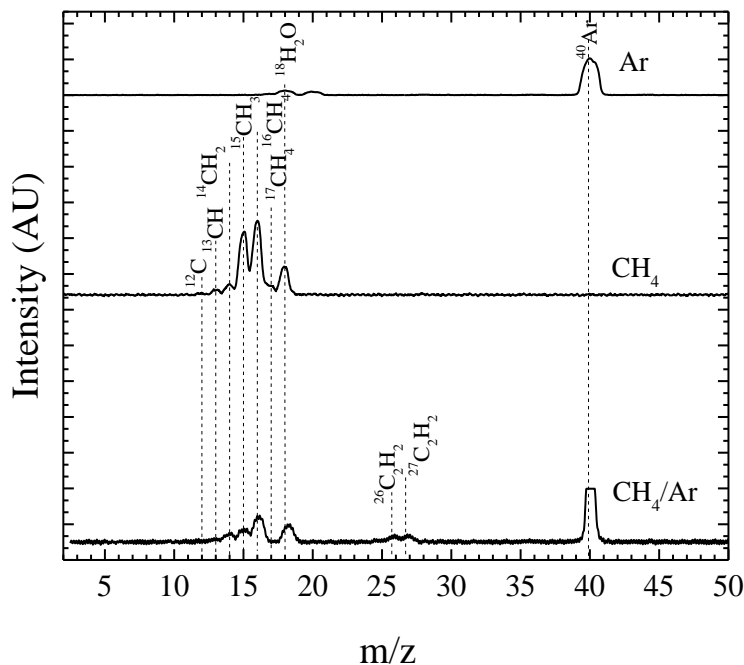
Figure 2-14. QMS of Ar, CH$_4$, and CH$_4$/Ar plasma (500W, 3mTorr, ionizer: 1mA). The relative intensities of the CH$_3$ and CH$_4$ signals suggested that the CH$_4$/Ar plasma was more dissociated than the CH$_4$ plasma, which led to the formation of acetylene (C$_2$H$_2$) and suggested that there was relatively more CH$_3$ present.

OES spectra of Ar, CH$_4$, and 50:50 CH$_4$/Ar plasmas at 500W and 10-15 mTorr were shown in Figure 2-15. The OES of Ar showed expected features of Ar, such as the ones at 750 and 763 nm. The OES of CH$_4$ plasma showed some weak bands and the Balmer series for atomic H. Mixing the Ar and the CH$_4$ plasma yielded a spectrum that largely only featured the Balmer series, with weak background signals that could be due to CH$_4$ bands or Ar. The relative intensity of these spectra suggested that even though the CH$_4$/Ar plasma was more dissociated than the CH$_4$ plasma, there would still be less atomic H present in the CH$_4$/Ar plasma than in the CH$_4$ plasma.
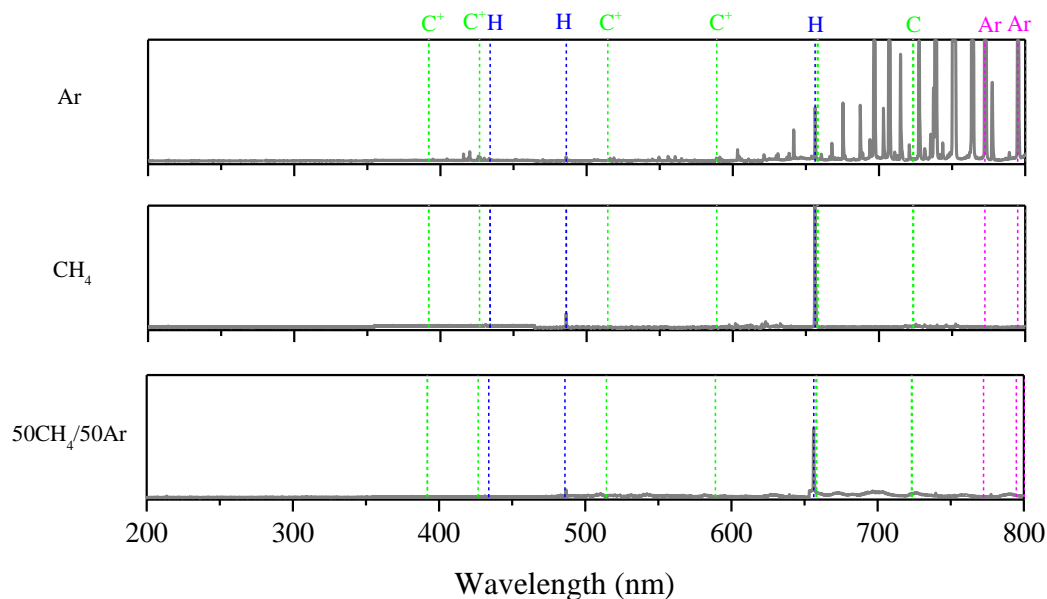
Figure 2-15. OES of different plasmas generated from Ar, CH₄ and CH₄/Ar (500W/10-15mTorr). All spectra are scaled to the detector's maximum intensity for comparison. The relative intensities suggest that there is less H present in the CH₄/Ar plasma than in the CH₄ plasma.

CH₄ and CH₄/Ar plasmas would be expected to deposit a C:H layer on the GST surface in addition to etching, which could passivate the GST surface. The passivation of Si by amorphous SiC$_x$:H had had been reported to improve when nitrogen was added to deposit SiC$_x$N$_y$:H (Martín 2002), so the mixture of nitrogen with CH₄ was also investigated.

QMS studies of N₂, CH₄ and N₂:CH₄ plasmas are shown in Figure 2-16. The QMS of the N₂ plasma showed the presence of both molecular and atomic nitrogen, with molecular nitrogen being the majority of the plasma. The QMS of CH₄ plasma showed the dissociation of CH₄ into CH$_x$ species. The majority of the plasma was CH₄ and CH₃, with significantly less CH₂ and CH and little to no C. The QMS of the mixed CH₄/N₂ plasma showed peaks at 26 and 27 m/z which were associated with the formation of CN and HCN, which confirmed the observed 388 nm line

in the OES. Another peak at 17 m/z was also observed and was associated with the formation of

NH_3. This also suggested that the peaks at 16 and 15 m/z could be made up of signals from both

CH_x and NH_x species. While the QMS was not capable of resolving 1 and 2 m/z signals for H and

H_2, the presence of NH_x and HCN species suggested that there would be less atomic H present in

the CH_4/N_2 plasma than in the CH_4 plasma alone. Literature reports on a-C:H:N deposition using

CH_4/N_2 plasmas also reported this effect (Clay 1996).
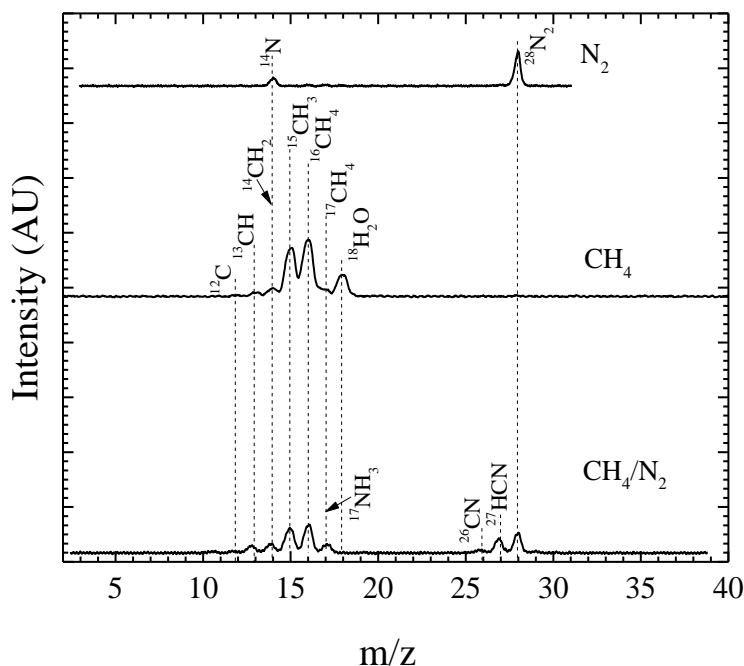
Figure 2-16. QMS of N_2, CH_4, and CH_4/N_2 plasmas (500W, 3mTorr, ionizer: 1mA). The CH_4/N_2 spectrum showed the presence of CN, HCN, and NH_x species, and the presence of these species suggested that there was less atomic hydrogen present in the CH_4/N_2 plasma than in the CH_4 plasma.

OES spectra of N_2, CH_4, and 50:50 CH_4/N_2 plasmas at 500W and 10-15 mTorr were shown

in Figure 2-17. The bands of N_2 were readily observable, as was the presence of atomic N lines at

742.3, 744.2, and 746.8 nm, although the three lines could not be independently resolved with the

Ocean Optics OES. The OES of CH_4 plasma showed some weak bands and the Balmer series for

atomic H. Mixing the N_2 and the CH_4 plasma yielded a spectra with features of both the N_2 and the CH_4 spectra, but a new peak at 388 nm was also observed, which was associated with the presence of CN in the plasma (Clay 1996). The relative intensities of the atomic H lines in the CH_4 and CH_4/N_2 spectra suggested that there was less atomic H present in the CH_4/N_2 plasma than in the CH_4 plasma.
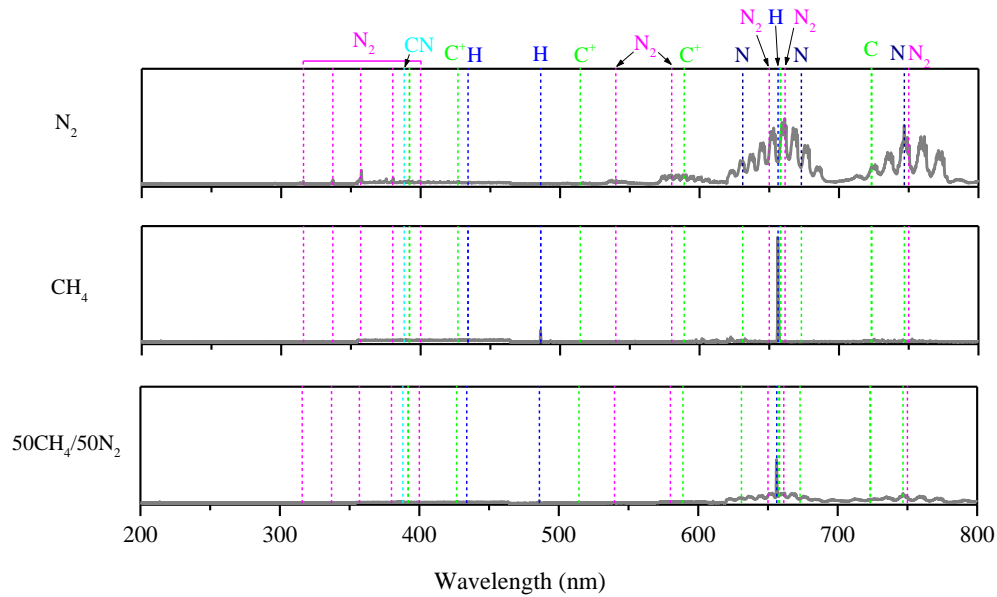
Figure 2-17. OES of different plasmas generated from N_2, CH_4 and CH_4/N_2 (500W/10-15mTorr). All spectra are scaled to the detector's maximum intensity for comparison. The relative intensities suggest that there is less H present in the CH_4/N_2 plasma than in the CH_4 plasma. A signal for CN species at 388 nm can be observed.

2.4.5 Ion Beam System and Sputtering of GST

A Commonwealth Scientific Kaufman ion source was installed in an ion beam chamber connected to the lower chamber of the ICP, as illustrated in Figure 2-6, and a small load lock was attached to the ion beam chamber. Samples could be transferred between the small load lock, the ion beam chamber, the lower chamber of the ICP chamber, and the transfer tube without needing

to break vacuum. The ion beam chamber itself did not have a pump installed and was opened to the ICP for pumping when the ion beam was in operation, and the small load lock was pumped by its own mechanical rotary vane pump, achieving pressures down to ~10^{-3} Torr. An ion gauge and Baratron gauge installed on the ICP were used to measure pressure. The Kaufman ion source could generate both Ar and O ion beams with energies down to 200 eV and operated at a pressure of ~10^{-5} Torr. Inside the Kaufman ion source, the DC discharge was generated using a potential difference across an anode and a cathode. Thermionic emission of electrons from a 0.25 mm tungsten cathode filament wire strikes and sustains the discharge, and a permanent magnet below the anode was used to confine the electrons emitted by the cathode. Ions were extracted from the discharge using an anode consisting of two graphite grids.

In this work, the Kaufman ion source was operated at three different energies using Ar: 1keV, 500eV, and 200eV. While a measurement of the ion beam current density was not available, measured ion beam current densities from the operating manual of the instrument were summarized in Table 2-29. These ion beam current densities listed in Table 2-29 should be an underestimate, as the values from the manual were measured at a distance of 20 cm from the ion beam source, whereas the ion beam in its setup for this work has the sample at approximately 15 cm from the ion beam.

Table 2-29. Ion beam current density at selected beam voltages, measured at 20 cm from the ion beam source, values taken from (Johnson 1999).

Beam Voltage (V)	Ion Beam Current Density (mA/cm^2)
200	0.2
500	1.2
1000	5

In plasma etching, both chemical and physical sputtering effects need to be considered. As previously discussed in Table 1-7, the sputtering yields of Ge, Sb, and Te are different and impacted by the binding energy of each element to other atoms of the same element. Furthermore,

studies of GST plasma etching using halogens have demonstrated both sputtering and chemistry affect the etching of GST with halogens. By etching the GST with and without bias to the wafer, it was determined that for lighter halogens (F and Cl) etching was more chemical in nature, while for heavier halogens (Br), etching was more physical in nature (Canvel 2019). Sputter yields for the chemistries considered in this work on Ge, Sb, and Te (and at the energies used in this work) are not all available in literature, especially for hydrogen, so the sputter yields were instead simulated using the software package Stopping and Range of Ions in Matter (SRIM 2013) and are shown in Table 2-30. Both 100V extraction bias and 200V ion beam sputtering were used in this work for experiments with downstream plasma etching, and 1keV sputter yields are provided for comparison. CH_4 is not considered, since no bias is applied in experiments in this work that involve a CH_4-containing plasma. For the sputtering atoms considered in Table 2-30, F, Cl, and Ar all result in sputtering of Ge, Sb, and Te at 100 – 1000 eV, which is consistent with literature. As such, the etching of GST with these plasmas should be considered to have both physical and chemical effects. On the other hand, hydrogen results in no sputtering at 100 and 200 eV, and almost no sputtering at 1keV, likely due to the small mass of the hydrogen atom relative to the other atoms considered here. The etching of GST with a hydrogen plasma is therefore considered to have only chemical effects.

Table 2-30. Simulated sputter yields for F, Cl, H, and Ar on Ge, Sb, and Te at 100, 200, and 1keV, calculated using SRIM 2013.0 – no sputtering

| | F | | | Cl | | |
	100 eV	200 eV	1keV	100 eV	200 eV	1keV
Ge	0.3	0.6	1.3	0.4	0.8	2.0
Sb	0.3	0.6	1.5	0.5	0.9	2.4
Te	0.3	0.7	1.9	0.6	1.1	3.2
	H			Ar		
	100 eV	200 eV	1keV	100 eV	200 eV	1keV
Ge	0	0	0.01	0.4	0.7	2.1
Sb	0	0	0.01	0.5	0.9	2.5
Te	0	0	0.	0.6	1.2	3.1

2.5 Evaluating Treatment Effects

As discussed in Chapter 1, the phase-change properties of GST are dependent on the ratio of Ge:Sb:Te, and the motivation behind how studying the etching of GST is to observe and understand how composition – and therefore phase-change properties – change. In order to compare the effects of each chemistry on GST composition, it is necessary to define a method by which to assess and compare changes in composition and crystallization temperature.

In order to compare changes in composition across different etch chemistries, a metric called change in composition (ΔC) is defined. This is simply the distance between the pre- and post-etch compositions on the crystallization temperature map and is calculated using the distance formula. For the crystallization temperature map, compositions are given as percentages and must sum to 100. As an example, for a pre-etch composition $Ge_{x1}:Sb_{x2}:Te_{x3}$ (or $Ge:Sb:Te=x_1:x_2:x_3$) and a post-etch composition of $Ge_{y1}:Sb_{y2}:Te_{y3}$ (or $Ge:Sb:Te=y_1:y_2:y_3$), ΔC would be calculated as follows:

$$\Delta C = \sqrt{(y_1 - x_1)^2 + (y_2 - x_2)^2 + (y_3 - x_3)^2} \qquad (2.4)$$

$$\text{where } x_1 + x_2 + x_3 = y_1 + y_2 + y_3 = 100$$

It is also important to recognize that ΔC is related to the change in crystallization temperature (ΔT_c) and that the relation between ΔC and ΔT_c is not a simple one. As an example, Figure 2-18 shows a hypothetical starting composition and two hypothetical post-etch compositions A (13.9:28.5:57.5) and B (21.9:34.4:43.7). Both A and B differ from the starting composition (17.9:31.5:50.6) by a ΔC of 8.5, but they lead to different ΔT_c values. The ΔT_c values are determined from the T_c map, and T_c values are read to the nearest 5ºC. Only the Ge:Sb:Te composition is considered in this analysis, other elements are not considered. Figure 2-19 shows

that the same ΔC can lead to differing ΔT_c. An ideal etch chemistry should have ΔC and ΔT_c as close to zero as possible.
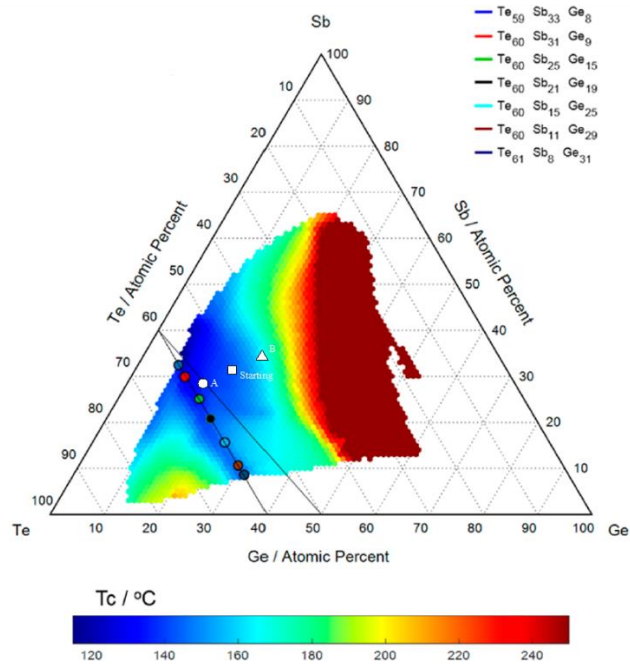
Figure 2-18. Crystallization temperature map of Ge-Sb-Te system (Guerin 2017). A hypothetical starting composition (□) and two hypothetical etched compositions A (○) and B (△) are shown. Compositions A and B have the same ΔC from the starting composition but result in different changes in crystallization temperature.
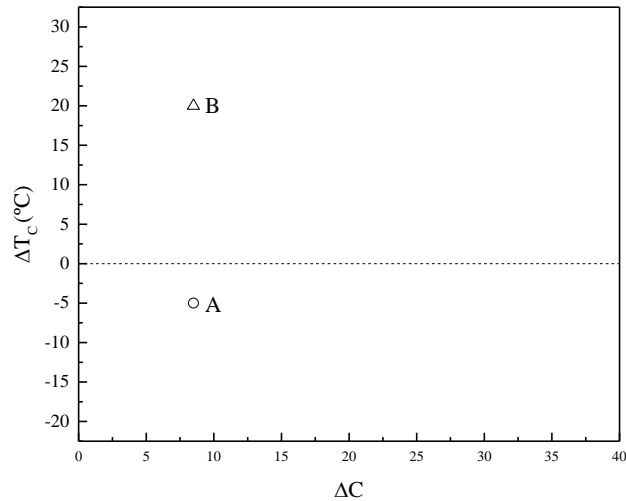
Figure 2-19. The change in crystallization temperature (ΔT_c) versus the composition change (ΔC) for the etch processes shown in Figure 2-18. An ideal etch process should have ΔC and ΔT_c as close to zero as possible.

In this chapter, the experimental methods and thermochemical analysis of different etch chemistries studied in the rest this work have been presented. Available literature on the etching of GST with halogen plasmas and thermochemical analysis has concluded that preferential removal was related to the boiling points of the etch products. From this data, it is suggested that plasma etching using hydrogen or methane-based chemistries would result in less preferential removal due to the lower boiling points and smaller range of boiling points of the associated etch products, which would help preserve composition and therefore phase-change properties during the etching of GST. The subsequent chapters present and analyze the effects of these chemistries on GST.

Chapter 3 Oxidation and Cleaning GeSbTe

Ambient oxidation was found to significantly change the composition and chemical reactivity of GST, especially by water vapor. The complexing of GST by the wet cleaning agents was found to differ from the complexing of the single elements. The polar solvents (citric acid, and ammonium hydroxide) not only removed more GST-oxides from GST than the less polar (DI water) and nonpolar solvent (isopropyl alcohol) but also resulted in greater composition change in polar solvents. The hypothesis that GST-oxides were susceptible to solvation by polar solvents was confirmed by first removing the native oxides by either HF acid, Ar ion beam, or a downstream Ar plasma then subject the metallic surface to wet cleaning. After the removal of the oxides, the composition change caused by the wet cleaning was similar between the polar and nonpolar solvents. However, crystallization temperature changes could be similar with or without removing the native oxides. This was concluded to be due to differences between GST and GST-oxide bonds, specifically the difference in polarity and bond energy. From these findings, it was determined that GST oxides should be removed prior to etching in subsequent studies to simplify analysis of the effects of each chemistry on GST.

3.1 Ambient Exposure and Oxidation of GeSbTe

To study the effects of ambient exposure on GST, GST films were first Ar sputter cleaned using a 1keV Ar ion beam for 3 min. to remove oxides, then exposed to environments consisting of N_2 and O_2 as well as a humid environment (30-90% humidity) generated with a ~~converted~~ glove box. These samples were also exposed to ambient conditions as part of the process of transferring samples between chambers, so the XPS was considered *ex-situ*. Figure 3-1, Figure 3-2, and Figure 3-3 illustrate the XPS spectra for GST films as-received, Ar sputter cleaned, and exposed to N_2, O_2, and water vapor, respectively.
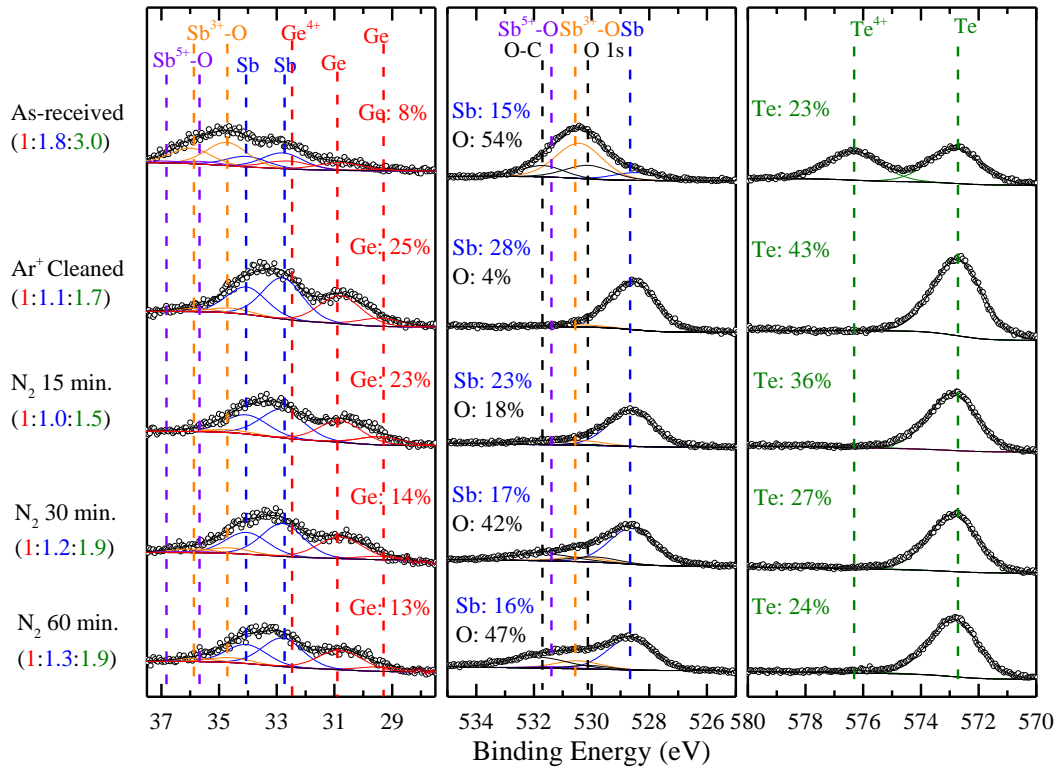
Figure 3-1. The effect of N₂ exposure at 20 Torr on GST samples with starting composition 1:1.8:3.0, followed by 1kV Ar ion beam cleaning for 1 min. then 15, 30 or 60 min. N₂ exposure.

The effectiveness of the Ar sputter clean in removing the oxides in the film can be observed in the XPS spectra in Figure 3-1, with O content reduced from 46% to 1%, and the oxidized components of Ge, Sb, and Te were not observed after the sputter clean. The as-received film showed significant oxidation of Ge, Sb, and Te, and the extent of oxidation roughly followed the order laid out by thermodynamics, as summarized in Table 2-1, with Sb being the most oxidized, followed by Ge then Te. Subsequent exposure to N₂ showed little to no reoxidation after 15 min. in the N₂ atmosphere. By 30 min., some oxidation of Sb could be observed, likely due to trace contaminants in the N₂, but little to no oxidation of the Ge or the Te was observed even after 60 min.
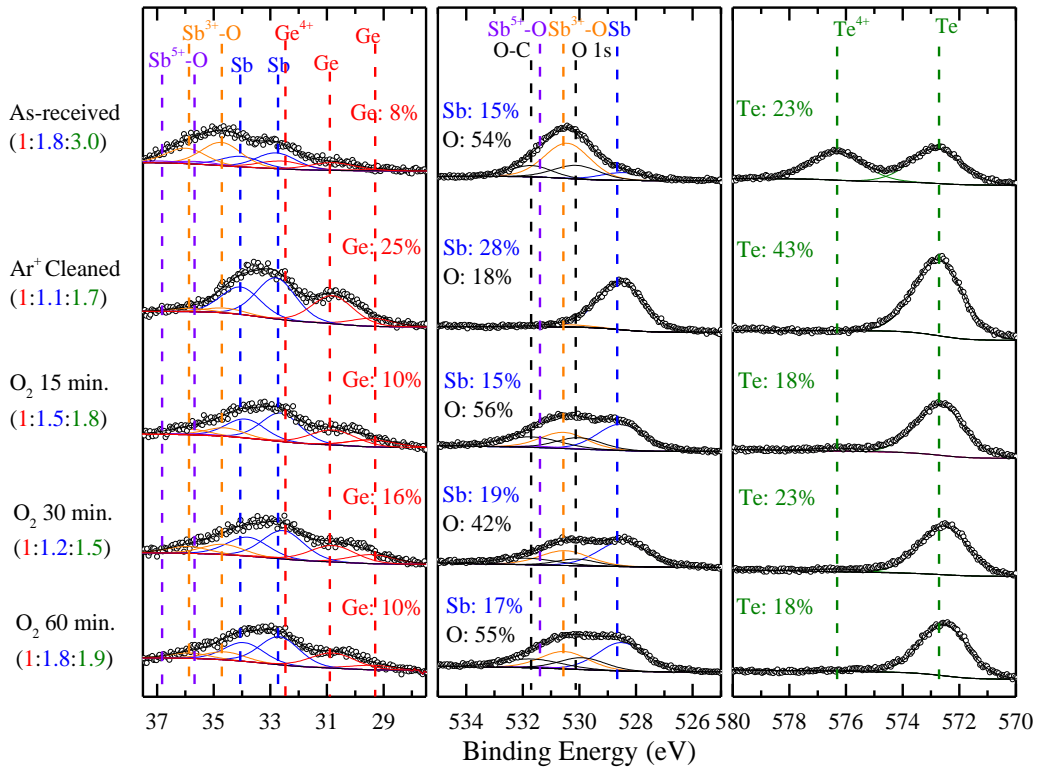
Figure 3-2. The effect of O$_2$ exposure at 20 Torr on GST samples with starting composition 1:1.7:2.3, followed by 1kV Ar ion beam cleaning for 1 min. then 15, 30 or 60 min. O$_2$ exposure.

The exposure of the cleaned GST to O$_2$, as shown in Figure 3-2, showed rapid re-oxidation of the GST film, with the O content of the film exceeding that of the as-received sample within 15 min. The O content appeared to saturate at 52-54% O at all tested times. Sb was observed to be the quickest to reoxidize, followed by Te then Ge. The cleaned GST exposed to a humid environment also showed a similar trend, with significant reoxidation of Sb occurring at all tested humidity levels after 30 min. while Ge and Te showed significantly less reoxidation than Sb. Compared to O$_2$ only, the humid environment resulted in comparable O content at 30% humidity (53% v. 52-54% for 30% humidity v. O$_2$ only) and resulted in higher O content on the surface at 70% and 90% humidity. From these experiments, it was concluded that water vapor resulted in the greatest reoxidation of the sputter-cleaned GST, followed by O$_2$ and then by N$_2$.
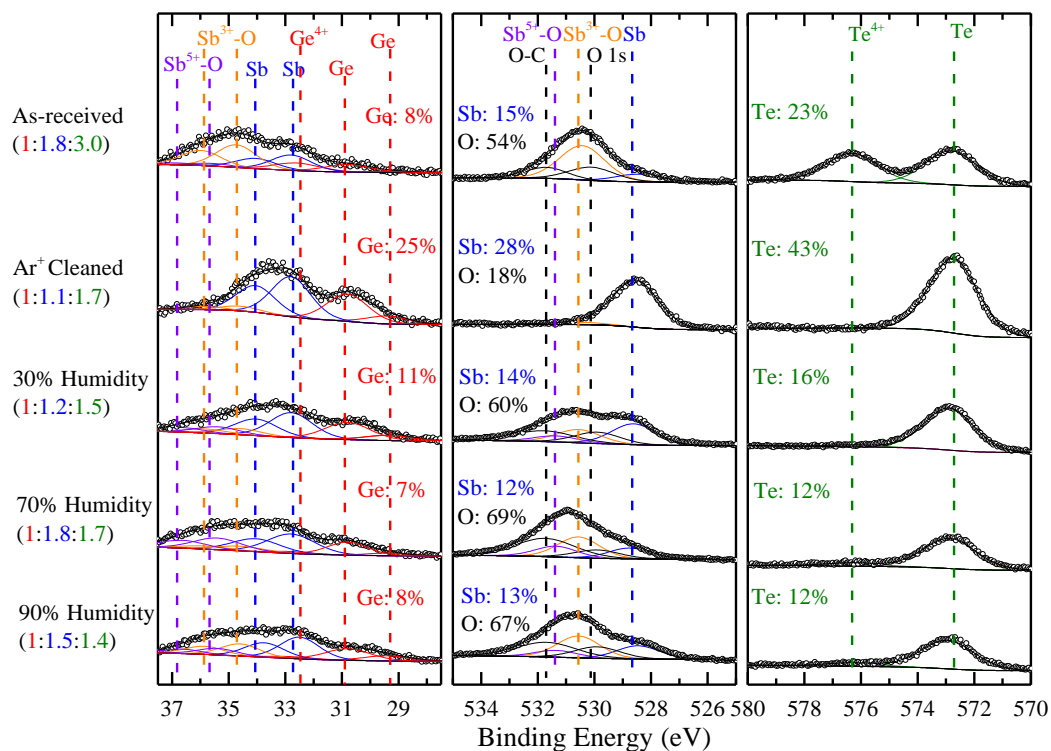
Figure 3-3. The effect of humidity exposure on GST samples with starting composition 1:1.8:3.0, followed by 1kV Ar ion beam cleaning for 1 min. then exposure to at 30%, 70%, and 90% humidity for 30 min.

3.2 Wet Cleaning of Ge, Sb, and Te

Wet cleaning of the constituent elements of GST was tested on Ge, Sb, and Te thin films using deionized (DI) water, isopropyl alcohol (IPA), dilute citric acid (CA), and dilute ammonium hydroxide (NH_4OH). Samples of Ge, Sb, and Te as received (i.e., with native oxide) were exposed to these wet cleans using the conditions discussed in Section 2.4.2.

The percent oxidation of Ge, Sb, and Te in their respective thin films as-received and after exposure to the four treatments is shown in Figure 3-4. This was determined by the ratio of oxidized states over the sum of the oxidized and metallic states for each element. Ge was mostly oxidized as-received, and it was found to be very susceptible to further oxidation, as all the films were shown to be almost entirely oxide. Ge was not detected after the NH_4OH treatment, so it was concluded that NH_4OH could rapidly remove Ge. Sb was also majority oxide as-received, but it

was comparatively resistant to further change in oxidation states, as all the treated Sb films became more metallic but did not change by more than 5-6% from the original percent oxidation. Meanwhile, Te was almost half metallic and half oxidized as-received, and the treated Te films show highly varied changes to the different treatments. After exposure to DI water and citric acid, the remaining Te film was almost entirely metallic. On the other hand, after exposure to isopropyl alcohol or ammonium hydroxide, the Te film was mostly oxidized.
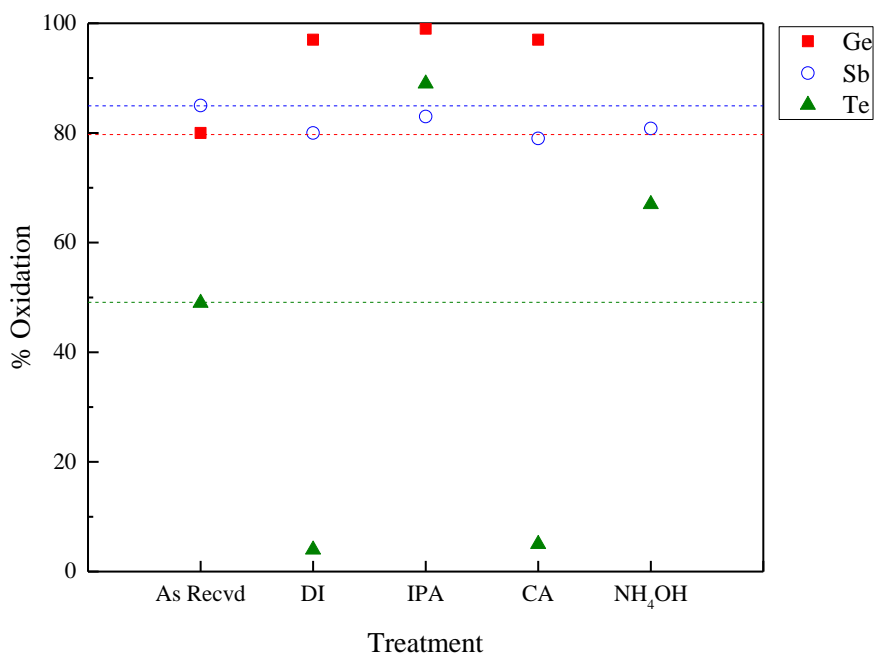
Figure 3-4. The percentage of oxidation of elemental compounds, Ge, Sb, and Te thin films, as-received and after exposure to DI water (DI), isopropyl alcohol (IPA), citric acid (CA), and ammonium hydroxide (NH4OH). The dashed lines indicate the percent oxidation of Ge, Sb, or Te on the as-received sample of each element. Ge was not detected by XPS after exposure to NH4OH and was assumed to be removed. Guidelines denote the ratio of metallic to oxide states in the as-received samples, to which each wet-cleaned sample should be compared. Ge oxidizes further in wet cleans, while Sb becomes more metallic. Te oxidation becomes very metallic after DI water and CA and very oxidized after IPA and NH4OH.

3.3 Wet Cleaning of As-Received GeSbTe

Solution phase wet clean studies were conducted on GST thin films to determine their effects on Ge:Sb:Te stoichiometry. Ambient exposure was minimized as much as could be managed but was still present throughout these studies, so all the XPS presented is considered *ex-situ*.

The XPS spectra of GST as-received and after exposure to DI water, isopropyl alcohol, citric acid, and ammonium hydroxide were shown in Figure 3-5. The as-received surface was significantly oxidized (51.9% O) and remained this way after exposure to DI water and IPA (43% O and 58.3% O, respectively). Treating the GST with dilute citric acid or ammonium hydroxide resulted in a decrease in oxidation (26.2% O and 18.6 % O, respectively). Differences in the changes of the GST and the individual elements in response to the wet clean treatments can also be observed. Ge tended to become more oxidized or, in the case of ammonium hydroxide, completely removed. However, this did not appear to always be the case in the ternary film, as the Ge was more oxidized after DI water and isopropyl alcohol, but less oxidized after citric acid ammonium hydroxide, and no preferential removal of Ge was observed. Similarly, the Sb, which stayed relatively constant in terms of metallic/oxidized ratio in these treatments as a pure film, became less oxidized after citric acid and ammonium hydroxide. Te became more oxidized after isopropyl alcohol in both single element and in GST. A trend that could be drawn from these experiments was that citric acid and ammonium hydroxide both result in decreased oxygen content, depletion of Sb, and enrichment of Te.
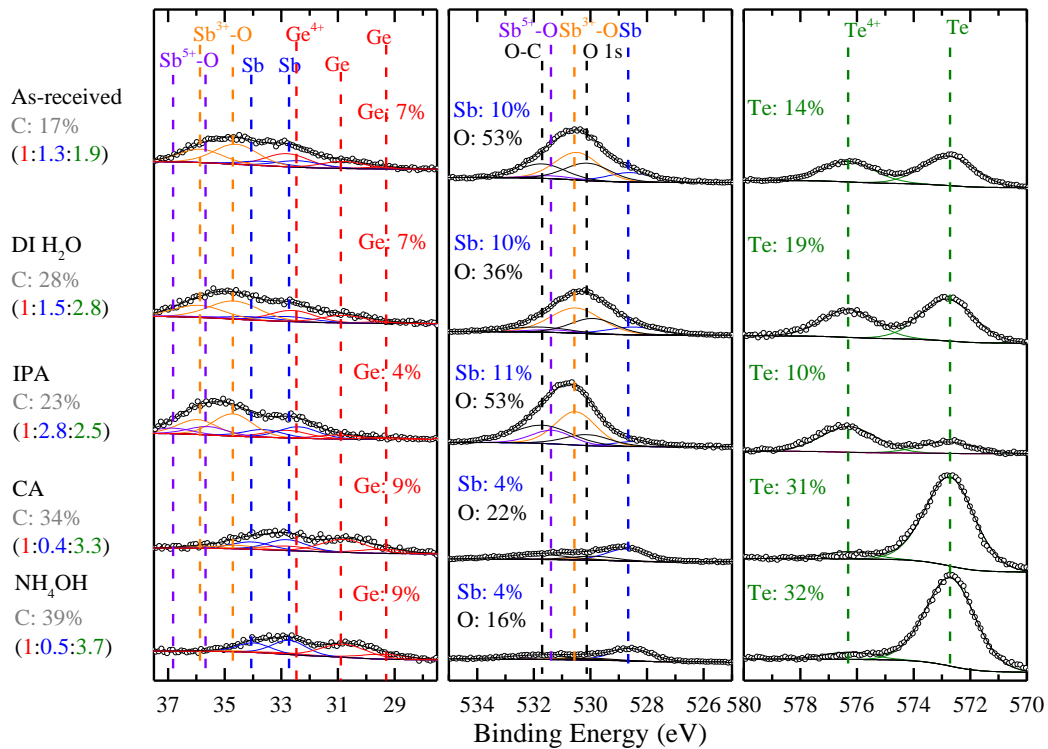
Figure 3-5. The effect of wet cleans on GST samples with starting composition 1:1.3:1.9, followed by exposure to DI water and IPA for 60 sec. and CA and NH4OH for 30 sec. CA and NH4OH resulted in preferential removal of oxidized GST.

Figure 3-6 shows the percent oxidation of Ge, Sb, and Te components in the GST samples shown in Figure 3-5. Here, the effects of each wet clean on the single element Ge, Sb, and Te films were not observed on the ternary GST. For GST, DI water, CA, and NH4OH all proved to be effective at removing oxides, especially CA and NH4OH. IPA also diminished oxidation for Ge and Te, but it also resulted in enhanced oxidation for Sb. It was concluded that the more polar solutions (citric acid, ammonium hydroxide, DI water) were more effective at removing oxides than the non-polar solution (isopropyl alcohol).
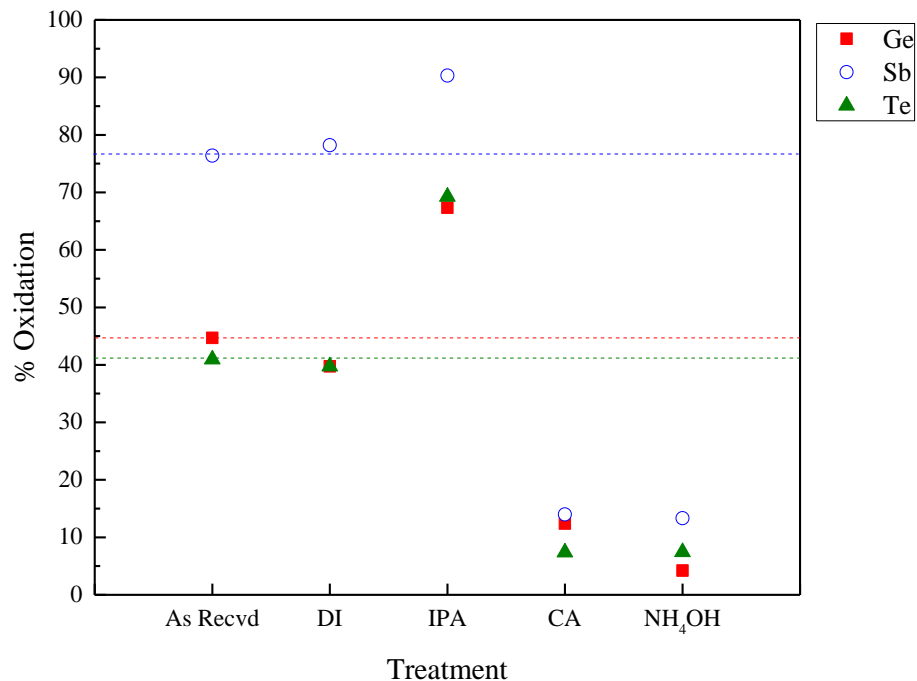
Figure 3-6. The percentage of oxidation of Ge, Sb, and Te components of GST samples in Figure 3-5. The as-received samples have the composition of 1:1.3:1.9. DI water, CA, and NH₄OH all resulted in diminished oxidation of Ge, Sb, and Te, while IPA enhanced oxidation of Sb and depleted oxidation of Ge and Te. This effect was thought to be related to the polarity of DI water, CA, and NH₄OH and the non-polarity of IPA.

Figure 3-7 summarizes these changes in composition due to the wet cleans on as-received GST. Sb and Te vary significantly with the different treatments, up to 30% in the case of citric acid and ammonium hydroxide, while Ge stays close (within 5%) in proportion to its as-received atomic percentage. Isopropyl alcohol resulted in the smallest change in composition of the tested wet cleans. The removal of Ge by NH₄OH was not observed on the GST sample, and it was concluded that the GST could be more stable in solution than its single element counterparts. The enrichment of Ge and depletion of Sb in citric acid also indicated that Sb-citrate complex formation could be preferred to Ge-citrate complex formation in this system.
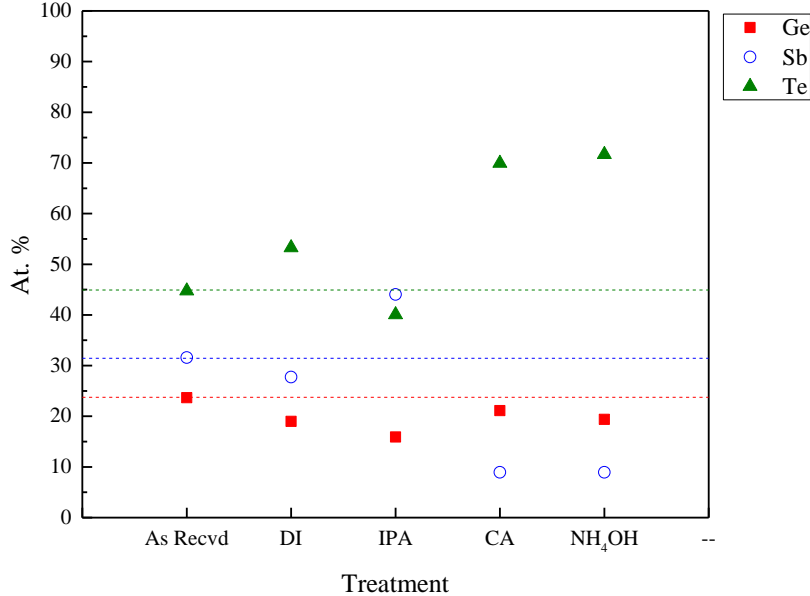
Figure 3-7. Atomic percentages of Ge, Sb, and Te determined from XPS in Figure 3-5 for GST thin films as-received, cleaned by DI water (DI), isopropyl alcohol (IPA), citric acid (CA), or ammonium hydroxide (NH4OH). Guidelines denote the composition of the as-received samples, to which the wet-cleaned samples should be compared. More polar solutions (DI, CA, NH4OH) resulted in greater composition change than non-polar solutions (IPA).

3.4 Cleaning of As-Received GeSbTe

With the finding in the previous section that the effects of different wet clean chemistries oxidized as-received GST could be affected by the polarity of the solutions, it was also considered that these effects could be due to the polarity of the Ge-O, Sb-O, Te-O bonds present on the as-received GST surface. To study the effects of the wet clean chemistries on metallic GST surface, GST surface oxides had to be removed. In order to accomplish this, three chemical processes were evaluated: hydrofluoric acid, Ar ion beam, and downstream Ar plasma.

Hydrofluoric acid (HF), which is commonly employed in the semiconductor industry to etch away silicon dioxide despite its unique chemical hazards. HF had been demonstrated to remove GST oxides after photoresist stripping with O_2 plasma (Canvel 2020). The XPS for GST

films as-received and after cleaning by DI water (60s) or dilute hydrofluoric acid (dHF) then DI water (both 60s) are shown in Figure 3-8. The dHF process was followed by the DI water clean in order to remove the dHF residues, which still had the capacity to be hazardous to human health. The dHF clean proved to be quite effective at removing GST oxides, with practically all of the Ge, Sb, and Te oxides removed after 60 seconds. However, this also resulted in major depletion of Sb and Te. This was mostly attributed to the removal of the oxides, as Sb should have been more heavily oxidized than Ge or Te, and it matched the result from literature where it was observed that HF-cleaned films were Te-rich (Canvel 2020).
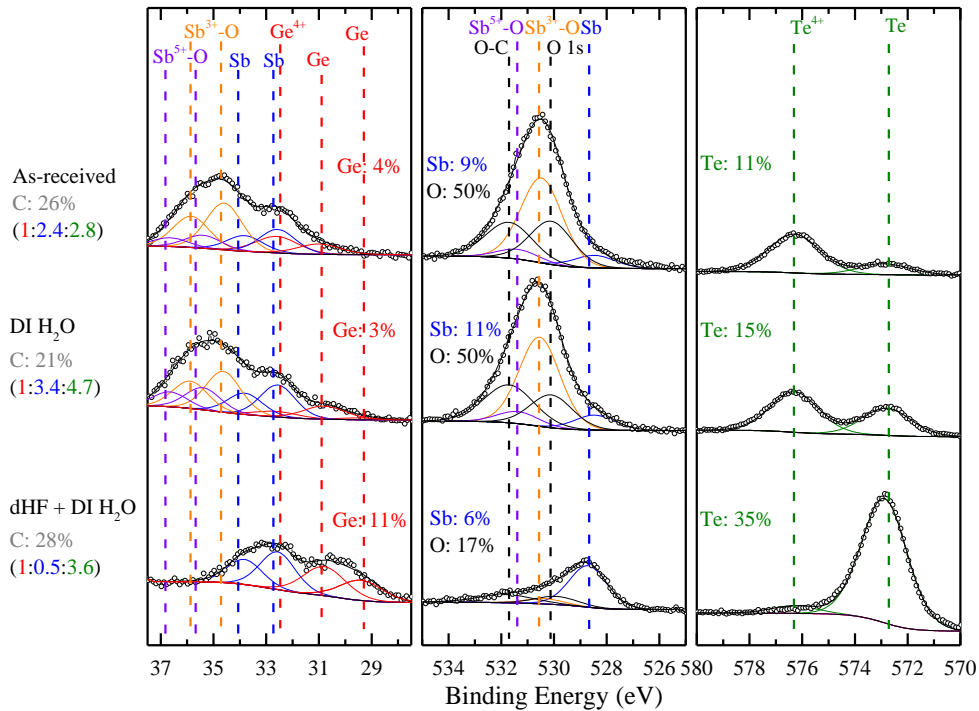
Figure 3-8. The effect of dilute hydrofluoric acid (dHF) on GST samples with starting composition 1:2.4:2.8, followed by exposure to DI water (60s) only or dHF (30s) followed by DI water (60s). GST was still oxidized after DI water alone, but dHF was able to remove the vast majority of the oxides but resulted in an Sb-depleted, Te-rich composition.

An Ar ion beam was also studied for use in removing the GST oxides. The XPS of GST films as-received and after sequential sputtering with a 200V Ar ion beam for 1 min. at a time,

shown in Figure 3-9, showed that the oxides, which were prevalent on the surface, were largely

removed after 1 min. Ar sputtering (57% O to 16% O) and almost completely removed after 2 min.

(6% O remaining).
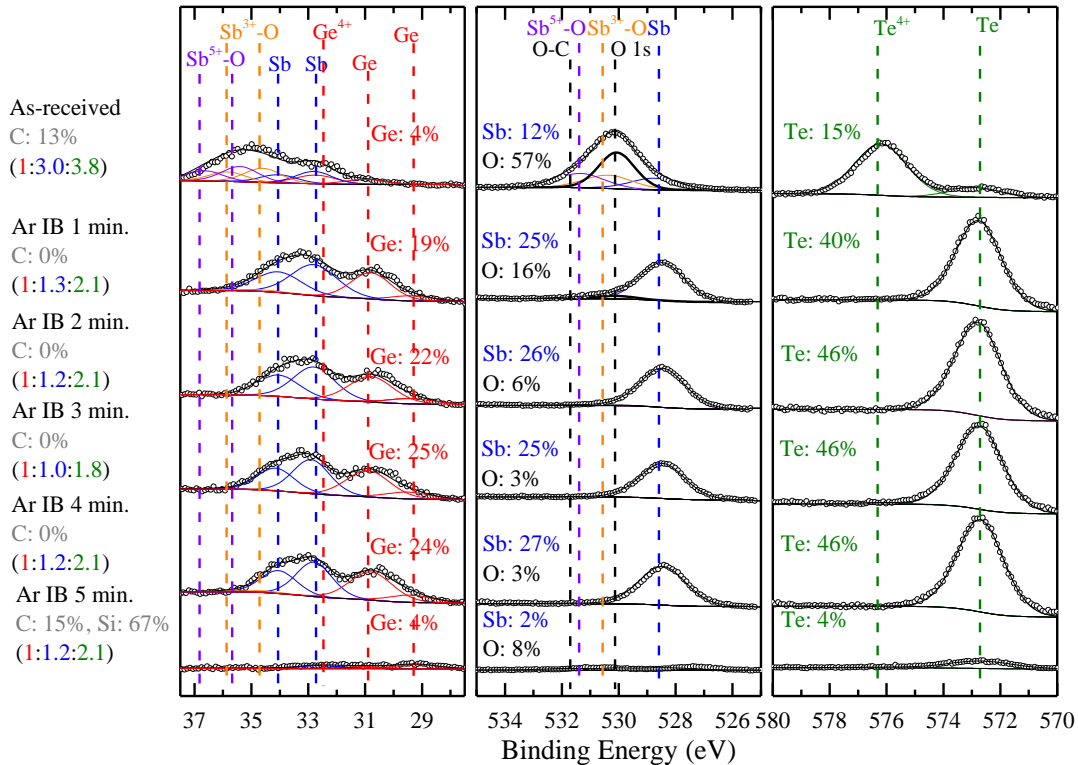
Figure 3-9. The effect of Ar ion beam sputtering on GST samples with starting composition 1:3.0:3.8, followed by 1-5 min. of 200V Ar ion beam sputtering. The GST was not exposed to atmosphere between sputtering and XPS, so the XPS was considered to be *in-situ*. Almost all the C and GST-oxides were removed after 1 min., and the GST was sputtered away after 5 min.

The continued sputtering did not appear to demonstrate preferential sputtering, as shown

in Figure 3-10, as the percentages of Ge, Sb, and Te stayed within a 5% range during the sputtering

of the film, before Si was observed in XPS, which indicated that the film has been sputtered away.

With a starting thickness of 100 nm and the assumption that at least 10 nm of GST was left after

4 min. of sputtering since Si was not observed, the sputter rate of the 200V Ar ion beam was

estimated to be between 20 and 22.5 nm/min. The composition in the middle of the sputtering was

approximately 1:1.0:1.8, which was the desired ratio of Ge to Sb but depleted of Te. This depletion

could be due to the higher sputtering yield of Te relative to Ge or Sb).
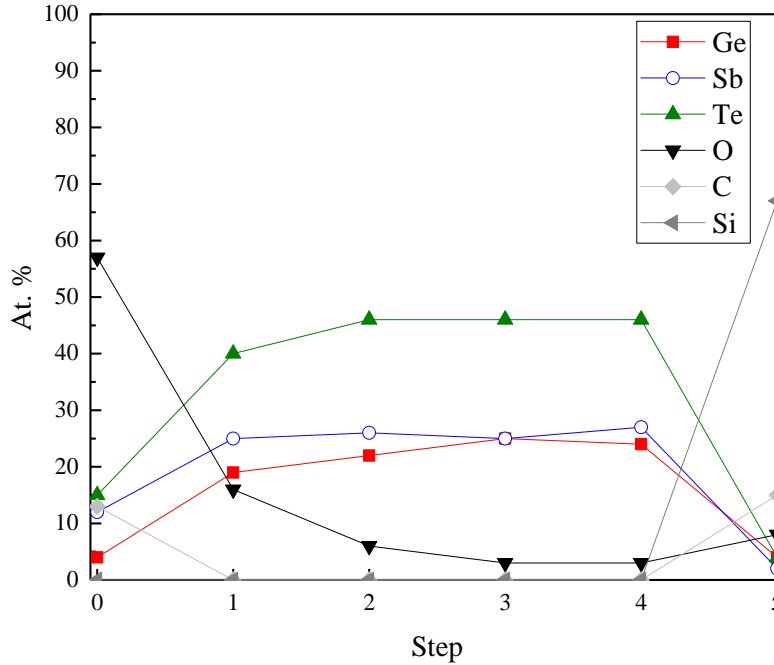
Figure 3-10. Ge, Sb, Te, O, C, and Si at. % as a function of sputtering time using a 200V Ar ion beam. Quantifications were determined from the XPS spectra shown in Figure 3-9. Ge, Sb, and Te composition was consistent during sputtering, albeit slightly depleted of Te, which was thought to be due to the high sputtering yield of Te.

Another method of cleaning the GST film using a downstream Ar plasma with an

extraction bias of 100V was also studied. This method was preferred over the ion beam as it did

not require the transfer of the sample between the ion beam chamber and the ICP chamber and

allowed for lower energy Ar sputtering than what the ion beam could manage. While there was

still some O content, as shown in Figure 3-11, it does not appear that the O was bound to the Ge

or Te, while Sb was mostly metallic. The majority of the O was bound to C. A composition of

1:1.0:2.4 Ge:Sb:Te was observed, which was close to the composition of the target (1:1.0:2.5).

91
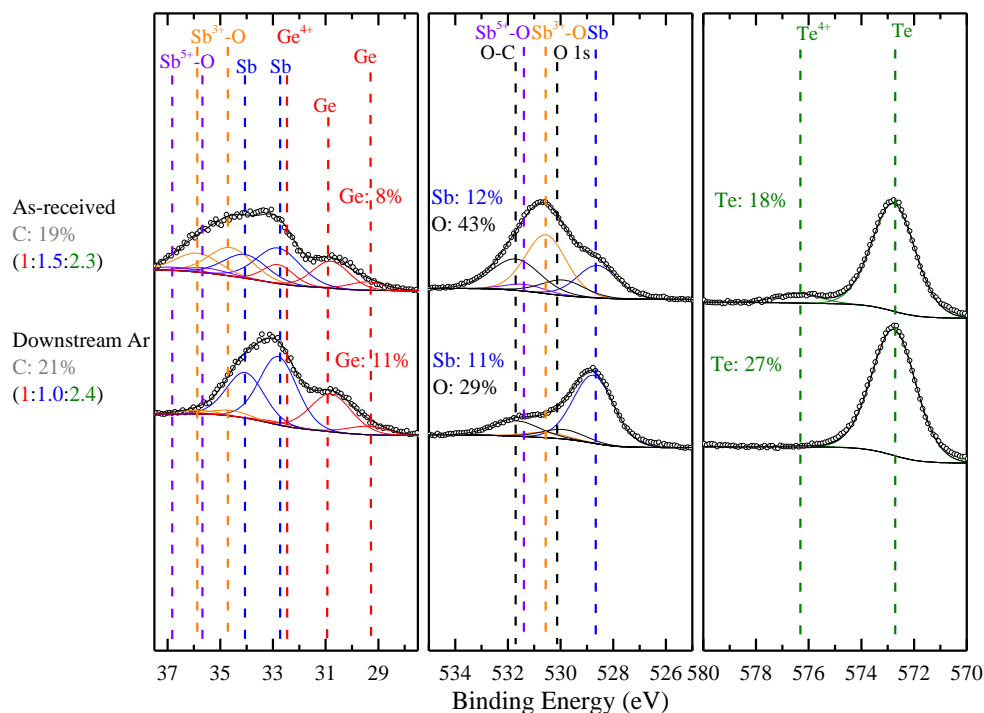
Figure 3-11. The effect of downstream Ar cleaning on GST samples with starting composition 1:1.5:2.3, followed by 5 min. of downstream Ar cleaning at baseline conditions. The GST was not exposed to atmosphere between sputtering and XPS, so the XPS was considered to be *in-situ*. While not all the O and C were removed, the presence of GST-oxides was greatly diminished, and the post-clean composition (1:1.0:2.4) was very close to the target composition (1:1.0:2.5).

The higher ion flux and ion energy from the ion beam was likely the reason for the depletion of Te, as Te has the highest sputtering yield among Ge, Sb, and Te, both in general and at the energy (200V) and angle (0º) used (see Table 1-7). The extraction bias of the downstream plasma needed to be limited to 100V to prevent sparks from forming in the bulk plasma and damaging the system. To compensate, the downstream Ar plasma was run for a longer time, 5 min. as opposed to 1 min. for the ion beam system.

While all three of these processes were capable of accomplishing this task, the use of the Ar ion beam and the downstream Ar cleaning were preferred since they allowed for *in-situ* XPS and resulted in GST that was close to 1:1.0 in Ge:Sb and slightly to moderately depleted of Te, while the HF clean resulted in a Te-rich surface. The Ar ion beam resulted in greater depletion of

Te, which was attributed to the high ion energy and flux of the ion beam compared to the downstream plasma. The depletion of Te was thought to be due to the high sputtering yield of Te relative to Ge and Sb.

3.5 Wet Cleaning of Sputter-Cleaned GeSbTe

To study the effect of the wet cleans on GST without the effect of the GST-oxides, samples of Ar ion beam cleaned GST were subjected to the same treatments. The Ar-cleaned GST was depleted in Sb and Te (Ge:Sb:Te 1:0.8:1.4). After Ar cleaning, the samples were transferred out of the ion beam system, treated with the wet cleans, then loaded for XPS analysis. Figure 3-12 shows the XPS spectra of GST as-received, after surface cleaning by a 500V Ar ion beam, and after both surface cleaning and wet clean treatments. The changes in composition are summarized in Figure 3-14. It was observed that the compositions did not change as significantly in comparison to the changes in composition summarized in Figure 3-7 and stayed close to the Te-depleted composition observed after the Ar ion beam clean. Citric acid and ammonium hydroxide both resulted in mild enrichment in Te and mild depletion of Sb, within 10% as opposed to the 30% observed on the as-received GST. DI water alone resulted in more noticeable depletion of Sb and enrichment of Te than citric acid or ammonium hydroxide. Isopropyl alcohol resulted in a composition very close to that of the Ar ion beam cleaned sample (within 5%), suggesting that isopropyl alcohol could be suitable for removing organic residues from GST without inadvertently changing the GST stoichiometry significantly. Both citric acid and ammonium hydroxide were dilute, and the results suggested that either may be able to aid a GST layer that was depleted of Te or enriched in Sb in recovering the stoichiometric composition. However, it should be noted that all these samples still showed significant O and C contamination, due to atmospheric and solution

93

exposure that could not be avoided upon removing the GST from the solution and drying the sample.
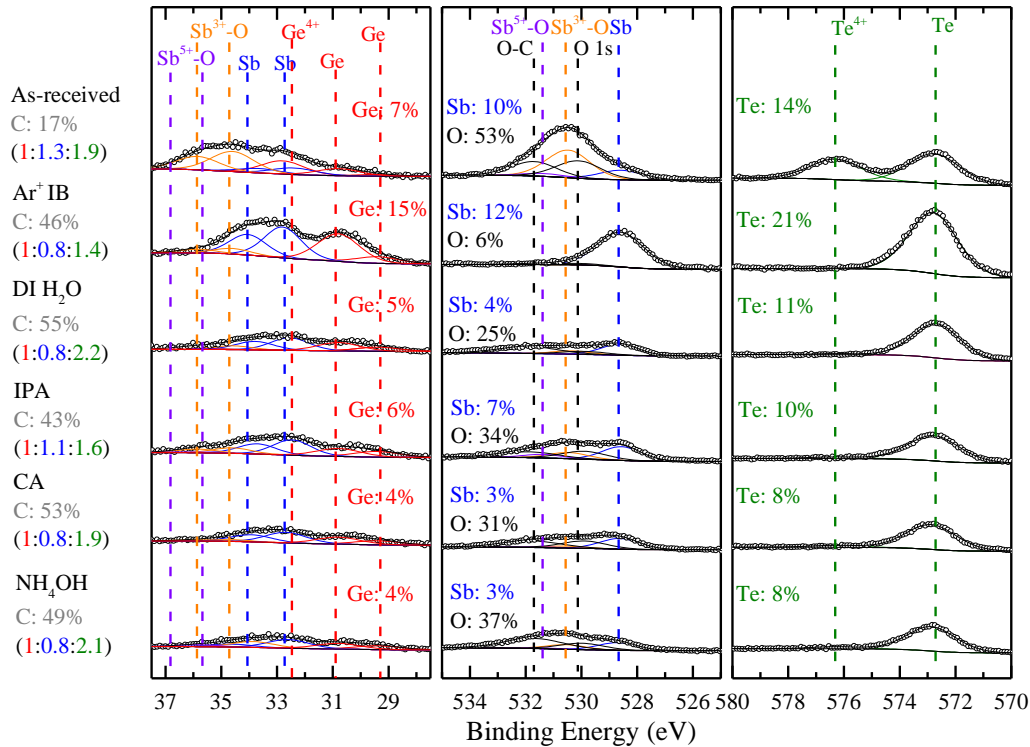
Figure 3-12. The effect of wet cleans on Ar ion beam cleaned GST samples with ion beam-cleaned composition 1:1.0:1.7, followed by 60 sec. of DI water or IPA and 30 sec. of CA or NH4OH. Significant O and C on the surface were unavoidable due to the *ex-situ* XPS. Changes in Ge:Sb:Te composition were smaller than those observed for wet cleaned as-received GST.

The percentage of oxidation of the GST samples post-wet clean is shown in Figure 3-13. The starting % oxidation after ion beam cleaning was quantified to be 0% for Ge, Sb, and Te, which was expected since all the GST-oxides had been removed by the Ar ion beam. Sb oxides and Ge oxides but not Te oxides were observed, which was consistent with the Gibbs energy of formation values that have been shown to predict preferential ambient oxidation in GST.
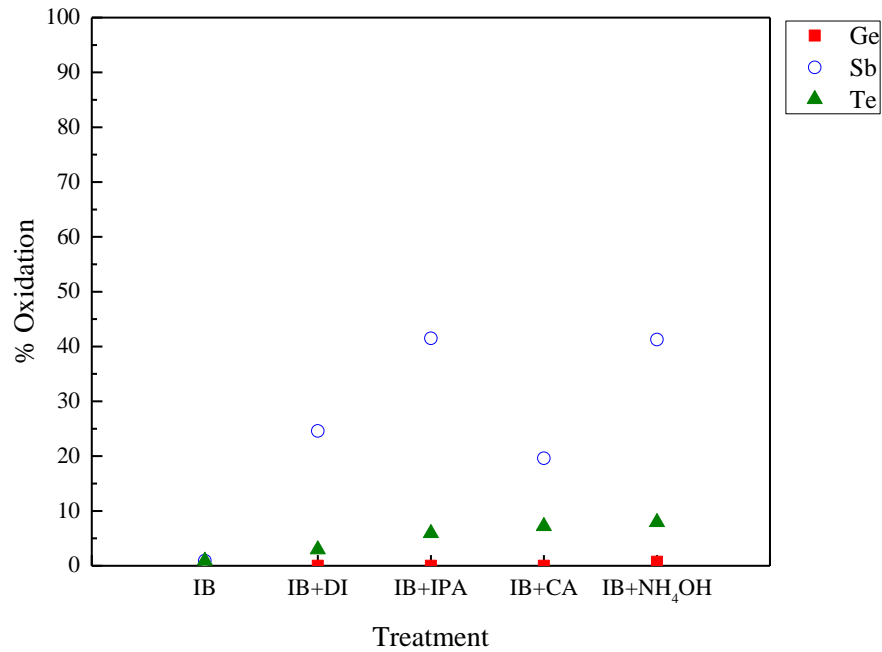
Figure 3-13. The percentage of oxidation of Ge, Sb, and Te components of GST samples shown in Figure 3-12. GST oxides were removed by ion beam cleaning, and the quantified oxidation of the cleaned sample showed 0% oxidation for Ge, Sb, and Te. The oxidation on the ion beam cleaned then wet cleaned samples showed that Sb then Te were the most oxidized, followed by Ge, which did not appear to be oxidized. This followed the Gibbs energy of formation values for the GST-oxides and was attributed to ambient exposure due the *ex-situ* nature of the XPS.
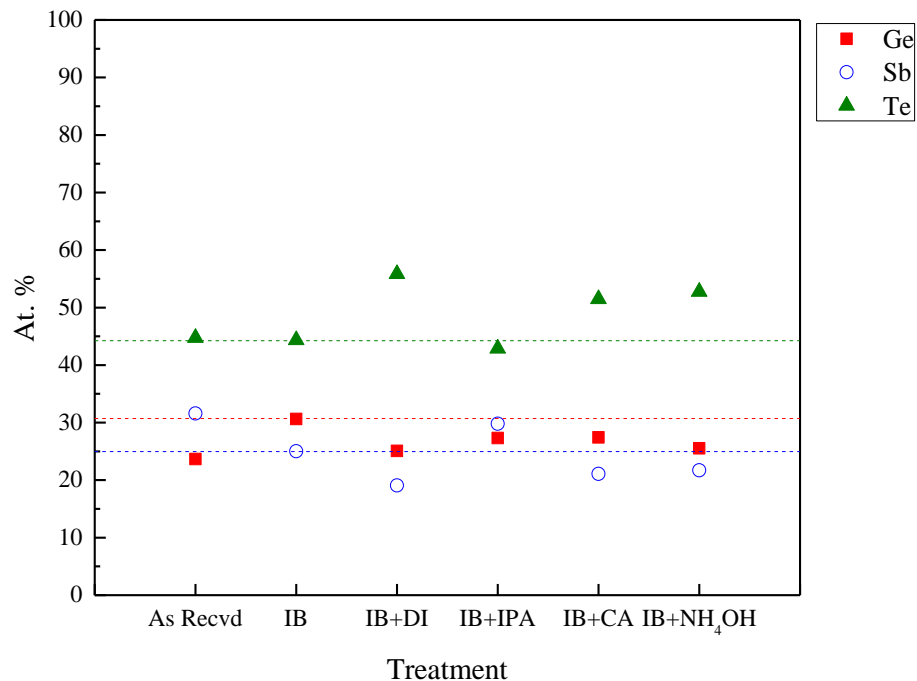
Figure 3-14. Atomic percentages of Ge, Sb, and Te determined from XPS in Figure 3-12 for GST thin films as-received, cleaned with an Ar ion beam sputter (IB), followed by DI water (DI), isopropyl alcohol (IPA), citric acid (CA), or ammonium hydroxide (NH₄OH). Guidelines denote the composition of the ion beam-cleaned GST, to which the wet-cleaned samples should be compared.

A comparison of Figure 3-7 and Figure 3-14 suggested that the presence of GST oxides led to different results in the wet cleaning of GST. The percentage change in these ratios was shown in Figure 3-15, and it was found that while the trend for changes in Sb and Te was the same (depletion of Sb, enrichment of Te), the extent to which this occurs was significantly greater (0% to -69% change in Sb ratio, 36% to 74% change in Te ratio, for sputter-cleaned v. as-received, respectively). This effect was associated with the addition of the citric acid, as DI water alone did not show such a disparity between the as-received and sputter-cleaned GST, as shown in Figure 3-16 (+21% v. 0% in Sb and +47% and +57% in Te, for as-received and sputter-cleaned, respectively).

96
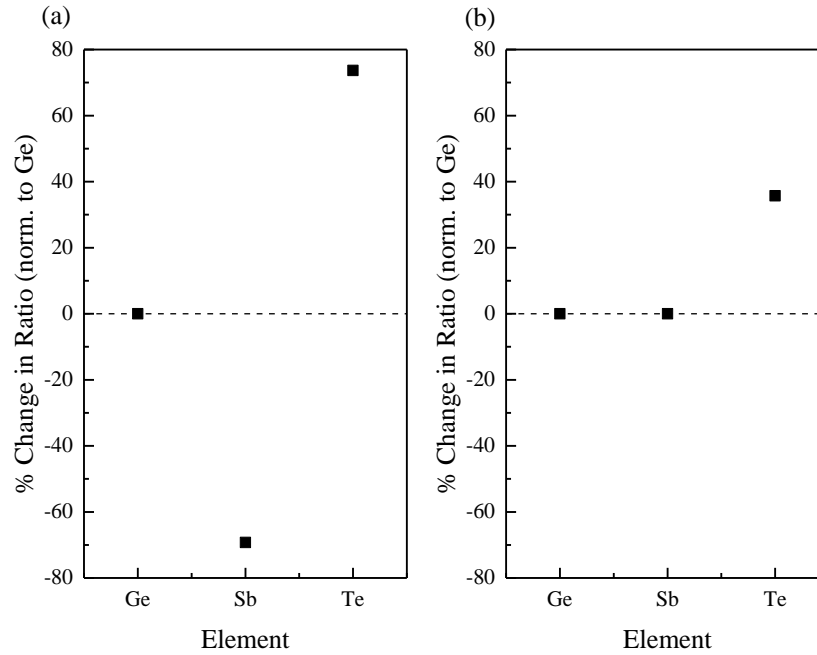
Figure 3-15. A comparison of the changes in composition ratio, normalized to Ge, after citric acid treatment on (a) as-received GST and (b) sputter-cleaned GST. The composition change is greater on the as-received GST than the sputter-cleaned GST, which was concluded to be due to the presence of GST-oxides on the as-received GST, which could be more susceptible to complexation with citric acid.
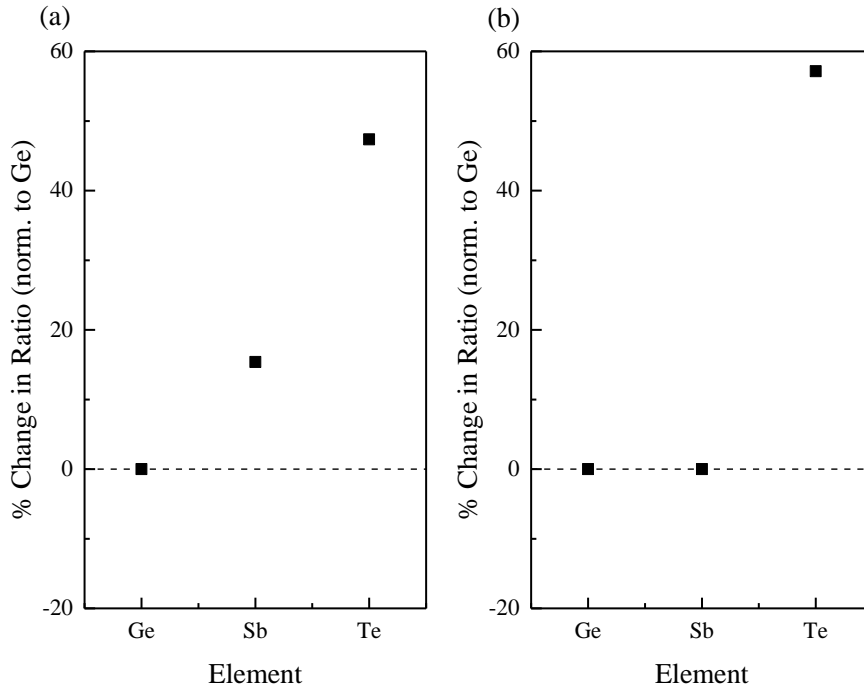
Figure 3-16. A comparison of the changes in composition ratio, normalized to Ge, after DI water treatment on (a) as-received GST and (b) sputter-cleaned GST. DI water alone results in changes to the composition ratio, but DI water was not as sensitive to the presence of GST-oxides as citric acid.

The observed effects can be explained by the oxidation on the as-received GST since there are some differences in simple bond properties between GST and GST oxides, summarized in Table 3-1. The bond energies of GST tended to be lower than those of Ge, Sb, and Te with O, and the electronegativity differences were much higher for the oxides than for Ge, Sb, and Te among themselves, indicating that GST oxides exhibited polar bonding while metallic GST exhibited only covalent bonding. While these simple properties do not tell the whole story of GST bonding (after all, the properties of GST also shift significantly with crystal phase, so these properties were unlikely to adequately capture the complexity of bonding in GST), they did suggest that GST oxides could behave very differently from metallic GST and may account for the difference in composition change between the as-received and sputter-cleaned GST, as shown in Figure 3-15

and Figure 3-16. Likewise, the changing bonding environment from pure Ge, Sb, or Te to ternary

GST is likely to be the cause for the differing response to the wet cleans.

Table 3-1. Table of bond energies and electronegativity difference of bonds in oxidized GST (Luo 2007, Haynes 2011).

Bond	Energy (kJ/mol)	$\Delta_{Electronegativity}$
Ge-Ge	264.4±6.8	0
Ge-Sb	142.4	0.04
Ge-Te	396.7±3.3	0.09
Sb-Sb	301.7±6.3	0
Sb-Te	277.4±3.8	0.05
Te-Te	257.6±4.1	0
Ge-O	660.3	1.43
Sb-O	434.0±42.0	1.39
Te-O	377.0±21.0	1.34
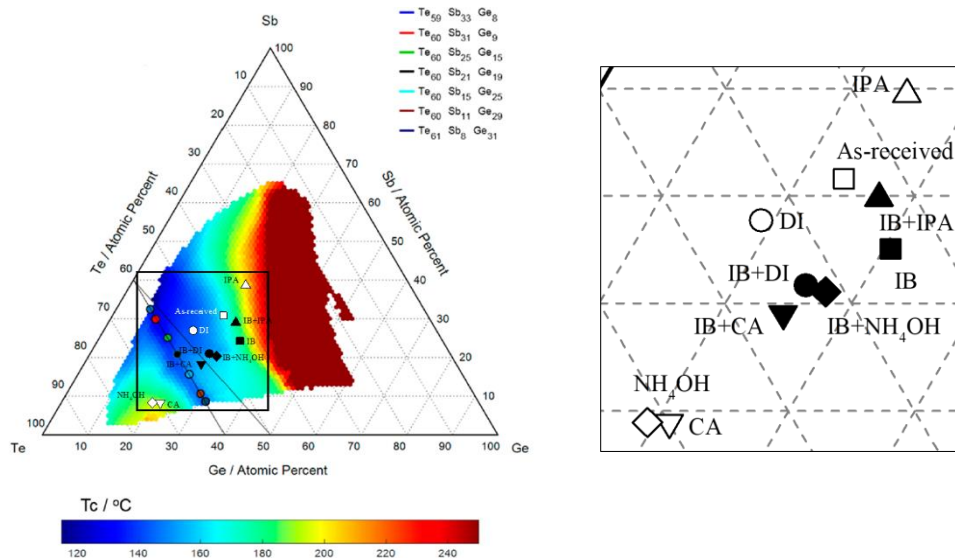
Figure 3-17. Crystallization temperature map of Ge-Sb-Te system (Guerin 2017). The GST compositions are shown for as-received GST (□) and after treatment with DI water (○), isopropyl alcohol (△), citric acid (▽), ammonium hydroxide (◇), as well as ion-beam cleaned GST (■) treated with DI water (●), isopropyl alcohol (▲), citric acid (▼), and ammonium hydroxide (◆). The distribution of these composition is expanded and shown on the right.
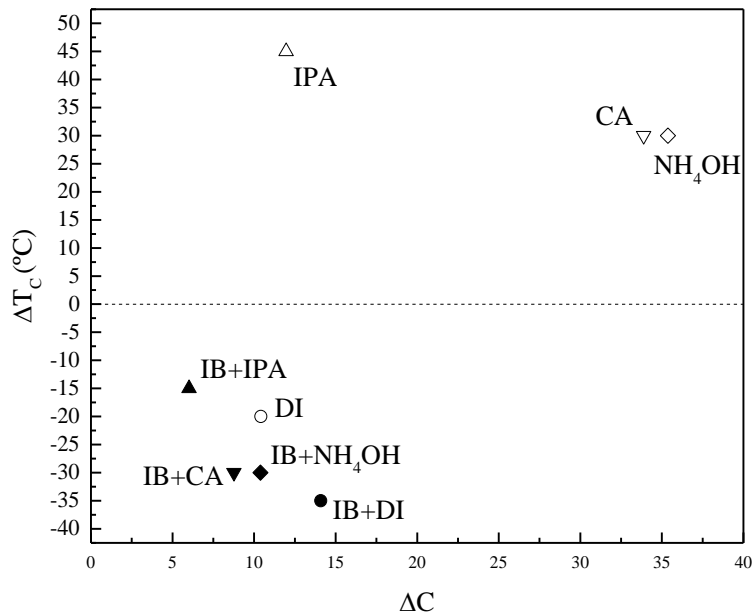
Figure 3-18. The change in crystallization temperature (ΔT_c) versus the composition change (ΔC) for the etch processes shown in Figure 3-17. Citric acid and ammonium hydroxide treatments on as-received GST result in greater composition change than DI water or IPA on as-received GST or any treatment on ion beam-cleaned GST. Despite the difference in the magnitude of composition change, citric acid and ammonium hydroxide both result in ~30ºC change in T_c, albeit in opposite directions.

The ambient oxidation of GST and the effects of wet cleaning on the composition of the GST surface were studied. Sputter-cleaned GST was exposed to atmospheres of nitrogen, oxygen, and water vapor, and it was found that water vapor resulted in the greatest extent of oxidation (64% O in 70% humidity for 30 min.), followed by oxygen (52% O after 30 min.) then nitrogen (29% O after 30 min.). It was concluded that water vapor was the most important factor in oxidation of GST.

DI water, isopropyl alcohol, citric acid, and ammonium hydroxide were studied. These were tested on single element Ge, Sb, and Te thin films as well as GST thin films with and without pre-cleaning by ion beam sputtering. The Ge thin films were found to oxidize in the wet clean

processes, while the Sb thin films were found to become more metallic. Te thin films showed the greatest variance in change in percent oxidation, falling from 49% down to 4% and 5 for DI water and citric acid, respectively, and ammonium hydroxide appeared to remove the majority of the Ge thin film. The GST film showed different behavior from the single element films when exposed to the same wet cleans. Citric acid and ammonium hydroxide were both able to remove the majority of the oxides, and DI water alone was also able to remove some oxides. Meanwhile, isopropyl alcohol was observed to result in greater oxidation of Ge, Sb, and Te. From this, it was concluded that the oxides could be more susceptible to removal by more polar solutions, which could be expected due to the polarity of the Ge-, Sb-, Te-O bonds. As-received GST, with its significant oxygen content, showed little change in Ge (varied within 5%) and significant depletion in Sb and enrichment in Te (up to 30%) as a result of citric acid and ammonium hydroxide. The removal of Ge by NH_4OH was not observed in GST, which suggested that complexation behavior was different between the single elements and the ternary compounds. The compositions of the as-received and wet cleaned GST are plotted on the crystallization temperature map in Figure 3-17, and it can be observed that citric acid and ammonium hydroxide wet cleaning of the as-received GST results in significant changes to composition.

Dilute HF, Ar ion beam cleaning, and downstream Ar cleaning were all capable of removing GST oxides. The dHF process was not preferred, as it resulted in a Te-rich (Ge:Sb:Te 1:0.5:3.6) surface and would still result in atmospheric exposure, as there was no integrated wet cleaning system on the transfer tube. Both the Ar ion beam and the downstream Ar plasma could remove the GST oxides, with the ion beam removing surface O and C more thoroughly than the downstream Ar process, and both treatments could recover the target GST ratio to some extent (Ge:Sb:Te 1:1:1.8 in the 200V Ar ion beam and 1:1:2.4 in the extracted downstream Ar). However,

the ion beam resulted in greater depletion of Te, which was thought to be due to the Te having a higher sputtering yield than Ge and Sb and to the fact that the ion beam would have a higher ion energy and flux than the downstream Ar plasma. The downstream Ar plasma also did not require an extra chamber transfer process and was preferred over the ion beam when available.

Ar ion beam cleaned-GST showed significantly less change in Ge:Sb:Te ratio after wet cleaning, as shown in Figure 3-9. Citric acid and ammonium hydroxide resulted in significantly less change to composition when oxides were removed beforehand. When comparing the Ge-normalized ratios, it was found that citric acid resulted in significantly more depletion of Sb on as-received GST (-69%) v. sputter-cleaned GST (-0%) as well as more enrichment of Te (+74% v. +36% for as-received v. sputter-cleaned, respectively). This effect was thought to be due to the citric acid since DI water alone did not lead to such significant changes in composition between the as-received and sputter-cleaned GST. Isopropyl alcohol had approximately the same effect on the as-received or sputter-cleaned GST, suggesting that it should be suitable for removing organic residues from GST. The difference in the behavior of the oxidized GST and the cleaned GST was attributed to the difference in the bonding of Ge, Sb, and Te among themselves and with oxygen. The bonds of Ge, Sb, and Te with oxygen are significantly more polar and generally have higher bond energy than the bonds of Ge, Sb, and Te among themselves. This reinforced the conclusion that the differing extent of the effects of the wet cleans was due to the GST oxides being more susceptible to the more polar solvents. This finding highlighted the need to clean GST films of their oxides to simplify the study of GST-plasma interactions in subsequent chapters.

Chapter 4 Etching of Ge, Sb, Te, and GeSbTe by Halogen Plasmas

Downstream halogen chemistries (Cl_2 and SF_6) were used to etch Ge, Sb, Te, and GST. The Cl_2/Ar plasma was found to significantly deplete the film of Ge and Sb and significantly enrich the film in Te (Ge:Sb:Te changed from 1:1.0:2.4 to 1:1.1:9.4) while also chlorinating the etched surface (10% Cl). This preferential removal was similar to the results observed when etching the Ge and Te thin films, as Ge thin films were found to etch rapidly (33.8 nm/min.) in the Cl_2/Ar plasma, while the Te thin film did not etch. The Sb thin film also did not etch in the Cl_2/Ar plasma but was still depleted in the ternary GST film, and this discrepancy was thought to be due to the reactivity of Cl_2 to Sb oxides versus metallic Sb. The etching of GST by SF_6/Ar plasma resulted in the enrichment of Sb and Te and depletion in Ge (Ge:Sb:Te changed from 1:1.0:2.4 to 1:1.3:2.5) but with a negligible etch rate of GST (thickness change was within SEM detection limit). This preferential removal was consistent with experiments on the single element Ge, Sb, and Te films, which found that Ge was susceptible to etch by SF_6/Ar (15.0 nm/min.), while Sb and Te did not etch in SF_6/Ar. Cl_2/Ar had a fast etch rate (13.1 nm/min.) but resulted in very significant change in stoichiometry (10% increase in Sb, 292% increase in Te), while SF_6 etching was considered negligible and resulted in less change in stoichiometry (30% increase in Sb, 4% increase in Te), less change in crystallization temperature, and very significant fluorination of the surface (57% F). Thermochemical analysis predicted preferential removal in GST due to halogen etching well, since preferential removal of Ge followed the volatility of the GST-halogen etch products, and the extent of halogenation followed GST-halogen bond energies.

4.1 Chlorine Plasma Etch of Ge, Sb, Te, and GST

Samples of Ge, Sb, and Te were exposed to downstream Cl_2/Ar plasma, approximately 50:50 Cl_2:Ar, at baseline conditions for 30 sec. Cl_2 was mixed with Ar to dilute the Cl_2 and help preserve the lifetime of the pumps on the ICP system. Cross-section SEM of these samples are shown in Figure 4-1, along with the cross-section SEM of a GST sample that was first sputter-cleaned using the downstream Ar plasma detailed in Section 3.4 for 5 min., followed by a downstream Cl_2/Ar plasma without vacuum break. The Cl_2 plasma was known to etch GST rapidly (as reported in Table 1-9), so the use of the bottom chamber helped to slow the etch rate and enable *in-situ* XPS study. The etching of Ge, Sb, Te, and the Ar-cleaned GST by the downstream Cl_2/Ar plasma showed that Ge was etched away the fastest (33.8 nm/min.), while Sb and Te did not appear to etch in the same time frame. Sb and Te samples were also etched for 1 and 3 min. in the same condition, but no etching was observed. XPS of the single-element samples was not available due to the small physical size of the samples. The GST etch rate was observed to be in between that of its slowest etching components (Sb and Te) and its fastest etching component (Ge). From the relative etch rates, or lack thereof, of Ge, Sb, and Te, it could be predicted that the etched GST surface would be depleted of Ge and enriched in Sb and Te. The relative inertness of the Sb and Te films to the Cl_2/Ar plasma combined with the relatively fast etch rate of GST seemed to suggest that bonding to Ge enhanced the etch rate of Sb and Te.
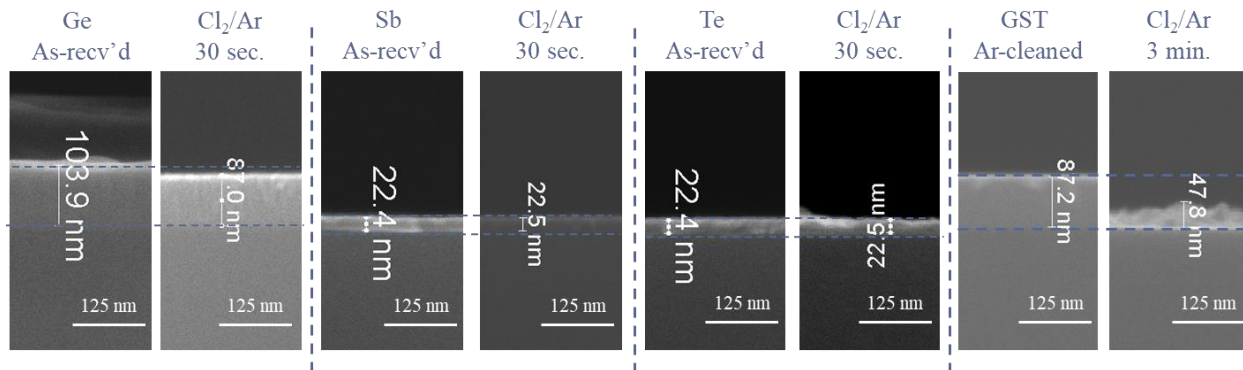
Figure 4-1. Cross-section SEM of Ge, Sb, Te, and GST films as-received or after downstream Ar cleaning (500W/100V$_B$/~15mTorr/5min.) and after etching in downstream 50Ar/50Cl$_2$ plasma (500W/100V$_B$/~15mTorr) for 30 sec. (or 3 min. for GST).
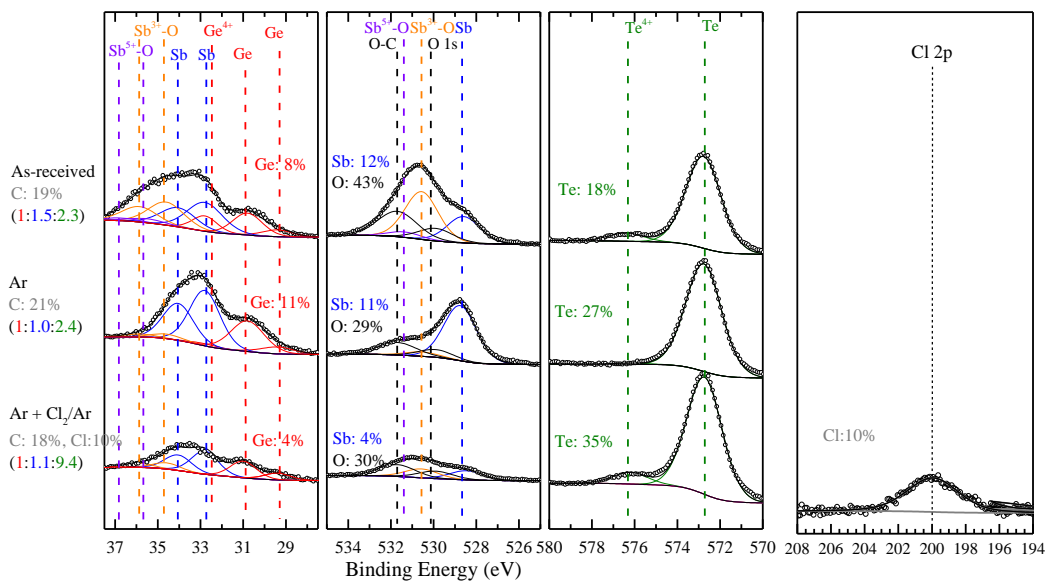
Figure 4-2. XPS spectra of a GST film as-received, a GST film after Ar clean at baseline conditions for 5 min., and a GST film after Ar clean followed by Cl$_2$/Ar plasma at baseline conditions for 30 sec. The composition of the GST film quantified by XPS for Ge, Sb, Te, O, and C is listed by the respective spectra, and C and Cl percentage and the ratio of Ge:Sb:Te, normalized by Ge is listed underneath each spectra label. The Cl$_2$/Ar plasma results in massive enrichment of Te, and the presence of Sb x+ and Te 4+ oxidation states is attributed to chlorination of the film.

XPS of the downstream Cl$_2$/Ar-etched sample, shown in Figure 4.2, showed a film that had a Ge:Sb ratio close to the desired stoichiometry (1:1.1 v. 1:1.0), but the film was so enriched in Te that the GST could be said to be heavily depleted of Ge and Sb, as observed in Figure 4-3. Using

105

the normalized composition Ge:Sb:Te=1:x:y defined in Ch. 2, the change in composition after the chlorine etching Ge:Sb:Te=1:1.1:9.4 (compared to that after Ar sputtering Ge:Sb:Te=1:1.0:2.4) was (1.1-1.0)/1.0=+10% for Sb and (9.4-2.4)/2.4=+292% for Te, indicating that the etched film was very enriched in Te. The Cl_2/Ar-etched film was also chlorinated (10%). Since the Te^{4+} peak observed near 576 eV (attributed to oxidized Te in the as-received spectrum) was not observed after Ar-cleaning (due to the removal of GST oxides), the Te^{4+} peak in the Cl_2/Ar -etched sample was attributed to chlorinated Te. A similar phenomenon was observed for Sb, although Sb oxides were not completely removed by the Ar-cleaning process. Chlorination was not readily observed for Ge. As noted in literature, this followed the boiling point trend of the GST-chlorine etch products, and it was concluded in literature that the changes in stoichiometry were due to the differences in boiling points (Kang 2011, Li 2016, Canvel 2019). It was also noted in a study of Ge-rich GST that Ge seemed to be especially susceptible to removal by halogen-containing plasmas (Canvel 2019), and the etching of the Ge, Sb, and Te thin films indicated that this was also the case in this work.
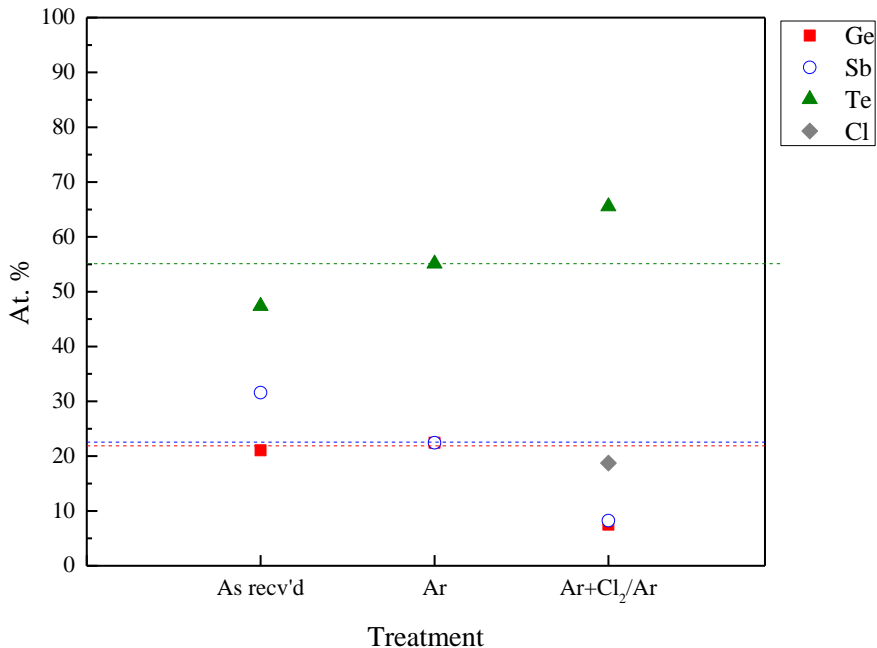
Figure 4-3. Atomic percentages of Ge, Sb, and Te determined from XPS for GST thin films as-received, cleaned by downstream Ar plasma, then exposed to downstream Cl_2 gas or downstream Cl_2 plasma. Guidelines denote the composition of the Ar-cleaned GST, to which the Cl_2/Ar -etched sample should be compared. Both Ge and Sb were depleted after Cl_2/Ar etch, while Te was significantly enriched.

It should be noted that there was one major difference between the etching of the GST film and the etching of the Ge, Sb, and Te films, which was that the GST was relatively oxide-free due to the downstream Ar pre-clean. The Ge, Sb, and Te thin films were not pre-cleaned due to the relative ease of sputtering Sb and Te and the thinness of the Sb and Te films (~20-25 nm thick as-received), which would have made SEM analysis extremely difficult. Thicker Sb and Te samples would have allowed for Ar-cleaning to remove the oxides from the film and enabled a better comparison to the Ar-cleaned GST, but they were difficult to grow by molecular beam epitaxy. As established in this work with the wet cleaning of GST (Section 3.3), the GST oxides can exhibit markedly different responses to chemical treatments, so the presence of Ge, Sb, and Te oxides on the single-element films may introduce some issues in applying single-element results to that of

the ternary film. While the etching of Sb and Te by Cl_2 plasma do not appear to have been reported before in literature, the etching of GaSb by Cl_2 plasma has been studied, and GaSb was found to be etched by Cl_2 plasma readily while GaSb oxides have been reported to be inert to etching by Cl_2 plasma (Smolinsky 1981). If Sb oxides were inert to Cl_2 plasma but Sb was readily etched by Cl_2 plasma, it could explain why the ambient-oxidized Sb thin film was inert to the downstream Cl_2/Ar plasma but Sb was removed in the Ar-cleaned ternary film.

4.2 Sulfur Hexafluoride Plasma Etch of Ge, Sb, Te, and GST

While the use of SF_6 plasma to etch GST has not been reported previously in literature, multiple fluorine-containing plasma chemistries have been studied, such as CF_4, C_4F_8, and CHF_3 (see Table 1-9). The use of these plasmas has been reported to etch GST more slowly than Cl_2 plasma, which was attributed to the deposition of a C-F layer that slows further etching (Kang 2011). The formation of the C-F layer was not expected when using SF_6 plasma.

Samples of Ge, Sb, and Te were exposed to SF_6/Ar plasma, approximately 50:50 SF_6/Ar, at baseline conditions for 3 min. in the bottom chamber of the ICP system. The Ar was needed to help sustain the discharge. Cross-section SEM of these samples are shown in Figure 4-4, along with the cross-section SEM of a GST sample that was first sputter-cleaned using Ar plasma for 5 min., followed by SF_6/Ar plasma without vacuum break for 3 min. XPS of the single-element samples was not available due to the small physical size of the samples.
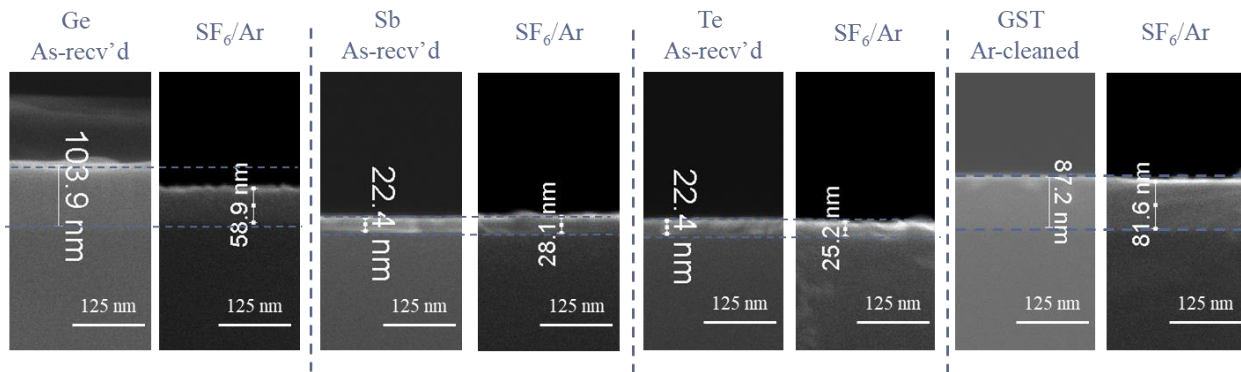
Figure 4-4. Cross-section SEM of Ge, Sb, Te, and GST films as-received or after downstream Ar cleaning for 5 min. at baseline conditions and after etching in downstream 50SF₆/50Ar plasma for 3 min. at baseline conditions.
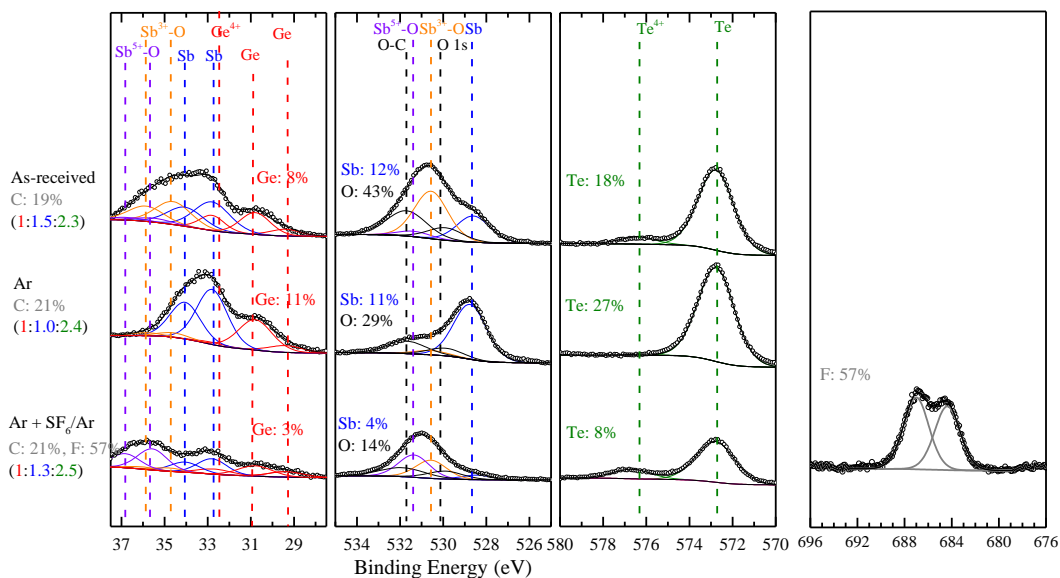
Figure 4-5. XPS spectra of a GST film as-received, a GST film after Ar clean at baseline conditions for 5 min., and a GST film after Ar clean followed by SF₆/Ar plasma at baseline conditions for 3 min. The composition of the GST film quantified by XPS for Ge, Sb, Te, O, and C is listed by the respective spectra, and C and F percentage and the ratio of Ge:Sb:Te, normalized by Ge is listed underneath each spectra label. GST signals were all attenuated due to the presence of significant F content, and the presence of Ge 4+, Sb x+, and Te 4+ was attributed to GST-F bonding.

The etching of the Ge, Sb, Te, and Ar-cleaned GST samples shows that Ge etched quite rapidly in the SF₆/Ar plasma, although not as rapidly as in downstream Cl_2/Ar (33.8 nm/min. v. 15±1.6 nm/min. for downstream Cl_2/Ar v. SF₆/Ar, respectively), while Sb and Te did not appear to etch at all. The Ar-cleaned GST did appear to be etched, albeit quite slowly (1.9±1.6 nm/min.).

From the relative ease of etching of Ge, Sb, and Te, it could be predicted that etching GST with downstream SF_6/Ar would result in a surface that was depleted of Ge and enriched in Sb and Te.
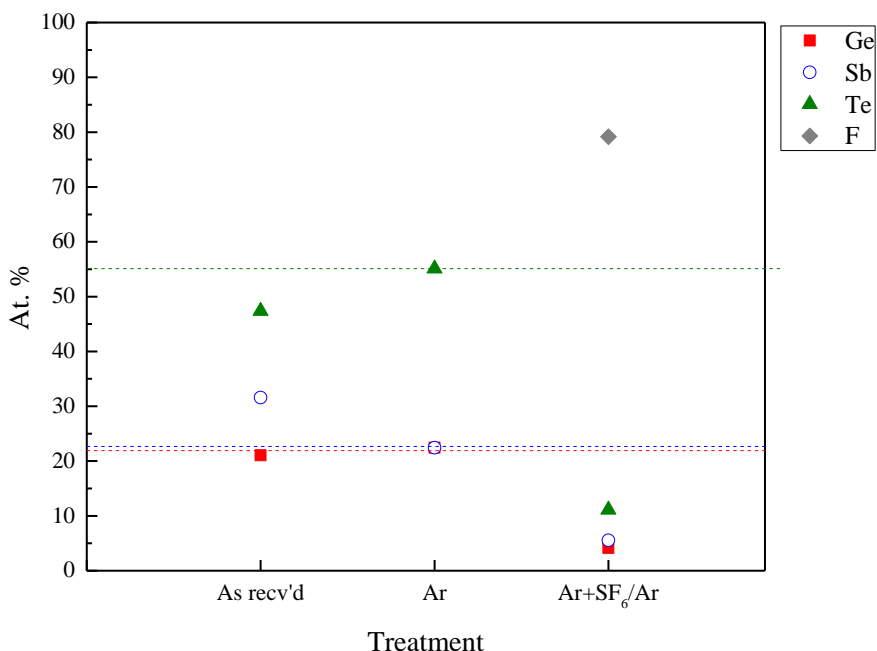
Figure 4-6. Atomic percentages of Ge, Sb, and Te determined from XPS for GST thin films as-received, cleaned by downstream Ar plasma, then exposed to downstream SF_6/Ar plasma. Guidelines denote the composition of the Ar-cleaned GST, to which the SF_6/Ar-etched sample should be compared.

XPS spectra of the GST film as-received, after Ar cleaning, and after both Ar cleaning and SF_6/Ar plasma, are shown in Figure 4-5 and summarized in Figure 4-6, showed that the SF_6/Ar plasma resulted in relatively little change to the GST compared to the Cl_2/Ar plasma. The SF_6/Ar -etched GST surface showed a composition that was slightly enhanced in Sb and Te compared to the Ar-cleaned sample, which followed the prediction drawn from the etching of the Ge, Sb, and Te samples. Using the normalized composition Ge:Sb:Te=1:x:y, the change in composition after the chlorine etching Ge:Sb:Te=1:1.3:2.5 (compared to that after Ar sputtering Ge:Sb:Te=1:1.0:2.4) was defined as (1.3-1.0)/1.0=+30% for Sb and (2.5-2.4)/2.4=+4% for Te, indicating that the SF_6/Ar -etched film was much closer to the desired stoichiometry than the Cl_2/Ar-etched film. However,

the XPS of the SF_6/Ar-etched GST film also showed significant fluorination of GST (57% F) compared to the Cl_2/Ar plasma, which matched well with the relevant GST-halogen bond energies analyzed in Section 2.1. The overall peak shapes of Ge, Sb, and Te spectra more closely resembled the as-received spectra as opposed to the Ar-cleaned spectra, and since there was no vacuum break between the Ar-cleaning and the SF_6/Ar treatment as well as significant fluorine content detected on the etched surface, the SF_6/Ar -etched GST was determined to be heavily fluorinated. No XPS peaks were identified as being due to the presence of sulfur. While no measurement of the changes in phase-change properties of these GST films was done in this work, it was assumed based on literature reports that halogenation of this magnitude would severely alter the phase change properties of the GST film (Park 2016).

In this chapter, the use of downstream Cl_2/Ar and SF_6/Ar plasmas to etch GST was studied. Etching of Ge, Sb, and Te thin films revealed that both Cl_2/Ar and SF_6/Ar were inert to Sb and Te, with no etch rate quantified for either element, while both chemistries were relatively reactive to Ge (33.8 and 15 nm/min. in Cl_2/Ar and SF_6/Ar, respectively). The Cl_2/Ar chemistry proved to be capable of etching the GST quickly (13.1 nm/min.) even in the reduced flux of the downstream process, while the SF_6/Ar chemistry was much slower (1.9 nm/min.). The Cl_2/Ar plasma resulted in slight enrichment of Sb and massive enrichment of Te in the etched film (+10% Sb, +292% Te). Although the change in Ge:Sb ratio from 1:1.0 to 1:1.1 suggested that Sb had been enriched, the magnitude of the Te enrichment meant that Sb had also been depleted, which was not suggested by the inertness of Sb to the Cl_2/Ar. This was thought to be due to the native oxidation on the Sb thin film, which had not been cleaned away due to the small starting thickness of the sample, as literature reported that Cl_2 plasma etched GaSb readily but did not etch GaSb oxides (Smolinsky 1981). SF_6/Ar demonstrated greatly reduced change in the stoichiometry of the etched GST as

111

compared to the Cl$_2$/Ar (+30% Sb, +2% Te). This matched well with the results on the Ge, Sb, and

Te thin films, since Ge had been shown to etch in SF$_6$/Ar, while Sb and Te had not been etched.

These findings for Cl$_2$/Ar and SF$_6$/Ar are summarized in Table 4-1, and the changes in Ge-

normalized ratio between the Cl$_2$/Ar and SF$_6$/Ar are shown in Figure 4-7.

Table 4-1. Summary of findings for downstream Cl$_2$/Ar and SF$_6$/Ar plasma etching of GST. Etch rates that are too slow to be conclusively considered etching (i.e., smaller than or close to error) are considered zero and italicized. * indicates that the film was cleaned of oxides prior to etch.

	Cl$_2$/Ar	SF$_6$/Ar
GST Etch Rate (nm/min.)	13.1±1.6*	*~0**
Ge Etch Rate (nm/min.)	33.8±10	15.0±1.6
Sb Etch Rate (nm/min.)	*~0*	*~0*
Te Etch Rate (nm/min.)	*~0*	*~0*
% Sb Change (norm. to Ge)	+10%	+30%
% Te Change (norm. to Ge)	+292%	+2%
% Halogen	10% Cl	57% F

The enrichment of Ge and depletion of Sb and Te, as well as the extent of halogen

incorporation on the etched GST surface, matched well with the thermochemical analysis in

Section 2.1. The etch product boiling points had predicted that Ge would be preferentially removed,

followed by Sb, then Te in the case of chlorine etching and by Te then Sb in the case of fluorine

etching, as shown in Figure 4-7(a) and Figure 4-8(a). Both these trends were confirmed by the

changes in Sb and Te summarized in Table 4-1 and Figure 4-7(b) and Figure 4-8(b). The extent of

halogenation also followed the known bond energies of Ge, Sb, and Te with F and Cl, since Ge-F

and Sb-F had greater bond energies than Ge-Cl and Sb-Cl, and the etched GST films were observed

to have significantly more F than Cl. However, the amount of fluorine incorporated in the film

after SF$_6$/Ar was quite large (57% F) and expected to alter the phase-change properties of the film.

While the preferential removal of Ge from the GST could be explained, the etch rates of the

individual Ge, Sb, and Te thin films in both Cl$_2$/Ar and SF$_6$/Ar plasmas, as shown in Figure 4-7(c)

and Figure 4-8(c), respectively, also suggested that Ge was depleted due to its susceptibility to

etching in these plasmas, as compared to Sb and Te.
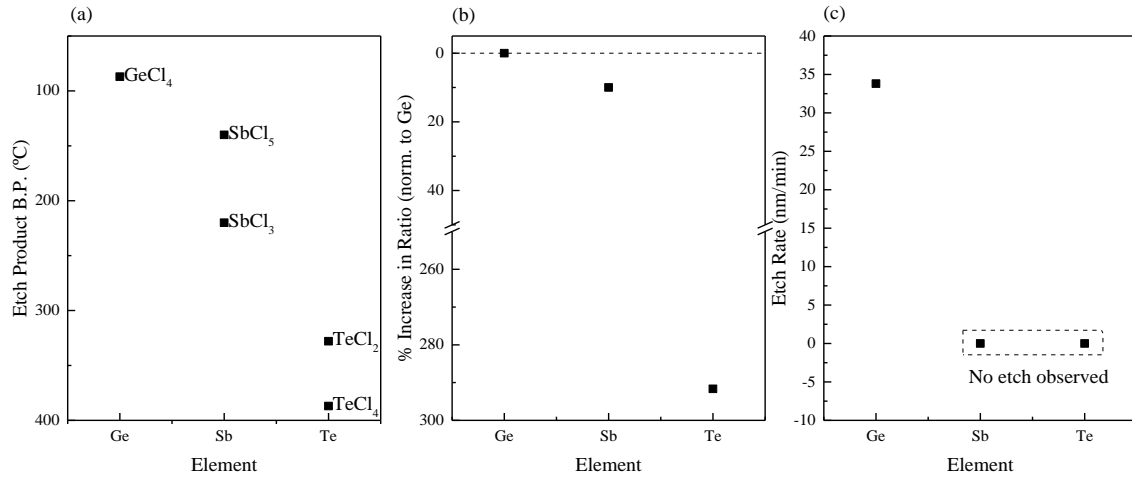
Figure 4-7. (a) Ge-Cl, Sb-Cl, Te-Cl etch product boiling points by element. (b) Change in composition ratio for each element in GST after etching in Cl_2/Ar plasma, determined from XPS quantification. (c) Ratio of the etch rate of each element in Cl_2/Ar normalized against the etch rate of Ge in downstream Cl_2/Ar plasma. The change in composition ratio in GST after etching Cl_2/Ar plasma followed the same order predicted by the boiling points of each element's etch products (Ge > Sb > Te). This order was also followed by the etch rates of Ge, Sb, and Te in the same plasma. Slower etching elements became enriched in the ternary compound, and Sb and Te were not observed to etch in Cl_2/Ar plasma.
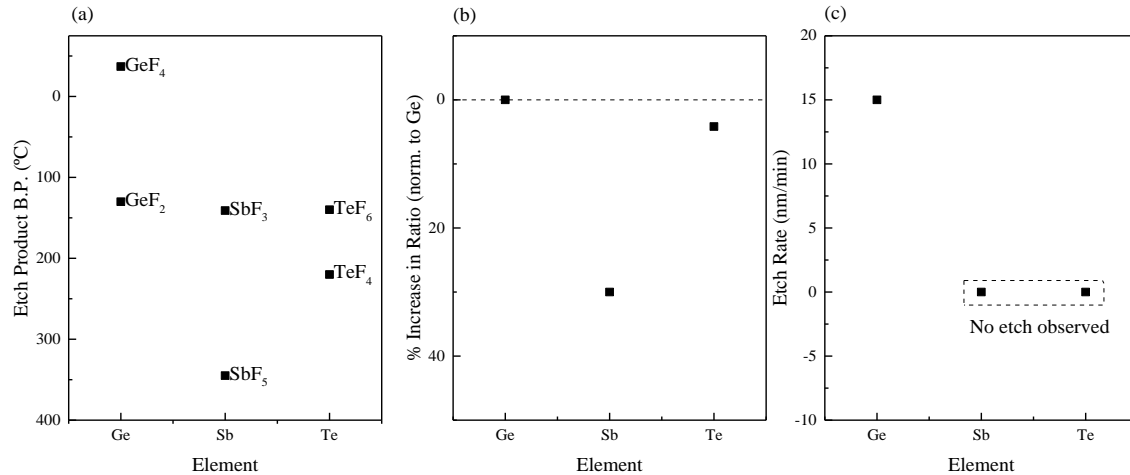
Figure 4-8. (a) Ge-F, Sb-F, Te-F etch product boiling points by element. (b) Change in composition ratio for each element in GST after etching in SF_6/Ar plasma, determined from XPS quantification. (c) Ratio of the etch rate of each element in SF_6/Ar normalized against the etch rate of Ge in downstream SF_6/Ar plasma. The change in composition ratio in GST after etching SF_6/Ar plasma followed the same order predicted by the boiling points of each element's etch products (Ge > Te > Sb). This order was also followed by the etch rates of Ge, Sb, and Te in the same plasma. Slower etching elements became enriched in the ternary compound, and Sb and Te were not observed to etch in SF_6/Ar plasma.
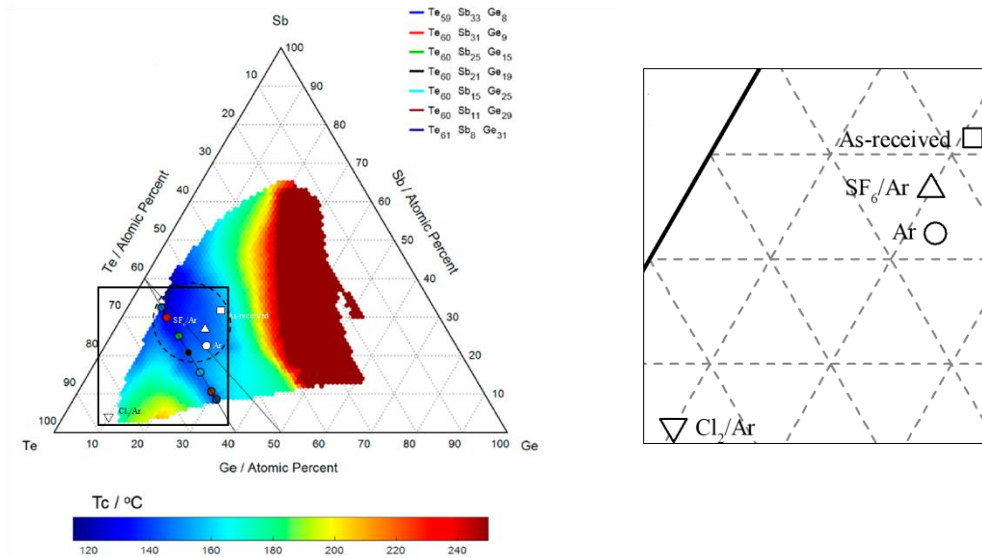
Figure 4-9. Crystallization temperature map of Ge-Sb-Te system (Guerin 2017). GST compositions as-received (□), after Ar plasma cleaning (○), and after Ar plasma cleaning followed by Cl_2/Ar (∇) and SF_6/Ar (△) plasma etching are shown. Cl_2/Ar plasma caused major changes in composition, while SF_6/Ar resulted in smaller changes in composition and stayed within the minimum crystallization temperature region marked with the dashed circle. The distribution of these composition is expanded and shown on the right.
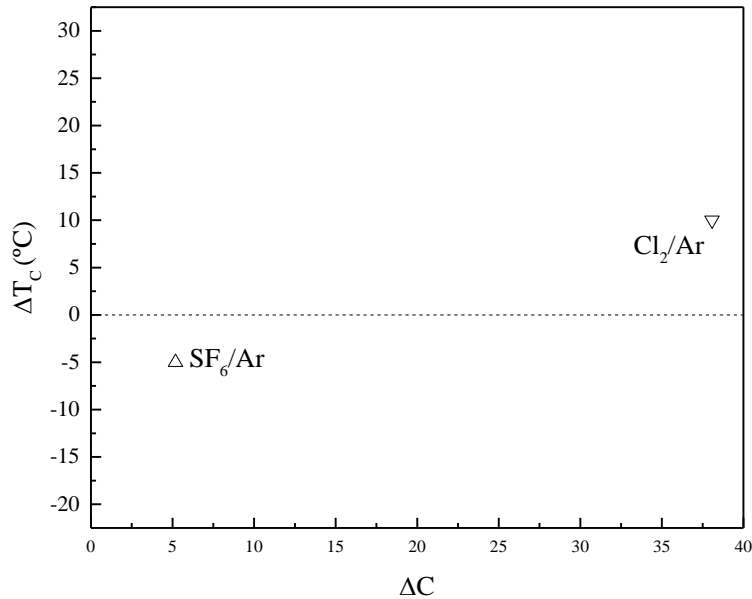
Figure 4-10. The change in crystallization temperature (ΔT_c) versus the composition change (ΔC) for the etch processes shown in Figure 4-9. Cl_2/Ar resulted in a greater change in composition ($\Delta C=38$) compared to SF_6/Ar ($\Delta C=5$). However, the expected change in ΔT_c was not much greater after Cl_2/Ar than after SF_6/Ar based on the composition-crystallization temperature analysis. The halogenation of the GST surface is expected to have an effect on phase-change properties, which is not accounted for in this analysis.

In summary, the use of Cl_2/Ar and SF_6/Ar to etch GST was studied, and it was found that both chemistries could etch GST, although the Cl_2/Ar resulted in major composition change compared to SF_6/Ar ($\Delta C=38$ for Cl_2/Ar v. $\Delta C=5$ for SF_6/Ar), as shown in Figure 4-9 and Figure 4-10. However, the change in crystallization temperature was not much higher for Cl_2/Ar ($\Delta T_c=10°C$) than for SF_6/Ar ($\Delta T_c=-5°C$). This T_c difference was determined using the closest T_c value to the Cl_2/Ar composition, since it fell outside the compositions that had been studied. It also needs to be considered that both chemistries result in halogenation of the surface, with SF_6/Ar resulting in particularly high fluorine incorporation (57% F, the surface is majority fluorine rather than Ge, Sb, and Te). It was also found that analysis of the halogen etch product properties could explain the preferential removal of Ge, Sb, and Te from the GST film and the relative extent of

halogen incorporation in the GST film post-etch. It was also determined that the etch rates of Ge, Sb, and Te could also be an important factor in explaining the preferential removal of these elements from GST.

Chapter 5 Etching of Ge, Sb, Te, and GeSbTe by a H_2 Plasma

The constituent elements of GST were each etched by hydrogen plasma to determine the etch rates and reaction products. SbH_y and TeH_z etch products were readily detected by QMS, while GeH_x etch products were not readily detected. Based on the etch rates of Ge, Sb, and Te thin films in the H_2 plasma (both directly and downstream), it was found that Te was most reactive to the hydrogen plasma while Ge was the least reactive, with Sb having intermediate reactivity. Etching of the as-received GST film directly in the H_2 plasma yielded an etch rate of 32.7 nm/min at baseline conditions. Etching sputter-cleaned GST thin films of Ge:Sb:Te 1:1.0:2.4 composition by downstream H_2 plasma resulted in a surface with a composition of 1:0.8:1.6, which was depleted of Te and Sb and enriched in Ge and matched the order given by the individual etch rates of Ge, Sb, and Te (Te > Sb > Ge). This was opposite to the order suggested by the etch product boiling points (Ge > Sb > Te), which indicated that H_2 plasma etching could be kinetically-limited. While no measurement of H content could be made using XPS, the XPS of the H_2-etched sample indicated that there were only metallic GST states, which suggested that there was little to no oxidation of the film. From these experiments, GST could be etched by H_2 plasma with less incorporated plasma species, but the H_2 plasma still resulted in noticeable depletion of the Sb and Te and noticeable change in crystallization temperature. It was also concluded that, unlike the halogen-based etches of GST, the boiling points of the etch products were not a predictor of which elements would be preferentially removed from the GST, while the relative susceptibility of each element to the plasma, as determined by the etch rates of the elemental thin films, was an accurate predictor of preferential removal.

5.1 Hydrogen Plasma Reaction with Ge, Sb, and Te

5.1.1 Hydrogen Etching of Ge

A Ge wafer was mounted in the line-of-sight of the QMS (position (1) in Figure 2-7) and directly exposed to H_2 plasma to measure the formation of etch products (GeH_x). The QMS spectrum is shown in Figure 5-1. The presence of Ge or GeH_x etch products was not observed using QMS, which may be due to a concentration of Ge etch product that is insufficient for detection by the QMS. This would be indicative of low reactivity of Ge to the H_2 plasma. It is also possible that the Ge etch product formed as clusters that were of a m/z ratio too large for the QMS to detect. Previous mass spectroscopy studies of GST etching showed the formation of a small amount of Ge_m clusters, accompanied by Ge_mH_n clusters with m/z as high as 1190 (Houška 2014) well beyond the detection range of the QMS used in this work.

In order to determine if Ge was etched at all by the H_2 plasma, a Ge thin film is mounted in position (2) and etched directly in H_2 plasma at baseline conditions. The etch rate of the Ge film in H_2 plasma was characterized by SEM and determined to be 3.3±1.6 nm/min. The etch rate of the Ge thin film was also measured in the downstream plasma configuration (position (3)) at baseline conditions. The etch rate measured in this configuration was too slow to conclusively be considered etching (0.6±1 nm/min.).
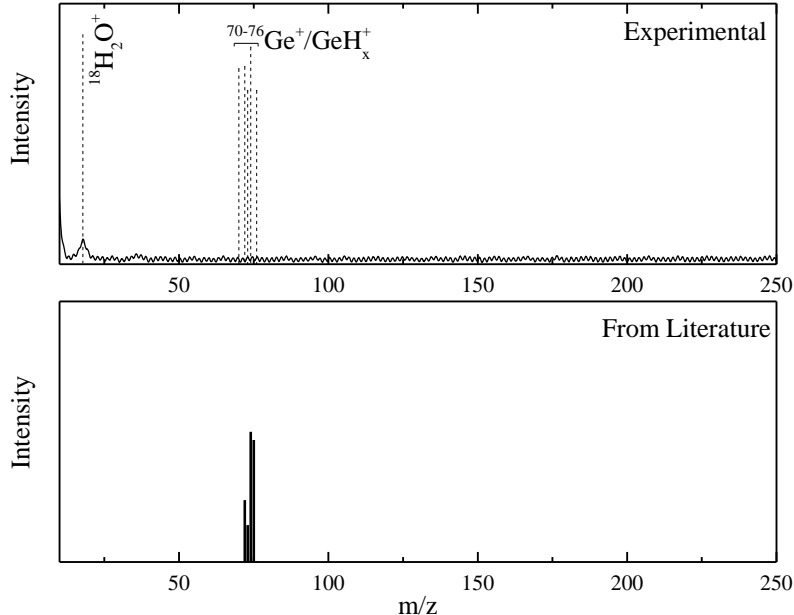
Figure 5-1. QMS measurement of a Ge wafer etched in H_2 plasma (500W/500V$_B$/10mTorr), the presence of GeH$_x$ etch product was not detected. A known spectrum for GeH$_4$ is shown for comparison (Saalfeld 1963).

Another confirmation that Ge was indeed etched by H_2 was determined by OES. Figure 5-2 shows the OES of H_2 plasma alone and in the presence of a Ge sample, as well as the OES of an Ar plasma on Ge samples. In this case, large pieces of Ge wafer used (approx. one quarter of a 4" Ge wafer). Comparing the OES results of Ge sample in H_2 plasma with the background H_2 plasma as well as Ge sample in Ar plasma, noticeable peaks of GeH at ~389.8 nm were observed.(Wang, Guanghong 2015), (Klement 2013). This shows that H_2 plasma was reactive to the Ge surface resulting in the formation of volatile GeH$_x$. The UV atomic emission of Ge (at 303.9 nm and 265 nm) was expected to be difficult to be observed in Ar and H_2 plasma. However, in an H_2/GeH$_4$ plasmas, the OES intensity of Ge at 303.9 nm is very short with respect to that of GeH at 389.8 nm. The clearest Ge spectrum between 200-800 nm was observed at 556.5 nm in Ar plasma in the presence of Ge sample but it was not observed in H_2 plasma.(Andrew 1959) This

concluded that in Ar plasma, the effect of sputtering leaves a trace of Ge in the plasma and in contrast, H_2 plasma showed a higher concentration of GeH_x rather than Ge. A small amount of N_2 impurity was also observed in H_2 and Ar plasmas from the second positive system of N_2 between 310-385 nm. Similar OES experiments for Sb and Te could not be performed due to the lack of sufficient Sb or Te samples.
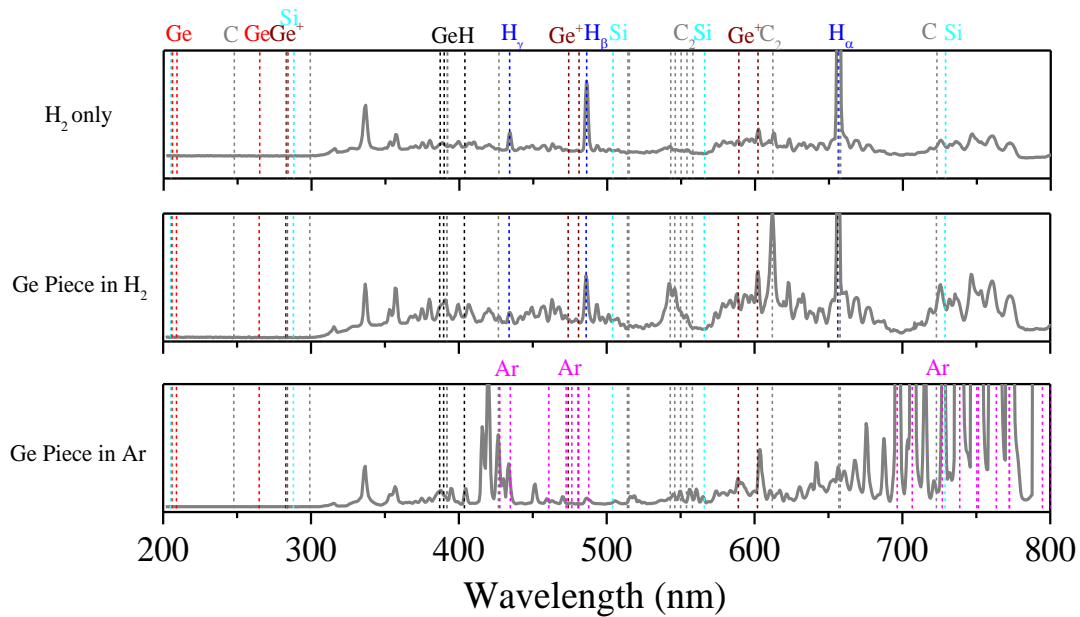
Figure 5-2. OES measurement of an H_2 plasma as a background spectra, Ge wafer etched in H_2 plasma (500 W/500 V_B/ 10mTorr) and Ar plasma (800 W/100 V_B/14 mTorr), the presence of GeH_x etch product was detected at 389.8 nm in H_2 plasma and a trace Ge in Ar plasma at 556.5 nm.

5.1.2 Hydrogen Etching of Sb

To assess the etching of Sb in H_2 plasma, an experiment analogous to the one presented in Figure 5-1 was carried out with the same plasma conditions (500W/-500V_B/10mTorr) on an Sb target in position (1), and the resulting QMS spectrum is shown in Figure 5-3. A peak at around 123-124 m/z was identified as the SbH_x etch product, which demonstrated that Sb can be etched more readily than Ge in an H_2 plasma. These results were further confirmed by etching an Sb thin film using the downstream H_2 plasma (500W/100V_B/15mTorr/position (3)). The Sb thin film

etched readily at these conditions at an etch rate of ~2.2 nm/min. OES was not available for Sb etch, since the Sb deposited readily on the windows in the chamber and prevented OES measurements.
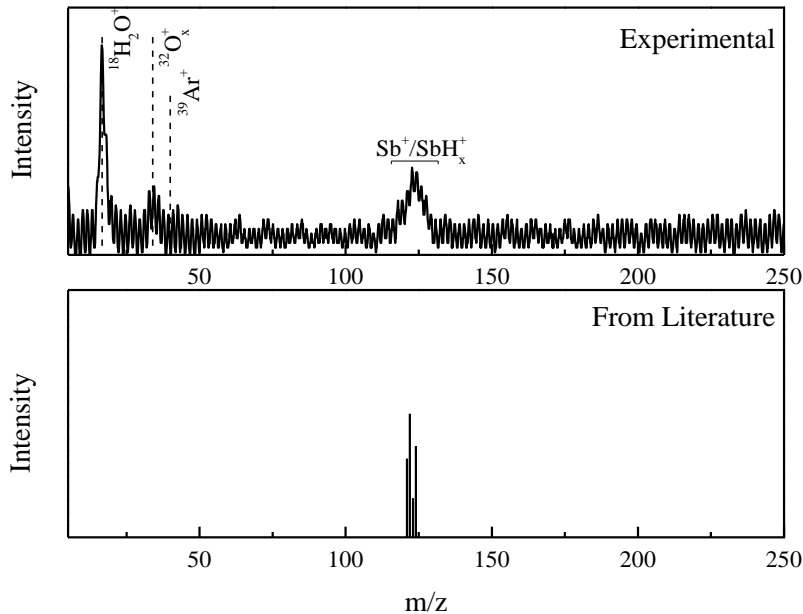
Figure 5-3 QMS measurement of Sb sputter target etched in H_2 plasma (500W/500V_B/10mTorr) showing the presence of a SbH$_x$ etch product. A known spectrum for SbH$_3$ is shown for comparison (Saalfeld 1963).

5.1.3 Hydrogen Etching of Te

The reactivity of Te in H_2 plasma was also assessed using the same conditions (500W/-500V_B/10mTorr) used for Ge and Sb at positions (1). The QMS results from directly exposing a Te sputter target to an H_2 plasma are shown in Figure 5-4(a), where a peak around 129-131 was identified as a TeH$_x$ etch product. If normalized against their respective background moisture peaks (m/z=18), the TeH$_x$ appeared to be relatively more intense than the SbH$_x$ peak, which suggested that Te may have a higher reactivity to H_2 plasma than Sb does. This was further confirmed upon exposing the Te to the downstream H_2 plasma at position (3) (500W/100V_B/15mTorr), and an etch rate of at least 4.5 nm/min. was determined by SEM. As was

the case for Sb, OES was also not available for Te etch, since the Te also deposited readily on the

windows in the chamber and prevented OES measurements.
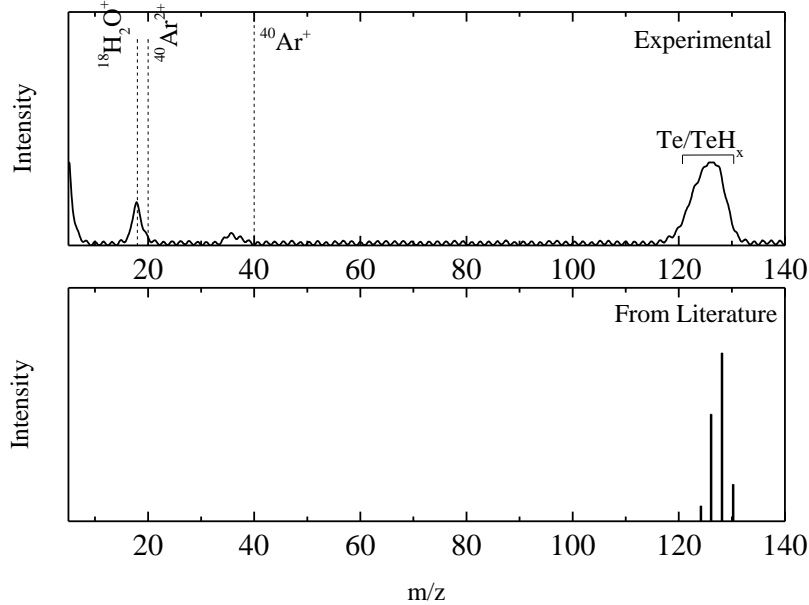
Figure 5-4. QMS measurement of Te sputter target etched in H2 plasma (500W/-500V$_B$/10mTorr) showing the presence of a TeH$_x$ etch product. A spectrum adapted of HgTe etched in H$_2$ plasma showing the QMS signals of TeH$_2$ is shown for comparison (Keller 1995).

The measured reaction products and etch rates for each constituent element are summarized

in Table 5-1. These results suggested that Ge has the lowest reactivity, followed by Sb, then Te.

This experimentally observed trend seems opposite to those predicted by the boiling points of the

etch products and the Gibbs free energy of reaction, as detailed in Section 0. However, this was

not a contradictory finding since the Gibbs free energies of reactions are equilibrium values and

not applicable to the non-equilibrium plasma processes nor predictive of the kinetics of the reaction.

The overall rate of material removal was affected by both the reaction between the surface and the

etchants to form the etch products and the desorption of said etch products from the surface. In a

reaction-limited process, the desorption of the etch product would be much faster than the

formation of the etch product. In a desorption-limited process, the formation of the etch product

123

would be much faster than the desorption of the etch product from the surface. For GST as a ternary compound, if Te was preferentially removed, followed by Sb, then Ge, then the trend would follow that of the reactivity of each element to the H_2 plasma, and the process could be considered to be kinetically-limited. On the other hand, if Ge was found to be preferentially removed, followed by Sb, then Te, then the trend would follow that of the boiling points of the GST-hydrogen etch products, which could suggest that the process was desorption-limited.

5.2 Hydrogen Plasma Reaction with GeSbTe

The etching of GST films by H_2 plasma was studied by exposing samples of GST to the H_2 plasma directly (position (2)). It was found that the GST film etched rapidly when directly exposed to H_2 plasma in the top chamber, with an etch rate of approximately 32.7 nm/min. Sb and Te thin films etched very rapidly, with the entire ~22 nm films etching away in a matter of seconds, and the etch rates were determined to be >240 nm/min. This was significantly faster than the rate measured for pure Ge thin films measured at the same position. The etch rates of the Ge, Sb, Te, and GST samples in both direct and downstream H_2 plasma etching were summarized in Table 5-1, and the SEM images of the downstream samples were shown in Figure 5-5. It should be noted that the etch rate of Ge in the downstream H_2 etch rate was smaller than its respective error and could be said not to have etched.
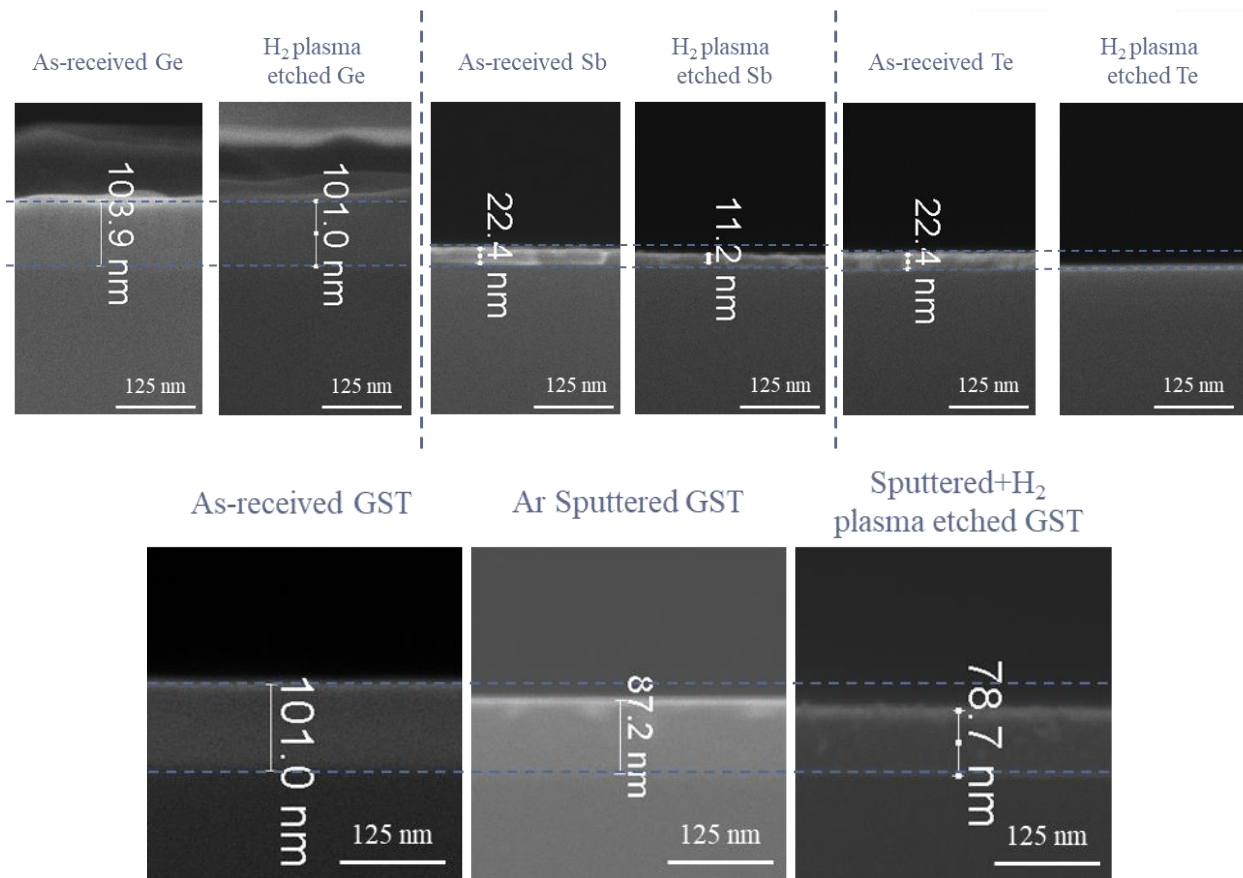
Figure 5-5. Cross-section SEM of GST as-received, after downstream Ar cleaning (5min.) and after downstream H_2 plasma (5min.), and cross-section SEM of Ge, Sb, and Te as-received and after downstream H_2 plasma (5min.). All samples were processed at baseline conditions.

Table 5-1. Summary of QMS and bottom chamber downsteam H_2 etch rate (ER) observations for Ge, Sb, Te, and GST. The etch rate of the GST film in the bottom chamber is measured after Ar pre-clean. Etch rates that are too slow to be conclusively considered etching (i.e., smaller than or close to error) are considered zero and italicized. * indicates that the sample was Ar-cleaned before etching.

Material	QMS analysis 10mTorr, $500V_B$ Position (1)	ER (nm/min) 15mTorr, $-100V_B$ Position (2)	Downstream ER (nm/min) 15mTorr, $100V_B$ Position (3)
Ge	Not observed	3.3±1.6	*~0*
Sb	Sb/SbH$_x$ observed	>240±5	2.2±1
Te	Te/TeH$_x$ observed	>240±5	> 4.5±1
GST	n/a	32.7±1.6	*0**

To study the etching of GST using H_2 plasma, the GST film was first subjected to an Ar pre-clean, and the cleaned Ar surfaced was exposed to the downstream H_2 plasma. The corresponding XPS spectra are shown in Figure 5-6. The XPS spectra of the as-received GST shows considerable oxidation of the Ge and Sb and noticeably Te was primarily metallic. After the Ar pre-clean, the Ge, Sb, and Te oxides were largely removed, and the resulting composition Ge:Sb:Te=1:1:2.4 was closer to that of the sputtering target ($Ge_1Sb_1Te_{2.5}$). There were still O content remaining, likely due to some carbon originating from the sample surface and holder.

The chemical composition of the surface changed significantly after the hydrogen plasma etch. The composition was determined to be depleted in both Sb and Te relative to Ge (Ge:Sb:Te=1:0.8:1.6). The oxygen content after the H_2 etch was minimal (3%), while the carbon content has increased from 21% to 29%. This believed to be due to the decrease in the oxygen content of the film, which causes the percentage of the other elements to increase to compensate, rather than contamination by a carbon source in the chamber. The etch rate for GST in the downstream H_2 plasma was determined to be approximately 1.7 nm/min. This was faster than the slowest etching element, Ge, and slower than the two faster etching elements, Sb and Te. However, it was also too small compared to the error of the SEM measurement and could be considered negligible.

This did not follow the trend suggested by the boiling points of GeH_4, SbH_3, and TeH_2, which would have predicted that Ge should be the most easily removed, followed by Sb, then Te. This does, however, follow the trend of the experimentally measured etch rates of Ge, Sb, and Te thin films in this same downstream H_2 setup. To compare the etch rate with the change in GST composition, the following analysis was carried out and shown in Figure 5-7. The change in

composition after the hydrogen etching Ge:Sb:Te=1:0.8:1.6 (compared to that after Ar sputtering

Ge:Sb:Te=1:1.0:2.4) was defined as (0.8-1.0)/1.0=-20% for Sb and (1.6-2.4)/2.4=-33% for Te.
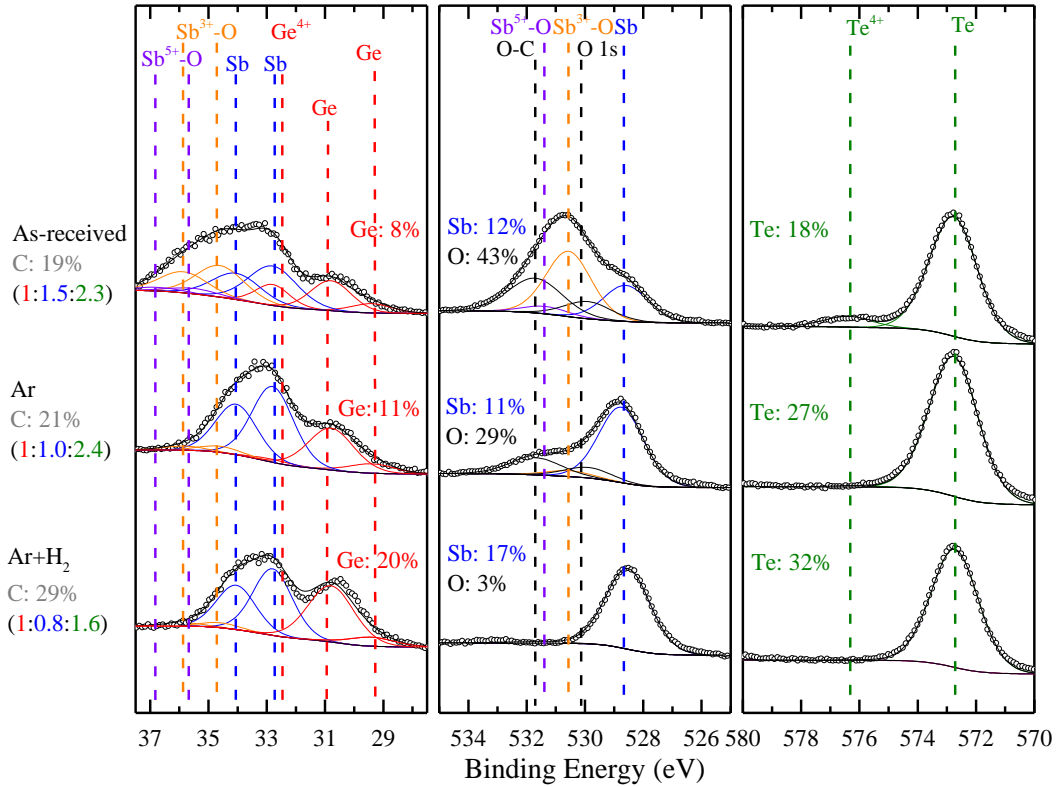
Figure 5-6. XPS spectra of a GST film as-received, a GST film after exposure to downstream Ar plasma beam, resulting in a film relatively free of GST oxides, and a GST film after a downstream Ar plasma beam clean followed by a downstream H_2 plasma exposure. Both the Ar and H_2 processes were carried out at baseline conditions for 5 minutes. The H_2 process resulted in depletion of Sb and Te and only metallic Ge, Sb, and Te were detected on the post-H_2 surface.
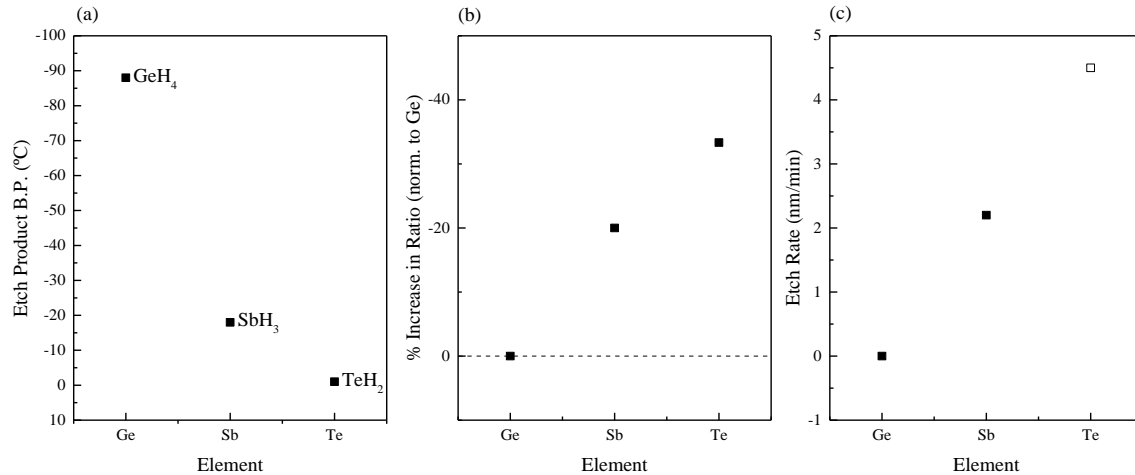
Figure 5-7. (a) Ge-H, Sb-H, Te-H etch product boiling points by element. (b) Change in composition ratio for each element in GST after etching in H_2/Ar plasma, determined from XPS quantification. (c) Ratio of the etch rate of each element in H_2/Ar normalized against the etch rate of Ge in downstream H_2/Ar plasma. The change in composition ratio in GST after etching H_2/Ar plasma did not follow the order predicted by the boiling points of each element's etch products (Te > Sb > Ge was observed, compared to the predicted Ge > Sb > Te). The observed order was also followed by the etch rates of Ge, Sb, and Te in the same plasma. Faster etching elements became depleted in the ternary compound. Ge was not observed to etch in H_2/Ar plasma, and the Te etch rate, represented with an open square, is a lower bound estimate and may be higher.

From the data presented in Table 5-1 and Figure 5-7, it can be concluded that the preferential removal of Ge, Sb, and Te from GST etched in H_2 plasma followed the order set by the etch rates of each individual element (Te > Sb > Ge) instead of the order suggested by the boiling points of the etch products (Ge > Sb > Te). The low boiling points of GeH_4, SbH_3, and TeH_2 etch products suggested that the desorption of GST-hydrogen etch products occurred readily, which was reported in literature to be the case for NH_3 plasma etching of GST (Park 2016). A thermally programmed desorption study reported that the desorption energy of TeH_2 from Te surfaces dosed with atomic hydrogen requires very little energy (0.10 eV) (Outka 1990), which could be further evidence that the desorption of etch products is not a limiting step. The change in composition due to H_2 plasma was suggested to be due to the reactions of Ge, Sb, and Te with H_2

plasma rather than desorption of the etch product from the surface, so it was concluded that the etching of GST by H_2 plasma could be kinetically-limited.

Another factor for the enhanced depletion of Te from the film could be due to the use of the Ar pre-clean step. While this was intended to remove the oxidized layer of GST that formed after the sputter deposition of the GST film and give a consistent GST oxide-free starting surface for the H_2 etch experiments, the Ar ion bombardment may have altered the bonding within the GST surface. While crystalline GST is commonly held to be a rock-salt type structure with one sub-lattice composed of Te and the other sub-lattice composed of Ge, Sb, and vacancies, with only Ge-Te and Sb-Te bonding existing (Yamada 1996), the films used in this work were amorphous GST. Amorphous GST may exhibit both tetrahedral and octahedral sites (Caravati, S. 2007) and the other four types of bonds between Ge, Sb, and Te (Ge-Ge, Ge-Sb, Sb-Sb, and Te-Te, bond energies summarized in Table 3-1), which are sometimes referred to as "wrong bonds" (Massobrio 2015). Work done by demonstrated that the use of ion bombardment (Sb and Xe ions) of amorphous GST surfaces reduced the Raman spectroscopy signal associated with $GeTe_4$ tetrahedral bonding, indicating that the Ge-Te bonds, despite having the highest bond energy among possible bonds between Ge, Sb, and Te, were preferentially broken (De Bastiani 2008). If a similar effect occurred in the GST films studied in this work due to Ar ion bombardment, this may have promoted the reaction of Te with H_2 and thus enhanced the depletion of Te in the H_2-etched GST film. It seemed unlikely that H_2 molecules or H atoms would have also contributed to this effect given how the low mass of these particles relative to Ar or Xe.
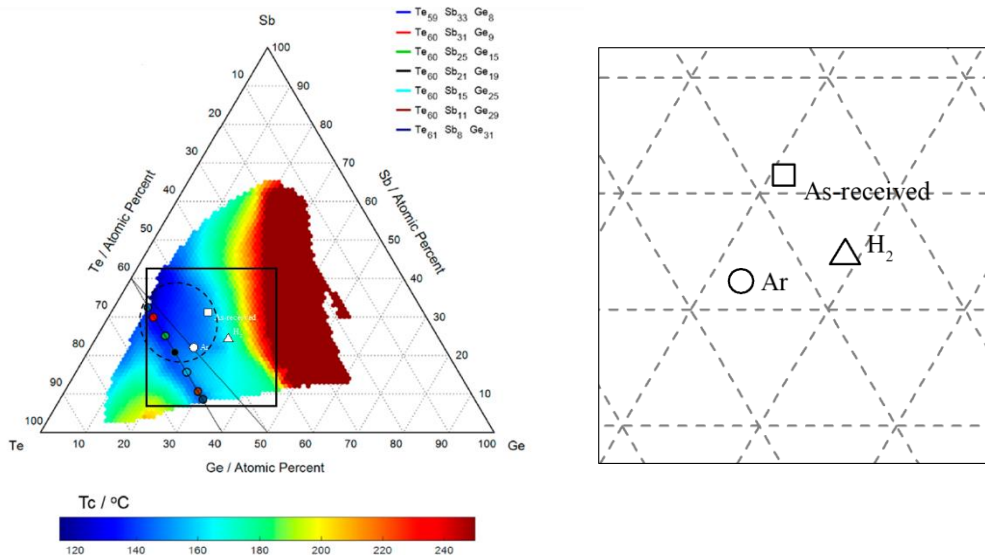
Figure 5-8. Crystallization temperature map of Ge-Sb-Te system (Guerin 2017). GST compositions as-received (□), after Ar plasma cleaning (○), and after Ar plasma cleaning followed by H₂ (△) plasma etching are shown. H₂ caused enough change in composition to leave the minimum crystallization temperature region marked with the dashed circle. The distribution of these composition is expanded and shown on the right.
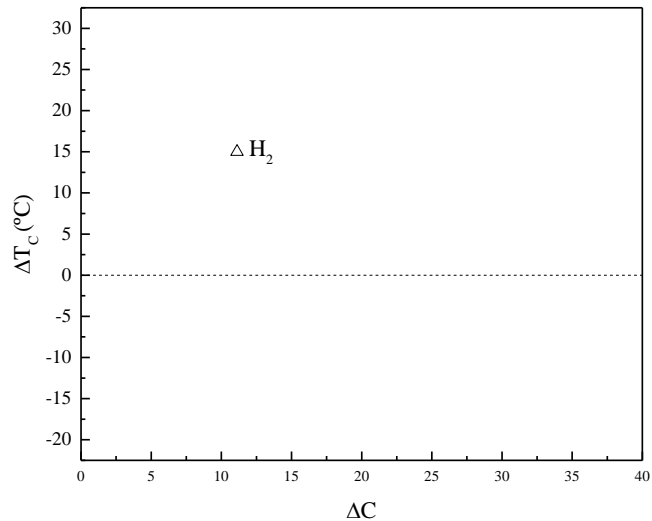
Figure 5-9. The change in crystallization temperature (ΔT_c) versus the composition change (ΔC) for the etch processes shown in Figure 5-8. H₂ resulted in a moderate change in composition (ΔC=11). However, the composition fell outside the minimum crystallization temperature region (ΔT_c=15°C).

The etching of GST using hydrogen plasma was demonstrated and studied. Thermodynamic analysis of the reactions of Ge, Sb, and Te with atomic hydrogen and the volatility of the etch products had suggested that these reactions would be thermodynamically favorable and that the etch products should be quite volatile, especially compared to the more commonly studied GST-halogen etch products (Table 2.8). The reactivity of each element in GST to the hydrogen plasma was then assessed by exposing a Ge wafer and Sb and Te targets directly to the H_2 plasma. SbH_x and TeH_x products were detected by QMS, but GeH_x etch products were not readily detected, although Ge was shown to etch in other experiments using OES and by measurement of its etch rate in H_2 plasma. When Ge, Sb, and Te thin films were exposed to downstream H_2 plasma (Table 5-1), Sb and Te were found to etch more rapidly than Ge, with Te being etched the fastest. From these studies, it was concluded that Ge was the least reactive to H_2 plasma, Te was the most reactive to the H_2 plasma, and Sb fell somewhere in-between. The etch rate of the GST in the direct H_2 plasma was measured to be 32.7 nm/min., demonstrating that H_2 plasma can be used to pattern GST, and a downstream H_2 plasma etch of GST and subsequent *in-situ* XPS found that the post-etch surface of GST was depleted of Sb and Te and enriched in Ge, with Te being relatively more depleted than Sb. Normalized to the Ge content, the Sb was depleted by 20% after the H_2 plasma etch, while the Te was depleted by 33%. This was concluded to be due to the reactivity of each element to the H_2 plasma rather than the volatility of the GST-hydrogen etch products, which had predicted that Ge should have been depleted. This finding indicated that the effects of the H_2 plasma etch of GST on stoichiometry could not be predicted by etch product volatility. On the other hand, the effects of the H_2 plasma etch of GST on stoichiometry could be predicted by the etch rates of Ge, Sb, and Te, which indicated the H_2 plasma etch of GST could be kinetically-limited, in contrast to the halogen-based plasma etching of GST. In addition, while hydrogen

plasma resulted Ge enrichment and Sb and Te depletion, which would be expected to have a negative impact on maintaining crystallization temperature (as shown in Figure 5-8 and Figure 5-9), hydrogen plasma had an advantage over halogen plasmas in that hydrogen plasma etched-GST presented only metallic states of Ge, Sb and Te.

Chapter 6 Etching of Ge, Sb, Te and GST by CH_4-based Plasmas

The downstream CH_4, CH_4/Ar, and CH_4/N_2 plasmas without extraction bias or grid were used to etch Ge, Sb, and Te thin films. Ge was inert to etching by these plasmas, while Te was etched by CH_4 and CH_4/Ar plasmas but not CH_4/N_2, and deposition was observed on Sb after all three plasmas. On the ternary GST film, the CH_4 plasma resulted in an etch rate of 16.8 nm/min. and in enrichment of Ge and depletion of Sb and Te, which did not follow the order given by the etch product boiling points. This preferential removal was also observed after etching by CH_4/Ar and CH_4/N_2 plasma, although the preferential removal was more pronounced after CH_4/Ar and less pronounced after CH_4/N_2. The addition of Ar to CH_4 plasma led to greater cracking of the CH_4, resulting in C deposition on the GST. The addition of N_2 to CH_4 plasma led to the formation of HCN and NH_x, which reduced the etch rate to 8.4 nm/min., likely due to the dilution of CH_4 and scavenging of atomic H. All CH_4 plasmas resulted in increased C content on the surface. Some N content was also observed after CH_4/N_2 (7% N), but nitridation of Ge, Sb, or Te was not observed. Among the CH_4-containing plasmas, CH_4/Ar plasma resulted in the largest changes in composition and crystallization temperature, while CH_4/N_2 plasma resulted in the smallest changes.

GST samples etched in CH_4/Ar were exposed to atmosphere, and it was found that Ge and Sb began to reoxidize after 10 min. in ambient conditions, while the reoxidation of Te was stalled for at least 60 min, thus showing that the C-H layer could passivate the GST surface and stall reoxidation.

6.1 CH_4 Plasma Etch of Ge, Sb, Te, and GeSbTe

A modified experimental setup was used, where the extraction ring and grid were removed to prevent clogging from C deposition while the sample was still held in the bottom chamber for *in-situ* XPS. Ge, Sb, and Te samples were etched in CH_4, CH_4/Ar and CH_4/N_2 plasmas at baseline conditions with no bias or grid for 1 min. The determined etch rates and their associated cross-section SEM were shown in Table 6-1 and Figure 6-1, respectively.

Table 6-1. Summary of etch rates of Ge, Sb, and Te thin films in CH_4, CH_4/Ar, and CH_4/N_2 plasma at baseline conditions with no bias. Etch rates that are too slow to be conclusively considered etching (i.e., smaller than or close to error) are considered zero and italicized. Negative values indicate that deposition was observed.

Etch Rate (nm/min.)	CH_4	CH_4/Ar	CH_4/N_2
Ge	5.6±5	*0*	*0*
Sb	-14.1±5	-11.3±5	-8.5±5
Te	14±5	8.4±5	*~0*

It was found that Ge etched slowly in CH_4 plasma at a rate of 5.6 nm/min. A Ge etch rate of 2.8 nm/min. was measured for both CH_4/Ar and CH_4/N_2 plasma, but this was smaller than the uncertainty in the measurement, so it was not conclusive whether Ge etched in these plasmas or not. Te was observed to etch in both CH_4 and CH_4/Ar plasmas but was not observed to etch in CH_4/N_2 plasma. On the other hand, Sb samples all appeared to become thicker after etching, suggesting that either deposition had occurred. XPS was not available for these samples due to the small physical size of the samples. The trends in etch rate of Ge, Sb, and Te suggested that Ge should be enriched after etching in CH_4, CH_4/Ar and CH_4/N_2 plasmas while Te should be depleted. Sb might also be expected to enrich if it was not etched by the CH_4, CH_4/Ar and CH_4/N_2 plasmas.
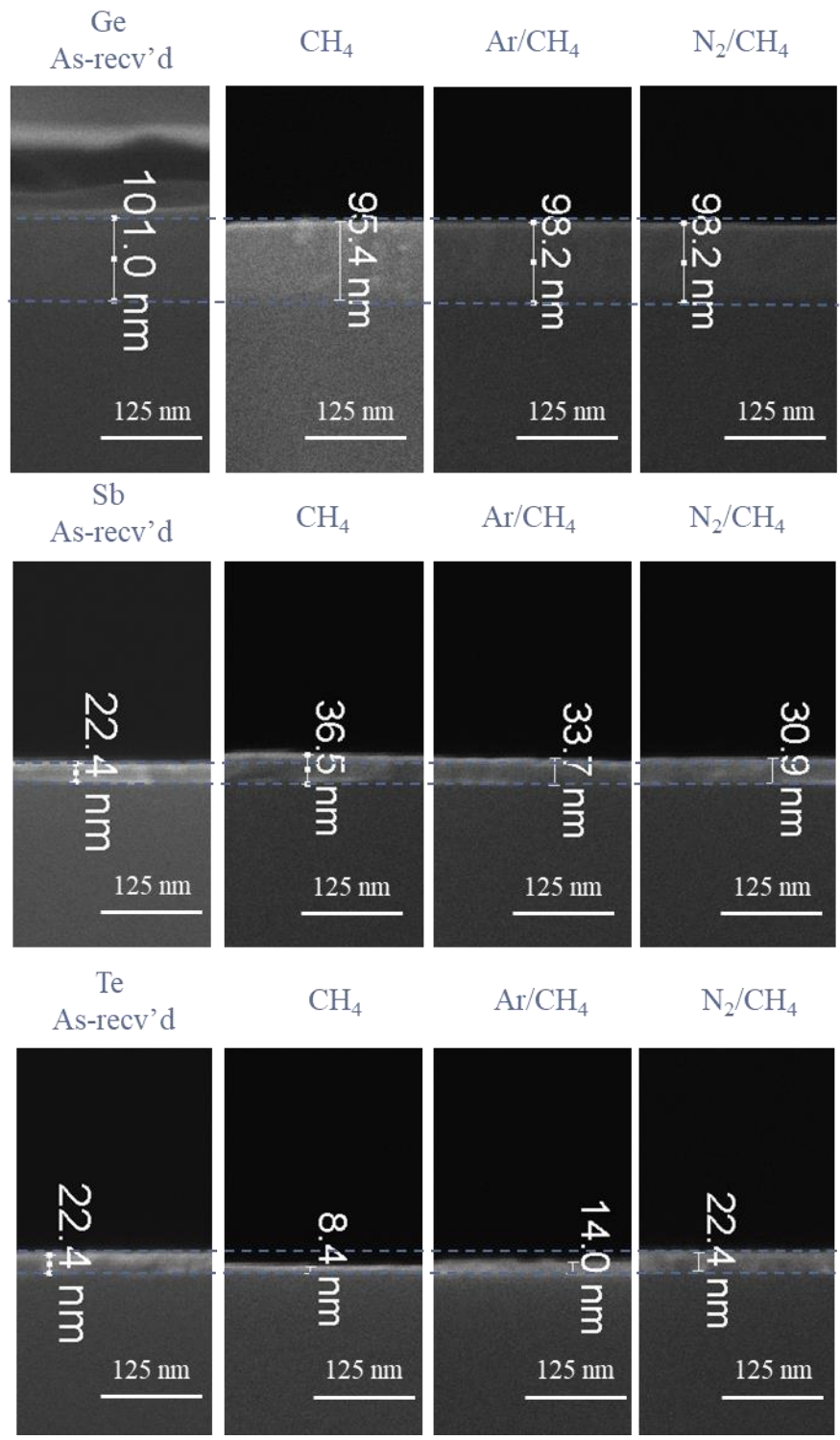
Figure 6-1. SEM of Ge, Sb, and Te as-received and after downstream etching in CH₄, CH₄/Ar, and CH₄/N₂ at baseline conditions for 1 min. with no extraction grid or bias

For the etching of GST samples, the ion beam was used to clean oxides from the GST since the downstream Ar process could not be used without the extraction ring and grid. The GST samples were cleaned with a 200V ion beam for 1 min., resulting in a Te-depleted Ge:Sb:Te composition of 1:1.0:1.6 with minimal O (3% O). C was still present on the surface (33% C). The ion beam-cleaned samples were then exposed to Ar, N_2, CH_4, CH_4/Ar and CH_4/N_2 plasmas at baseline conditions for 1 min. The CH_4/Ar and CH_4/N_2 plasmas were both approximately 50:50 in feed composition. With no extraction bias or grid installed, the plasma was simply allowed to emanate-from the top chamber of the ICP system to the bottom chamber.
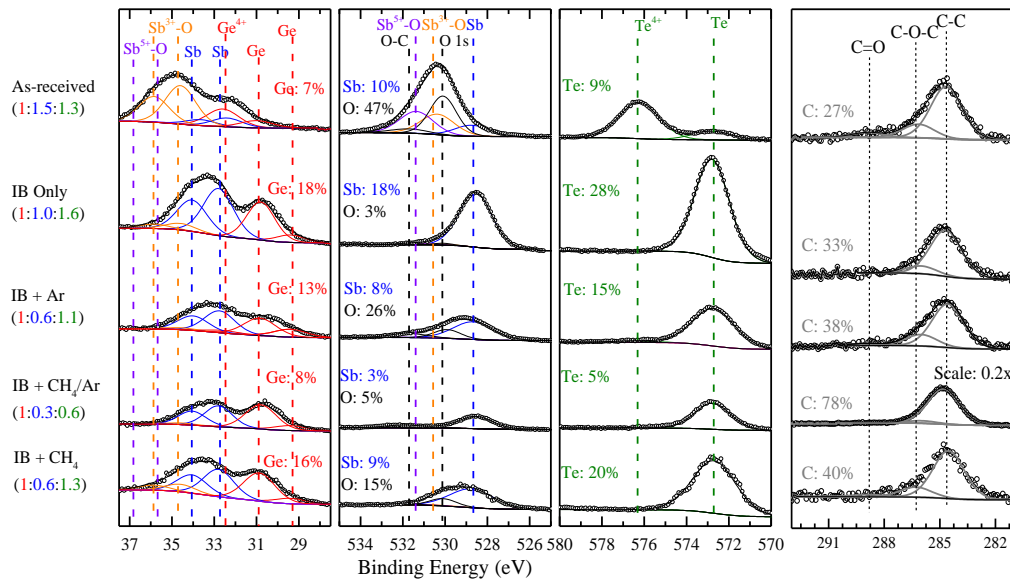
Figure 6-2. XPS of GST processed in bottom chamber with no extraction bias or gridded orifice. The GST samples were cleaned with an Ar ion beam sputter (200V/1min.), then exposed to the downstream plasma (upper chamber conditions: 500W/15mTorr/1min.).

Figure 6-2 shows the XPS of the GST sample as-received, after ion beam cleaning, and after ion beam cleaning followed by Ar, CH_4/Ar or CH_4 plasma. All tested chemistries show depletion of Sb and Te, with the CH_4/Ar plasma showing the most thorough depletion of Sb and Te, going from Ge:Sb:Te of 1:1.0:1.6 to 1:0.3:0.6, which was a 70% decrease in Sb content and a 63% decrease in Te content, normalized to Ge ratio. The Ar plasma was not expected to result in

appreciable sputtering since there was no bias applied and self-bias alone should have been on the order of 10-20V. The change in composition after the Ar plasma was attributed to oxygen contamination, either in the Ar feed itself or from the gas line, which was shared with O_2. The CH_4 plasma alone demonstrated less depletion of Sb and Te, going from 1:1.0:1.6 to 1:0.6:1.3 instead. Both CH_4/Ar and CH_4 deposited C (78% and 40%, respectively) on the etched GST. The C content after CH_4/Ar plasma was particularly high and may present a challenge in process integration if the C must be removed post-etch. The changes in Ge, Sb, and Te content were summarized in Figure 6-3.
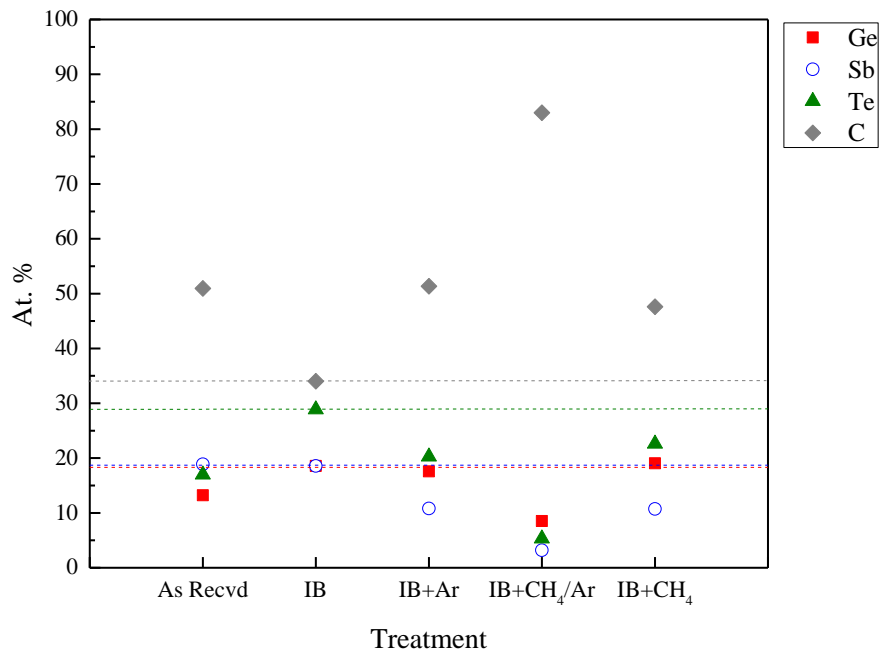
Figure 6-3. Atomic percentages of Ge, Sb, and Te determined from XPS for GST thin films as-received and processed GST films. The GST samples were cleaned with an Ar ion beam sputter (200V/1min.), then exposed to the downstream plasma (upper chamber conditions: 500W/15mTorr/1min.) Ar, $50CH_4/50Ar$, and CH_4 plasma, as determined by in-situ XPS analysis. Guidelines denote the composition of the ion beam cleaned samples, to which the processed samples should be compared. The CH_4/Ar plasma resulted in greater depletion of Sb and Te and enrichment of Ge than either CH_4 or Ar alone.

Figure 6-4 shows the XPS of the GST sample as-received, after ion beam cleaning, and after ion beam cleaning followed by N_2, CH_4/N_2 or CH_4 plasma. As with the CH_4/Ar plasma, depletion of Sb and Te was also observed after CH_4/N_2 plasma. However, the depletion of Sb and Te was reduced compared to the CH_4/Ar plasma, and the deposition of C was not excessive (33% C). Nitrogen was detected on the surface after N_2 plasma and CH_4/N_2 plasmas (7% each), but GST-nitrides were not observed on the surface after either treatment. As such, all N on the surface was considered to be bonded to C. The changes in Ge, Sb, and Te content were summarized in Figure 6-5.
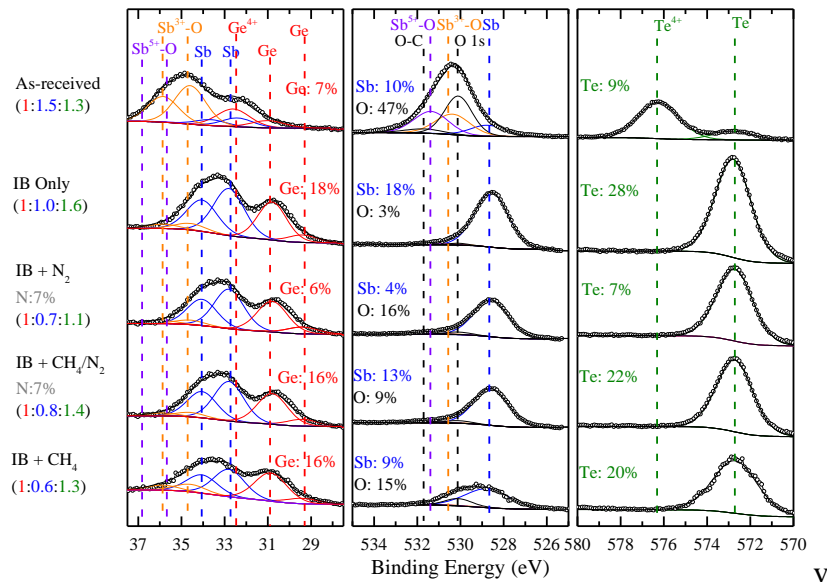
Figure 6-4. XPS of GST samples cleaned with an Ar ion beam sputter (200V/1min.), then exposed to the downstream N_2, CH_4 and CH_4/N_2 plasmas at baseline conditions for 1 min. No prominent Ge x+, Sb x+, or Te x+ peaks appear after N_2 or CH_4/N_2, so it was concluded that no nitridation of the GST had occurred.

The etch rates of the samples in CH_4, CH_4/Ar, and CH_4/N_2 plasmas were determined to be 16.8 nm/min. and 8.4 nm/min. for CH_4 and CH_4/N_2, respectively. The CH_4/Ar -exposed sample was determined to have deposition on the surface, at a rate of 28.1 nm/min. The cross-section SEM for these samples is shown in Figure 6-6
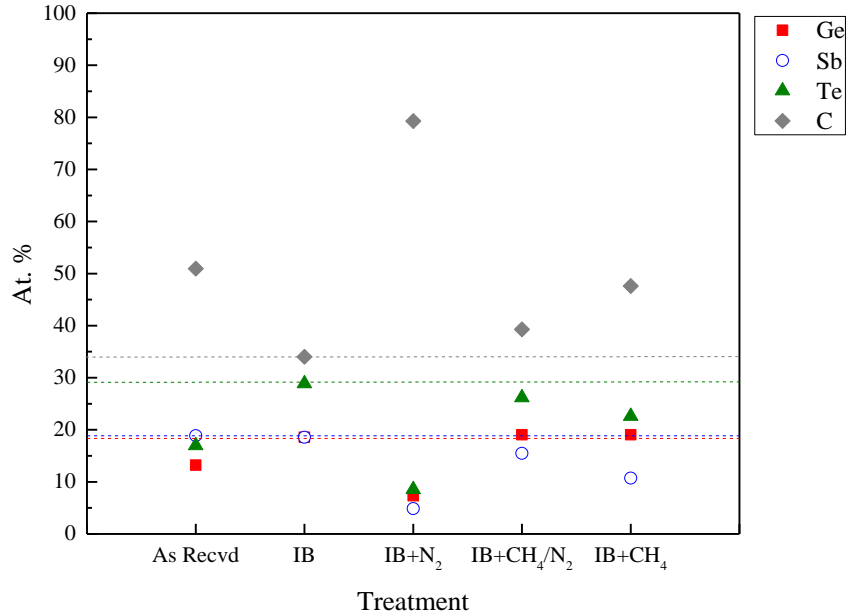
Figure 6-5. Atomic percentages of Ge, Sb, and Te determined from XPS for GST thin films as-received and processed GST films. The GST samples were cleaned with an Ar ion beam sputter (200V/1min.), then exposed to the downstream N_2, $50CH_4/50N_2$, and CH_4 plasmas at baseline conditions, as determined by in-situ XPS analysis. Guidelines denote the composition of the ion beam cleaned samples, to which the processed samples should be compared. The CH_4/N_2 plasma resulted in less enrichment of Ge and depletion of Sb and Te than the N_2 or CH_4 plasmas alone.
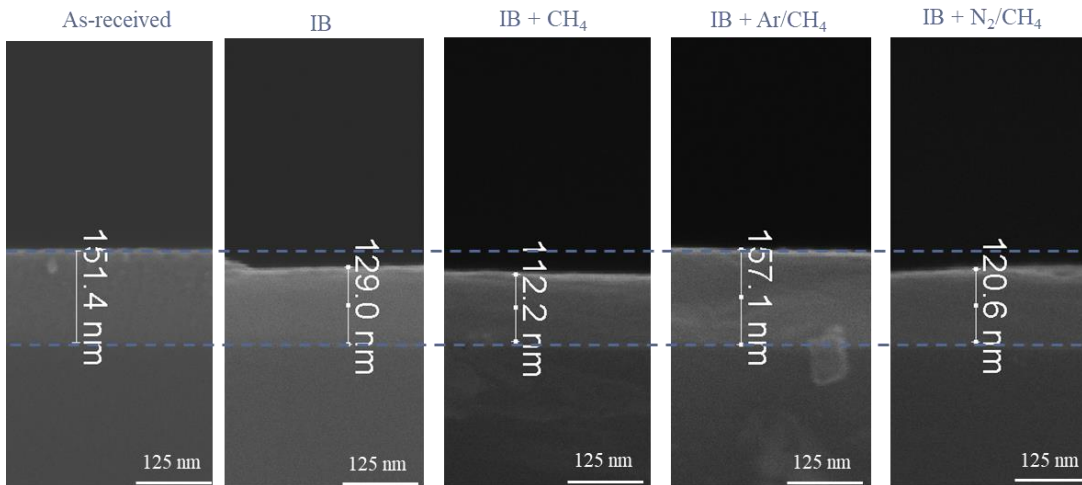
Figure 6-6. Cross-section SEM of GST as-received, after IB clean (200V/1min.), followed by exposure to CH_4, CH_4/Ar, and CH_4/N_2 plasma at baseline conditions with no extraction grid or bias for 1 min.

From these experiments, it was determined that CH_4 and CH_4/N_2 could be used to etch GST, while CH_4/Ar resulted in the deposition of C on the GST surface. All samples showed depletion of Sb and Te and enrichment of Ge, which was similar to the trend observed for H_2 plasma in Chapter 5 but opposite to the etch product boiling points analyzed in Section 2.1. The preferential removal was partially explained by the etching of the Ge, Sb, and Te samples. Ge was found to etch slowly in CH_4 and was not concluded to etch in CH_4/Ar or CH_4/N_2, so it would be expected to be enriched in the etched GST film. Te was found to etch faster than Ge in CH_4 and CH_4/Ar plasmas, so depletion in the GST film could be expected. This may have been true for CH_4/N_2, but the etch rates of Ge and Te were too slow to be conclusively quantified. The Sb thin films appeared to have deposition on them but were depleted in the GST films, and in this case the etching or deposition on the elemental film was not predictive of the enrichment or depletion of that element in GST.
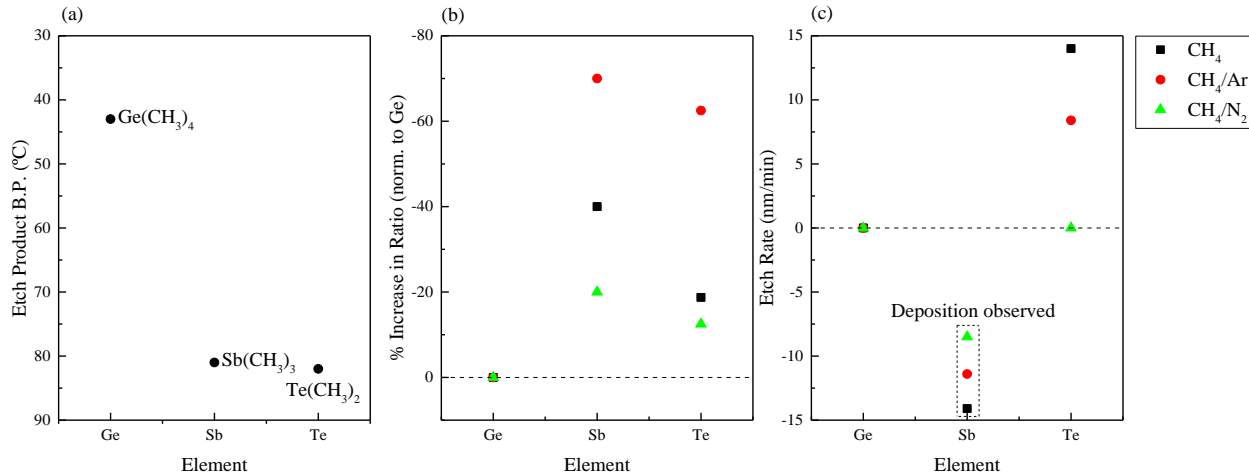
Figure 6-7. (a) Ge-CH₃, Sb-CH₃, Te-CH₃ etch product boiling points by element. (b) Change in composition ratio for each element in GST after etching in CH_4, CH_4/Ar, and CH_4/N_2 plasmas, determined from XPS quantification. (c) Etch rate of each element in CH_4, CH_4/Ar, and $CH_4/$. The change in composition ratio in GST after etching any plasma did not follow the order predicted by the boiling points of each element's etch products (Te > Sb > Ge was observed, compared to the predicted Ge > Sb > Te). The observed order was partially followed by the etch rates of Ge, Sb, and Te in the same plasmas. Faster etching elements became depleted in the ternary compound.

Figure 6-7 summarized the changes in composition ratio after CH_4, CH_4/Ar, and CH_4/N_2 plasma etching of GST. The boiling points of the Ge, Sb, and Te etch products, shown in Figure 6-7(a), suggested preferential removal of Ge, Sb and Te in the order of Ge > Sb > Te. However, enrichment of Ge and depletion of Sb and Te was observed after etching with all three plasmas, resulting in preferential removal in the order of Sb > Te > Ge, as shown in Figure 6-7(b). CH_4/Ar resulted in the greatest amount of Sb and Te depletion and C deposition. It was shown in Section 2.4.4.4 that the addition of Ar promoted further cracking of the CH_4, which could make more atomic H available for reaction and thus lead to greater depletion of Sb and Te. However, OES data suggested that the dilution of the CH_4 with Ar resulted in less atomic H being present, and the cross-section SEM showed that there was significant deposition on this sample. While the Ge, Sb, and Te signals were still readily observed by XPS, the C content was very high (78% C), and the

SEM data suggested that the deposited C layer was so thick that the XPS was no longer analyzing the GST surface. It may be that the surface was majority C but with Ge, Sb, and Te embedded within it.

The CH$_4$/N$_2$ etch resulted in the smallest amount of Sb and Te depletion of the chemistries tested in this chapter, suggesting that it may be the most suitable for GST etch. While literature on the reactions of CN or NH$_x$ with GST was not available, the N present in the etched surface did not appear to be bonded to Ge, Sb, and Te, so any potential etch products may have been readily volatilized. It was also considered that CN and NH$_x$ may scavenge atomic H species, which could be the reason for the less significant depletion of Sb and Te that was observed.

The etch rates of the individual elements in the CH$_4$-containing plasmas partially explained the preferential removal of Ge, Sb, and Te. Ge was inert to etching and enriched in the ternary film after etching by all three plasmas, while Te was observed to etch in CH$_4$ and CH$_4$/Ar plasmas and depleted in the ternary film after etching by all three plasmas. It is speculated that Te would have etched in CH$_4$/N$_2$, but the rate was too slow to be captured in the tested time frame. Sb was observed to be depleted in the ternary film after etching by all three plasmas, but the Sb films were thicker after exposure to the plasma and an etch rate could not be determined. The etch rates of Ge and Te do suggest that the etching of GST by CH$_4$, CH$_4$/Ar, and CH$_4$/N$_2$ plasmas may be kinetically-limited rather than limited by the desorption of the etch products.

6.2 Passivation of the GST Surface by CH$_4$

The CH$_4$-containing plasmas studied in this work were all noted to result in the deposition of C on the surface of the etched plasma, and it was considered possible that the C-H layer could protect or passivate the GST layer from ambient oxidation.

To test whether the GST could be passivated by the C-H layer, a sample of GST was directly exposed to a 10:90 CH_4/Ar plasma at baseline conditions. The CH_4/N_2 plasma was not tested due to concerns about the toxicity of CN and NH_x species. The exposed samples were then left in ambient conditions for 1, 10 and 60 min., and the XPS of these samples is shown in Figure 6-8. It was found that the C-H layer could stall the reoxidation of the sample as a whole, since only 15% O was detected on the surface after 60 min. Ge and Sb were observed to begin reoxidizing after 10 min. in ambient conditions, while Te was not observed to reoxidize until 60 min. in ambient conditions, although Te is also slower to reoxidize due to the smaller Gibbs energy of formation of its oxide. As such, the C-H layer could be considered to be a beneficial side-effect of the etch process that could passivate the GST layer for 10 min. to stall Ge and Sb reoxidation.
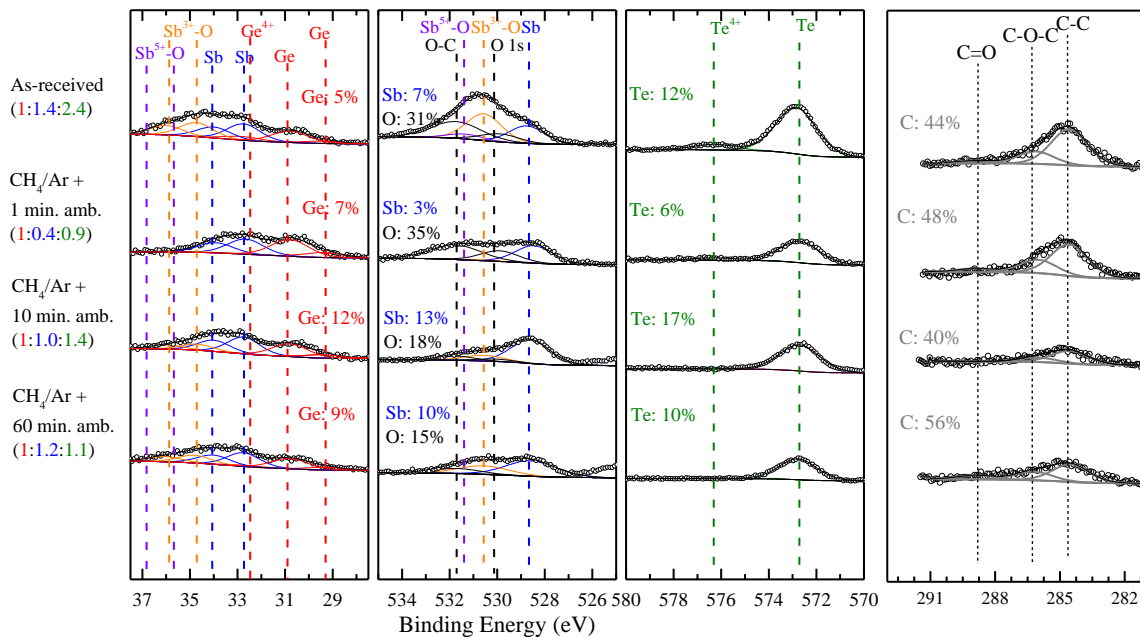
Figure 6-8. XPS of GST after processing by direct exposure to 10:90 CH_4/Ar plasma at baseline conditions followed by 1, 10, and 60 min. ambient exposure. Ge and Sb reoxidation were observed after 10 min. ambient exposure.

The use of CH_4 and CH_4-containing plasmas to etch GST was studied. Etching of Ge, Sb, and Te samples with CH_4, CH_4/Ar, and CH_4/N_2 plasma showed that Ge was relatively inert to all three plasmas, while Te did demonstrate etching in CH_4 and CH_4/Ar plasmas (14 and 8.4 nm/min.,

respectively) but not in CH_4/N_2. Sb thin films appeared to be ~10 nm thicker after treatment by any CH_4 plasma. The results of etching on Ge, Sb, and Te were used to suggest what might occur on GST samples, and it was predicted that Ge would enrich while Te would deplete.

The effects of the CH_4, CH_4/Ar, and CH_4/N_2 plasmas on ion beam-cleaned GST were also studied, and it was found that Ge was enriched while Sb and Te were depleted in all three plasmas, which was similar to the effect of H_2 plasma shown in Chapter 5. It also followed the prediction made for Ge and Te based on the etching of the Ge and Te thin films. After the CH_4 plasma, the Ge:Sb:Te ratio changed from 1:1.0:1.6 to 1:0.6:1.3. The CH_4/Ar plasma showed a greater depletion of Sb and Te (1:1.0:1.6 to 1:0.3:0.6), while CH_4/N_2 showed reduced depletion of Sb and Te (1:1.0:1.6 to 1:0.8:1.4), and these compositions are shown in Figure 6-9. Despite the moderate changes in composition after CH_4 and CH_4/N_2, there were still large changes to crystallization temperature, as shown in Figure 6-10. All CH_4 plasmas also demonstrated increasing C content on the surface (from 33% to 40%, 78%, and 33% for CH_4, CH_4/Ar, and CH_4/N_2, respectively). Some N content was also observed after CH_4/N_2 (7% N), but nitridation of the GST was not observed. CH_4 and CH_4/N_2 plasmas were shown to etch GST at 16.8 nm/min. and 8.4 nm/min., respectively. The CH_4/Ar-exposed sample was determined to have deposition on the surface, at a rate of 28.1 nm/min.
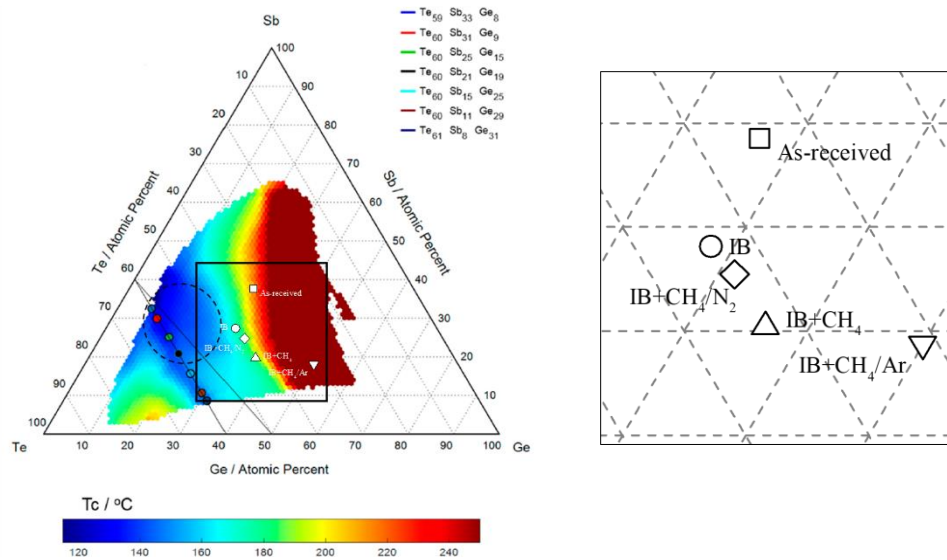
Figure 6-9. Crystallization temperature map of Ge-Sb-Te system (Guerin 2017). GST compositions of ion beam-cleaned (○), CH_4 (△), CH_4/Ar (▽) and CH_4/N_2 (◇) plasma etched samples are also shown, in comparison to the starting composition (□). CH_4/Ar resulted in the greatest changes to composition and crystallization temperature while CH_4/N_2 resulted in the smallest changes. The distribution of these composition is expanded and shown on the right. None of the compositions, including the ion beam sputtered composition, fall within the minimum crystallization temperature region.
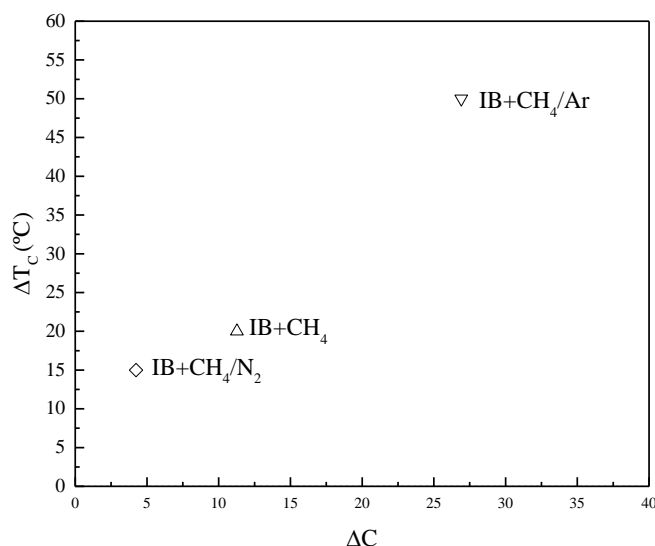
Figure 6-10. The change in crystallization temperature (ΔT_c) versus the composition change (ΔC) for the etch processes shown in Figure 6-9. CH_4 and CH_4/N_2 resulted in large changes to crystallization temperature despite only resulting in moderate changes to composition. CH_4/Ar resulted in significant changes to both composition and crystallization temperature.

The increased depletion of Sb and Te after CH_4/Ar plasma could be due to increased cracking of the CH_4 as a result of adding Ar, which would increase the amount of H available for reaction, and H had been shown to deplete Sb and Te in Chapter 5. However, OES data suggested that there would be less H present due to the dilution of CH_4 with Ar, and XPS and SEM data suggested that CH_4/Ar plasma resulted in C deposition on the surface that was thick enough that the XPS was no longer measuring GST. Meanwhile, while there were no literature reports on possible reactions of GST with CN species, the presence of CN or NH_x could scavenge free atomic H in the plasma and reduce the amount of H available for reaction, which could help prevent depletion of Sb and Te due to reaction with H. The depletion of Sb and Te by CH_4-based plasmas did match the order of the boiling points of the GST-CH_3 etch products. Since there was some agreement between Ge and Te etch rates and Ge enrichment and Te depletion in the CH_4 and

CH_4/Ar plasmas, it was concluded that the etching of GST by CH_4-based plasmas might be kinetically-limited.

It was concluded that CH_4/N_2 maintained the GST ratio best out of the tested chemistries but also resulted in the deposition of a C-H-N layer. A GST sample etched in CH_4/Ar was exposed to atmosphere, and it was found that Ge and Sb began to reoxidize after 1 min. in ambient conditions, while the reoxidation of Te was stalled for at least 10 min. It was determined that the C-H layer provided only limited protection from ambient exposure.

Chapter 7 Summary

The development of next-generation memory devices requires the use of complex material system. Phase-change random access memory relies on a phase-change material, GST, for its ability to change between crystalline and amorphous phases. However, these phase-change properties are sensitive to the composition of GST, and if the composition is not controlled, the fabricated device could fail to operate. GST composition is known to be altered during etching by halogen plasmas and wet cleaning and other processes that may or may not be avoidable during the manufacture of a phase-change memory device.

Study of the ambient oxidation of GST showed that it was most sensitive to the presence of water vapor in ambient conditions. The wet cleaning of GST using DI water, isopropyl alcohol, citric acid, and ammonium hydroxide showed that the as-received GST was susceptible to changes in oxidation of Ge, Sb, and Te. This was thought to be due to the polarity of the solutions and the presence of GST-oxides on as-received GST. The polar metal-O bonds might be more susceptible to interactions with polar solutions like citric acid and less susceptible to non-polar solutions like isopropyl alcohol. Cleaning the GST oxides from the surface and studying the effects of the wet cleans on sputter-cleaned GST showed that, while the same trends in Ge and Te enrichment and Sb depletion were observed, citric acid and ammonium hydroxide caused less change in composition, due to the lack of GST-oxides on the sputter-cleaned GST. Overall, the GST wet cleans were shown to be strongly influenced by the presence of GST-oxides. Studies of the plasma etching of GST would be done on sputter-cleaned surfaces to avoid the effects of GST-oxides.

Various plasma etch chemistries were studied on cleaned GST, as well as the individual elemental thin films Ge, Sb, and Te, and these are summarized in Table 7-1. The effects of the plasma etch chemistries and the wet cleans are summarized qualitatively in Table 7-2.

148

Table 7-1. Table of etch rates (ER) of Ge, Sb, Te, and GST in tested plasma chemistries, along with normalized change in % Sb and % Te and % halogen and % carbon in the etched films. Results that would disqualify or potentially disqualify the use of an etch chemistry for GST, such as excessive halogenation or change in composition are underlined. Results that suggest that a chemistry is suitable for etching GST are bolded. Etch rates that are too slow to be conclusively considered etching (i.e., smaller than or close to error) are given as 0 and italicized. * indicates that the film was cleaned of oxides prior to etch. Negative values indicate that deposition was observed.

	Cl_2/Ar	SF_6/Ar	H_2	CH_4	CH_4/Ar	CH_4/N_2
GST ER (nm/min.)	13.1±1.6*	*0**	*0**	16.8±5*	-28.1±5*	8.4±5*
Ge ER (nm/min.)	33.8±10	15±1.6	*0*	*0*	*0*	*0*
Sb ER (nm/min.)	~0	~0	2.2±1	-14.1±5	-11.3±5	-8.5±5
Te ER (nm/min.)	~0	~0	>4.5±1	14±5	8.4±5	~0
Ge:Sb:Te before etch	1:1.0:2.4	1:1.0:2.4	1:1.0:2.4	1:1.0:1.6	1:1.0:1.6	1:1.0:1.6
Ge:Sb:Te after etch	1:1.1:9.4	1:1.3:2.5	1:0.8:1.6	1:0.6:1.3	1:0.3:0.6	1:0.8:1.4
% Sb Change	+10%	+30%	-20%	-40%	-70%	-20%
% Te Change	+292%	+2%	-33%	-19%	-62%	-12%
% Halogen or Carbon	10% Cl	57% F	29% C	40% C	78% C	33% C
ΔC (Eqn (2.4)	38.1	**5.2**	11.1	11.3	26.9	**4.2**
ΔT$_c$ (ºC)	**10**	**-5**	**15**	20	50	**15**

Table 7-2. Summary of the effects of each wet clean or plasma treatment on Ar-sputtered GST studied in this work and their preferential removal of Ge, Sb, and Te from GST.

Treatment	Effect on Ge	Effect on Sb	Effect on Te	Other Effects
DI water	Depletes	Depletes	Enriches	Ambient oxidation
Isopropyl alcohol	Depletes	Enriches	Depletes	Ambient oxidation
Citric acid	Depletes	Depletes	Enriches	Ambient oxidation
Ammonium hydroxide	Depletes	Depletes	Enriches	Ambient oxidation
Cl_2/Ar plasma	Depletes	Enriches	Enriches	Chlorination
SF_6/Ar plasma	Depletes	Enriches	Enriches	Fluorination
H_2 plasma	Enriches	Depletes	Depletes	
CH_4 plasma	Enriches	Depletes	Depletes	C deposition
CH_4/Ar plasma	Enriches	Depletes	Depletes	C deposition
CH_4/N_2 plasma	Enriches	Depletes	Depletes	C deposition

It was concluded in literature for GST-halogen etching that the preferential removal of Ge, Sb, and Te followed the trend set by the volatility of the etch products, as determined by boiling points of said etch products. In this work, studies of Ge, Sb, and Te thin films found that for the halogen chemistries, Ge was the most easily etched, while Sb and Te were not significantly etched by halogens. For H_2 plasma, the trend in preferential removal (Ge enriched, Sb and Te depleted) did not follow the etch product boiling point trend at all (it was, in fact, the opposite), but the preferential removal did follow the trend set by the etch rates of Ge, Sb, and Te in the H_2 plasma, where it was found that Ge etched slowest, followed by Sb and then by Te. For CH_4 and CH_4-containing plasmas, Ge was also enriched and Sb and Te were also depleted, which followed the observation that Ge was barely etched by CH_4 while Te was etched faster and Sb seemingly was deposited on by the CH_4 plasma. It can be observed from the reported etch rates reported in

Table 7-1 that if Sb or Te have an etch rate lower than Ge, they would be enriched in the etched GST film, as shown by the Cl_2/Ar and SF_6/Ar plasmas. It was also observed that if Sb or Te have an etch rate higher than Ge, they would be depleted in the etched GST film, as shown by the H_2 plasma. This was also observed to be the case for Te in the CH_4 and CH_4/Ar plasmas. On

the other hand, this trend did not hold if an etch rate could not be reported, either due to deposition, which was the case for Sb in all CH_4-containing plasmas, or the etch depth was too small to be determined by SEM therefore an etch rate cannot be reported, which was the case for CH_4/N_2 plasma. Overall, the use of the boiling point trend to predict preferential removal only held true for halogen chemistries and did not prove to be the case for H_2 or CH_4 plasmas. Instead, the etching of single element Ge, Sb, and Te films in the same plasma chemistries proved to be a more consistent predictor of preferential removal, despite the thinness of the samples preventing the pre-cleaning of the single element films and making SEM characterization difficult.

From

Table 7-1, the merits of each etch chemistry can now be evaluated. It was determined that both of the studied halogen chemistries (Cl_2/Ar and SF_6/Ar) depleted Ge and enriched Sb and Te in the GST film, with Cl_2/Ar resulting in unacceptably high enrichment of Te (+292%). Ar/SF_6 demonstrated more suitable enrichment of Sb and Te, but Sb enrichment was still high (+30%). Neither could be considered suitable due to the quantity of halogen species left on the surface after etching, and SF_6/Ar demonstrated negligible etching of GST. While H could not be detected by XPS, literature reports suggested that there would be little to no H in the film after etching with H_2 plasma, but the H_2 plasma etching was also considered to be detrimental to GST crystallization temperature due to the depletion of Sb and Te. The CH_4-containing plasmas also demonstrated depletion of Sb and Te, with CH_4/Ar resulting in severe depletion (-70% and -62% for Sb and Te, respectively), while CH_4/N_2 resulted in relatively less depletion (-20% and -12% for Sb and Te, respectively). This was considered to be the smallest overall change in composition of any of the chemistries studied so CH_4/N_2 could be considered to be the most suitable etch chemistry for GST from that perspective. Additionally, the use of composition change percentages alone as the metric

151

to evaluate how effective an etch chemistry is disregards other factors in the relationship between crystallization temperature and composition.

Looking back on Figure 1-5 (reproduced here as part of Figure 7-1), one can see that the targeted $Ge_2Sb_2Te_5$ composition was at a minimum for the crystallization temperature but lay at the edge of a region of the crystallization temperature map where the crystallization temperature began to rise quickly. This change in crystallization temperature versus the change in composition meant that the composition change alone could be misleading in assessing the effect of a particular etch process, as was discussed in Section 2.5. Based on the position of the targeted $Ge_2Sb_2Te_5$ composition, an ideal etching process can vary in terms of Te enrichment or depletion, but Ge depletion and Sb enrichment are both desirable. Both the halogen plasmas studied in this work meet these criteria, but they have their aforementioned drawbacks. Cl_2/Ar etching resulted in Ge depletion and Sb enrichment, but the Te enrichment was too great. The resulting composition was outside the edge of the reported temperature map, but appears to be within 40ºC of the minimum crystallization temperature (Guerin 2017). SF_6/Ar also met these criteria without any excessive enrichment or depletion of any one element, and the resulting composition after SF_6/Ar stays within the minimum T_C region. However, SF_6/Ar also resulted in severe halogenation of the GST film, which would lead to longer term reliability concern. Furthermore, the etching of GST by SF_6/Ar was negligible.
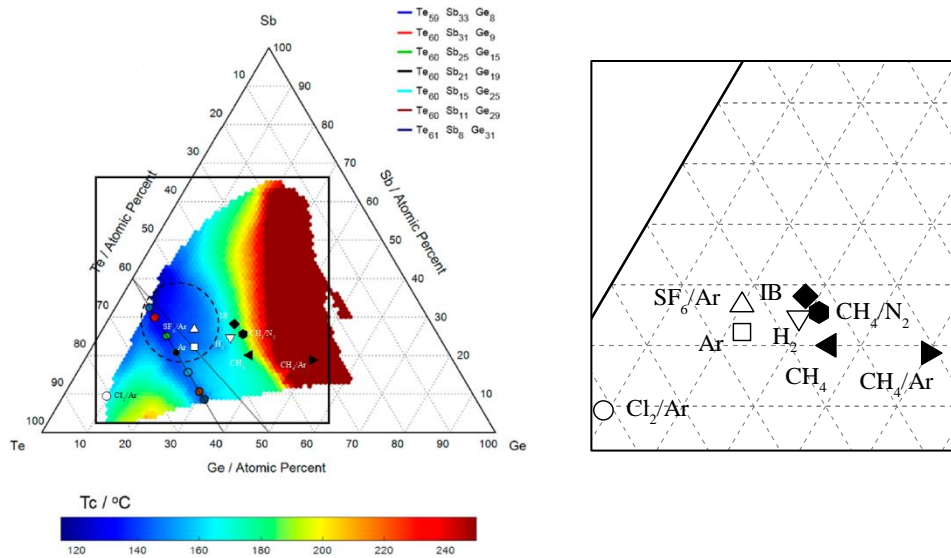
Figure 7-1. Crystallization temperature map of Ge-Sb-Te system (Guerin 2017). GST compositions of plasma-etched samples from

Table 7-1 are also shown, with only the composition of Ge, Sb, and Te considered. The Cl_2/Ar (○), SF_6/Ar (△), and H_2 (▽) etched compositions should be compared to the Ar sputtered composition (□), and the CH_4 (◄), CH_4/Ar (►), and CH_4/N_2 (⬢) etched compositions should be compared to the ion beam sputtered composition (◆). Within the ion beam sputtered samples, CH_4/N_2 resulted the smallest composition and crystallization temperature changes. Among the downstream Ar sputtered samples, SF_6/Ar resulted in the smallest composition and crystallization temperature changes. The distribution of these composition is expanded and shown on the right.

153
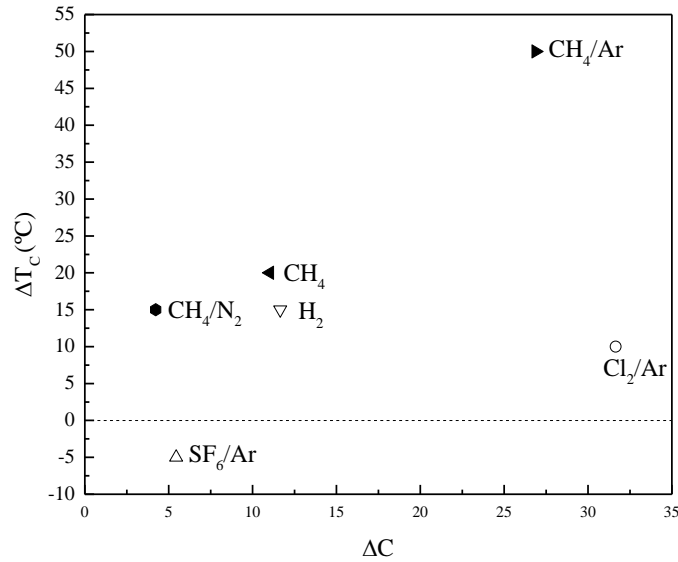
Figure 7-2. The change in crystallization temperature (ΔT_c) versus the composition change (ΔC) for the etch processes shown in Figure 7-1. SF_6/Ar results in the smallest changes to composition and crystallization temperature, but this analysis does not account for the extensive fluorination of the surface. CH_4/N_2 results in the next smallest changes to composition and crystallization.

On the other hand, the CH_4/Ar etching, which resulted in less composition change than the Cl_2/Ar etch, still resulted in a crystallization temperature that appeared to be over 2 times the minimum and ~50ºC higher than the initial ion beam cleaned surface. Likewise, the CH_4/N_2 etch, which resulted in the smallest change in composition compared to its initial surface (ion beam-cleaned), resulted in a composition with a lower crystallization temperature rise (~15ºC). Meanwhile, the H_2 etch, which resulted in greater composition change than the CH_4/N_2 etch when compared to its starting composition (the downstream Ar-cleaned target composition), resulted in a similar change in crystallization temperature.

In addition, one could envision that (as shown in Figure 7-3) if the CH_4-containing etches were at the same starting composition as the other etches, the direction in which the CH_4/N_2 changes the composition would still result in greater crystallization temperature change than

154

SF$_6$/Ar. However, SF$_6$/Ar etching resulted in excessive fluorination of the etched film, the CH$_4$/N$_2$ etch would be the recommended process among the etching chemistries studied in this work, followed by the H$_2$ etch. These etches showed the best performance in the more critical metric, the maintenance of crystallization temperature, while still avoiding halogenation of the surface. A rough estimate using values from literature suggests that the reduction in composition change by using CH$_4$/N$_2$ etching over Cl$_2$/Ar etching could result in an approximately 26% decrease in the power needed to reset a PCM cell (0.12 mW) (Boniardi 2010). For a voltage of 3.7 V, which is typical of lithium polymer batteries, this would equate to a reduction of 0.032 mAh per write operation. While a small energy value on its own, this could be beneficial in situations where available is energy constrained, such as in a smartphone, where a typical battery at time of writing had a capacity of 2815 mAh (iPhone 12).
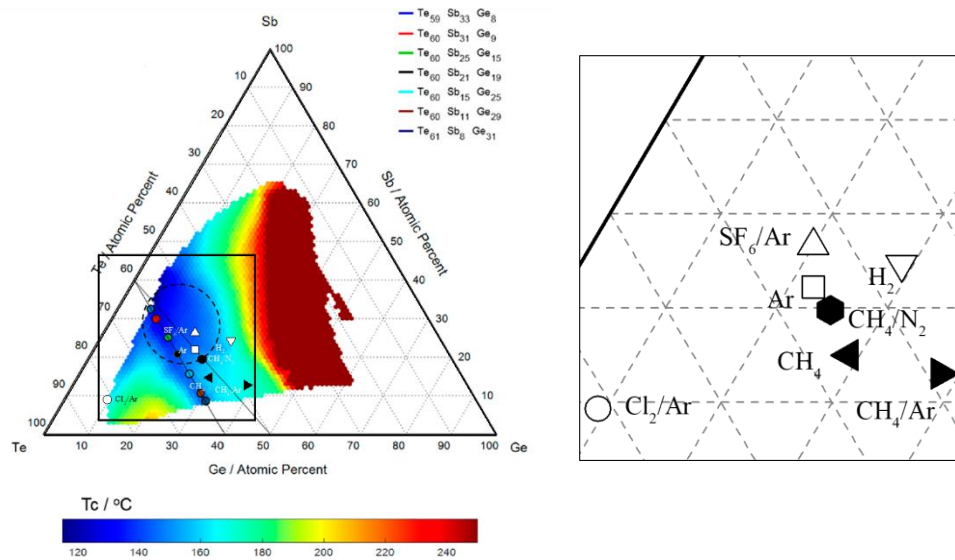
Figure 7-3. Crystallization temperature map of Ge-Sb-Te system (Guerin 2017). GST compositions of plasma-etched samples from

Table 7-1 are also shown, with only the composition of Ge, Sb, and Te considered. The CH$_4$ (◄), CH$_4$/Ar (►), and CH$_4$/N$_2$ (⬢) etched compositions have been translated such that their starting composition (□) matches those of the Cl$_2$/Ar (○), SF$_6$/Ar (△), and H$_2$ (▽) etched compositions to ease comparison. The SF$_6$/Ar chemistry resulted in the smallest composition and crystallization temperature changes but also had significant fluorination of the surface, while the CH$_4$/N$_2$ chemistry resulted in the next smallest changes but falls just outside the minimum crystallization temperature region. The distribution of these composition is expanded and shown on the right.

It was also proposed that a mix of processes could be used to process GST while maintaining Ge:Sb:Te stoichiometry. The preferential removal of each element from GST as a result of each of the wet clean and plasma treatments studied in this work was summarized in Table 7-2. From this table, a sequence of H$_2$ plasma and then Cl$_2$/Ar plasma could be used, since the enrichment of Ge and depletion of Sb and Te from the H$_2$ plasma etch could be counteracted by the Cl$_2$/Ar plasma, although there may be complications from the halogenation of the GST after Cl$_2$/Ar plasma. Another possibility would be to use isopropyl alcohol and citric acid or ammonium

156

hydroxide wet cleans after the H_2 plasma, although this would require measures to avoid ambient oxidation.

While this work found that CH_4/N_2 and H_2 plasmas were capable etchants for GST that not only resulted in satisfactorily small changes to crystallization temperature but also avoided surface damage in the form of halogenation, it should be recognized that GST has other phase-change properties that also need to be maintained in addition to crystallization temperature, such as the change in electrical resistivity between amorphous and crystalline states or changes in optical reflectivity. These other properties do not follow the same relationship with composition that crystallization followed, and the selection of the etch chemistry may change if these other properties need to be simultaneously optimized (Guerin 2017).

Follow-up studies would help to answer questions that arose or could not be answered during the course of this work. While this work demonstrates that preferential removal due to Cl_2 and SF_6 plasma etching can be partially explained by reactivity to the etch chemistry (as determined by etch rates), the conclusion drawn in literature explains preferential removal in halogen plasma etching etch product volatility. Further studies are needed in order to better understand which phenomenon (etch product volatility or chemical reactivity) determines the order of preferential removal. One study would be determining whether Sb and Te are truly inert to Cl_2 and SF_6 etching as elemental thin films or whether they etch too slowly to measure an etch rate in the time tested. Similarly, the etch rate for Te in H_2 plasma should also be measured, although in this case, the etch rate was too fast to be measured. The etch rate of GST in direct SF_6 plasma should also be measured, since it was shown in this work that, for the case of H_2 plasma, etch rate could differ greatly between direct and extracted plasma etching.

Another study to enable better understanding of plasma etching of GST would be to better determine the volatility of halogen etch products of GST using thermally programmed desorption, which would provide a more accurate comparison of etch product volatility than comparing boiling points. These could be compared against similar studies for the hydrogen and methane plasma etch products to determine how different etch product volatility is between the different sets of plasma etch products and how much of a role volatility plays in determining preferential removal. Lastly, more work is needed to understand the etching of GST using CH_4 plasma. Measurements of the etch products would confirm whether or not $Ge(CH_3)_4$, $Sb(CH_3)_3$, and $Te(CH_3)_2$ are being formed. The reaction of the Sb thin film to the tested CH_4 plasmas also needs to be better studied since deposition was observed by SEM and no chemical characterization could be done with *in-situ* XPS due to the small sample size. Improved understanding of how each elemental thin film reacts to the CH_4-containing plasmas would provide further proof that preferential removal is determined by etch product reactivity.

This serves as the most critical finding of this work: the etch rates of the constituent components of GST can be utilized as a type of kinetic analysis to study etch behavior of the ternary compound when thermochemical analysis such as etch product boiling points was not sufficient to delineate etching behavior. One can imagine that this approach could be extended to other complex materials used in the semiconductor industry such as InGaZnO. While logistically more difficult to accomplish due to the need for single element films, this concept can become a tool for developing plasma etch chemistries in the future.

Appendices

Appendix A. Inductively-Coupled Plasma Standard Operating Procedure
Emergency Shut Down Procedures for ICP Plasma Etcher

I. In case of Cl_2 is smelled
1. Close tank valve.
2. Close others valve if possible. The diaphragm valve D4, located directly behind chamber, and the regulator R1 on Cl_2 cylinder located in gas cabinet to the right of the MFC cabinet.
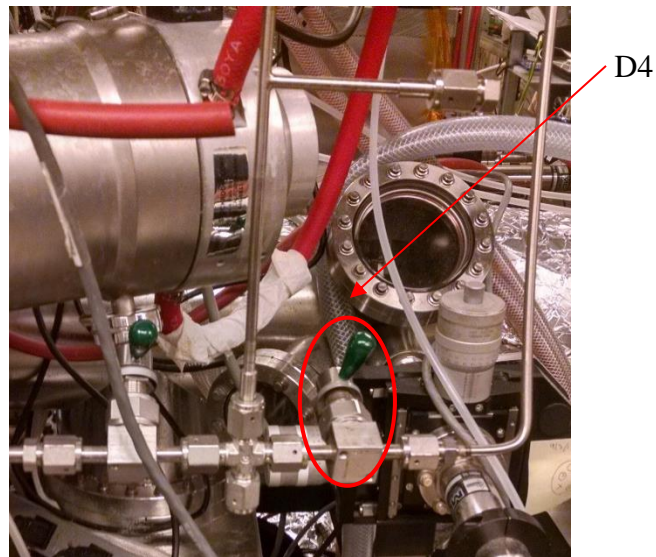
Figure 1. D4 valve directly behind chamber for delivery of non-corrosive gases
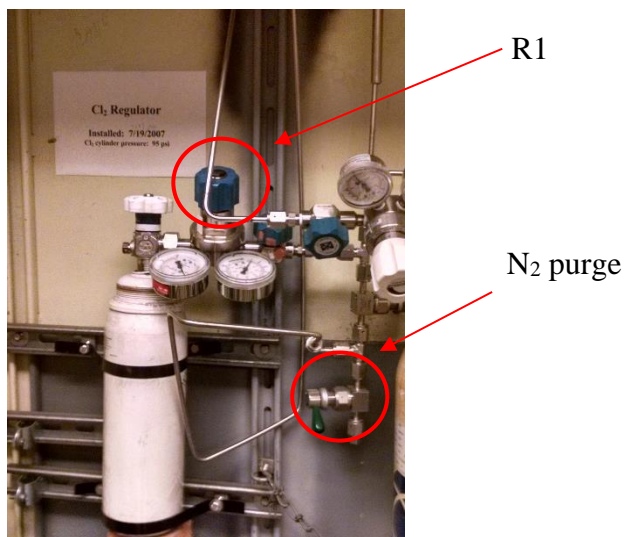
Figure 2. R1 regulator located in chlorine gas cabinet

3. Evacuate.
4. Contact EH&S as needed.

<u>II. In case a noise is heard from turbo molecular pump on Main Chamber</u>
1. Close manual gate valve between turbo pump and chamber.

Gate Valve
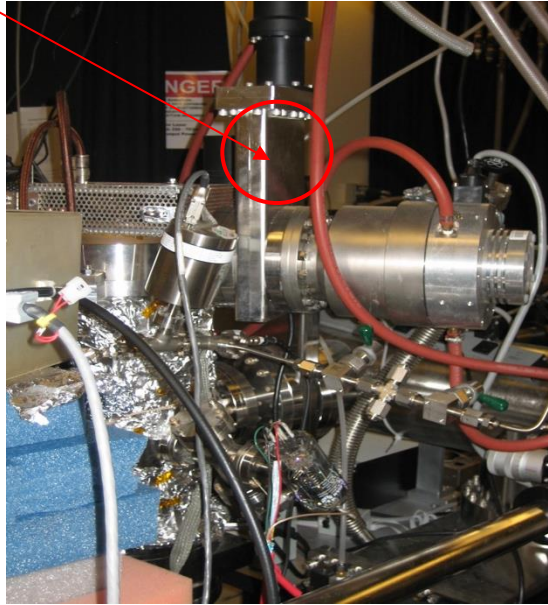
Figure 3. Gate Valve for Main Chamber Turbo Pump

2. Turn off the turbo molecular pump buy pushing the "stop" button on the controller.

Stop button

(read label to

Figure 4. Turbo Pump Controller for Chamber

3. Isolate mechanical pump by closing manual valve between turbo and MP.

<u>III. In case a noise is heard from mechanical pump on Chamber</u>
1. Close manual gate valve between turbo pump and chamber. (See Figure 3)
2. Turn off the turbo molecular pump by pushing the "stop" button on the controller. (See Figure 4)

3. Switch off the pump by turning off the breaker.

IV. In case a noise is heard from Cryopump on Chamber
   1. Close the pneumatic gate valve between ICP and Cryopump by pressing the corresponding switch on the control box (trace the cable if unsure). (See Figure 5)
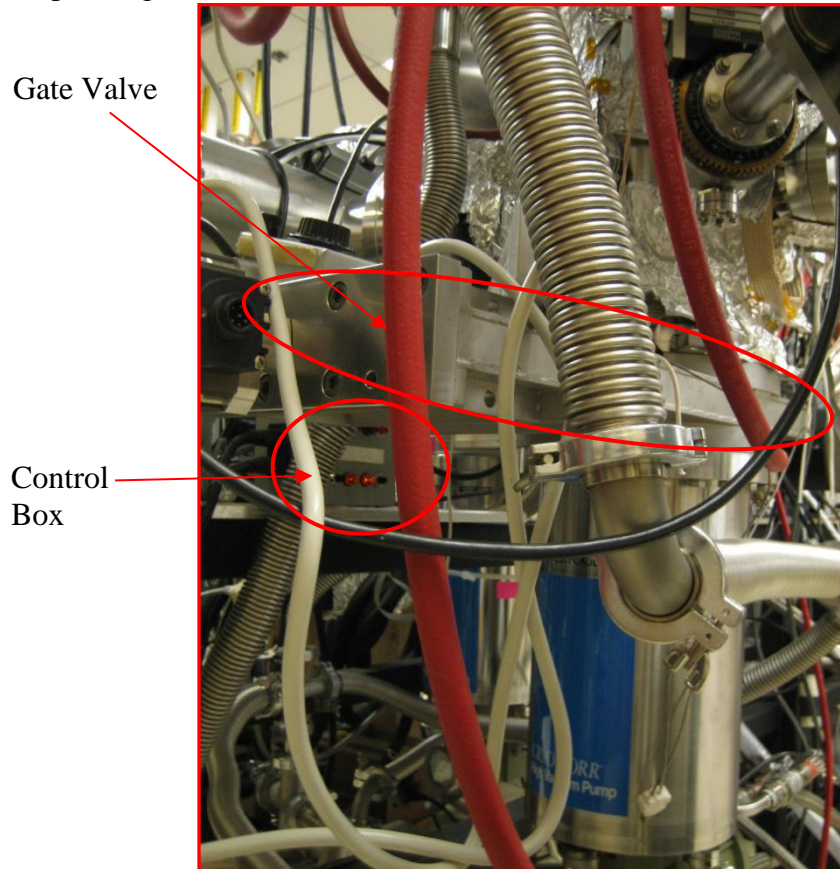
Figure 5. Gate Valve between Cryopump and ICP

   2. Ensure that the roughing valve between the cryopump and the chamber mechanical pump is closed.

   3. Turn off the cryopump by flipping the white circuit breaker on the compressor (See Figure 6 - in the event of pump failure this may turn off automatically – check to see if the unit is operating).
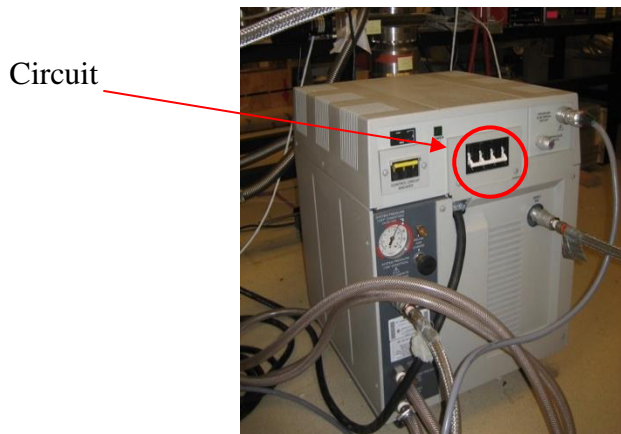
Figure 6. Compressor and Circuit Breaker Switch in Off position

V. In case noises are heard from any of the electronics
   1. If units have power switches turn them off, and unplug all units (see pictures below).
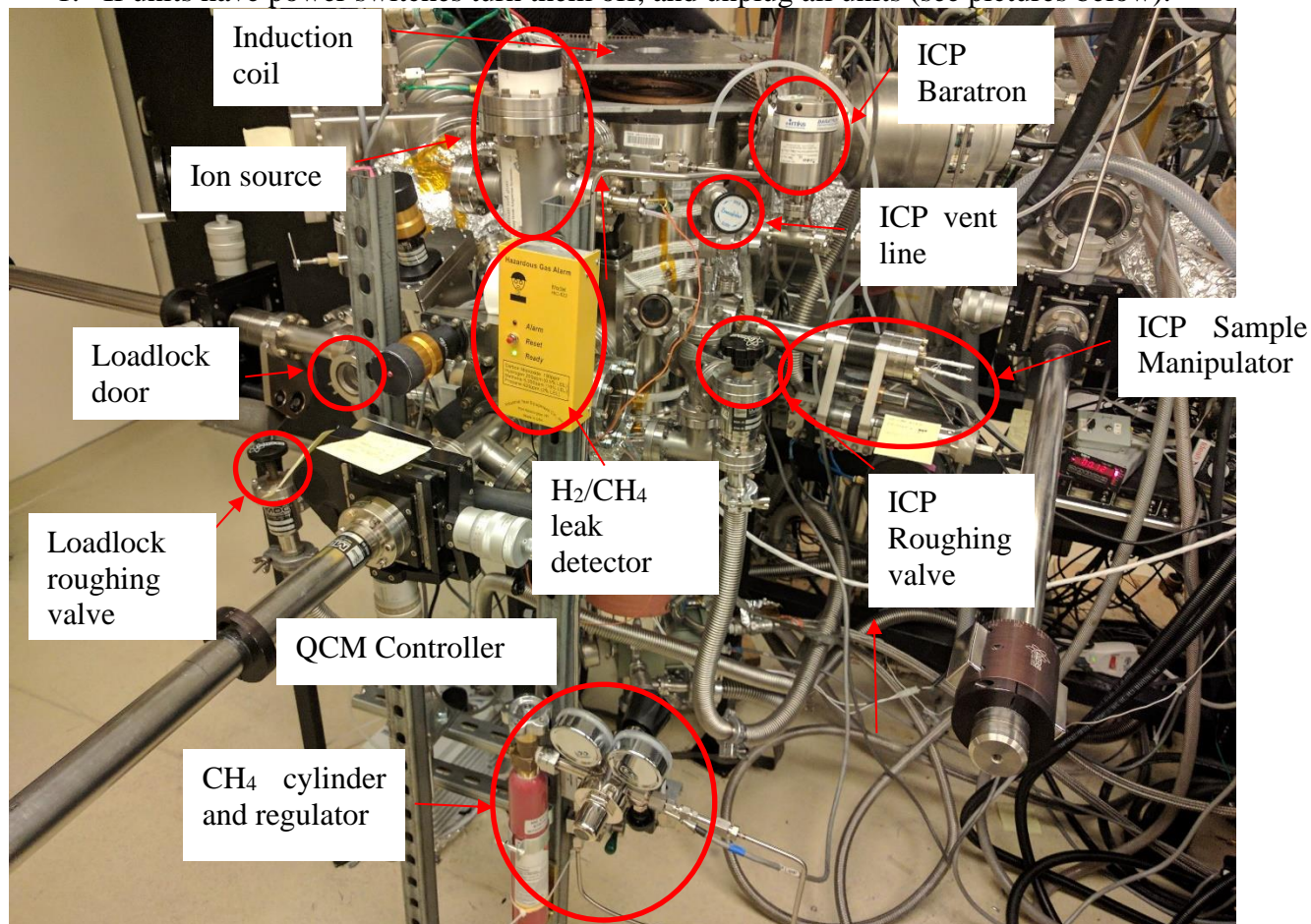
Figure 7. Diagram of ICP etcher chamber setup

Operation Procedures for Plasma Etcher

    1. Pump down the main chamber (Note: The chamber's default state should be pumped down, check the pressure reading on the ion gauge to verify. The following steps should only be taken if you aware that the chamber has been vented and not pumped back down).

a. THE FOLLOWING INTERLOCKS FOR THE PUMP DOWN PROCEDURE MUST BE MET TO BEGIN PUMPING: COOLING WATER FOR MAIN CHAMBER TURBO PUMP MUST BE ON, COOLING WATER FLOW TO COMPRESSOR SHOULD BE BETWEEN 2.3 AND 3.5 GPM).

b. Check that all the flanges are tightened and all the valves are in the closed position.

c. Check all the cables are correctly connected.

d. Check the uy moil level in the mechanical pump, which should be 2/3 full in view window.

e. Check MP and its exhaust for liquid leaks. (oil, condensation, exhaust fluid)

f. Turn on MP by turning on the switch. The thermocouple gauge reading should start going down within 20 seconds. If not, turn off the pump and check connections to chamber, turbopump and cryopump for vacuum leaks.

g. Wait until MP reaches the base pressure ~60 mTorr. This process may take several minutes if system was shut down for some time.

h. If the Baratron gauge on the chamber is blinking (indicating pressure >300 mTorr) or appears to be rising over 50 mTorr, gradually open the roughing valve on the upper body of the chamber to pump down using the MP. If the gas lines have been exposed to ambient conditions, diaphragm valve D3 and D4 should be open so that the gas lines could be pumped down as well. Rough pump the chamber using MP until a base pressure of ~75-85 mTorr is achieved.

i. After the TC gauge reaches the base pressure, close roughing valve between chamber and MP and gradually open roughing valve between TMP and MP.

1. Before TMP is turned on, check:

1. The cooling water is running

2. **The roughing valve between the chamber and MP should be always CLOSED while the TMP is on.**

3. If TMP is running, the base pressure should be achieved right away. (This would occur only if MP was turned off for less than approximately 10 minutes and TMP was isolated prior to shut off of MP)

4. If pumping down after TMP has been off for a few hours it may be safer to purge TMP1 with N_2 using the N_2 MFC for 30 seconds. Then gradually open the roughing valve and wait until base pressure is reached in MP1.

j. Open the gate valve between TMP and chamber. At this stage, the TC gauge readout should **NOT** vary at all.

k. Turn on TMP by pushing the start button on the Leybold controller, unless already on. The green acceleration indicator should turn on. The chamber pressure from Baratron gauge readout should start decreasing in 20 seconds.

l. Within 5 minutes, the turbo molecular pump should reach full speed and the yellow indicator should be on normal.

- If any strange noise is heard from TMP, turn it off right away by pushing the off button on the controller.
- If corrosive gas is anticipated to be used, 36 sccm industrial level nitrogen (corresponding to ~50 mTorr rise in TC pressure) should be provided through the purging port on the bottom of the pump by opening valve D5 and switching on the MFC "N_2 ind." on the control panel once the pump has reached full rotation, which is indicated by the normal light being lit on the TMP1 controller. (Refer to Leybold 361C Turbo Molecular Pump manual.)

m. After the Baratron gauge readout reaches 0.1 mTorr or lower, turn on the ion gauge by pushing the "ON" button on the ion gauge controller for IG1.

n. Wait until the chamber reaches the base pressure 2.0×10^{-8}. This process may take up to couple of days depending on how long the chamber has been under atmosphere.

- If the chamber has been exposed to ambient or pumping system has been off for more than a day, baking the chamber is necessary to achieve base pressure and remove any build up on the sidewalls of the chamber. Two heating tapes are used to bake the chamber. **Do NOT** turn on the power over 20% of the full range on the variable transformer to prevent over-heating. At this point the chamber pump down procedure is complete. If no processing is to be performed system should be left in this idle state.
  After base pressure in the chamber is achieved, plasma processing can begin using the following procedure. If a sample is to be processed the following procedure must be followed to load the sample in to the chamber. However, it is better to warm up the plasma before processing a sample, in which case skip to steps 3-6, and then return to step 2 and repeat the following steps.

2. Transfer the sample from transfer tube to the chamber:

a. See instructions for loading a sample from the loadlock in the Transfer Tube SOP.

b. Move the cart into position for transfer to the ICP.

c. Before opening the gate valve between the ICP and the TT check that their pressures are roughly equivalent. If the ICP pressure is too high the gate valve between the TT and its cryopump/turbo pump can be closed briefly. Ensure that no gas is flowing into the ICP.

d. Open the gate valve (G4) using the controller box (trace the cable to ensure). Check the ion gauge controllers on both the ICP and TT to ensure that the pressure has not changed significantly.

e. Secure the sample by sliding the holding fork attached to the end of the transfer arm around the upper groove of the sample holder.

f. Using the manipulator, lift the sample off the cart. Verify that the arm has cleared the cart (a setting of about 5.5 on the Y-axis manipulator is sufficient).

g. Slowly slide the transfer arm forward to move the sample into the ICP chamber.

h. Visually confirm the location of the sample in relation to the sample stage pin by checking through the viewport on the lower section of the ICP chamber.

i. Lower the sample holder onto the protruding pin. Visually confirm.

j. Slowly begin sliding the transfer arm out. The holder should stay on the stage.

k. When re-entering the transfer tube ensure the height of the transfer arm is readjusted so as not to hit the cart or holding pin in front of the ICP chamber.

l. Fully withdraw the transfer arm into the tube so that it has cleared the gate valve.

m. Close the gate valve (G4) between the ICP and TT.

With the sample loaded, if necessary, plasma processing can begin. Processing gases must be introduced into the reactor prior to striking plasma by performing the following procedure. Proceed to step 3, 4, or 5 depending on plasma chemistry.

3. Feed in process gas for plasma for inert gas only:

o. Check that the chamber is at the base pressure of 2 x 10^{-8}.
p. Check regulators for all the desired gases (N_2, Ar, O_2) by opening the gas tank.
q. Check the cylinders are filled with enough gas to obtain required flow rate.
r. **Turn off the ion gauge**, which cannot go above $1x10^{-3}$.
s. Open the pneumatic valves for gases to be used before the Mass Flow Controller (MFC), which are V1, V3, and V5.
t. Gradually open the corresponding valve after the MFC, which are V2, V4, and V6, to prevent a large pressure difference to the MFCs.
u. Adjust the set point on the MFC control unit to desired flow rate for each gas.
v. Open Diaphragm valve D3 and then gradually open D4. The chamber pressure should go slightly higher; wait until it goes back to the base pressure. This will pump down the gases which have been sitting in the line.
w. Zero the Baratron gauge so as to accurately measure chamber pressure once gases begin to flow in.
x. Turn on the MFCs for the gases to be used. Wait until a steady flow is achieved. Do fine adjustments if needed.
y. Record pressure achieved in chamber after steady flow is reached

4. Feed in flammable process gas (CH_4) only:

THE FOLLOWING INTERLOCK FOR CORROSIVE GAS USE MUST BE MET TO BEGIN: N_2 PURGE TO MAIN CHAMBER AND QMS TURBO PUMPS MUST BE ON.

a. Check that the chamber is at the base pressure of 1.0 x 10^{-7}.
b. Check that the flammable gas detector is showing a green "Ready" light and no alarm is detected, indicating by a flashing red light and beeping noise.
c. Check there is enough CH_4 gas in the cylinder and the regulator is CLOSED. (This regulator should always be closed while CH_4 gas is not in use.)
d. **Turn off the ion gauge**.
e. Gradually open Diaphragm valve D9. The chamber pressure should go slightly higher; wait until it goes back to the base pressure.
f. Adjust the set point on MFC control unit, which is channel 1, to desired flow rate for CH_4 gas.
g. Open the valve on CH_4 cylinder and the isolation valve after the regulator. Adjust the regulator to get 12 Torr outlet pressure
h. Gradually open the Diaphragm valve D8 and then D9 for.
i. Zero the Baratron gauge, so as to accurately measure pressure of the chamber.
j. Turn on the MFC. Wait until the steady flow is achieved. Do fine adjustments if needed.
k. Record pressure in chamber once steady flow is achieved.
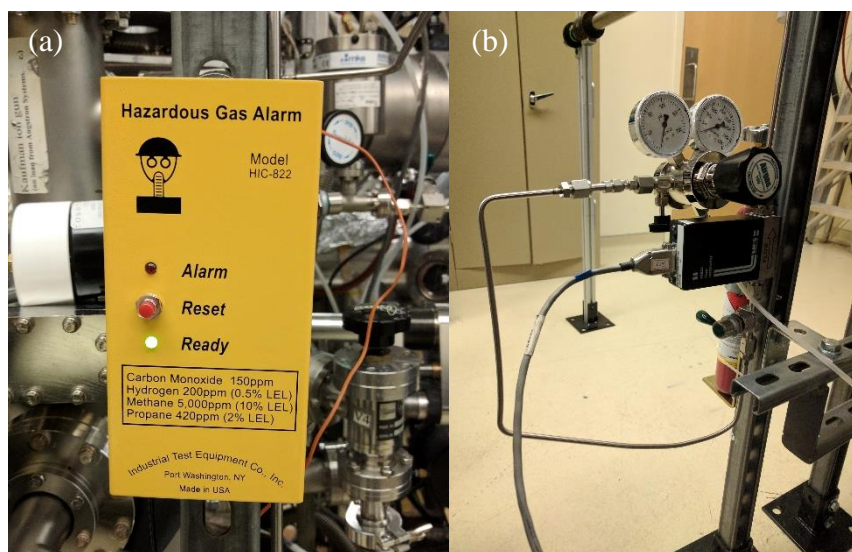
Figure 8 (a) Hazardous gas alarm during normal operation. The "Alarm" red light will be illuminated and an alarm will sound upon detection of lower limits of explosive gases. (b) Methane lecture bottle, regulator, and post-regulator valve.

5. **Feed in corrosive process gas (Cl_2 and/or BCl_3) only:**

   THE FOLLOWING INTERLOCK FOR CORROSIVE GAS USE MUST BE MET TO BEGIN: N_2 PURGE TO MAIN CHAMBER AND QMS TURBO PUMPS MUST BE ON.

   l. Check that the chamber is at the base pressure of 1.0×10^{-7}.
   m. Check there is enough Cl_2 gas in the cylinder and the regulator is CLOSED. (This regulator should always be closed while Cl_2 gas is not in use.)
   n. Check that 36 SCCM nitrogen is supplied to the purging ports of Turbopumps 1 and 2.
   o. **Turn off the ion gauge**.
   p. Gradually open Diaphragm valve D4. The chamber pressure should go slightly higher; wait until it goes back to the base pressure.
   q. Adjust the set point on MFC control unit, which is channel 1, to desired flow rate for Cl_2 gas.
   r. Open the valve on Cl_2 cylinder and the isolation valve after the regulator. Adjust the regulator to get 12 Torr outlet pressure. Then close gas cabinet door.
   s. Gradually open the Diaphragm valve D1 and then D2 for Cl_2 and/or D6 and D7 for BCl_3. Close the gas cabinet door.
   t. Zero the Baratron gauge, so as to accurately measure pressure of the chamber.
   u. Turn on the MFC. Wait until the steady flow is achieved. Do fine adjustments if needed.
   v. Record pressure in chamber once steady flow is achieved.

6. **For corrosive gas and inert gas mixture (Cl_2, BCl_3, Ar, O_2, N_2):**

   THE FOLLOWING INTERLOCK FOR CORROSIVE GAS USE MUST BE MET TO BEGIN: N_2 PURGE TO MAIN CHAMBER AND QMS TURBO PUMPS MUST BE ON.

a. Check that the chamber is at the base pressure of 9.0×10^{-8}.
b. Check there is enough Cl_2 and or BCl_3 gas in the cylinder.
c. The regulators should be CLOSED. (This regulator should always be closed while Cl_2 gas is not in use.)
d. Check 36 SCCM nitrogen is supplied to the purging ports of Turbopumps 1 and 2.
e. **Turn off the ion gauge**.
f. Gradually open Diaphragm valve D3 and D4. The chamber pressure should go slightly higher; wait until it goes back to the base pressure.
g. Adjust the set points on MFC control unit to desired flow rates for gases.
h. Open the regulator on Cl_2 cylinder/ and or BCl_3 at their respective gas tanks.
i. Open the pneumatic valves, for the inert gas, before the MFC (V1, V3, and V5) first, and then open the corresponding valve after the MFC (V2, V4, and V6).
j. Turn on the MFCs for the inert gases.
k. Gradually open the Diaphragm valve D1 and then D2 for Cl_2 and/or D6 and D7 BCl_3.
l. Close the gas cabinet doors.
m. Turn on the Cl_2 and/or the BCl_3 MFC. Wait until the steady flow is achieved. Do the fine adjustment if needed.
n. Record chamber pressure once flows have stabilized.

7. Turning on the plasma

THE FOLLOWING INTERLOCK FOR PLASMA GENERATION MUST BE MET TO BEGIN: 1. INDUCTION COIL FAN ON.

a. Ensure the fan on the induction coil is plugged in and operating.
b. Turn on the main power of the RF generator (Seren R1000) by flipping the main power switch.
c. Turn on the main power of the matching network tuning controller (RFPP 761 Unit) and ensure its operation mode is set to "Auto".
d. If bias is desired, turn on the main power and bipolar voltage control of the DC bias controller (Kepco BOP 500M).
e. If etching in the lower chamber is desired, turn on the filament power supply (Harrison Labs 6263A). Let all the electronics units warm up for 30 - 45 minutes.
f. Flow the process gases (pressures should be adjusted in steps 2-4).
g. Set the RF generator to the desired source power (500W) and press the "RF on" button. A red light should indicate RF power is being supplied.
h. If plasma does not strike, check that the reflected power as indicated on the generator display is not higher than 70 W, or that no warnings are displayed. If the reflected power is low, consider increasing the gas flow using the appropriate MFC. If the power is high or if warnings are displayed, turn off the RF supply by pressing the "RF on" button again and check the connections between the generator, matching network and source coil.
i. If bias is desired, set the DC bias to the appropriate voltage.
j. If etching in the lower chamber is desired, set the filament power supply to ~2 Amps. Usually this should be done a minute or two before the experiment to ensure the filament is receiving current (indicated by a reddish glow).

k. After the process is finished, turn off the RF power by pushing the "RF on" button on the front panel of the Seren R1000. Processes should not exceed 15 minutes so as to not over heat system.
l. Turn off the corrosive process gases first on the MFC.
m. Leave the inert gases running for about 5 minutes.
n. Turn off the MFCs, close the corresponding pneumatic valves and the Diaphragm valve D4 and D3 for Cl_2 and/or D6 and D7. BCl_3.
o. After the Baratron gauge readout reaches 0.1 mTorr or below, turn on the ion gauge by pushing the "1/T set" button on the ion gauge controller and push channel 1.
p. Turn off TMP1 purging nitrogen.
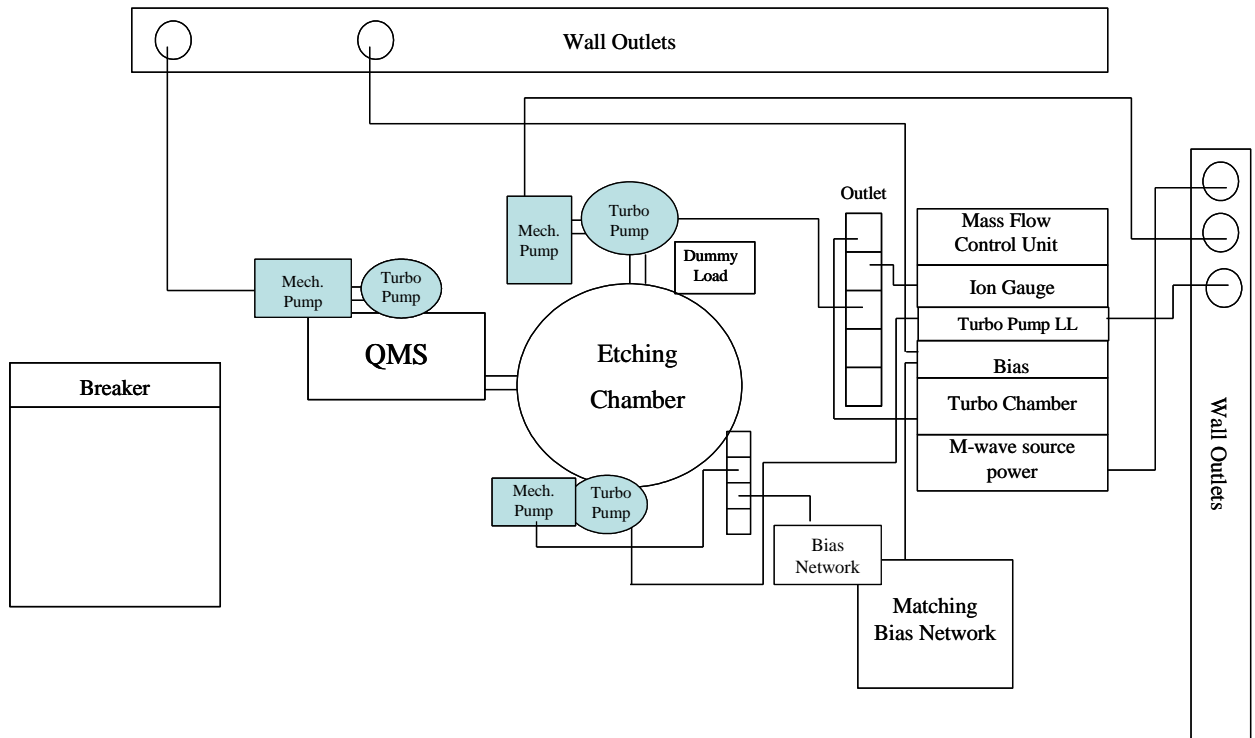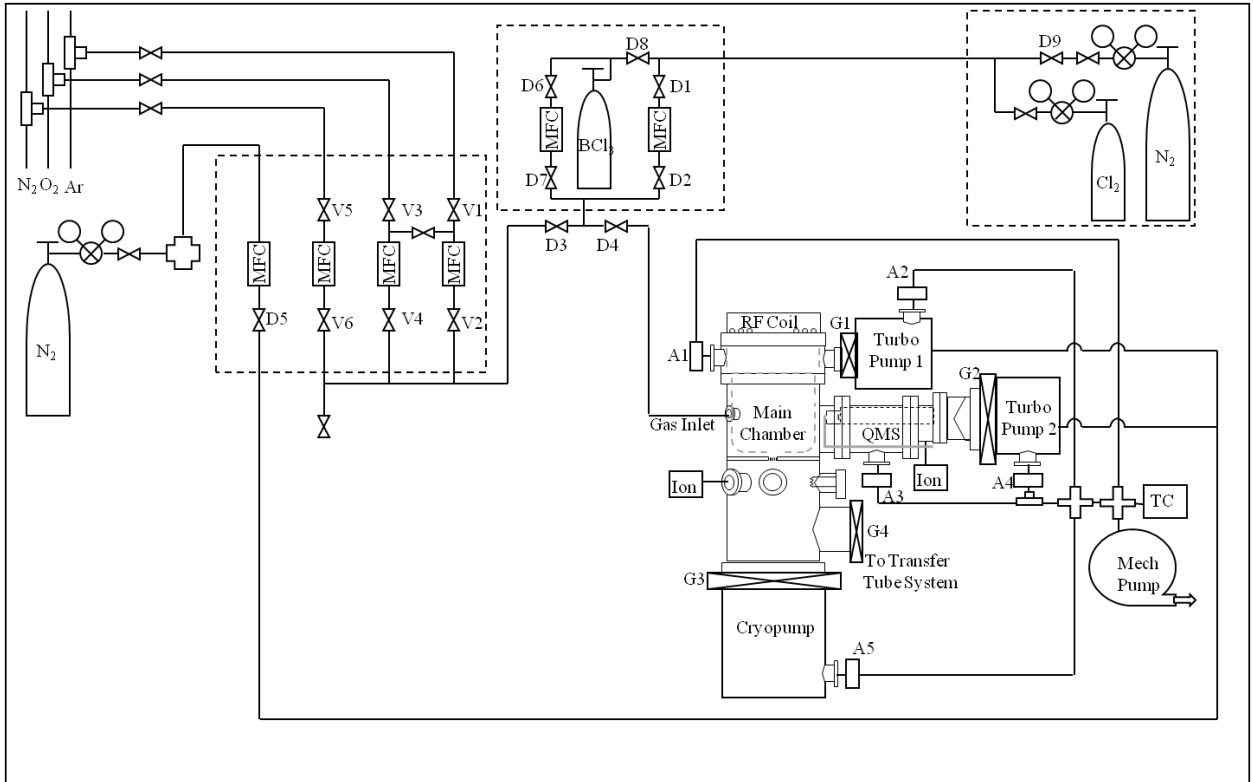
Figure 9. Diagrams of ICP gas lines and sources and power connections.
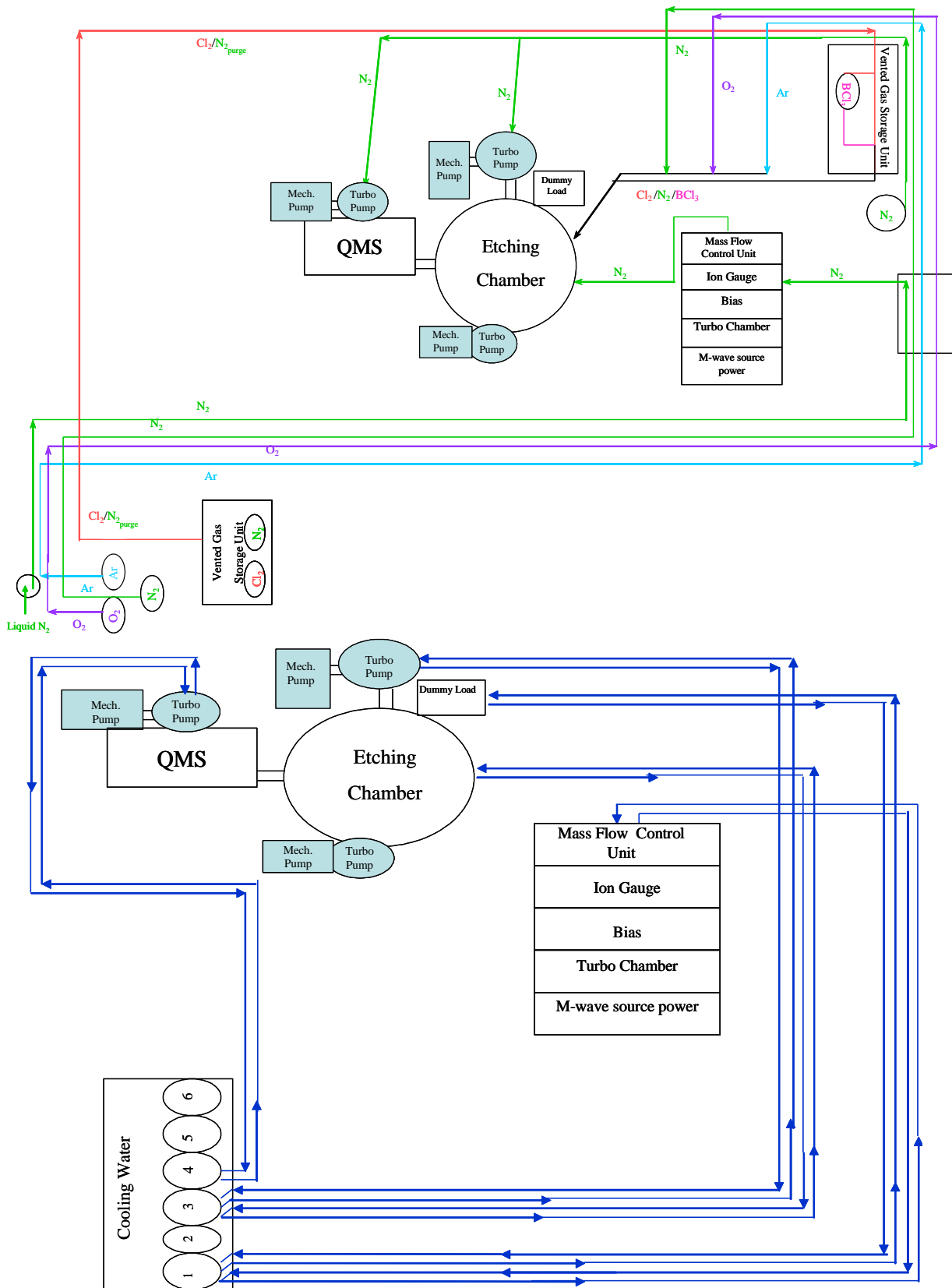
Figure 10. Diagrams of ICP hazardous gas line purging and cooling water connections

Appendix B.   Ion Beam Standard Operating Procedure
Emergency Shut Down Procedures for Ion Source Chamber

I. In case there is issue with discharge or beam electronics
1. Turn off the right "Beam" switch located on the left-hand side of the panel, next to the "Source" switch
2. Turn the "Neutralizer", "Cathode", and "Discharge" dials counter-clockwise until they stop.
3. Turn off the Source switch.
4. Turn off the "Power" switch.
5. Turn off Ar gas switch on MFC.
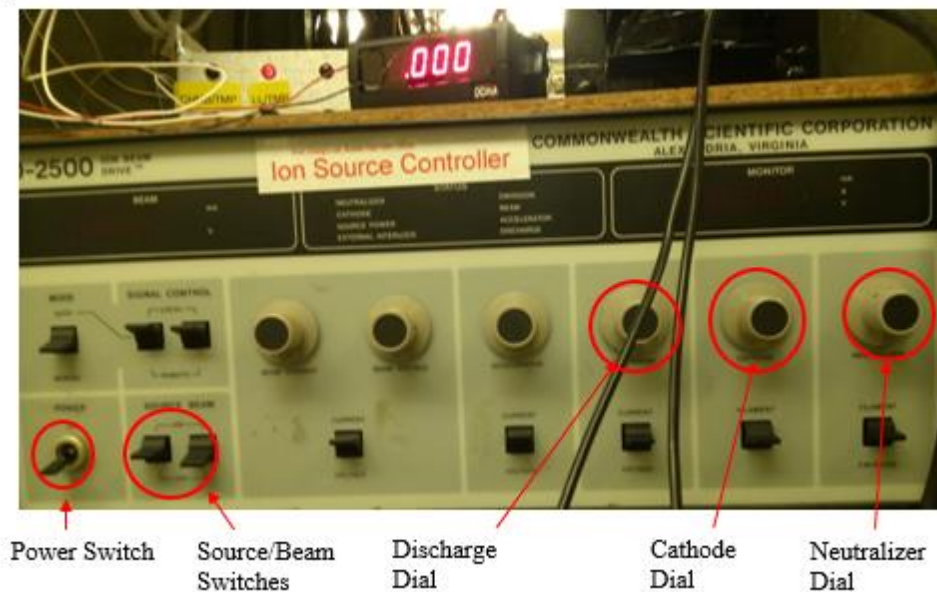
Figure 11. Ion source controller

II. In case a noise is heard from turbo molecular pumps on ICP Chamber
4. Close manual gate valves between turbo pumps and ICP chamber, manual gate valve between ion gun and ion gun chamber, and gate valve between ion gun chamber and ICP chamber.
5. Turn off the turbo molecular pumps by pushing the "stop" button on the two Leybold controllers.
6. Close the manual valve on the back of the TMP connecting the TMP to the mechanical pump.
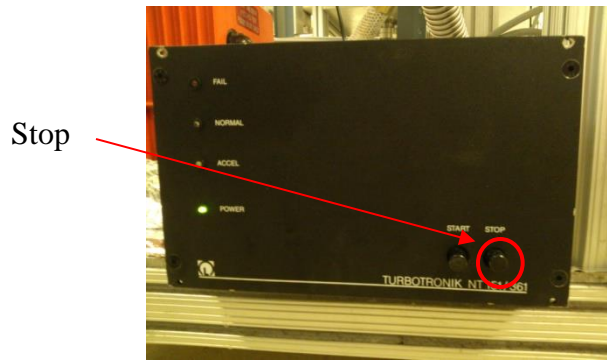
Figure 12. Leybold controller for ICP chamber turbo pump and mass spectrometer turbo pump.

III. In case a noise is heard from mechanical pump on ICP Chamber

4. Close the two manual gate valves between the TMPs and the ICP chamber and the gate.
5. Turn off the turbo molecular pumps by pushing the "stop" button on the Leybold controller.
6. Close the valve connecting the back of the TMPs to mechanical pump.
7. Turn off the mechanical pump using the toggle switch located on the rear of the mechanical pump body and unplug the mechanical pump power cord.

IV. In case noises are heard from any of the electronics

2. If units have power switches turn them off, and unplug all units.

Operation Procedures for Ion Source Chamber

1. **Pumping down the entire system (Note: The chamber's default state should be pumped down; ensure that the gate valve located between the ion beam chamber and ICP chamber is open and check the pressure reading on the ICP chamber ion gauge to verify. If the gate valve is closed, turn off the ion gauge controller for the ICP chamber. Verify that all gas lines to the ICP and ion beam chamber are closed. Close the ICP cryo pump gate valve, and leave the two gate valves to the TMPs on the ICP chamber open. Monitor the Baratron gauge on the ICP, and slowly open the gate valve between Ion Beam and ICP chamber, ensuring that the Baratron readout does not go above 50 on the pressure readout. Once completely open, and the Baratron reads single digits or zero, open the gate valve to the cryo pump. The following steps should only be taken if you aware that the chamber has been vented and not pumped back down).**

a. THE FOLLOWING INTERLOCKS FOR THE PUMP DOWN PROCEDURE MUST BE MET TO BEGIN PUMPING: COOLING WATER FOR MAIN CHAMBER ICP TURBO PUMP AND MASS SPECTROMETER TURBO PUMP MUST BE FLOWING AT 2.0-3.5GPM).
z. Check that all the flanges are tightened and all the valves are in the closed position.
aa. Check all the cables are correctly connected.
bb. Check the oil level in the mechanical pump on the ion beam chamber load lock, which should be 2/3 full in view window.
cc. Check MP and its exhaust for liquid leaks. (oil, condensation, exhaust fluid).

dd. Check that the Baratron and thermocouple gauges are on.

ee. Turn on MP by turning on the switch on the power strip. The thermocouple gauge reading should start going down within 20 seconds. If not, turn off the pump and check connections to chamber and turbopumps for vacuum leaks. Ensure load lock 2.75" CF quartz door and roughing valve to mechanical pump are closed

ff. Slowly open the manual gate valve between the 2.75" CF 6 way cross load lock and ion beam chamber.

gg. Slowly open the roughing valve on the load lock and wait for the chambers to reach base pressure (Baratron readout of ~0.037, corresponding to 37mTorr).

4.
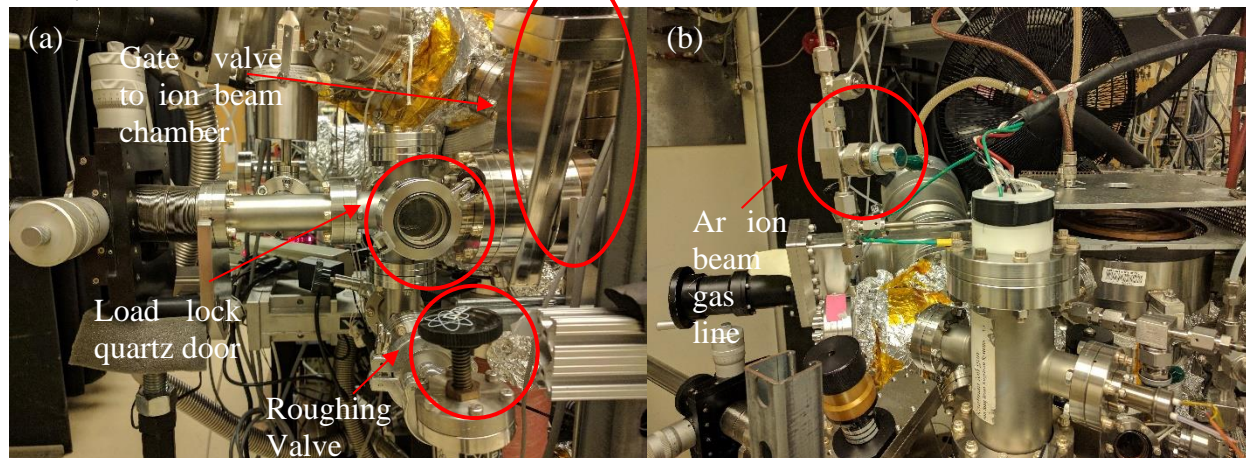
Figure 13. (a) Roughing valve for load lock and ion beam chamber. (b) Ar gas line for ion source

a. Close the gate valve between the load lock chamber and ion beam chamber and slowly open manual gate valve between ion gun and ICP main chamber, while keeping an eye on the ICP chamber Baratron gauge.

b. Slowly open Ar ion beam gas line valve to pump out the gas line. Check the ICP Baratron gauge and ensure the pressure does not exceed 50mTorr.

c. Once the ICP Baratron has reached below 1mTorr, turn on the ion gauges by pressing the IG1 and IG2 buttons on the ion gauge controller. If the pressure reads above 5.0×10^{-5} Torr, shut off ion gauge by pressing the IG1 button and wait several minutes before turning the gauge back on.
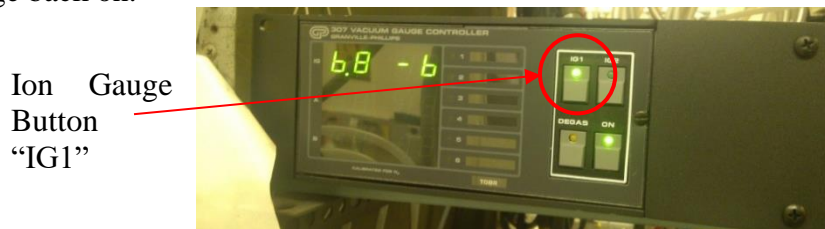
Figure 14. ICP Chamber Ion Gauge

5. **Turning on the ion source controller (Note: the sample must already be loaded and the chamber must be already pumped down).**

q. Ensure the Ar gas line valve is open.

r. Leave IG1 on the ICP ion gauge turned on
s. Set the set point on the Ion Beam MFC to 0.50 and monitor the ion gauge until it reaches about 5×10^{-6} Torr
t. Turn on left source beam switch. Do not turn on the right source beam switch yet.
u. Hold down discharge switch to the voltage setting and adjust the discharge dial until the monitor reads 40.0 V.
v. Hold up discharge switch to the current setting and adjust the cathode dial until the monitor reads 0.25 mA.
w. Turn on right source beam switch.
x. Hold neutralizer switch to the emission setting and adjust the neutralizer dial until the monitor reads a value close to the value displayed on the beam display. This value should be about 5 mA.
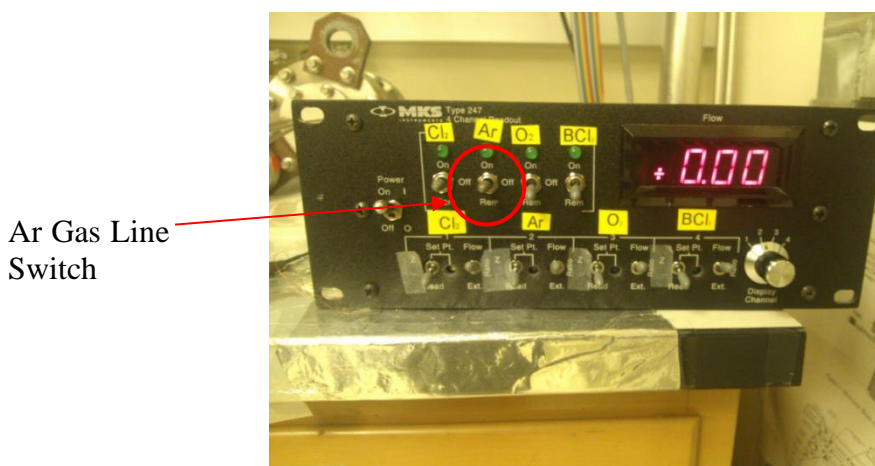
Figure 15. MFC with Ar gas line switch.

6. Turning off the ion source controller.

6. Turn off the right beam switch
7. Turn the neutralizer, cathode, and discharge dials counter-clockwise until they stop.
8. Then the left source switch.
9. Turn off the power switch.
10. Turn off Ar gas switch on MFC.
11. Turn on ion gauges by pressing the IG1 and IG2 buttons on the ion gauge controller.
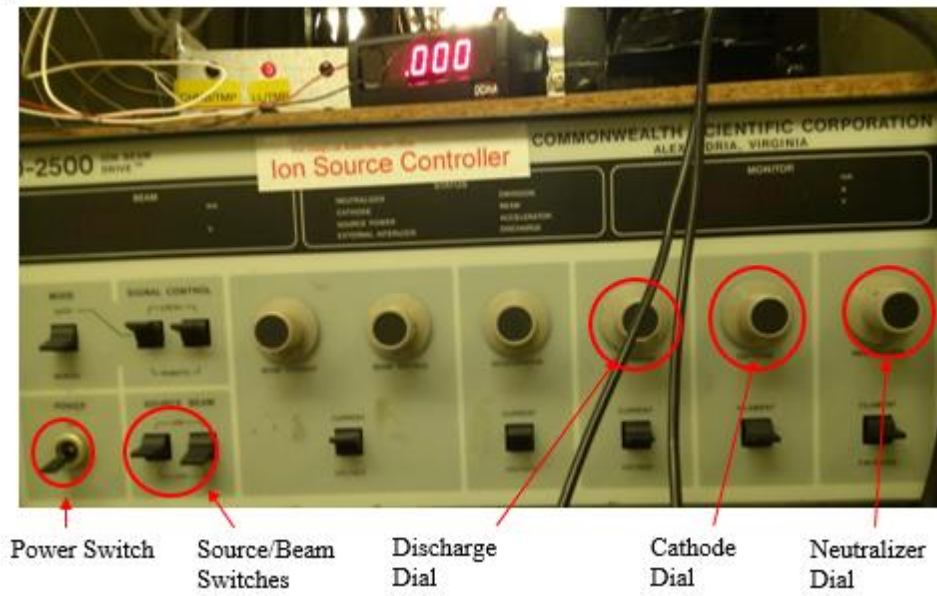
Figure 16. Ion source controller.

Appendix C.   Chamber Schematics

ICP reactor							
Main chamber – Side view							
University of California, Los Angeles, Department of Chemical and Biomolecular Engineering							
Part		Material	Stainless steel				
Filename		Scale	Yes	Units	inch	Quantity	1
Designer	Yunpeng Yin(MIT)	Date	6/11/2003				
Revised by		Date					
Contractor	Applied Vacuum Technologies	Date	6/11/2003				
Comments			Tolerance			+/- .0001	

ICP reactor

Main chamber – Isometric view

O-ring groove
see detail
Drawing #1-2 front view

10" OD flange, without holes
Nonrotatable

Port 9

Port 8

Port 5

Port 6

Port 7 (view port)

Port 1

Port 4

Port 2

10" OD flange, clearance holes,
nonrotatable, with 4 steel brackets
welded at 45, 135, 225, 315 degree,
looking at drawing #1-7 bottom
view for the detail dimentions

Reference plane

Port 3
(Viewport)

University of California, Los Angeles, Department of Chemical and Biomolecular Engineering							
Part		Material	Stainless steel				
Filename		Scale	Yes	Filename		Scale	Yes
Designer	Yunpeng Yin(MIT)	Date	6/11/2003				
Revised by		Date					
Contractor	Applied Vacuum Technologies	Date	6/11/2003				
Comments				Tolerance		+/- .0001	

ICP reactor

Main chamber – Front view

University of California, Los Angeles, Department of Chemical and Biomolecular Engineering							
Part		Material	Stainless steel				
Filename		Scale	Yes	Filename		Scale	Yes
Designer	Yunpeng Yin(MIT)	Date	6/11/2003				
Revised by		Date					
Contractor	Applied Vacuum Technologies	Date	6/11/2003				
Comments				Tolerance		+/- .0001	

ICP reactor

Main chamber – Top view

University of California, Los Angeles, Department of Chemical and Biomolecular Engineering							
Part		Material	Stainless steel				
Filename		Scale	Yes	Filename		Scale	Yes
Designer	Yunpeng Yin(MIT)	Date	6/11/2003				
Revised by		Date					
Contractor	Applied Vacuum Technologies	Date	6/11/2003				
Comments				Tolerance		+/- .0001	

ICP reactor

Main chamber – Button view

University of California, Los Angeles, Department of Chemical and Biomolecular Engineering

Part		Material	Stainless steel				
Filename		Scale	Yes	Filename		Scale	Yes
Designer	Yunpeng Yin(MIT)	Date	6/11/2003				
Revised by		Date					
Contractor	Applied Vacuum Technologies	Date	6/11/2003				
Comments			Tolerance		+/- .0001		

ICP reactor

Main chamber – QMS chamber

3.9800

0.4533

All Leak-Check slots are vertical
unless otherwise indicated

1.5467

4.1233

Axis 1

4.1333

6.0"OD Flange, 4.0"OD tube, CF
Nonrotatable, tapped
Leak-Check slots are parellel
to axis 1

4.1333

3.9800

6.0"OD Flange,CF
4.0"OD tube
Nonrotatable
Tapped

6.0"OD Flange,CF
4.0"OD tube
Nonrotatable
Tapped

University of California, Los Angeles, Department of Chemical and Biomolecular Engineering							
Part		Material	Stainless steel				
Filename		Scale	Yes	Filename		Scale	Yes
Designer	Yunpeng Yin(MIT)	Date	6/11/2003				
Revised by		Date					
Contractor	Applied Vacuum Technologies	Date	6/11/2003				
Comments				Tolerance		+/- .0001	

ICP reactor

Sample stage

University of California, Los Angeles, Department of Chemical and Biomolecular Engineering							
Part		Material	Stainless steel				
Filename		Scale	Yes	Filename		Scale	Yes
Designer	Yunpeng Yin(MIT)	Date	6/11/2003				
Revised by		Date					
Contractor	Applied Vacuum Technologies	Date	6/11/2003				
Comments				Tolerance		+/- .0001	

ICP reactor

Quartz in the ICP chamber

(10.0)

1 (0.5)

(0.5)

(0.71)

University of California, Los Angeles, Department of Chemical and Biomolecular Engineering							
Part		Material	Stainless steel				
Filename		Scale	Yes	Filename		Scale	Yes
Designer	Yunpeng Yin (MIT)	Date	6/11/2003				
Revised by		Date					
Contractor	Applied Vacuum Technologies	Date	6/11/2003				
Comments			Tolerance		+/- .0001		

Transfer Tube

University of California, Los Angeles, Department of Chemical and Biomolecular Engineering							
Part		Material	Stainless steel				
Filename		Scale	Yes	Filename		Scale	Yes
Designer	Jane Chang (MIT)	Date	1994				
Revised by		Date					
Contractor	Applied Vacuum Technologies	Date	1994				

Appendix D.   Quadrupole Mass Spectrometry Standard Operating Procedure
Emergency Shutdown

1. Turn off the UTI100C Electronics Controller by follow the sequence labeled below in the order indicated.
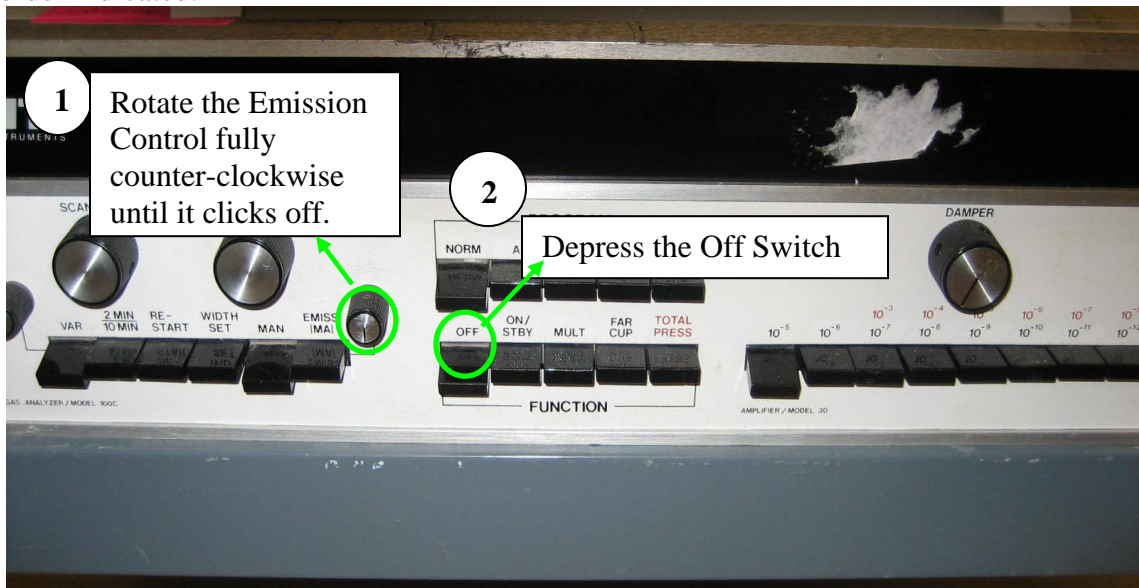
Figure 17. QMS control interface emergency shutdown procedure.

2. Turn off the oscilloscope by pressing the power button:

Figure 18. QMS oscilloscope emergency shutdown.

Operating Procedures

1. Check the base pressure of the system, which should be about $2.8*10^{-8}$ Torr. Write the base pressure in the logbook.
2. Check the connections between the Spectrometer and the Interface Box, the Interface Box and the

185

Spectrometer Control Unit (SCU), the SCU and the Oscilloscope, and the Oscilloscope and the Computer (Illustrated below). Turn on the computer.
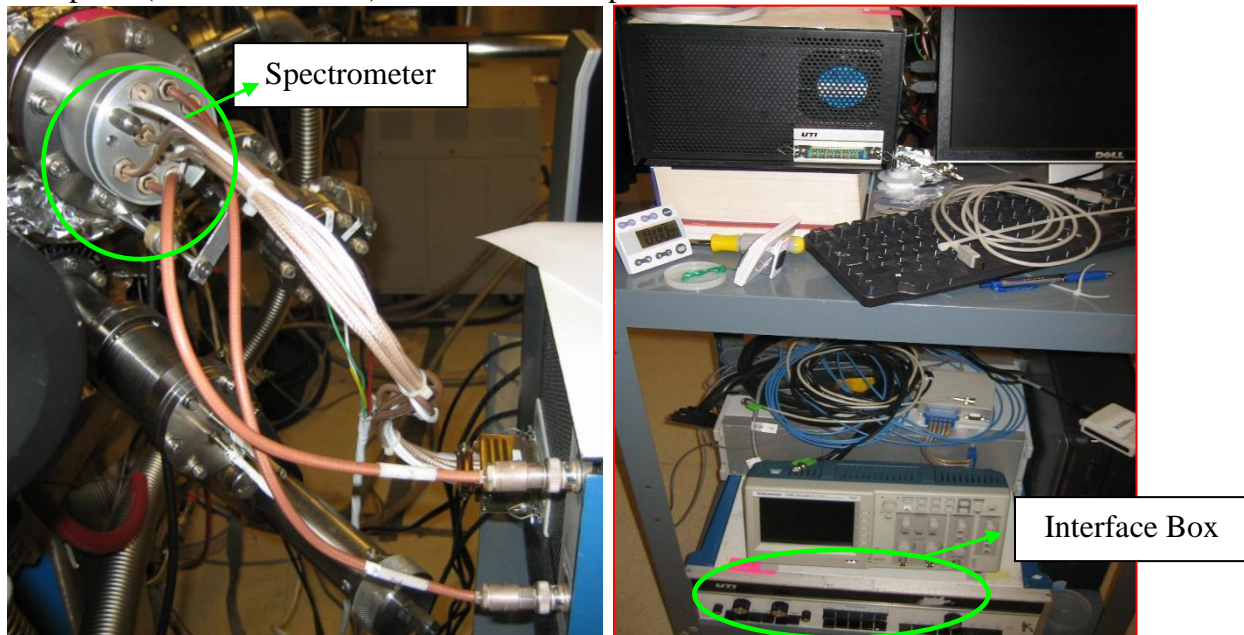
Figure 19. QMS interface and interface box connections.

3. Ensure that the power cable into the SCU is plugged in. Check that the following switches are depressed (labeled below): "Var" and "Man" in the Scan section, "Norm" in the Program Section, "Off" in the Function Section and "10^{-5}" in the Damper Section. Also make sure the emission control is off (rotated fully counter-clockwise).
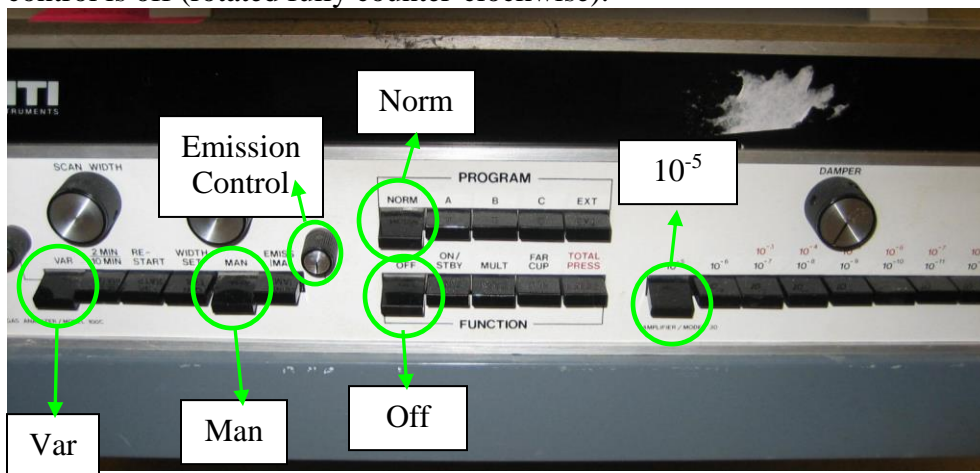
Figure 20. QMS interface switches default positions

4. Depress the "On/Stby" switch on the SCU directly to the right of the "Off" switch. Let the electronics warm up for 30 minutes. Power on the oscilloscope by pressing its power button. Windows should indicate that new USB device has been plugged in and will give you the option of selecting software to view the device.
5. Select TekDesktopAcquisition (the TDS 1012B should be selected as device by default).
6. After the electronics have warmed up set the scan center and width using the Scan Control section of the SCU. To set the center "Man" has to be depressed. To set the width, "Width Set" has to be depressed and "Man" should be released. Both of these values are set by using the corresponding

rotary controls above the switches (can be seen in the preceding image). The scan center set by "Man" should be quite accurate to within a single m/z value.

7. Flow gas and strike plasma as required by your experiment.
8. Monitor the QMS pressure. The maximum operating pressure for QMS is $5*10^{-6}$ Torr.
9. Start the QMS scan by releasing the "Man" switch, and depressing "Emiss (mA) and "Mult" switches at the same time. Adjust the emission current using the rotary control (max = 0.2 mA). If no signal is seen adjust the Damper (max = 10^{-9}).
10. Monitor the scan on the oscilloscope and adjust the visual as necessary using the controls for the y- and x-axis. A visual can be captured using the Tektronic software "Data Capture" button.
11. After finishing all the experiments, close the software and transfer all the data files to the server.
12. Turn off the power to the SCU by using the steps outlined below:

2 Rotate the Emission Control fully counter-clockwise until it clicks off.

5 Depress the Off Switch

1 Depress the 10^{-5} switch on the damper control

4 Depress the "Manual" switch.in the Scan Control section

3 Release both the Emission and Multiplier Switches simultaneously
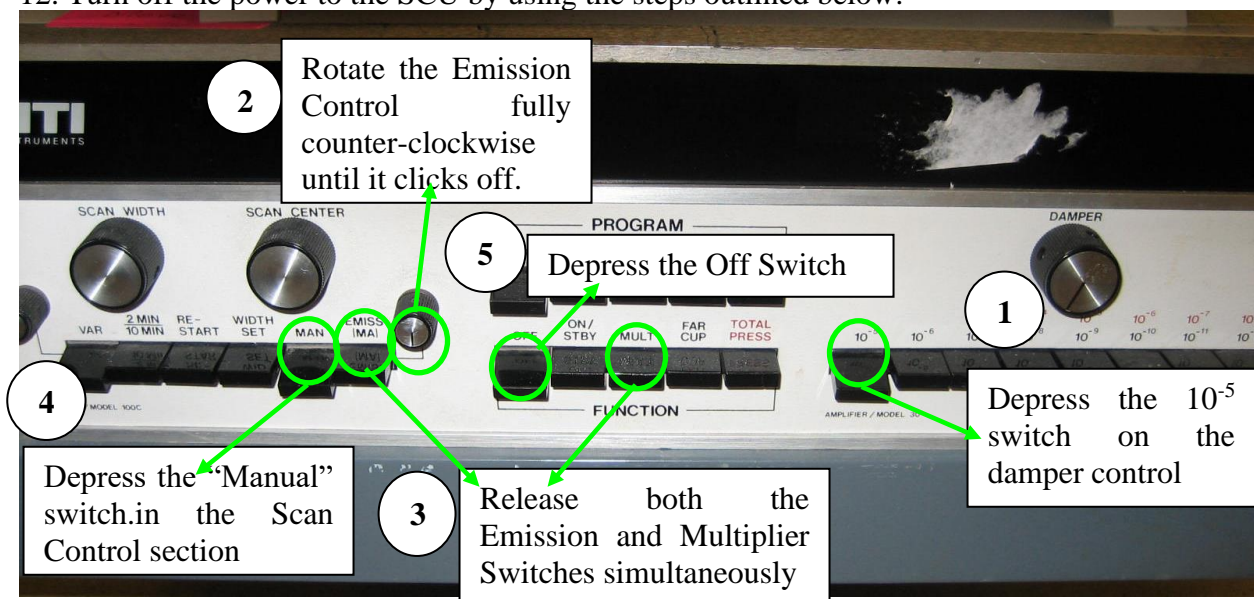
Figure 21. QMS shutdown procedure.

13. Turn off the oscilloscope by pressing its power switch.
14. Finish filling out the logbook.

Appendix E.   Langmuir Probe Standard Operating Procedure
Emergency Shutdown
I. In case of an emergency overpressure situation in the plasma etcher

3. Stop any current scans using the Hiden ESPsoft software: STOP SCAN

4. If necessary, pull the probe tip out of the etcher main chamber and back it's housing unit by homing the z-stage: Probe → Home ZStage.

5. Exit the Hiden ESPsoft program: File → Exit.

6. Turn off the Langmuir probe electronics by pressing the "OFF" switches on the front panels of both electronics units.

II. In case probe has been driven into the closed gate valve

1. Immediately stop the motor of the z-stage by pressing "Cancel" on the "Probe Positioning" window of the ESPsoft software.

2. Home the z-stage.

3. At this point, the Langmuir probe housing will need to be disassembled off the etcher system in order to assess damage to the probe.

Schematic and Description
The Hiden Analytical Langmuir Probe system consists of the following components:
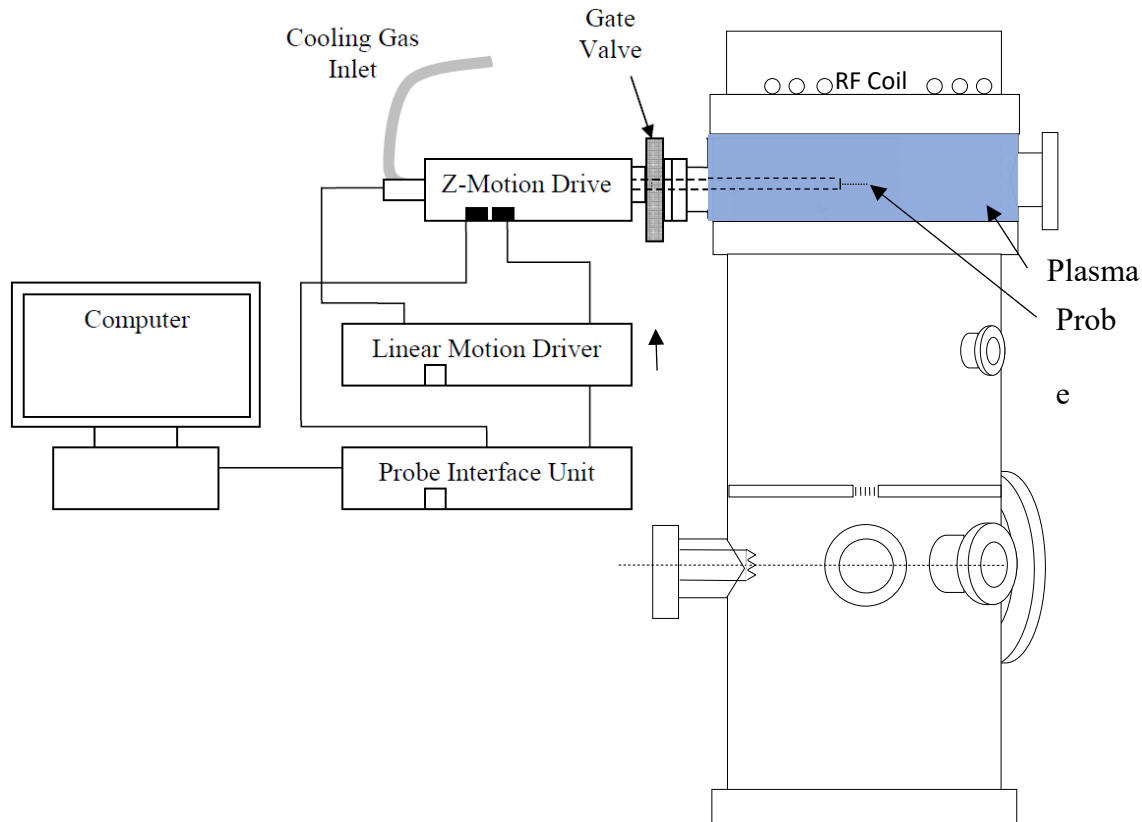
Figure 22: Schematic of Langmuir Probe System showing connection of components.

Operating Procedures
I. Probe Operation and Data Collection

This section details how to set up and perform scans for plasma analysis.

1. Check that the etcher system is at base pressure. Then slowly open the Langmuir probe gate valve. If the Langmuir probe housing has been isolated for a long time, a significant amount of gas may have accumulated in the Langmuir probe bellow and the pressure in the chamber will rise once the gate valve seal has been cracked open. Slowly opening the valve will help protect the etcher main chamber turbopump.

2. Turn on the Langmuir probe and z-drive electronics units and warm up for 30 minutes before acquiring data.

3. Open the ESPsoft program on the diagnostics computer.

4. With the gate valve is open, advance the probe into the main chamber by selecting Probe → Z-Stage, then entering the desired insertion distance (in cm) in the Park position prompt, then

selecting "Move Now" and "Ok". (parking the probe tip at the center of the main chamber requires a position of 26.67 cm)

5. Set the desired parameters for acquisition by selecting Probe → Edit, and then inputting all desired parameters.

6. Once a plasma is struck, an data can be acquired by selecting Probe → Run, then entering the amount of acquisitions, naming the file, and selecting "Start".

II. Probe Tip Replacement

This section details how to uninstall the Langmuir probe from the vacuum chamber and replace the probe tip

1. Home the z-drive and close the manual gate valve connecting the Langmuir probe house from the main chamber.

2. Remove screws holding the outer housing to the z-drive chassis, then take off the outer housing.

3. Disconnect the cables connecting the back end of the 2 ¾" CF flange (the end that the probe is attached to on the inside), then, while holding the flange (and probe) in place, remove the bolts connecting the CF flange to the bellow valve.

4. While *carefully* and *firmly* holding the bellow valve in place with one hand, and holding the CF flange/probe in the other, advance the z-drive forward in small (~2 cm) increments until the probe can be safely removed from the bellow. It is *very important* to secure the bellow valve while doing this as when it is compressed it will want to spring out sideways! Allowing this to happen could damage the fragile bellow weldings and cause a leak.

5. Replace the probe tip using gloves and clean tongs.

6. To replace the probe, follow this procedure in reverse order, making sure to hold the probe steady while retracting the z-stage. Colliding the probe tip with the bellow while retracting could damage the new tip!

7. Once the probe CF flange is reattached to the bellow and the housing cover is replaced, the bellow volume will have to be opened to the etcher while it is isolated from all turbopumps in order to protect them (remember the bellow volume will be at atmospheric pressure!).

8. Rough pump the chamber and then pump down with the turbopump, as instructed in the etcher system operation procedures.

III. Troubleshooting

This section details major problems occurring on the Langmuir probe and the steps taken

to fix them.

Spring 2007:

It was found that some plasma conditions (e.g. BCl_3-containing chemistries) lead to rapid degradation of the collected current. This is due to deposition on the probe tip while it is idle. In order to avoid deposition on the tip and prolong the lifetime of each probe tip, the following procedures are suggested:

    a. Always keep the Langmuir probe retracted into the housing with the gate valve closed for any experiments that do not require data acquisition using the Langmuir probe.
    b. Keep experiments as short as possible whenever the Langmuir probe is in use(this applies to all plasma conditions!)
    c. If a potentially depositing plasma chemistry will be in use, always set the "Idle Park Potential" of probe (in the Probe → Edit menu) to a high negative voltage (~-80 V) right before striking plasma, and return the idle park potential to 0 V once the plasma has been turned off. This will induce ion bombardment of the probe with the plasma on which will prevent a deposition layer from developing.
    d. In addition, in the Probe → Edit menu, turn on the automatic cleaning during for data acquisition in depositing plasmas by selecting the checkbox next to "Automatic Cleaning On" as well as "20 ms clean/5 ms data acq.", and set the "Cleaning *Potential" to a high negative voltage (~ -80 V).*

Appendix F.   Optical Emission Spectroscopy Standard Operating Procedure
Optical Emission Spectrometer

(Ocean Optics S2000)

Emergency Shutdown

1. Stop the program, and no further shutdown procedure is required.
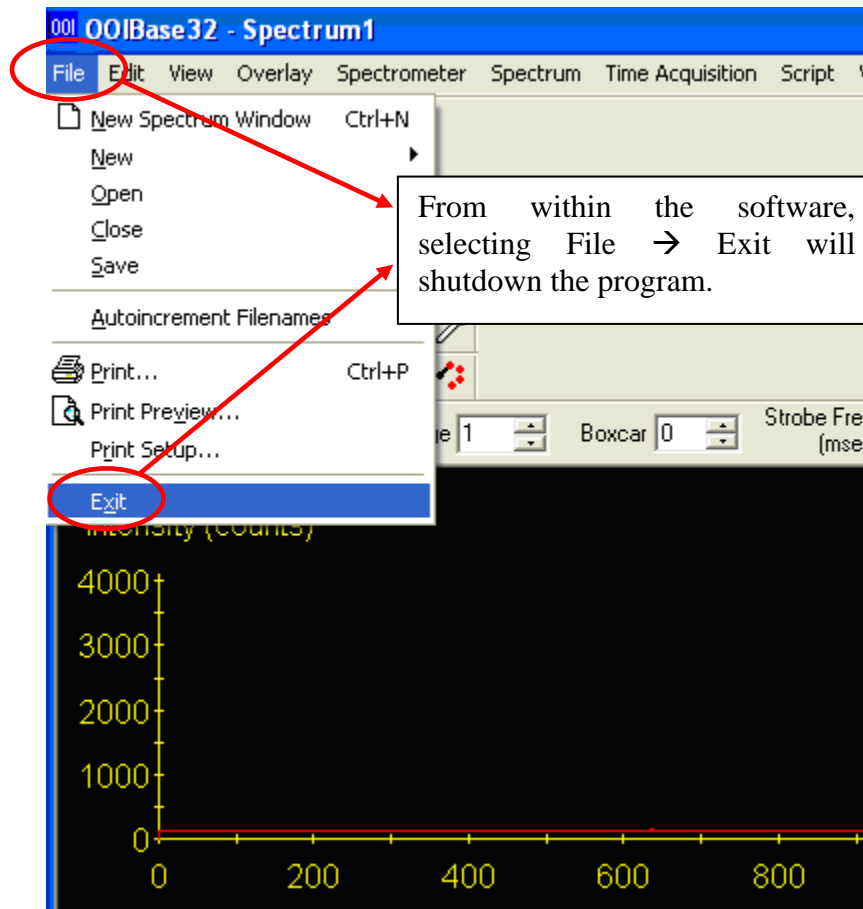
Figure 23. Ocean Optics S2000 shutdown

Moving the Spectrometer

1. The modules need to be moved are optical fibers and the S2000 module where the fibers are attached.
2. The ADC1000-USB module is used for the computer on the ECR etcher (or other computers with the software properly installed if needed)

Operation Procedure

1. Have Optical fiber and cable connections ready
    a. ECR/ICP Etcher
        i. One end of the fiber points to the light source (plasma)
        ii. The other side of the fiber plugged into the S2000 module.
        iii. S2000 module connects to ADC1000-USB (S/N ADUD6666) converter
        iv. USB cable goes from ADC1000-USB to the computer USB port
    b. PEALD
        i. One end of the fiber points to the light source (ECR plasma)
        ii. The other side of the fiber plugged into the S2000 module.
        iii. S2000 module connects to the OES-17-pin-cable
2. Start the OOIBase 32 program
3. Load the configuration file:
    a. Go to Spectrometer → Open Configuration
    b. Load c:\Program Files\Ocean Optics\OOIBase32\Default.spec
4. Enable channels:
    a. Go to Spectrometer → Configure
    b. Select Wavelength Calibration → Spectrometer Channel
    c. For Master, Slave 1, Slave 2, Slave 3, and Slave 4: check Channel Enabled Box.
    d. Click OK
5. Set proper integration time and time of average required.

Wavelength Calibration Settings:

These calibrations are set in the *.spec, the file that currently loads properly is located in Jerry's directory in the main Ocean Optics\OES folder.

Settings for Each Channels

Channel	Coefficient	
Master	First Coefficient	0.090373707
	Second Coefficient	-5.97073E-06
	Third Coefficient	-1.95468E-10
	Intercept	196.1413853
Slave 1	First Coefficient	0.081748312
	Second Coefficient	-7.10533E-06
	Third Coefficient	0
	Intercept	327.2303174
Slave 2	First Coefficient	0.109883634
	Second Coefficient	-1.01124E-05

	Third Coefficient	0
	Intercept	437.7008054
Slave 3	First Coefficient	0.167191118
	Second Coefficient	-1.32075E-05
	Third Coefficient	-4.41513E-10
	Intercept	585.698979
Slave 4	First Coefficient	0.154308212
	Second Coefficient	-1.49556E-05
	Third Coefficient	0
	Intercept	786.4959131

Optical Emission Spectrometer

(Lam Research OES2)

Installation Instructions:
Requirements:
- The SW has been sucessfully tested on Windows 7 PCs. At this time, the OES2 driver is not compatible with Windows 10 PCs.
- A high-speed USB port (USB 2.X or later) is required for communication with the OES2 (avoid using a shared hub)
- The powered-up OES2 must be available to complete the installation
-

Hardware
The OES2 hardware is shown below.

Figure 24. OES2 hardware and USB connections.

Only two connections are required: power and USB. The USB cable is a USB 2.0 Mini to USB 2.0 Type A.
This procedure does not include instructions for connecting the power.

Device Driver Installation
1. Do not connect the OES2 USB until directed below; if already connected, disconnect it now
2. Create a new permanent folder on the C: or D: drive called **OES2**
3. Copy the installation zip file 'OES2 SW Installation V1.0.zip' from the server to this new folder
4. Unzip the file to this new folder
5. With the OES2 USB disconnected, run the driver installation program 'HSdriver.exe' from the unzip folder. The following window will appear, click **Next**
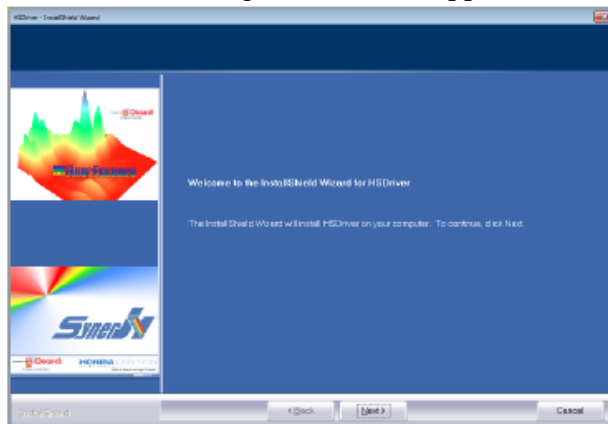
Figure 25. Device driver installation screen

6. Accept the License Agreement, click **Next**
7. On the next page, enter Lam for both User Name and Company Name, click **Next**
8. Use the default destination folder, click **Next**
9. Click **Install** to begin the installation
10. After about 10 seconds, the following screen appears, select **Next**

Figure 26. Device driver installation continued.

11. Accept the EULA, click **Next**.
12. The following screen is displayed while the drivers are being installed
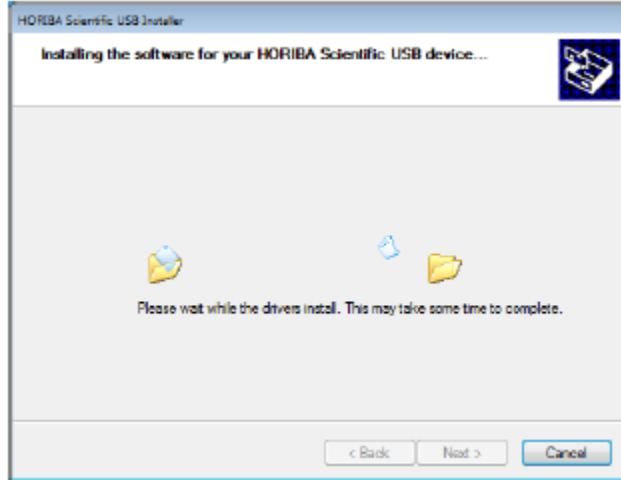
Figure 27. Device driver installation continued.

13. Once completed, the following screen appears indicating the successful installation. Click **Finish**. Click **Finish** again to exit the Installation Wizard.

Figure 28. Device driver installation continued.

14. Direct connect the USB cable between the OES2 and the PC USB 2.X port (avoid using a USB hub). Make sure the OES2 is powered up.
15. Open Device Manager and verify that the device appears as shown below
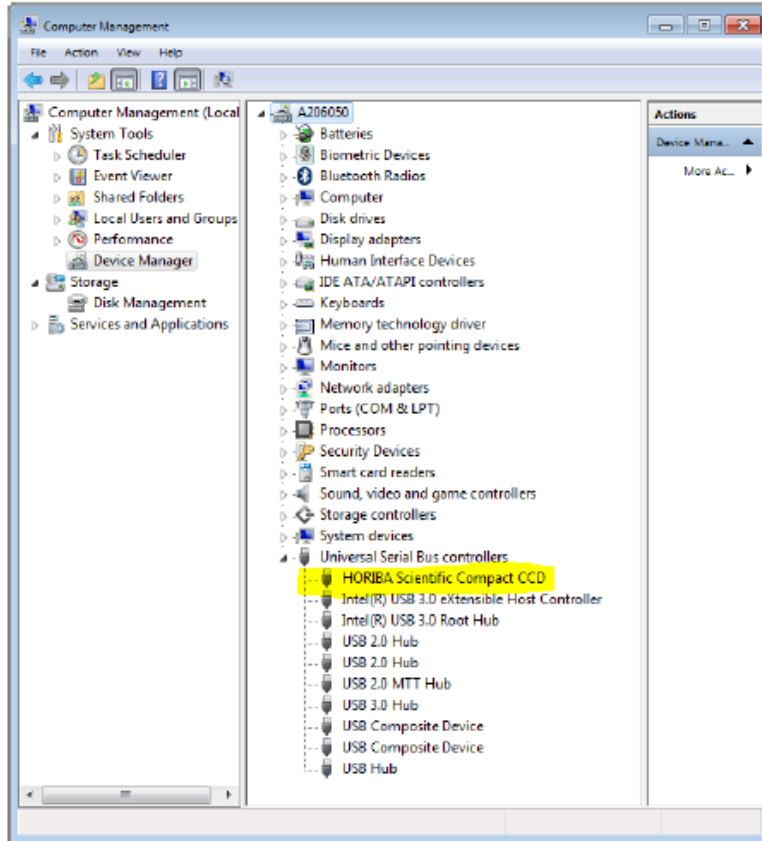
Figure 29. Device driver installation continued.

OES2 Monitor Program Installation

Lam provides a stand-alone program to monitor the OES2 spectra. This program is shipped as a single file in the zip folder. Follow these steps to install this program:

1. In the unzip folder, select 'OESiUnitTest.exe', right-click, and select **Create shortcut**
2. Rename the shortcut **OES2 Monitor**
3. Drag the shortcut to the desktop

Running the OES2 Program

To run the OES2 Monitor program, select the **OES2 Monitor** shortcut from the desktop. The following screen appears. Make sure Device Type 'OES2' is checked in the top right corner.
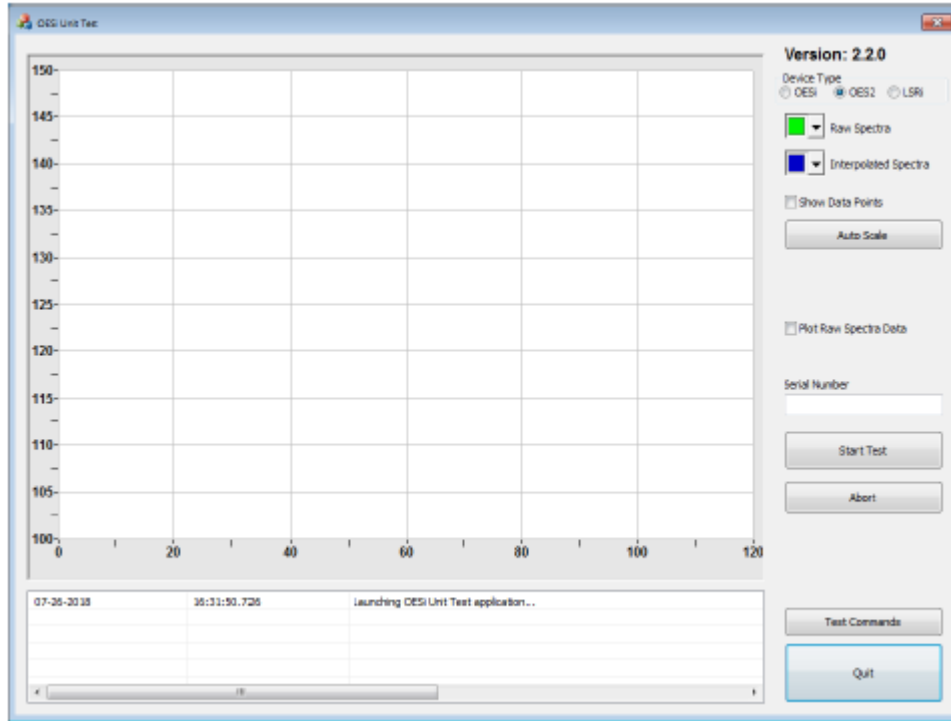
Figure 30. OES software interface

Press the **Start Test** button and the unit should immediately collect and display spectra as shown below.
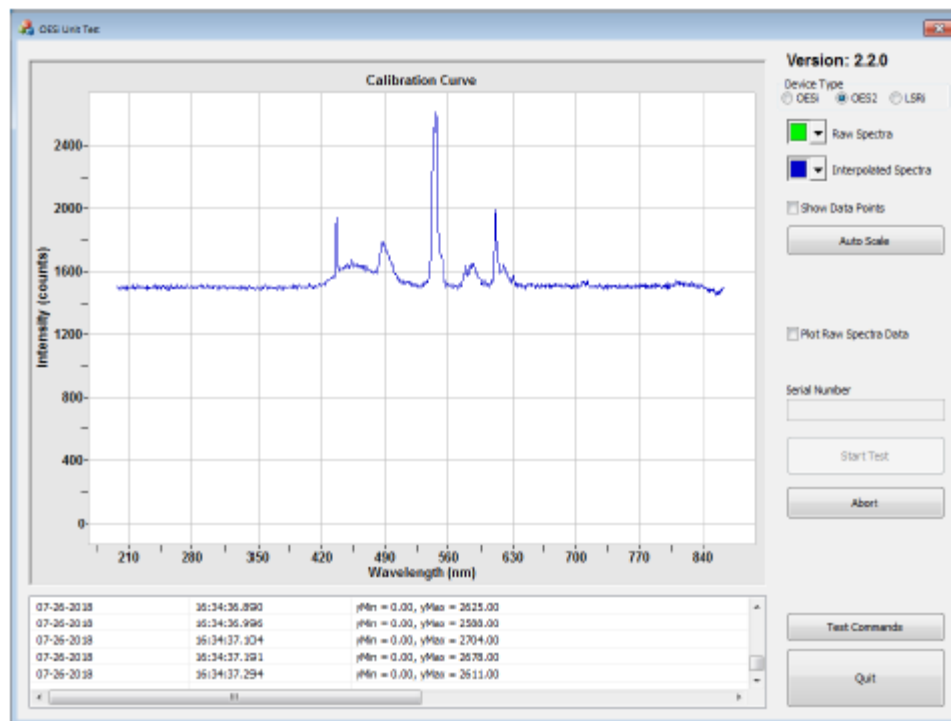
Figure 31. OES software interface with sample spectra

If you need to write the data to a file, click on Test Commands and set the settings to match those in the following figure and also check Save to Data. You may need to click Initialize Device to get the OES to respond to commands in the Test Commands window. Click on Execute to start collecting data, and the file should be saved the OES2 folder.
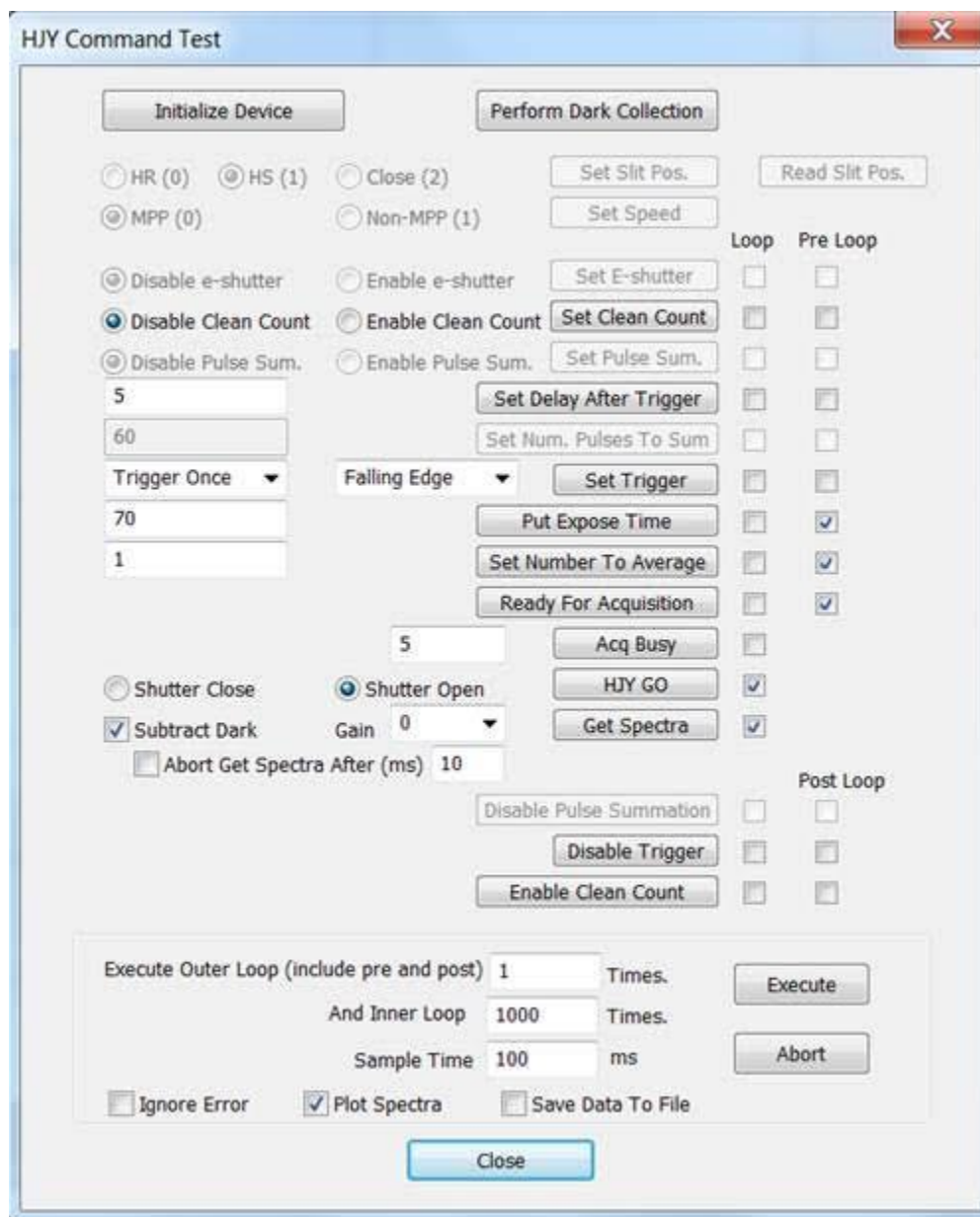
Figure 32. OES software settings for saving data to file.

Appendix G.   X-Ray Photoelectron Spectroscopy Standard Operating Procedure
Emergency Shutdown Procedure

1. Make sure the transfer loading arm from the tube is all the way out of the XPS chamber and then close the gate valve to the transfer tube.
2. Turn off X-ray source by pressing "Power" button on TX-400 unit (should be lit, light will turn off when pressed) and then "HV Off" button ("HV On" button will be illuminated, will turn "HV Off" button green when pressed) on the SL600 unit. If there is time, wait for water to flow to cool the anode for ~ 1 minute. Then, turn off the chiller power.
3. Turn off energy analyzer by turning off ESCA kV and power switches on boxes from bottom to top (lens, detector, control and display)
4. Turn off software by pressing the Stop Expt/Kill Data switch until experiment stops.
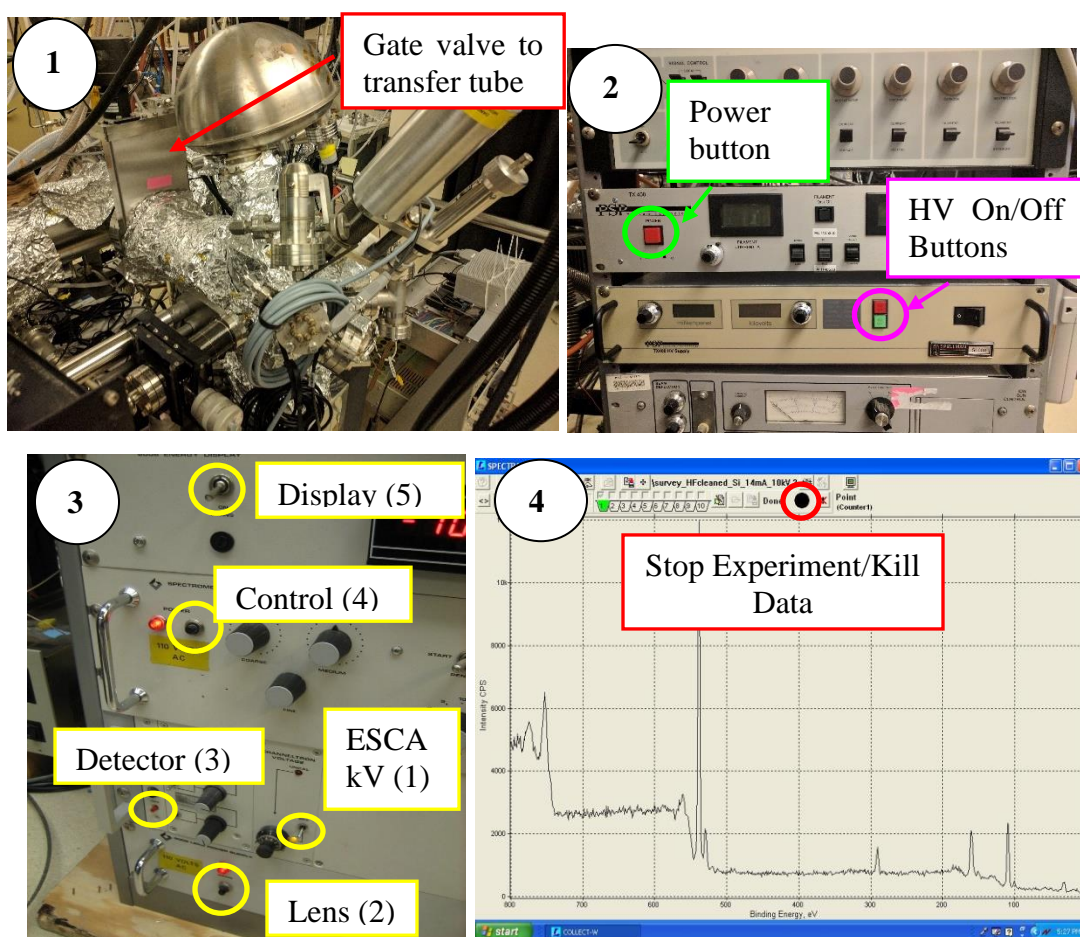
Figure 33. XPS emergency shutdown procedures.

Operating Procedure

1. Before transferring the sample, make sure the x-ray source is backed all the way out to a setting of about 0.2 mm on the motion manipulator. Move the sample stage away from the gate valve to a setting of 5.0 on the axial manipulator. Raise the stage to a setting of 4.25 on the height manipulator. Center the stage in the chamber by setting the lateral

manipulator to a value of 6.2. Ensure the stage is vertical, 263° on the rotation manipulator. **Be careful as the stage rotates easily.**
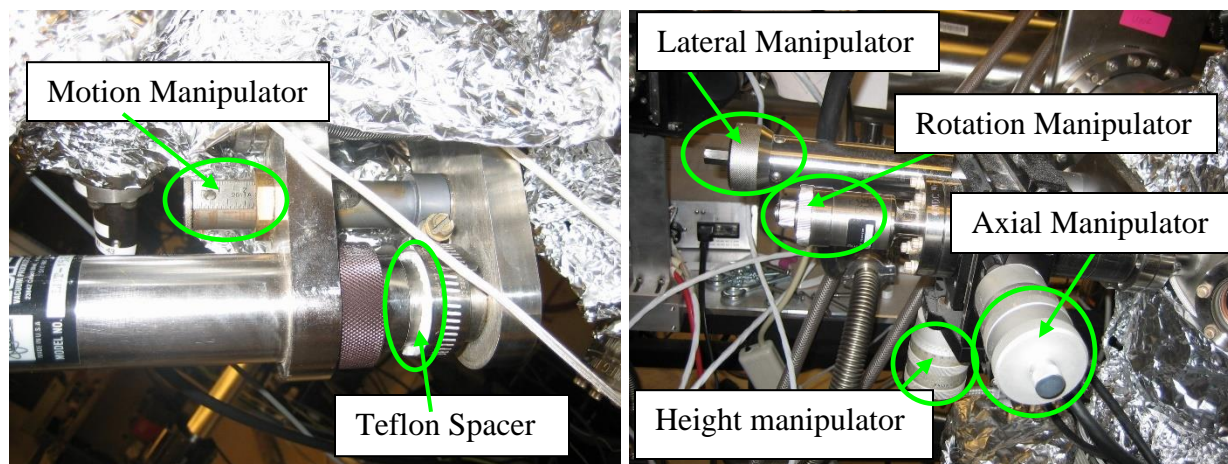
Figure 34. XPS sample manipulators

2. Check the pressure on the XPS using the ion gauge controller (base is ~5 x 10^{-10} Torr, but anything below 5 x 10^{-9} Torr is acceptable. If the pressure is above the 10^{-9} Torr range check the ion pump controller for current reading – should read ~10^5 – 10^6 A). Check the pressure on the TT using its ion gauge controller, pressure should be between ~4 x 10^{-9} to 2 x 10^{-8} Torr (if it is higher check that the gate valve between the turbopump and the TT is open, if it is not, then open it using the controller box (trace the cable to be sure)). Once both pressures are in the requisite range open the gate valve between the TT and XPS using the corresponding controller box (trace the cable if unsure).
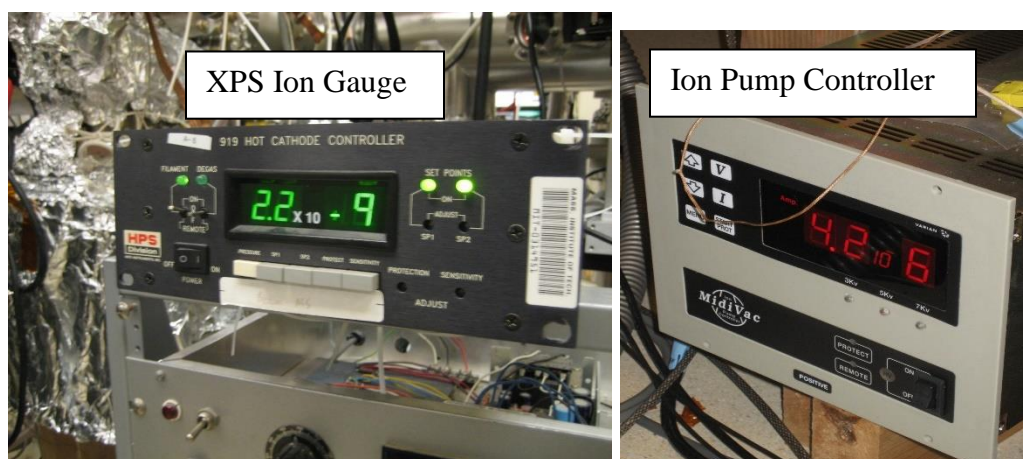
Figure 35. XPS ion gauge readout and ion pump controller

3. Slide the transfer arm into the tube **slowly**, checking the viewport occasionally to make sure that you do not collide with the stage or x-ray source. The manipulator settings on the arm should be X-setting = 5.5 (black) and Y-setting = ~7.5 (black). Make sure the stage is aligned with the sample using the lateral manipulator (value of 6.2) (pictured in

201

Step 1 on previous page). At this point you may have to raise the sample or lower the stage to provide the necessary vertical clearance. Lower the sample onto the stage. Retract the fork completely, being cautious to clear the transfer cart, and close the gate valve between the tube and the XPS.

4. *Move the sample stage closer to the source. The sample stage has been aligned to center the x-ray beam with the center of the puck sample holder at the following position: 4.0 on the axial manipulator, 6.25 on the height manipulator 6.8 on the lateral manipulator. Select the angle theta, which is the angle between the sample surface and the detector axis, using the rotational control - 240° (typical setting) corresponds to a 90° take off angle and 270° to a 60° take-off angle. This angle can be manipulated to take advantage of angle-resolved XPS. Move the x-ray source closer to the sample surface by setting the motion manipulator to a value of 2.2. NOTE: If a sample is substantially thicker than a standard 4" wafer, or the sample is affixed to sit above this height, you will need to adjust the sample stage settings.*

5. Check the pressure in the XPS chamber – it should be at or below 7×10^{-9} Torr. Turn on the analyzer by turning on the switches labeled in the left picture below – from top to bottom: Display, Control, Detector, Lens, then ESCA kV. Turn on the x-ray source by pressing the Power button on the TX-400 unit. Select the Mg or Al anode, and turn on the NESLAB HX-75 Chiller (This should result in the Water Trip Fault light becoming unlit). Press "FILAMENT On/Off" (this should result in the button lighting up with a green light to indicate that the filament is on). At this point neither the Pressure Trip Fault nor Water Trip Fault interlock lights should be lit. If they are seek assistance from a senior lab member or cautiously check all connections from electronics to the unit.
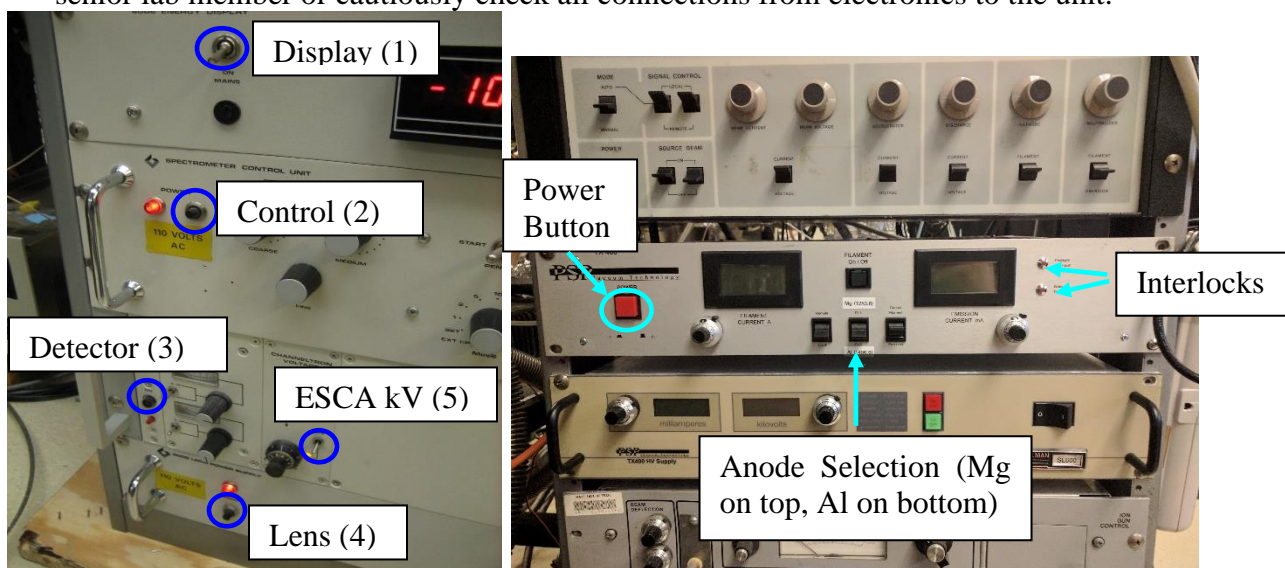
Figure 36. XPS detector and X-ray source controls and start-up order
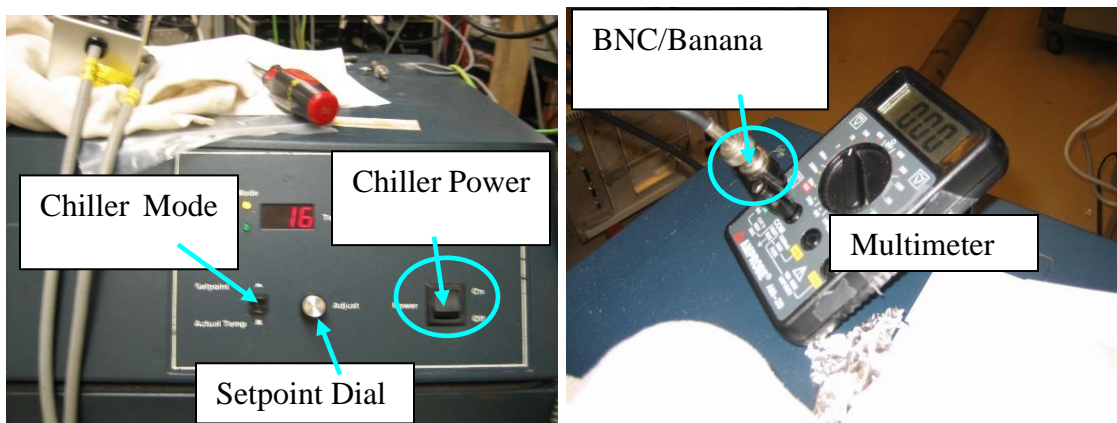
Figure 37. X-ray source chiller front panel controls and flow rate check.

6. Check the chiller setpoint by pushing in the chiller mode switch. This should read 17 degrees. If it has changed adjust the setpoint dial while keeping the mode switch depressed. Check the flow rate by plugging in the BNC/Banana Plug connection to the multimeter. When set to measure DC Voltage the multimeter should give a reading of over 3.4 V. Allow all the electronics to warm up for 10 minutes before running an experiment.

7. Launch the software program SPECTRA by double clicking the icon labeled SPECTRA in the center of the desktop. To save time before the experiment begins you can define your regions (survey, detailed, etc) by clicking the Edit Region Info Button. Also confirm that the software is configured for the anode you selected in Step 5, by clicking the Tools Button, then clicking "Setup Card" in the menu that pops up. In the dialogue box that pops up you can select either Mg (1253.6 eV) or Al (1486.6 eV) in the Excitation field.
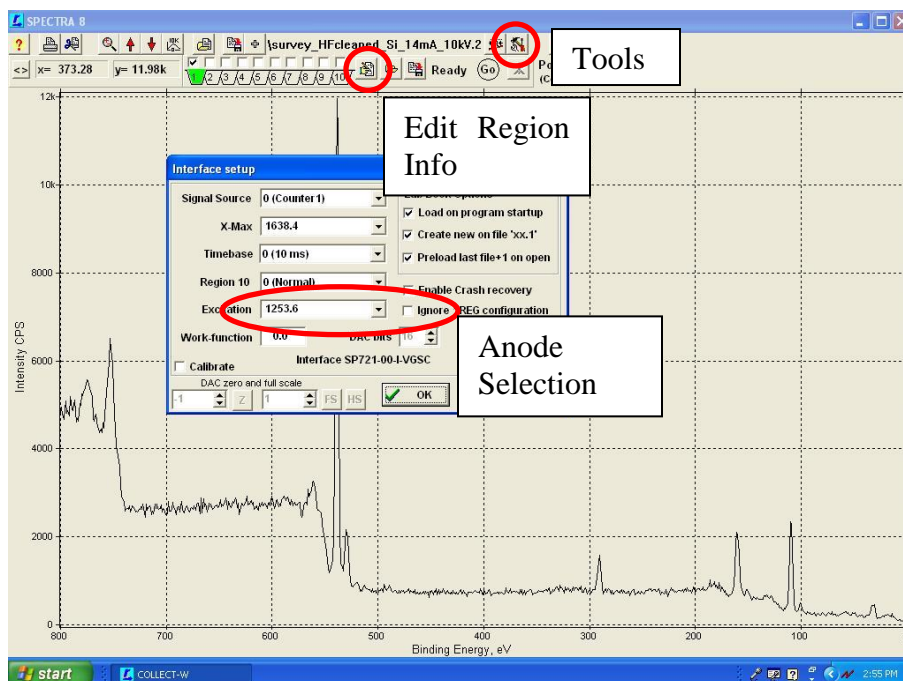
Figure 38. Data acquisition interface

8. Once the electronics have warmed up, check that the Spectrometer Control Unit is set to COMP mode and that the Energy Selector corresponds to the Binding Energy (BE) of the anode you selected earlier in Step 5.
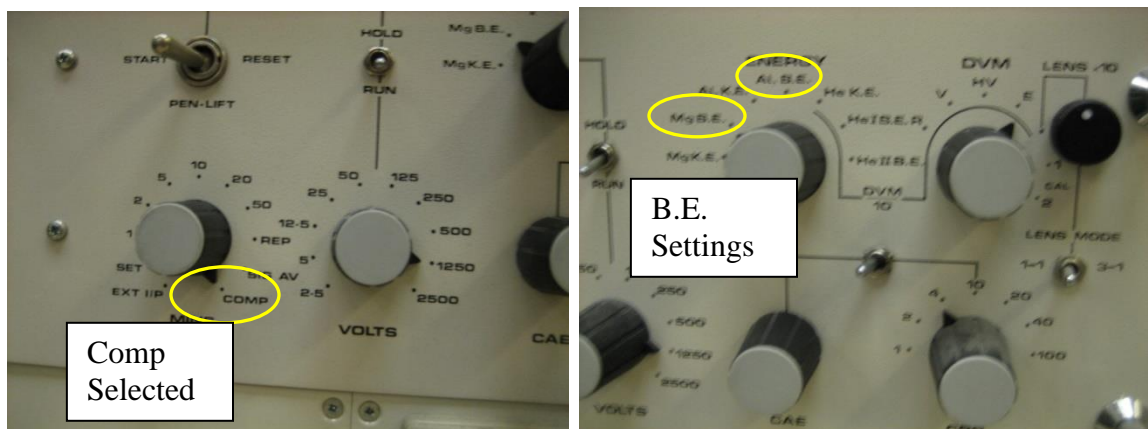
Figure 39. Spectrometer control unit settings.

9. On the TX-400 unit, check to ensure that the "FILAMENT On/Off button" is illuminated. Slowly turn the "FILAMENT CURRENT" potentiometer (dial) located on the left of the panel, below the "FILAMENT CURRENT" display up to 1.75A, being careful to do this over the course of 2-3 minutes to ensure slow warming up of the filament. The pressure can, at times, spike to up to 2×10^{-8} Torr, especially upon reaching ~1.0A, but should decrease quickly. When it has returned to 10^{-9} Torr, go to the SL600 unit *below* the TX-400 unit and press the red "HV ON" button and adjust the voltage potentiometer (right-hand dial) so that the "kilovolts" display reads 10.0kV. At this point, the "EMISSION CURRENT" display on the TX-400 unit (right-hand display) should read between 3.0-5.0 mA. Upon first use of the day, a 1.75A and 10kV setting may not accomplish this level of emission current, in which case, slowly increase the "FILAMENT CURRENT"

10. Monitor the pressure throughout this process, which should still be in the 10^{-9} range. Once the "EMISSION CURRENT" display reads between 3.0 and 5.0mA, turn the "EMISSION CURRENT" potentiometer (right-hand dial on TX-400 unit) to 120%. This is accomplished upon full clockwise rotation of the dial to display a white "1" at the top edge of the dial and corresponding "20" in black lettering on the dial itself (which is graduated into increments of 2%).

11. Locate the toggle switch, labeled "Control Filament" on top and "Emission" on bottom, immediately to the right of the anode selection switch on the TX-400 unit. Upon powering up, this should be set to "Control Filament". Once 10kV and between 3-5mA has been achieved, and the "EMISSION CURRENT" potentiometer is set to 120%, flip this switch down to "Emission". This will put the two units into Emission control mode for x-ray source operation. The voltage on the SL600 unit will remain constant; however, you may see a small change in the "EMISSION CURRENT" and "FILAMENT CURRENT" display.

12. Slowly increase the "kilovolt" potentiometer on the SL600 unit up to 15.00kV. Rarely, some arc-over may occur and the unit will decrease voltage. Once 15.00kV is reached on the "kilovolt" display, return to the "EMISSION CURRENT" potentiometer and slowly

increase this up to 20.00mA while simultaneously monitoring the pressure. The setting of 20mA and 15kV is the **MAXIMUM** allowable power for the x-ray source. **DO NOT** increase past this point on the control units, otherwise there is risk of filament failure. At this point, return to the control computer an begin the run. In the SPECTRA window press the circular button marked "Go" to the right of the Edit Regions Button.
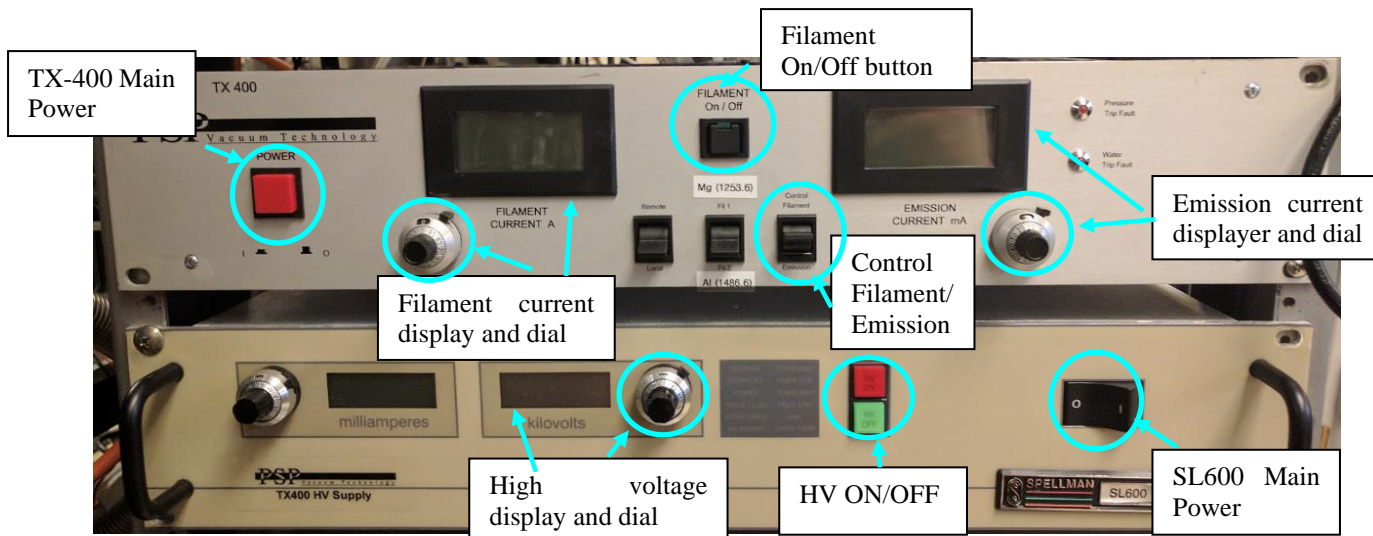
Figure 40. X-ray source controls

13. Once the scans are finished, first ramp down the "EMISSION CURRENT" to 5.0mA and "kilovolts" to 10kV by turning down the dials slowly. Flip the toggle switch back to "Control filament" and continue decreasing the "kilovolts" potentiometer down to 0. Press "HV OFF" (the light should turn green on that button) and then decrease the "FILAMENT CURRENT" potentiometer to 0. Press the "FILAMENT On/Off" button to turn off the filament. The green light should then become unlit. You can leave the "EMISSION CURRENT" potentiometer dial set to where it is for all future runs, as this is the set point that you will use when turning the unit from "Control Filament" mode to "Emission" mode.

14. If you are going to do more scans but the pressure has increased significantly over the course of your run, the system can be left in this state while it pumps down. If the pressure has not increased significantly, you can adjust the region info and then run more scans at your discretion without having to turn off the HV/I_E switches.

15. If you will not run anymore scans, leave the chiller on for a 5-10 minutes after finished to ensure complete cooling of the anode. After waiting the allotted time, you may then press the main I/O power switch on the SL600 unit and red "Power" button on the TX-400 unit to completely turn off the power to both units. Turn off the chiller. Turn off the analyzer electronics by turning off ESCA kV first, then the boxes from bottom to top (in reverse order from Step 5). Remove your sample from the chamber if desired.

Appendix H.   Transfer Tube Standard Operating Procedure
Emergency Shutdown Procedure

1. Ensure that all transfer arms are in the fully withdrawn position (i.e. they are not extended into any reactor chambers).

2. Close all electrically operated gate valves on the system using the control boxes located on the transfer tube table. (In the event of a power outage, this should automatically happen). Visually inspect that this has taken place whenever possible by looking through the appropriate windows on the transfer tube. In the event that a manual gate valve is present, close it by hand.

Gate valves can be seen through these viewports

Example of a manual gate valve

This switch closes the gate valve (trace power cable to gate valve to confirm).
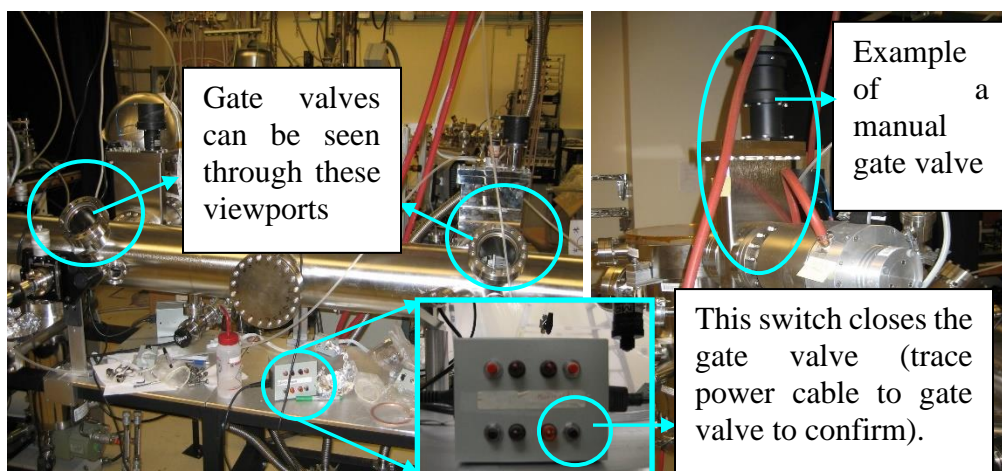
Figure 41. Transfer tube emergency shutdown.

3. Press the stop button on all the turbo pump controllers (in the event of the power outage the controllers should all turn off).

Stop button (read label to confirm)

Figure 42. Turbo pump controller emergency shutdown

4. If power is still available, allow the turbo pumps 10-15 minutes to wind down and then close all the roughing valves between the turbo pumps and their backing mechanical pumps. In the event of power loss close these valves immediately.

Roughing valves between turbo (and cryo) pump and mechanical pump (trace flexible hoses to confirm)
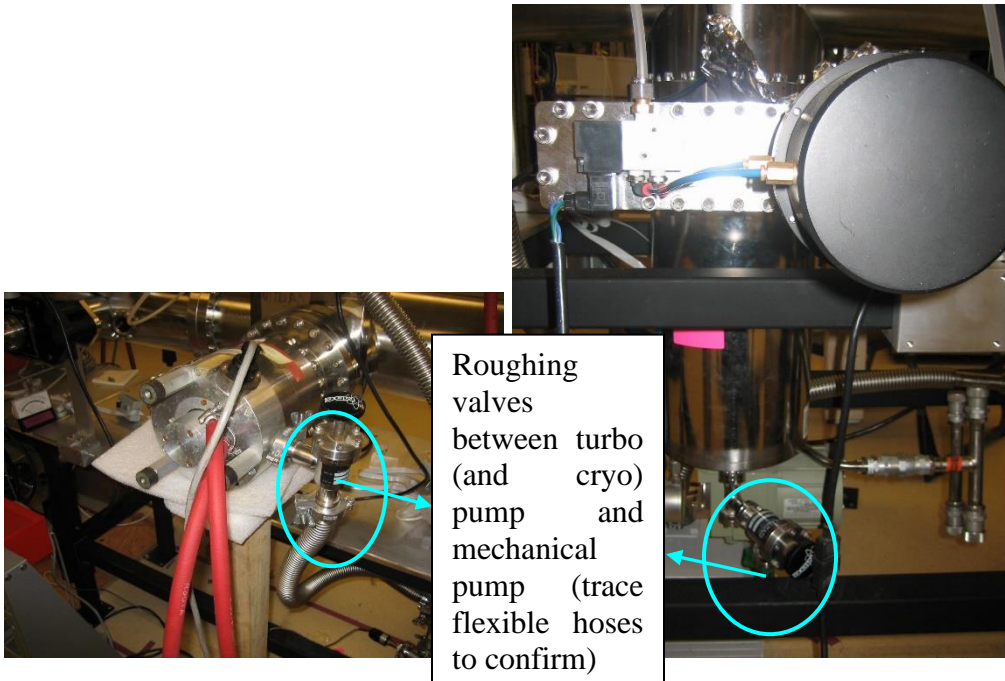
Figure 43. Roughing valve closure.

5. Use your discretion to turn off the mechanical pump on the tube, situated under the table.

Power switch for the pump is located on the pump itself, near the front.
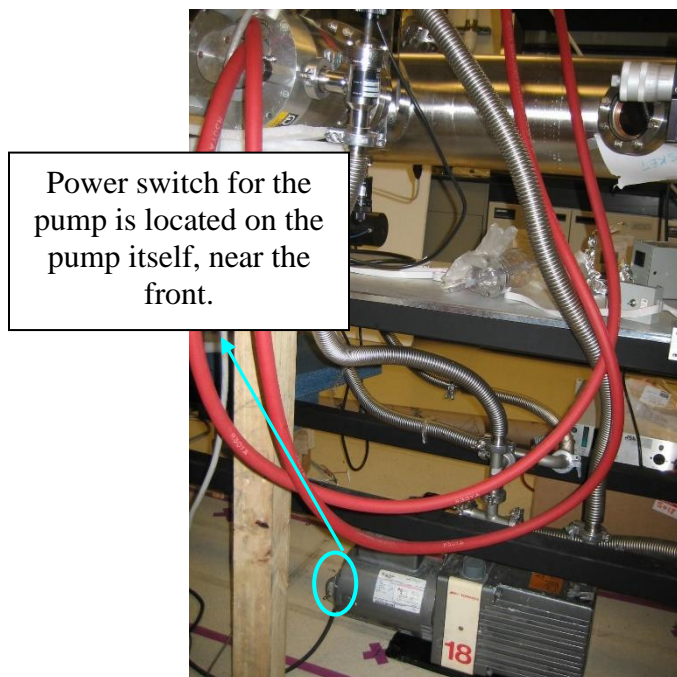
Figure 44. Transfer tube mechanical pump shutdown.

6. The pressure of the transfer tube is displayed on a readout/controller located on the tube table next to the loadlock (this controller monitors the loadlock and transfer tube pressure), facing the north side of the room. Monitor the pressure regularly.
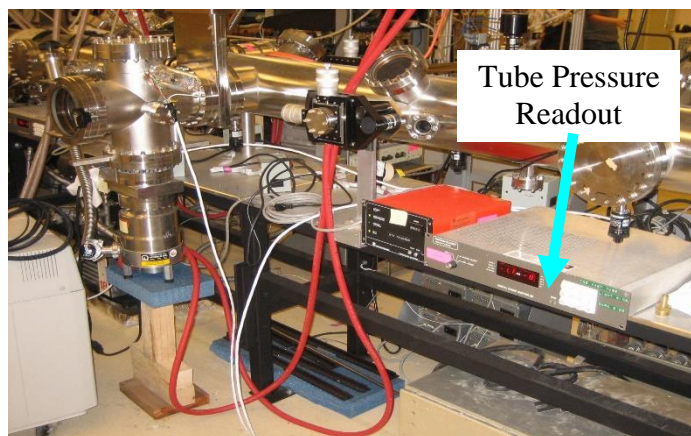
Figure 45. Transfer tube pressure readout.

7. Double check that the gate valve above the cryopump is shut and the rough valve between the cryopump and the mechanical pump is closed (this should have been done in the previous steps). Turn off the CTI 9600 Compressor connected to the cryopump by flipping the white circuit breaker to the "off" position.
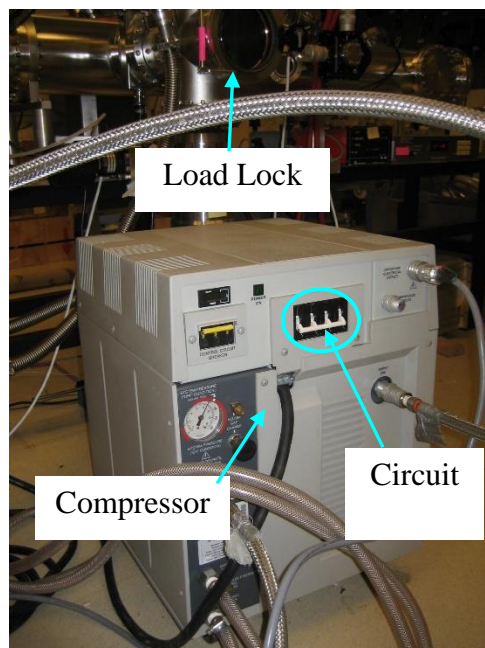
Figure 46. Cryopump compressor controls.

Operating Procedures

Please refer to the following labeled picture when performing Steps 1 and 2.
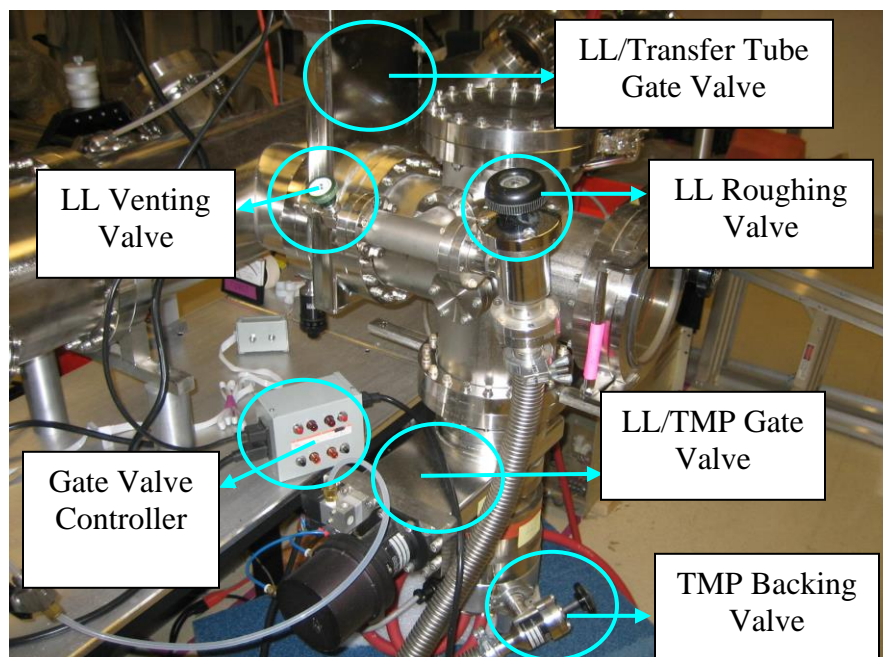
Figure 47. Transfer tube load lock valves and valve controls.

1. To load a sample, the loadlock must first be vented. Ensure that the gate valve between the load lock and the transfer tube is CLOSED. Close the gate valve between the LL turbo and the LL. Ensure that the roughing valve between the LL and its mechanical pump is also closed. Vent the load lock by SLOWLY opening the green venting valve. Within a short time period the load lock door should open easily. Close the green venting valve. **DO NOT UNDER ANY CIRCUMSTANCES OPEN THE GATE VALVE BETWEEN THE LL AND ITS TURBO WHILE THE LOAD LOCK IS VENTED!** Place your sample holder on the pin holder inside of the load lock. If you used screws to secure your sample, ensure that the screws are facing you.

2. Close the LL door and slightly tighten the handle. Isolate the LL turbo pump and the TT turbo pump by closing the roughing valve between these pumps and their backing mechanical pump (trace the flexible hoses to confirm the pump identity). Open the roughing valve between the load lock and the mechanical pump slowly while pressing in the door. Readjust the tightness of the screw handle, but **do not overtighten**. Verify that the LL is pumping down by checking the pressure on the thermocouple gauge attached to the mechanical pump**. Note that the turbopumps can only be isolated for ~5 minutes.** When the pressure has reached ~10 mTorr, close the roughing valve to the LL. Open the valves backing the LL and TT turbo pumps and open the gate valve to the LL turbo. Monitor the pressure using the LL ion gauge.

3. When the pressure in the LL is ~1 x 10^{-6} Torr, sample transfer is possible. In this case the pressure in the tube should be ~10^{-8} Torr. (If the loadlock pressure is ~5 x 10^{-7} Torr, then the pressure in the tube can be ~10^{-9} Torr). When the pressures are at the requisite levels open the gate valve between the LL and the transfer tube. Check for pressure spikes using the TT ion gauge**.**

4. Use the transfer arm to place the sample holder onto the cart (recommended settings are on the transfer arm, but exercise caution when carrying out this operation). Try to ensure that the tines of the loading fork extend past the edge of the sample holder nearest to you. **Also remember that the arm cannot be lifted to its maximum value if it is near the limit of its lateral extension.**

209

Make adjustment in small increments, consistently checking to ensure that nothing is strained. Retract the transfer arm completely and close the LL/TT gate valve.
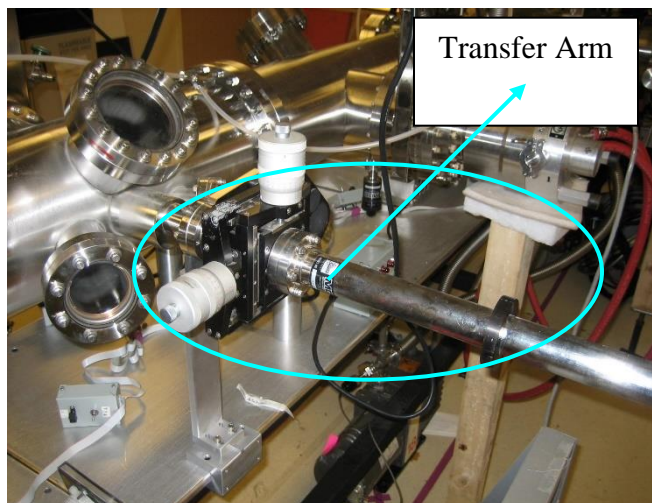
Figure 48. Transfer tube transfer arm.

4. Use the control knob situated at the eastern end of the tube to move the cart to the desired chamber. **If the cart is having problems moving, closing the gate valve between the tube and its turbo pump often rectifies this situation. However, remember to reopen the valve after moving the cart into place.** Use the transfer arm to lift the sample holder off the cart and place it into the chamber. Retract the arm completely and then close the chamber/TT gate valve.
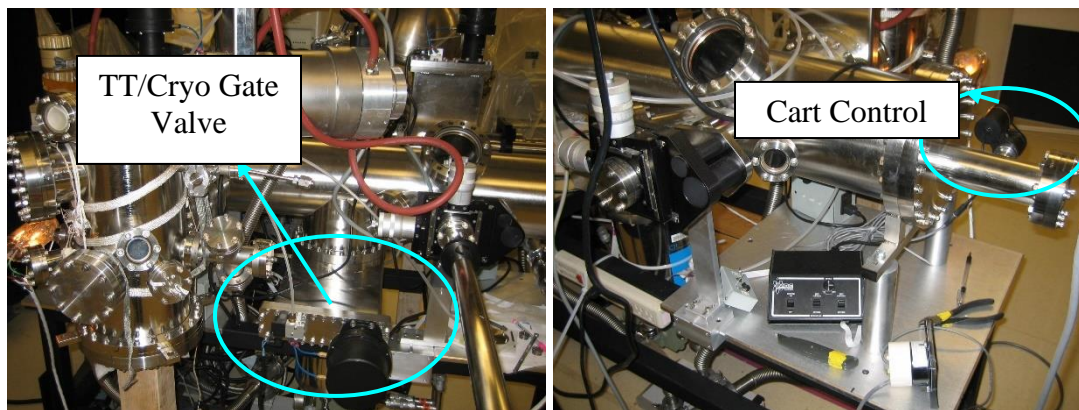
Figure 49. Transfer tube cryopump gate valve and transfer cart controls.

5. To transfer samples from chambers to the transfer tube, first make sure the experiment has been fully halted (i.e. there is no gas flow, plasma, etc.) and that the chamber has been pumped down to its base pressure for ~15-30 minutes, then open the chamber/TT gate valve. Use the transfer arm to remove the sample from the chamber and place it into the transfer cart. Retract the transfer arm completely, close the chamber/TT gate valve.

Appendix I.   HSC Chemistry Procedure
HSC Operating Procedure

1. Run HSC. The menu shown below in Fig. 50 should appear.
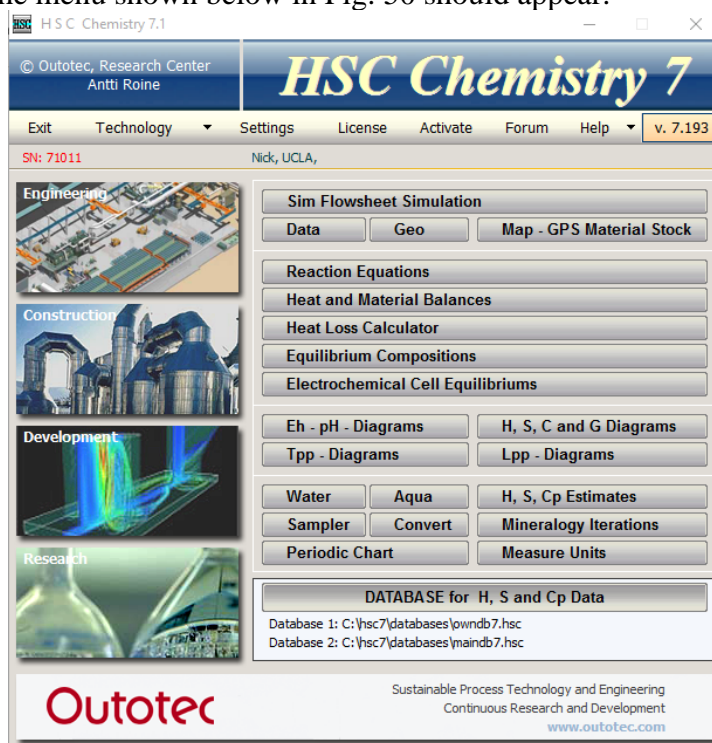
Figure 50. Main Menu of HSC Chemistry 7.

2. Click on "DATABASE for H, S and Cp Data". The menu shown in Fig. 51 below should appear.
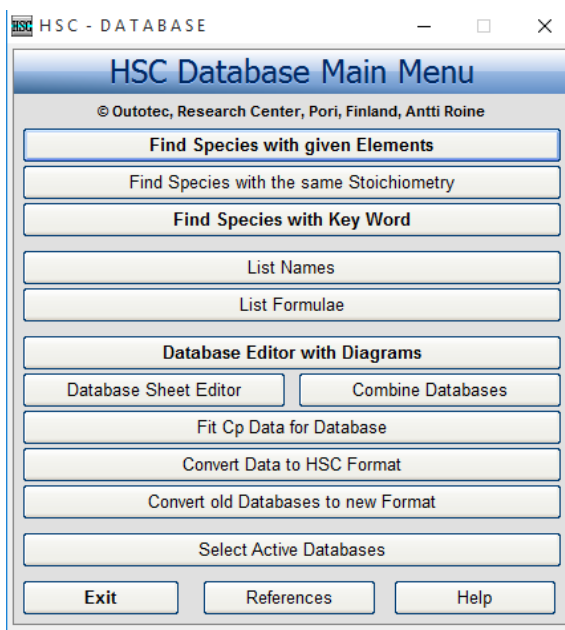
Figure 51. HSC Database Main Menu.

211

3. Click on "Database Editor with Diagrams". The screen shown in Fig. 52 below should appear.
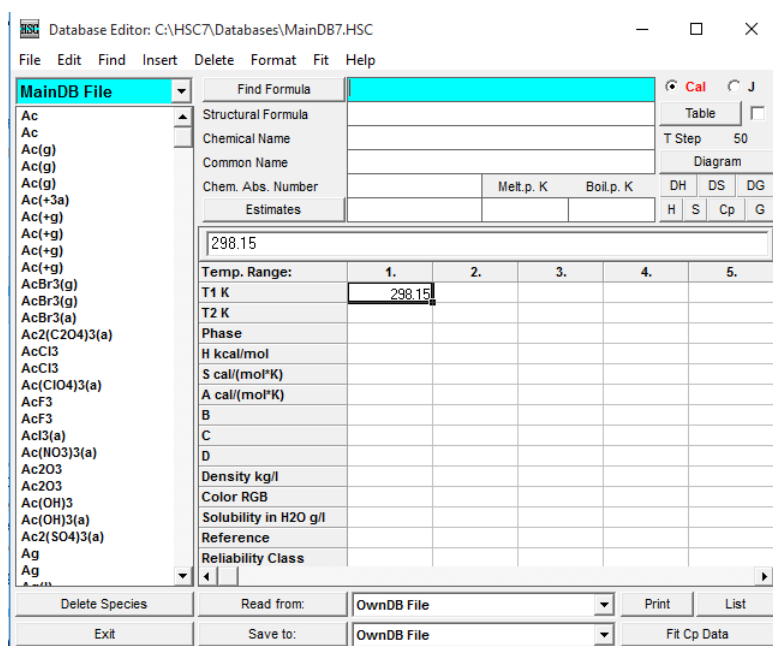
Figure 52. Database Editor.

4. Values can be set to be reported in joules and calories using the radio buttons in the top right hand corner. The database can be searched by entering a formula in the "Find Formula" field highlighted in teal and clicking on "Find Formula". The desired species can be selected from the list on the left hand side.
5. Once a desired species has been found, thermodynamic data can be displayed using the "Table" button in the upper right hand corner. Clicking "Table" should bring up two screens, shown below in Fig. 53 and Fig. 54. SiO_2 is being used as an example compound.
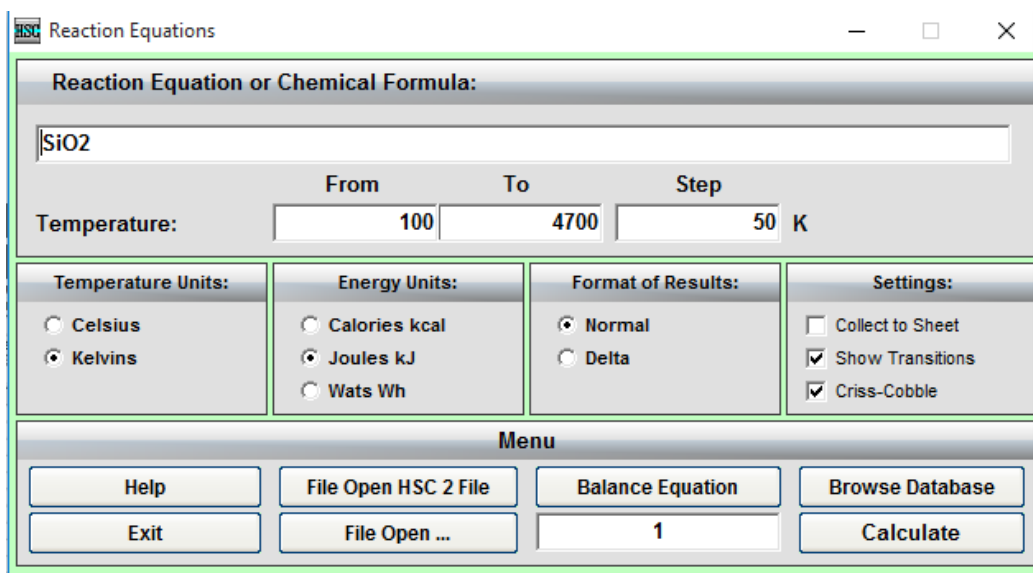
Figure 53. Reaction Equations.

Figure 54. Thermodynamic Results.

6. Results format can be cycled between Normal and Delta using the radio buttons beneath "Format of Results". The table of values given in Fig. 54 can be updated by pressing the "Calculate" button in the lower right of Fig. 54. The temperature range can be altered by changing the temperature values in Fig. 54.

Appendix J.   CasaXPS Procedure
CasaXPS Operating Procedure

1. Run CasaXPS. The screen below in Fig. 55 should appear.

Figure 55. CasaXPS start screen.

2. Raw XPS data can be opened using File > Convert. All the XPS data in the folder will be converted. The XPS spectra will appear on the left and a table showing all the scans from each XPS run will appear on the right, which can be used to navigate the XPS data.

Figure 56. CasaXPS screen with converted, unprocessed data.

3. The XPS data can be calibrated using Spectrum Processing. This can be accessed by clicking on the XPS data then pressing F8 or using Options > Processing…. The peak to calibrate to can be selected by clicking in the XPS data or by entering its numerical BE value in the Measured box, and the value to calibrate to can be entered in the True box. This calibration can then be applied using Apply to Selection, which will make the adjustment for all highlighted XPS scans in the navigation table on the right side of the screen.

214

Figure 55. Energy calibration example using Carbon.

4. The background for the XPS data can be generated using Quantification Parameters. This can be accessed by clicking on the XPS data then pressing F7 or using Options > Narrow Quantify… or Options > Wide Quantify…. Both bring up the same options in windows of differing widths. The background is generated by clicking Create under the Regions tab. Multiple background types, such as Linear, Shirley, and Tougaard are available and can be selected by typing them into the box for BG Type. Changes made in Quantification Parameters must be confirmed by pressing Enter.
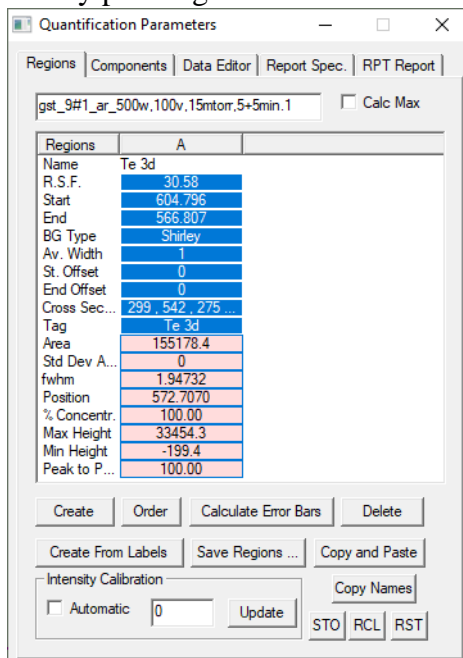
Figure 56. Background generation using Quantification parameters.

5. Once generated, the background will appear in the left side of the screen and will encompass the entirety of the scan. The background should be resized by dragging the edges of the background region around using the mouse. If needed, multiple background regions can be generated.
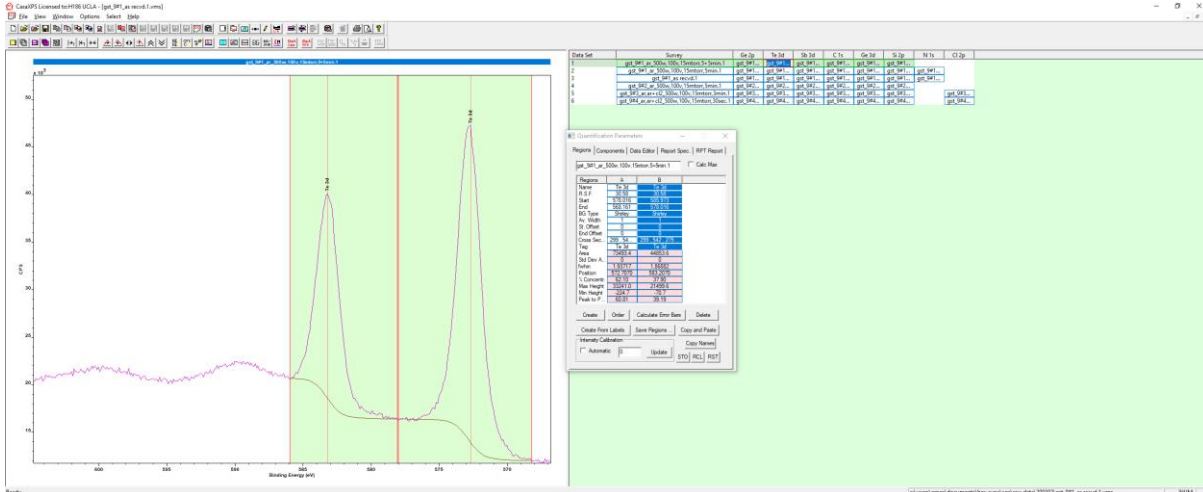
Figure 57. Multiple backgrounds generated and resized.

6. Now that the backgrounds are generated, the XPS data can be fit using the Components tab. Peaks can be generated using Create or Create x 2. Yellow highlighted boxes are constraints and can be given as ranges in the format of x,y or as multiples of another peak's values. The line shape is usually given as a mixture of Gaussian and Lorentzian line shapes. The percentage of the line shape that is Gaussian is specified in the parentheses, for examples, the GL(30) line shape used in Fig. 58 is 30% Gaussian and 70% Lorentzian. Once all the peaks for the model are entered, the data can be fit by clicking Fit Components. The Component data can be exported using the Report Spec. tab, and the XPS curves can be exported using the Save Tab to ASCII button shown in Fig. 58.
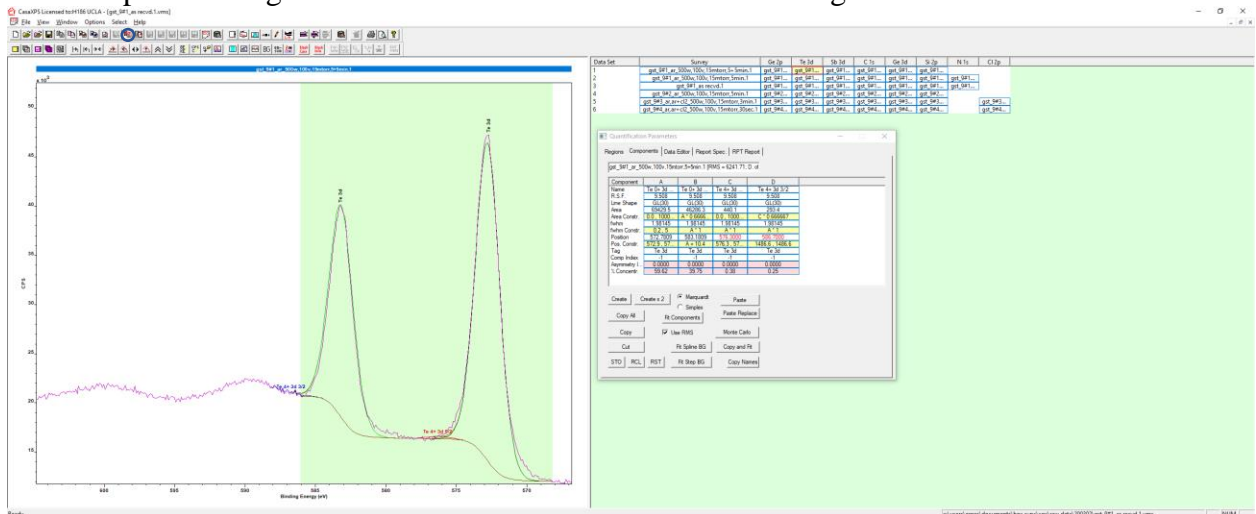
Figure 58. Example of fitted Te 3d data. The Save Tab to ASCII button is circled.

216

BIBLIOGRAPHY

Akola and R. Jones (2007). "Structural phase transitions on the nanoscale: The crucial pattern in the phase-change materials Ge 2 Sb 2 Te 5 and GeTe." Physical Review B **76**(23): 235201.

Akola, R. Jones, S. Kohara, S. Kimura, K. Kobayashi, M. Takata, T. Matsunaga, R. Kojima and N. Yamada (2009). "Experimentally constrained density-functional calculations of the amorphous structure of the prototypical phase-change material Ge 2 Sb 2 Te 5." Physical Review B **80**(2): 020201.

Alman, D. A., D. N. Ruzic and J. Brooks (2000). "A hydrocarbon reaction model for low temperature hydrogen plasmas and an application to the Joint European Torus." Physics of plasmas **7**(5): 1421-1432.

Anam, M. K. and E. C. Ahn (2019). "Understanding the effect of dry etching on nanoscale phase-change memory." Nanotechnology **30**(49): 495202.

Anderson, H., J. Merson and R. Light (1986). "A kinetic model for plasma etching silicon in a SF6/O2 RF discharge." IEEE transactions on plasma science **14**(2): 156-164.

Andrew, K. L. and K. Meissner (1959). "Arc spectrum of germanium." JOSA **49**(2): 146-161.

Arciniega, J. G., E. Prokhorov, F. E. Beltran and G. Trapaga (2012). "Crystallization of Ge: Sb: Te Thin Films for Phase Change Memory Application." Crystallization: Science and Technology: 433.

Badaroglu, M. (2017). "International roadmap for devices and systems." More Moore: https://irds. ieee. org/roadmap-2017.

Bedford, D. and D. Smith (1990). "Variable-temperature selected ion flow tube studies of the reactions of Ar+, Ar+ 2 and ArH+ n (n= 1-3) ions wi H2, HD and D2 at 300 K and 80 K." International journal of mass spectrometry and ion processes **98**(2): 179-190.

Boniardi, M., D. Ielmini, A. L. Lacaita, A. Redaelli, A. Pirovano, I. Tortorelli, M. Allegra, M. Magistretti, C. Bresolin and D. Erbetta (2010). Impact of material composition on the write performance of phase-change memory devices. 2010 IEEE International Memory Workshop, IEEE.

Canvel, Y., S. Lagrasta, C. Boixaderas, S. Barnola, Y. Mazel, K. Dabertrand and E. Martinez (2020). "Modification of Ge-rich GeSbTe surface during the patterning process of phase-change memories." Microelectronic Engineering **221**: 111183.

Canvel, Y., S. Lagrasta, C. Boixaderas, S. Barnola, Y. Mazel and E. Martinez (2019). "Study of Ge-rich GeSbTe etching process with different halogen plasmas." Journal of Vacuum Science & Technology A **37**(3): 031302.

Caravati, M. Bernasconi, T. Kühne, M. Krack and M. Parrinello (2009). "Unravelling the mechanism of pressure induced amorphization of phase change materials." Physical review letters **102**(20): 205502.

Caravati, S., M. Bernasconi, T. D. Kühne, M. Krack and M. Parrinello (2007). "Coexistence of tetrahedral- and octahedral-like sites in amorphous phase change materials." Applied Physics Letters **91**(17): 171906.

Chang, C.-C., C.-Y. Hung, K.-F. Kao, M.-J. Tsai, T.-R. Yew and T.-S. Chin (2010). "Phase transformation in Mg–Sb thin films." Thin Solid Films **518**(24): 7403-7406.

Chatham, H., D. Hils, R. Robertson and A. Gallagher (1983). "Reactions of He+, Ne+, and Ar+ with CH4, C2H6, SiH4, and Si2H6." The Journal of chemical physics **79**(3): 1301-1311.

Christophorou, L. G. and J. K. Olthoff (2000). "Electron interactions with SF 6." Journal of Physical and Chemical Reference Data **29**(3): 267-330.

Clauset, A., S. Arbesman and D. B. Larremore (2015). "Systematic inequality and hierarchy in faculty hiring networks." Science Advances **1**(1): e1400005.

Clay, K., S. Speakman, G. Amaratunga and S. Silva (1996). "Characterization of a-C: H: N deposition from CH4/N2 rf plasmas using optical emission spectroscopy." Journal of applied physics **79**(9): 7227-7233.

Cosby, P. C. and H. Helm (1992). Dissociation rates of diatomic molecules, SRI INTERNATIONAL MENLO PARK CA.

Dan, G., L. Bo, L. Ying, S. Zhitang, R. Wanchun, L. Juntao, X. Zhen, L. Shilong, Z. Nanfei and R. Jiadong (2015). "The effect of oxygen plasma ashing on the resistance of TiN bottom electrode for phase change memory." Journal of Semiconductors **36**(5): 056001.

Davies, D., L. Kline and W. Bies (1989). "Measurements of swarm parameters and derived electron collision cross sections in methane." Journal of Applied Physics **65**(9): 3311-3323.

De Bastiani, R., A. M. Piro, M. G. Grimaldi, E. Rimini, G. A. Baratta and G. Strazzulla (2008). "Ion irradiation-induced local structural changes in amorphous Ge2Sb2Te5 thin film." Applied Physics Letters **92**(24): 241925.

Denysenko, I., S. Xu, J. Long, P. Rutkevych, N. Azarenkov and K. Ostrikov (2004). "Inductively coupled Ar/CH 4/H 2 plasmas for low-temperature deposition of ordered carbon nanostructures." Journal of Applied Physics **95**(5): 2713-2724.

Ellis, W. C., C. R. Lewis, A. P. Openshaw and P. B. Farnsworth (2016). "The effects of added hydrogen on noble gas discharges used as ambient desorption/ionization sources for mass spectrometry." Journal of The American Society for Mass Spectrometry **27**(9): 1539-1549.

Engelhardt, A. and A. Phelps (1963). "Elastic and inelastic collision cross sections in hydrogen and deuterium from transport coefficients." Physical Review **131**(5): 2115.

Feng, J., Y. Zhang, B. Qiao, Y. Lai, Y. Lin, B. Cai, T. Tang and B. Chen (2007). "Si doping in Ge 2 Sb 2 Te 5 film to reduce the writing current of phase change memory." Applied Physics A **87**(1): 57-62.

Gao, F., H. Li, W. Yang, J. Liu, Y.-R. Zhang and Y.-N. Wang (2018). "Experimental and numerical investigations of electron characteristics in 2 MHz and 13.56 MHz inductively coupled hydrogen plasmas with an expansion region." Physics of Plasmas **25**(1): 013515.

Gordillo-Vázquez, F. J., M. Camero and C. Gómez-Aleixandre (2005). "Spectroscopic measurements of the electron temperature in low pressure radiofrequency Ar/H2/C2H2 and Ar/H2/CH4 plasmas used for the synthesis of nanocarbon structures." Plasma Sources Science and Technology **15**(1): 42.

Gourvest, E., B. Pelissier, C. Vallée, A. Roule, S. Lhostis and S. Maitrejean (2012). "Impact of oxidation on Ge2Sb2Te5 and GeTe phase-change properties." Journal of The Electrochemical Society **159**(4): H373-H377.

Guerin, S., B. Hayden, D. W. Hewak and C. Vian (2017). "Synthesis and Screening of Phase Change Chalcogenide Thin Film Materials for Data Storage." ACS Comb Sci **19**(7): 478-491.

Guerin, S., B. Hayden, D. W. Hewak and C. Vian (2017). "Synthesis and Screening of Phase Change Chalcogenide Thin Film Materials for Data Storage." ACS Combinatorial Science **19**(7): 478-491.

Gupta, V., S. Kapur, S. Saurabh and A. Grover (2019). "Resistive Random Access Memory: A Review of Device Challenges." IETE Technical Review: 1-14.

Hayashi, M. (1990). "Electron collision cross sections determined from beam and swarm data by Boltzmann analysis Nonequilibrium Processes in Partially Ionized Gases ed M Capitelli and JN Bardsley." NATO ASI Series B: Physics **1990**: 220.

Haynes, W. (2011). "CRC Handbook of Chemistry and Physics, (Internet Version 2011)." Taylor Francis Group: Boca Raton, FL.

Heintze, M., M. Magureanu and M. Kettlitz (2002). "Mechanism of C 2 hydrocarbon formation from methane in a pulsed microwave plasma." Journal of Applied Physics **92**(12): 7022-7031.

Herrebout, D., A. Bogaerts, M. Yan, R. Gijbels, W. Goedheer and E. Dekempeneer (2001). "One-dimensional fluid model for an rf methane plasma of interest in deposition of diamond-like carbon layers." Journal of Applied Physics **90**(2): 570-579.

Hisamoto, D., W.-C. Lee, J. Kedzierski, H. Takeuchi, K. Asano, C. Kuo, E. Anderson, T.-J. King, J. Bokor and C. Hu (2000). "FinFET-a self-aligned double-gate MOSFET scalable to 20 nm." IEEE Transactions on Electron Devices **47**(12): 2320-2325.

Houška, J., E. M. Peña-Méndez, J. Kolář, J. Přikryl, M. Pavlišta, M. Frumar, T. Wágner and J. Havel (2014). "Laser desorption time-of-flight mass spectrometry of atomic switch memory Ge2Sb2Te5bulk materials and its thin films." Rapid Communications in Mass Spectrometry **28**(7): 699-704.

Iio, M., M. Goto, H. Toyoda and H. Sugai (1995). "Relative Cross Sections for Electron-Impact Dissociation of SF6 into SFx (x= 1− 3) Neutral Radicals." Contributions to Plasma Physics **35**(4-5): 405-413.

Jiménez-Redondo, M., M. Cueto, J. L. Doménech, I. Tanarro and V. J. Herrero (2014). "Ion kinetics in Ar/H 2 cold plasmas: the relevance of ArH+." RSC advances **4**(107): 62030-62041.

Johnson, B. (1999). Guide to Operations for the 3 cm Ion Source. Alexandria, VA, Commonwealth Scientific Corporation.

Kang, M.-H. Jeon, J.-Y. Park, M. S. Jhon and G.-Y. Yeom (2011). "Etch Damage of Ge2Sb2Te5 for Different Halogen Gases." Japanese Journal of Applied Physics **50**(8): 086501.

Kang, J. S. Oh, B. J. Park, S. W. Kim, J. T. Lim, G. Y. Yeom, C. J. Kang and G. J. Min (2008). "X-ray photoelectron spectroscopic study of Ge[sub 2]Sb[sub 2]Te[sub 5] etched by fluorocarbon inductively coupled plasmas." **93**(4): 043126.

Kau, D., S. Tang, I. V. Karpov, R. Dodge, B. Klehn, J. A. Kalb, J. Strand, A. Diaz, N. Leung and J. Wu (2009). A stackable cross point phase change memory. Electron Devices Meeting (IEDM), 2009 IEEE International, IEEE.

Keller, R. C., M. Seelmann-Eggebert and H. J. Richter (1995). "Reaction chemistry and resulting surface structure of HgCdTe etched in CH4/H2 and H2 ECR plasmas." Journal of Electronic Materials **24**(9): 1155-1160.

Kent, A. D. and D. C. Worledge (2015). "A new spin on magnetic memories." Nature nanotechnology **10**(3): 187.

Klement, P., C. Feser, B. Hanke, K. v. Maydell and C. Agert (2013). "Correlation between optical emission spectroscopy of hydrogen/germane plasma and the Raman crystallinity factor of germanium layers." Applied Physics Letters **102**(15): 152109.

Kline, L. E., W. D. Partlow and W. E. Bies (1989). "Electron and chemical kinetics in methane rf glow-discharge deposition plasmas." Journal of Applied Physics **65**(1): 70-78.

Kokkoris, G., A. Panagiotopoulos, A. Goodyear, M. Cooke and E. Gogolides (2009). "A global model for SF6 plasmas coupling reaction kinetics in the gas phase and on the surface of the reactor walls." Journal of Physics D: Applied Physics **42**(5): 055209.

Kolobov, A. V., J. Tominaga, P. Fons and T. Uruga (2003). "Local structure of crystallized GeTe films." Applied Physics Letters **82**(3): 382-384.

Kraus, P., C. Gösweiner, A. Tamtögl, F. Apolloner and W. E. Ernst (2016). "Adhesion properties of hydrogen on Sb(111) probed by helium atom scattering." EPL (Europhysics Letters) **114**(5): 56001.

Kurepa, M. and D. Belic (1978). "Electron-chlorine molecule total ionisation and electron attachment cross sections." Journal of Physics B: Atomic and Molecular Physics **11**(21): 3719.

Lacaita, A. L. (2006). "Phase change memories: State-of-the-art, challenges and perspectives." Solid-State Electronics **50**(1): 24-31.

Lallement, L., A. Rhallabi, C. Cardinaud, M. Peignon-Fernandez and L. L. Alves (2009). "Global model and diagnostic of a low-pressure SF6/Ar inductively coupled plasma." Plasma Sources Science and Technology **18**(2): 025001.

Lee, C., D. Graves, M. Lieberman and D. Hess (1994). "Global model of plasma chemistry in a high density oxygen discharge." Journal of the Electrochemical Society **141**(6): 1546.

Lee, C. and M. A. Lieberman (1995). "Global model of Ar, O2, Cl2, and Ar/O2 high-density plasma discharges." Journal of Vacuum Science & Technology A: Vacuum, Surfaces, and Films **13**(2): 368-380.

Lennon, M., K. Bell, H. Gilbody, J. Hughes, A. Kingston, M. Murray and F. Smith (1988). "Recommended data on the electron impact ionization of atoms and ions: Fluorine to nickel." Journal of Physical and Chemical Reference Data **17**(3): 1285-1363.

Li, J., Y. Xia, B. Liu, G. Feng, Z. Song, D. Gao, Z. Xu, W. Wang, Y. Chan and S. Feng (2016). "Direct evidence of reactive ion etching induced damages in Ge2Sb2Te5 based on different halogen plasmas." Applied Surface Science **378**: 163-166.

Lide, D. R. (2004). CRC handbook of chemistry and physics, CRC press.

Lu, Y., S. Song, Y. Gong, Z. Song, F. Rao, L. Wu, B. Liu and D. Yao (2011). "Ga-Sb-Se material for low-power phase change memory." Applied Physics Letters **99**(24): 243111.

Luo, Y.-R. (2007). Comprehensive handbook of chemical bond energies, CRC press.

Malyshev, M. and V. Donnelly (1997). "Determination of electron temperatures in plasmas by multiple rare gas optical emission, and implications for advanced actinometry." Journal of Vacuum Science & Technology A: Vacuum, Surfaces, and Films **15**(3): 550-558.

Malyshev, M. V., V. M. Donnelly and S. Samukawa (1998). "Ultrahigh frequency versus inductively coupled chlorine plasmas: Comparisons of Cl and Cl2 concentrations and electron temperatures measured by trace rare gases optical emission spectroscopy." Journal of Applied Physics **84**(3): 1222-1230.

Martín, I., M. Vetter, A. Orpella, C. Voz, J. Puigdollers and R. Alcubilla (2002). "Surface passivation of n-type crystalline Si by plasma-enhanced-chemical-vapor-deposited amorphous SiC x: H and amorphous SiC x N y: H films." Applied Physics Letters **81**(23): 4461-4463.

Massobrio, C., J. Du, M. Bernasconi and P. S. Salmon (2015). Molecular dynamics simulations of disordered materials, Springer.

Mendez, I., F. J. Gordillo-Vázquez, V. J. Herrero and I. Tanarro (2006). "Atom and ion chemistry in low pressure hydrogen DC plasmas." The Journal of Physical Chemistry A **110**(18): 6060-6066.

Miao, N., B. Sa, J. Zhou, L. Xu, Z. Sun and R. Ahuja (2010). "Investigation on Ge 5− x Sb x Te 5 phase-change materials by first-principles method." Applied Physics A **99**(4): 961-964.

Moore, G. E. (2006). "Cramming more components onto integrated circuits, Reprinted from Electronics, volume 38, number 8, April 19, 1965, pp. 114 ff." IEEE Solid-State Circuits Society Newsletter **11**(3): 33-35.

Morgan, W. (1992). "A critical evaluation of low-energy electron impact cross sections for plasma processing modeling. i: Cl 2, F 2, and HCl." Plasma Chemistry and Plasma Processing **12**(4): 449-476.

Moulder, J. F. (1995). "Handbook of X-ray photoelectron spectroscopy." Physical electronics: 230-232.

Nakano, T., H. Toyoda and H. Sugai (1991). "Electron-impact dissociation of methane into CH3 and CH2 radicals II. Absolute cross sections." Japanese Journal of Applied Physics **30**(11R): 2912.

Outka, D. A. (1990). "The adsorption of atomic hydrogen on tellurium and formation of H2Te." Surface science **235**(2-3): L311-L318.

Park, J. H., J. H. Kim, D. H. Ko, Z. Wu, D. H. Ahn, S. O. Park and K. H. Hwang (2016). "Use of NH3 etchant for voids suppression to enhance set cycles in CGeSbTe-based phase change memory devices." Thin Solid Films **616**: 502-506.

Pokrovski, G. S. and J. Schott (1998). "Experimental study of the complexation of silicon and germanium with aqueous organic species: implications for germanium and silicon transport and Ge/Si ratio in natural waters." Geochimica et Cosmochimica Acta **62**(21-22): 3413-3428.

Rao, F., Z. Song, K. Ren, X. Li, L. Wu, W. Xi and B. Liu (2009). "Sn 12 Sb 88 material for phase change memory." Applied Physics Letters **95**(3): 032105.

Raoux, S., W. Wełnic and D. Ielmini (2009). "Phase change materials and their application to nonvolatile memories." Chemical reviews **110**(1): 240-267.

Rauf, S., P. L. Ventzek, I. C. Abraham, G. A. Hebner and J. R. Woodworth (2002). "Charged species dynamics in an inductively coupled Ar/SF 6 plasma discharge." Journal of applied physics **92**(12): 6998-7007.

Rogoff, G. L., J. M. Kramer and R. B. Piejak (1986). "A model for the bulk plasma in an RF chlorine discharge." IEEE transactions on plasma science **14**(2): 103-111.

Roine, A. (2018). HSC Chemistry. Pori, Outotec.

Ryan, K. and I. Plumb (1990). "A model for the etching of silicon in SF 6/O 2 plasmas." Plasma chemistry and plasma processing **10**(2): 207-229.

Sa, B., J. Zhou, Z. Song, Z. Sun and R. Ahuja (2011). "Pressure-induced topological insulating behavior in the ternary chalcogenide Ge 2 Sb 2 Te 5." Physical Review B **84**(8): 085130.

Saalfeld, F. E. and H. J. Svec (1963). "The mass spectra of volatile hydrides. I. The monoelemental hydrides of the group IVB and VB elements." Inorganic Chemistry **2**(1): 46-50.

Salahuddin, S., K. Ni and S. Datta (2018). "The era of hyper-scaling in electronics." Nature Electronics **1**(8): 442-450.

Schulz-von Der Gathen, V., J. Röpcke, T. Gans, M. Käning, C. Lukas and H. Döbele (2001). "Diagnostic studies of species concentrations in a capacitively coupled RF plasma containing CH4-H2-Ar." Plasma Sources Science and Technology **10**(3): 530.

Seah, M. (2005). "An accurate semi-empirical equation for sputtering yields, II: for neon, argon and xenon ions." Nuclear Instruments and Methods in Physics Research Section B: Beam Interactions with Materials and Atoms **229**(3-4): 348-358.

Seah, M., C. Clifford, F. Green and I. Gilmore (2005). "An accurate semi-empirical equation for sputtering yields I: for argon ions." Surface and interface analysis **37**(5): 444-458.

Shen, M., T. Lill, N. Altieri, J. Hoang, S. Chiou, J. Sims, A. McKerrow, R. Dylewicz, E. Chen, H. Razavi and J. P. Chang (2020). "A Review on Recent Progress in Patterning Phase Change Materials." Journal of Vacuum Science & Technology A.

Shim, K. H., Y. H. Kil, H. D. Yang, B. K. Park, J. H. Yang, S. Kang, T. S. Jeong and T. S. Kim (2012). "Characteristics of germanium dry etching using inductively coupled SF6 plasma." Materials Science in Semiconductor Processing **15**(4): 364-370.

Smolinsky, G., R. Chang and T. Mayer (1981). "Plasma etching of III–V compound semiconductor materials and their oxides." Journal of Vacuum Science and Technology **18**(1): 12-16.

Stanski, T. and B. Adamczyk (1983). "Measurements of dissociative ionization cross section of SF6 by using double collector cycloidal mass spectrometer." International Journal of Mass Spectrometry and Ion Physics **46**: 31-34.

Sun, Z., S. Kyrsta, D. Music, R. Ahuja and J. M. Schneider (2007). "Structure of the Ge–Sb–Te phase-change materials studied by theory and experiment." Solid state communications **143**(4-5): 240-244.

Sun, Z., J. Zhou, A. Blomqvist, B. Johansson and R. Ahuja (2009). "Formation of large voids in the amorphous phase-change memory Ge 2 Sb 2 Te 5 alloy." Physical review letters **102**(7): 075504.

Tachibana, K., M. Nishida, H. Harima and Y. Urano (1984). "Diagnostics and modelling of a methane plasma used in the chemical vapour deposition of amorphous carbon films." Journal of Physics D: Applied Physics **17**(8): 1727.

Talib, Z. A. and M. Saporoschenko (1992). "Drift-tube studies of SF3+ and SF5+ ions in SF6 gas." International journal of mass spectrometry and ion processes **116**(1): 1-12.

Tarnovsky, V., H. Deutsch, K. Martus and K. Becker (1998). "Electron Impact Ionization of the SF 5 and SF 3 free radicals." The Journal of chemical physics **109**(16): 6596-6600.

Votta, A., F. Pipia, E. Ravizza, S. Spadoni, S. Rossini, L. Brattico and M. Alessandri (2012). Effect of wet cleanings on GST surface: XPS characterization. Solid State Phenomena, Trans Tech Publ.

Wagner, C., W. Riggs, L. Davis, J. Moulder and G. Muilenberg (1979). "Handbook of X-ray Photoelectron Spectroscopy, Perkin-Elmer Corp." Eden Prairie, MN **38**.

Wang, B. Liu, Z. Song, S. Feng, Y. Xiang and F. Zhang (2009). "Acid and Surfactant Effect on Chemical Mechanical Polishing of Ge[sub 2]Sb[sub 2]Te[sub 5]." Journal of The Electrochemical Society **156**(9).

Wang, G., C. Shi, R. Hu, L. Zhao, G. Wang, H. Diao and W. Wang (2015). "In situ optical emission spectroscopy diagnostics of glow discharges in SiH 4/GeH 4/H 2." RSC Advances **5**(23): 18029-18034.

Wong, H.-S. P., S. Raoux, S. Kim, J. Liang, J. P. Reifenberg, B. Rajendran, M. Asheghi and K. E. Goodson (2010). "Phase change memory." Proceedings of the IEEE **98**(12): 2201-2227.

Wong, H.-S. P. and S. Salahuddin (2015). "Memory leads the way to better computing." Nature nanotechnology **10**(3): 191.

Yamada, N. (1996). "Erasable Phase-Change Optical Materials." MRS Bulletin **21**(9): 48-50.

Yoon, S.-M., N.-Y. Lee, S.-O. Ryu, Y.-S. Park, S.-Y. Lee, K.-J. Choi and B.-G. Yu (2005). "Etching characteristics of Ge2Sb2Te5 using high-density helicon plasma for the nonvolatile phase-change memory applications." Japanese Journal of Applied Physics **44**(6L): L869.

Yoon, S.-M., N.-Y. Lee, S.-O. Ryu, Y.-S. Park, S.-Y. Lee, K.-J. Choi and B.-G. Yu (2005). "Etching Characteristics of Ge2Sb2Te5Using High-Density Helicon Plasma for the Nonvolatile Phase-Change Memory Applications." Japanese Journal of Applied Physics **44**(No. 27): L869-L872.

Zheng, J., A. Iijima and N. Furuta (2001). "Complexation effect of antimony compounds with citric acid and its application to the speciation of antimony (III) and antimony (V) using HPLC-ICP-MS." Journal of Analytical Atomic Spectrometry **16**(8): 812-818.

Zhou, X., L. Wu, Z. Song, F. Rao, K. Ren, C. Peng, S. Song, B. Liu, L. Xu and S. Feng (2013). "Phase transition characteristics of Al-Sb phase change materials for phase change memory application." Applied Physics Letters **103**(7): 072114.

Air Liquide. (2010). "Hydrogen telluride MSDS." Retrieved Apr 24, 2020, from https://www.msds-al.co.uk/assets/file_assets/SDS_074-CLP-HYDROGEN%20TELLURIDE.pdf.

American Elements. (2015, May 15). "Trimethylantimony MSDS." Retrieved Apr 24, 2020, from https://www.americanelements.com/trimethylantimony-594-10-5

EpiChem Inc. (2005, May). "Dimethyltelluride MSDS." Retrieved Apr 24, 2020, from https://web.archive.org/web/20060319183512/http://www.epichem.com/metalorganics/pdfs/dimethyltelluride.pdf.

Sigma-Aldrich Corp. (2020, Apr 4). "Tetramethylgermanium MSDS." Retrieved Apr 24, 2020, from https://www.sigmaaldrich.com/MSDS/MSDS/DisplayMSDSPage.do?country=US&language=en&productNumber=396354&brand=ALDRICH&PageToGoToURL=%2Fsafety-center.html